DEVELOPMENT OF SUPPORTED COBALT CATALYST FOR FISCHER-TROPSCH SYNTHESIS

A Thesis Submitted to the College of Graduate and Postdoctoral Studies

in Partial Fulfillment of the Requirements For the

Degree of Doctor of Philosophy

in the Department of Chemical and Biological Engineering

University of Saskatchewan

Saskatoon, SK, Canada

By

VAHID VOSOUGHI

PERMISSION TO USE

In presenting this thesis in partial fulfilment of the requirements for a Postgraduate degree from the University of Saskatchewan, I agree that the Libraries of this University may make it freely available for inspection. I further agree that permission for copying of this thesis in any manner, in whole or in part, for scholarly purposes may be granted by Dr. Ajay K. Dalai and Dr. Nicholas Abatzoglou who supervised my thesis work, or in their absence, by the Head of the Department or the Dean of the College in which my thesis work was done. It is understood that any copying or publication or use of this thesis or parts thereof for financial gain shall not be allowed without my written permission. It is also understood that due recognition shall be given to me and to the University of Saskatchewan in any scholarly use which may be made of any material in my thesis.

Requests for permission to copy or to make other use of material in this thesis in whole or part should be addressed to:

Head of the Department of Chemical and Biological Engineering
University of Saskatchewan
57 Campus Drive
Saskatoon, Saskatchewan

Canada, S7N 5A9

or

Dean
College of Graduate and Postdoctoral Studies
University of Saskatchewan
Room 116, 110 Science Place Thorvaldson Building,
Saskatoon, SK CANADA S7N 5C9

ABSTRACT

Fischer–Tropsch Synthesis (FTS) is a major part of feed-to-liquid (XTL) technologies which convert syngas ($H_2 + CO$) into clean liquid hydrocarbon fuels and specialty chemicals. Understanding and developing FTS catalysts using mesoporous materials are of main interest in the present work. In the first step, the research focused on developing Co-based catalyst supported on multiwalled carbon nanotubes (MWCNTs). The functionalization of CNTs and its impact on the performance of corresponding catalysts on FTS were studied. Different concentrations of nitric acid were used as oxidizing agent and the higher HNO_3 concentration (70 wt. %) generated more defects on the CNT walls where the Co species were located. This resulted in higher cobalt dispersion in the catalyst and correspondingly higher catalytic activity. The effects of the pelletization on the physico-chemical and mechanical properties of Fe/CNT catalyst in FTS were also investigated. Further, the limitation of N_2 adsorption technique for textural characterization of CNTs was studied as compared to transmission electron microscopy. The findings of this work confirmed that the inter-tubular space between CNTs in N_2 adsorption are considered in the estimation of the pore volume and average pore diameter of CNTs.

Further, the high surface area and large pore size mesoporous alumina was synthesized and utilized as a support for Co catalyst. Stability of mesoporous alumina in the presence of aqueous and organic solvents during Co impregnation was examined and the corresponding catalysts were tested in FTS. Mesoporous alumina supported cobalt catalyst prepared by organic solvents (ethanol and acetone) retained the textural properties of the support, even with higher cobalt loading (30 wt. %), and resulted in better physicho-chemical and catalytic properties in FTS. Further studies were carried out to optimize the operational conditions (temperature, pressure, flow rate) for mesoporous alumina supported catalyst. Mesoporous alumina support was modified with lanthanum and cerium and their catalytic performance were investigated in FTS reaction. Furthermore, two different chelating agents (NTA and EDTA) were also incorporated to examine the possible improvement in the dispersion and reducibility of the catalysts and their performance in FTS. As a baseline for comparison, the same modification was applied to γ-alumina supported cobalt catalysts, which were characterized prior to FT reaction. Findings of this work showed that the NTA is more promising chelating agent to improve the cobalt dispersion and catalytic performance in FTS. Finally, the promoter effects on CO conversion and C_{5+} selectivity for mesoporous alumina supported cobalt catalyst in FTS were investigated. The addition of Mn and Y transition metals (1 % molar ratio relative to Co) led to marginal impact on Co dispersion, extent of reduction, and corresponding catalyst performance in FTS. Among the noble metal (Pt, Re, Ru, Ir) used, addition of

platinum resulted in high reducibility, moderate activity, but lower C_{5+} selectivity and stability for FTS Co catalyst, whereas, rhenium-promoted catalyst exhibited higher C_{5+} selectivity, hydrocarbon productivity, and stability, as compared to Pt- and Ir-promoted catalysts. Ruthenium was found to be the most active and selective to heavier hydrocarbons, favors the catalyst stability, reducibility, and dispersion of Co significantly.

ACKNOWLEDGMENTS

I would first like to express my gratitude to Dr. Ajay K. Dalai, my supervisor, for providing me this opportunity to develop my research skills and knowledge, for his guidance, patience, and support in the course of my PhD program. I also appreciate Dr. Nicolas Abatzoglou, my co-supervisor for his valuable comments and positive attitudes.

I am also thankful of my advisory committee members Dr. Jafar Soltan, Dr. Richard Evitts, Dr. Hui Wang, and Dr. Andrew Grosvenor for their questions and constructive comments which resulted in deepening my knowledge and improving the quality of my research work. Special thanks to Dr. Mehdi Nemati, Head of Department of Chemical and Biological Engineering, for being an excellent teacher and for his professional demeanor that I learned from.

Many thanks to postdoctoral fellow, Dr. Sandeep Badoga, for his technical assistance and for the scientific discussions we had which were very fruitful to my research work and publications.

I gratefully acknowledge RLee Prokopishyn, Richard Blondin, and Heli Eunik, technicians in Department of Chemical and Biological Engineering, for their technical assistance with characterization instruments, analyses, and the required troubleshooting throughout of PhD studies.

Last but by no means least, my profound appreciation goes to all my family members for their thoughts, emotions, and all supports which inspired me along the way.

TABLE OF CONTENTS

LIST OF TABLES

LIST OF FIGURES

LIST OF ABBREVIATIONS

AAO	Anodic aluminum oxide
AC	activated carbon
ASF	Anderson-Schulz-Flory
ATR	Autothermal reforming
BC	Black carbon
BET	Brunauer-Emmett-Teller
BJH	Barret-Joyner-Halenda
BTL	Biomass-to-liquid
CA	Chelating agent
CMK	Trade name for a carbon purchased. It is an ordered mesoporous carbon prepared using a mesoporous silica as template
CNF	Carbon nanofibers
CNH	Carbon nanohorns
CNT	Carbon nanotubes
CTL	Coal-to-liquid
CVD	Chemical vapor deposition
DOR	Degree of reduction
EDTA	Ethylenediaminetetraacetic acid
FWHM	full-width at half-max
FTS	Fischer-Tropsch synthesis
GHSV	Gas hourly space velocity
GTL	Gas-to-liquid
HC	Hydrocarbon
HRTEM	High-resolution transmission electron microscopy
HTFT	High-temperature Fischer-Tropsch
IUPAC	International Union of Pure and Applied Chemistry
LTFT	Low-temperature Fischer-Tropsch
NTA	Nitrilotriacetic acid
OMC	Ordered mesoporous carbon
MWCNTs	Multiwalled carbon nanotubes
POX	Partial oxidation
PSD	Pore size distribution

SEM	Scanning electron microscopy
SMR	Steam methane reforming
TEM	Transmission electron microscopy
WGS	Water-gas shift
XRD	X-ray diffraction
XTL	Feed-to-liquid

NOMENCLATURES

a	characteristic length
$C_{A,s}$	Concentration of component A on the surface
C_{WP}	Weisz–Prater criterion
D	metal dispersion (%); diameter of sphere pellet; binary diffusivity
$D_{corr.}$	Corrected dispersion (%)
D_{eff}	effective diffusivity (cm^2/s)
d_{XRD}	mean diameter of crystallites (nm)
K	constant value corresponding to the crystallite shape
L	length of cylindrical pellet, length of CNT
m-Al_2O_3	Mesoporous alumina
n_t, n_{cl}, and n_{op}	total number of nanotubes, the number of closed-ended, and the number of open-end nanotubes per unit mass
V_m	monolayer volume $\left(\frac{\text{STP cm}^3}{\text{g}}\right)$
r_p	pore radius
r_c	capillary radius
R	catalyst particle radius
S	Surface area; product selectivity
SSA	specific surface area $\left(\frac{\text{m}^2}{\text{g}}\right)$
T	diameter/thickness of cylinder
ϕ	Thiele modulus
β	full width at half max or integral breadth in radian
Θ_B	Bragg angle (diffraction angle)
ρ	Molar density $\left(\frac{g}{cm^3}\right)$
ρ_c	catalyst density
γ	Surface tension $\left(\frac{\text{dyne}}{\text{cm}}\right)$
σ	crushing strength (kPa); collision factor (Å)
λ	X-ray wavelength
η	effectiveness factor

CHAPTER 1: INTRODUCTION AND RESEARCH OVERVIEW

1.1 Research motivation

Achieving an alternative and clean energy has been a major incentive for industry and research to address the challenges regarding the conventional routes for production of transportation fuels and value-added hydrocarbons. Global climate change, local air pollution, energy supply security, associated gas flaring, and stranded natural gas discovery are some of the present issues and concerns for the energy sector to tackle with. Feed-to-liquid or XTL technologies where X could be coal (C), natural gas (G), biomass (B), and wastes/oil residues (W) is an indirect liquefaction process to convert any carbonaceous resources to liquid fuels. This approach consists of three main processes (Fig. 1.1): (i) transforming the carbon-containing feedstock to carbon monoxide and hydrogen (syngas), (ii) converting the syngas to a broad spectrum of hydrocarbons (C_1 to C_{100}), and (iii) refining the produced hydrocarbons to targeted final products (i.e. gasoline, diesel, jet fuel, oxygenates, etc). Irrespective of the carbon source, the intermediate syngas (H_2 + CO) product can be catalytically converted to sulfur- and aromatic-free transportation fuels and chemicals through Fischer-Tropsch synthesis (FTS) [1–4].

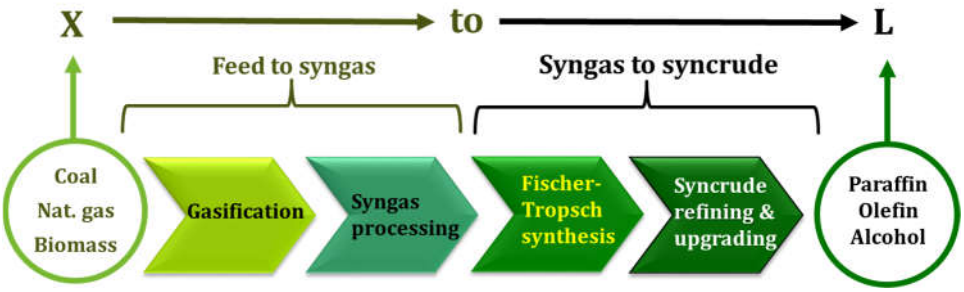

Figure 1.1 Schematic of the XTL technology

Different feed-to-syngas processes can be employed to synthesize the H_2 + CO gas mixture such as: catalytic and non-catalytic partial oxidation (POX), gasification, autothermal reforming (ATR), carbon dioxide reforming, and steam methane reforming (SMR). Depending on the quality of produced syngas (i.e. H_2-enriched or -deficient), the following syngas to syncrude (synthetic crude) process can be designed accordingly. For example, syngas with a lower H_2/CO ratio (< 1.8) is preferred for high-temperature Fischer-Tropsch (HTFT) synthesis ($260-320$ °C) using iron based catalyst in which olefinic and medium range hydrocarbons (HCs) are favored. Conversely, syngas with a higher H_2/CO ratio ($\geq$

1.8) is preferred for low-temperature Fischer-Tropsch (LTFT) synthesis (210 − 240 °C) using cobalt and ruthenium based catalysts in which formation of long chain paraffinic hydrocarbons are favored [2,5,6]. It is also well-known that the Co and Ru based catalysts are more productive (active) than iron catalyst. Higher price and scarcity of the Ru leave cobalt as a preferred option for LTFT. Furthermore, its lower activity for water-gas shift (WGS) reaction and higher stability in presence of water as compared to iron, which secures cobalt as an optimum active metal for LTFT reaction. The nature of support material, its textural properties, and catalyst preparation methods could substantially influence the crystallite size, dispersion, reducibility, and the metal-support interactions in the catalyst thus the performance of FT reaction [5,7,8]. Understanding and developing of FT catalyst mainly Co-based, using mesoporous supports such as multiwalled carbon nanotubes (MWCNTs) and mesoporous alumina (m-Al_2O_3) are the main objectives of this study.

1.2 Knowledge gaps

Based on the literature review presented in the second chapter, the following knowledge gaps are identified and are addressed in this research work:

(I) Studies on the influences of concentration of nitric acid as an oxidation agent on MWCNTs and Co/MWCNT catalysts for FTS are limited.

(II) Limited literature has been reported on the impact of binder and palletization for FTS Fe/CNT catalysts.

(III) Stabilization of mesoporous alumina with high textural properties during the catalyst preparation and using the resulting cobalt catalysts in FTS have not been studied.

(IV) Research on the influences of chelating agents (CAs) and support modifiers on mesoporous alumina supported cobalt catalysts for FTS is limited.

(V) The influence of promoters on the performance of mesoporous alumina supported cobalt catalysts in FTS has not been explored.

1.3 Hypotheses

(I) Applying higher nitric acid concentration will cause more defects on MWCNTs skeleton and provide higher amount of anchoring sites for cobalt metal which is favorable for metal dispersion and activity of Co/MWCNT catalyst in FTS.

(II) Higher binder concentration would result in better mechanical properties and stability for Fe/CNT catalyst

(III) Using organic solvents for preparation of Co catalyst supported on the mesoporous alumina would lead to limited collapse and changes in the textural properties of the support as compared to aqueous solvent.

(IV) Addition of chelating agents and support modifiers might affect the metal-support interaction. Therefore, the dispersion and reducibility of cobalt supported on the mesoporous alumina as well as its catalytic performance in FTS could be influenced.

(V) It is assumed that the addition of noble and transient metals on mesoporous alumina supported cobalt catalyst would increase the cobalt dispersion and enhance its reducibility, which would lead to better performance of the catalysts in FT reaction.

1.4 Objectives

The overall objective of this work is to investigate parameters affecting the performance of Co/CNT, Fe/CNT and Co/mAl_2O_3 catalysts for conversion of syngas into transportation fuels range of hydrocarbons. The sub-objectives of this research to meet the overall objective and to improve the catalysts' performance are as following:

(I) To examine the effects of different nitric acid concentrations (e.g. 35, 50, and 70 wt. %) on physico-chemical properties of CNTs and Co/CNT catalyst in FTS.

(II) To examine different concentrations of the bentonite binder (10, 15, and 20 wt. %) and pellet shapes (spherical and cylindrical) on the performance of Fe/CNT catalyst in FTS.

(III) To study the suitability of N_2 adsorption technique for structural characterization of the CNTs.

(IV) To attempt retaining the structural properties of mesoporous alumina during Co based catalyst preparation, using organic solvents (ethanol, acetone) and find the optimum operational conditions for active and selective catalyst in FTS.

(V) To investigate the impact of chelating agents (e.g. NTA, EDTA), and support modifiers (e.g. La, Ce) on the physico-chemical properties of mesoporous alumina supported Co catalysts and their performance in FTS.

(VI) To explore the suitable promoters (e.g. Pd, Pt, Re, Ru, Mn, Ir, Y) for mesoporous supported cobalt catalyst in FTS, favoring the CO conversion and C_{5+} selectivity.

1.5 Thesis layout

In this study, various CNT and mesoporous alumina supported catalysts were prepared, thoroughly characterized, and examined in industrially relevant conditions for FT in micro fixed- bed reactor. The

preparation methods, employed characterization techniques and results, as well as the catalysts performance were discussed in upcoming chapters. The sub-objectives of this research are divided into 6 phases and the outcomes are discussed in chapters 3 to 8. Chapter 2 is the background study pertaining to Fischer-Tropsch literature.

Chapter 3 addresses the suitability of N_2 adsorption analysis for structural characterization of MWCNTs with different textural properties including surface area, pore diameter and pore volume, either synthesized or purchased in comparison with transmission electron microscopy (TEM). Chapter 4 explores the influence of different nitric acid concentrations as oxidizing agents on CNTs physico-chemical properties and consequently on the performance of Co/CNT catalysts in FT synthesis. In chapter 5, the effects of different pellet shapes (cylinder and sphere) using three different binder loadings on the industrial application of Fe/CNT catalysts in FT synthesis were discussed.

In chapter 6, the synthesis of mesoporous alumina (mAl_2O_3) with high surface area, large pore volume and diameter, and its stabilization during the Co catalyst preparation using different solvents were investigated. Moreover, different Co loadings supported on mAl_2O_3 were prepared and examined for the activity and selectivity in FT reaction. In chapter 7, the effects of nitrilotriacetic acid (NTA) and ethylenediaminetetraacetic acid (EDTA) chelating agents (CAs) as well as cerium and lanthanum modifiers on the properties of Co/mAl_2O_3 catalyst and their performance in FTS were studied. In chapter 8, the impact of various promoters (Pt, Pd, Ru, Re, Mn, Ir, and Y) on Co/mAl_2O_3 were investigated. Finally, the major findings of the entire phases as well as the recommendations for the potential future works are summarized in Chapter 10.

CHAPTER 2: LITERATURE REVIEW

Some materials from this chapter have been published in the following research papers:

- V. Vosoughi, S. Badoga, A. K. Dalai, N. Abatzoglou, "Effect of Pretreatment on Physicochemical Properties and Performance of Multiwalled Carbon Nanotube Supported Cobalt Catalyst for Fischer−Tropsch Synthesis", Ind. Eng. Chem. Res. 2016, 55, 6049−6059.
- V. Vosoughi, S. Badoga, A.K. Dalai, N. Abatzoglou, "Modification of mesoporous alumina as a support for Co-based catalyst in Fischer-Tropsch Synthesis", Fuel Proc. Tech., 2017, 162, 55-65.
- V. Vosoughi, A. K. Dalai, N. Abatzoglou, Y. Hu, "Performances of promoted cobalt catalysts supported on mesoporous alumina for Fischer-Tropsch synthesis", Appl. Catal. A: Gen., 2017, 547, 155-163.

Contribution of PhD candidate

The literature review in this chapter was conducted and written by Vahid Vosoughi with discussion and suggestions contributed by Dr. Ajay Dalai.

Contribution of this Chapter to the Overall Ph.D. Research

This chapter provides a literature review focusing on the background, chemistry, kinetics, catalyst support materials, catalyst active metals and promoters for the Fischer–Tropsch synthesis.

2.1 Background and future of Fischer-Tropsch synthesis

The reaction in which carbon monoxide and hydrogen mixture (syngas) could be converted into methane at atmospheric pressure over Ni and Co catalysts was first reported by Sabatier and Senderens in 1902 [9]. In 1913, BASF revealed in their patent that CO hydrogenation can produce more hydrocarbons at higher temperature and pressure. Franz Fischer and Hans Tropsch in 1920's followed this and provided more details about the mechanism of syngas conversion to liquid hydrocarbons using iron and cobalt catalysts which finally led to the first commercial plant of FT process in 1936. Large scale HTFT and LTFT plants employing different reactors with iron catalyst were later developed by SASOL in South Africa in 1950s, 1970s and 1980s. As shown in Table 2.1, since 1990s other companies also started commercial GTL projects mostly using Co–based catalysts.

Table 2.1 Major commercial GTL plants (Adopted from reference [9] with permission from the Elsevier; see Figure G.1 in Appendix G)

Company	Project location	Catalyst/Reactor type	Capacity (barrel/day)	start-up date
Shell	Bintulu, Malaysia	Co/SiO_2; LTFT multi-tubular fixed bed	14500	1992
PetroSA	Mosselbay, South Africa	Fused Fe/K; HTFT circulating fluidized bed	22000	1993
Sasol-QP (Oryx)	Ras Laffan, Qatar	Co/Al_2O_3; LTFT slurry phase	34000	2007
Shell (Pearl)	Laffan, Qatar	Co/TiO_2; LTFT multi-tubular fixed bed	140000	2011
Chevron-Sasol	Escravos, Nigeria	Co/Al_2O_3; LTFT slurry phase	34000	2013

Since 2013, the government of China restarted investing on the large scale indirect CTL projects with more environmentally stringent regulations. Shehua's Ningxia, Yankuang, Yitai, Lu'an are the major industrial groups trying to further develop the CTL production targeting 30 mtpa (mega tons per annum) by 2020 [10,11].

On June 2017, Velocys PLC, the frontier in small scale GTL and BTL technology using intensified microchannel reactors, was selected by U.S. Department of Agriculture (USDA) to receive the phase II loan guarantee for the commercial-scale BTL plant. This plant capacity will be 1400 barrels of diesel per day consuming 1000 tonnes of woody residue feedstocks from southeast resources in US [12].

Alberta Energy Regulator (AER) approved of Expander Energy Inc. on July 2017 to build Canada's first commercial GTL with 500 bbl/d of paraffinic diesel and naphtha capacity at Carseland [13].

2.2 Chemistry of Fischer–Tropsch synthesis

CO and H_2 reagents react on the surface of the heterogeneous catalyst to form monomer units in-situ. FT kinetics proceeds with polymerization reactions of monomers to produce broad range of HCs based on C-number ($C_1 - C_{80+}$). This dual nature of FT synthesis is the reason to be called as a non-trivial surface polymerization reaction [2,14].

The multicomponent product ranges from low to high molecular weight in different forms of linear, branched, and oxygenated hydrocarbons (equations 2.1 to 2.6) [2,15]:

Methanation: $H_2 + CO \longrightarrow CH_4 + H_2O \quad \left(\Delta H^0_{298} = -247 \frac{kJ}{mol}\right)$ (2.1)

Paraffins: $(2n+1)H_2 + nCO \longrightarrow C_nH_{2n+2} + nH_2O$ (2.2)

Olefins: $2nH_2 + nCO \longrightarrow C_nH_{2n} + nH_2O$ (2.3)

Alcohols: $2nH_2 + nCO \longrightarrow C_nH_{2n+2}O + (n-1)H_2O$ (2.4)

Aldehydes Ketones: $(2n-1)H_2 + nCO \longrightarrow C_nH_{2n}O + (n-1)H_2O$ (2.5)

Carboxylic acids / Esters: $(2n-1)H_2 + nCO \longrightarrow C_nH_{2n}O_2 + (n-2)H_2O$ (2.6)

The first three reactions represent the main products of FT reaction which are linear paraffins (alkanes) and α-olefins (α-alkenes) comprising tail gas (C_1 –C_2), LPG (C_3 – C_4), naphtha (C_5 – C_{11}), middle distillate (jet fuel / kerosene / diesel: C_{12} – C_{22}), low-molecular-weight wax (C_{23} – C_{32}), and high-molecular-weight wax (> C_{33}). The last three reactions representing the formation of oxygenates (alcohols, aldehydes, ketones, carboxylic acids, and esters) are assumed to be the side reactions for the FTS. There are two more reactions which takes place during FTS, namely water-gas-shift (WGS) and Boudouard reactions as shown in equations 2.7 and 2.8 [16]:

WGS reaction: $CO + H_2O \rightleftharpoons CO_2 + H_2 \quad \left(\Delta H^0_{298} = -41 \frac{Kj}{mol}\right)$ (2.7)

Boudouard reaction: $2\,CO \leftrightharpoons C + CO_2 \quad \left(\Delta H^0_{298} = -172 \frac{Kj}{mol}\right)$ (2.8)

Assuming paraffins and olefins (C_{2+}) production through reactions 2.2 and 2.3 are desired for FTS, the consuming ratio of H_2/CO might vary depending on the extent of other reactions. For example, extent of methane formation as an undesired product, would influence the usage ratio and product distribution in reactions 2.2 and 2.3. Potassium promoter can reduce methane production in Fe-based catalyst. In general, high temperature operating condition in FTS favors faster hydrogenation, which leads to higher methane formation. Despite Fe catalyst is used in HTFT it has comparable methane selectivity to LTFT Ru-based catalyst, but lower than Co catalyst. Nickel has the highest tendency for methanation among the active metals for FTS. Furthermore, extent of WGS reaction 2.7 influences the main FT reactions 2.2 and 2.3. WGS reaction produces H_2 for FTS, which is beneficial for hydrogen-deficient syngas as a feed

driven from coal or biomass resources. Also, WGS reaction would be less active in LTFT condition and in the presence of Co and Ru catalysts. However, it is more active in HTFT condition and in the presence of Fe catalyst. Moreover, the higher FT reaction temperature (> 240 °C) leads to decrease in number of surface monomers, decrease in average length of HC chains, and excessive deposition of elemental carbon (i.e. reaction 2.8), which acts as a deactivation factor for the FT catalyst. The Boudouard reaction is assumed to be the main reaction responsible for carbon deposition in FTS. Its higher activation energy of about 113 kJ/mole as compared to that of the main FT reactions with 93 kJ/mole for Co catalyst shows that it has more temperature-sensitive kinetics [2,17].

With negative heat of formation ($\Delta H_{298}^{0} < 0$) for CH_4 and all C_{2+} hydrocarbons and average heat of 140 kJ/mole of produced HC, the FTS is considered as a highly exothermic reaction [2,15]. Therefore, an efficient heat transfer mechanism need to be taken into account for designing a reactor to carry out the FTS without temperature buildup. Moreover, CO hydrogenation thermodynamically favors methane formation over C_{2+} path, hence the temperature, pressure, syngas composition, syngas flowrate, and the catalyst composition need to be optimised considering the targeted C_{2+} product cut.

2.3 Kinetics of Fischer–Tropsch synthesis

Proposing the elementary steps and intermediates which leads to conversion of $CO+H_2$ reactants into long–chain hydrocarbons through different pathways has been an ongoing research since the discovery of FTS. Multi–step polymerization of syngas in FT reactions consists of the following stages in all proposed mechanisms: (1) reactant adsorption, (2) chain initiation, (3) chain growth, (4) chain termination, (5) product desorption, (6) re-adsorption and further reaction. Depending on the assumptions for the elementary steps of a mechanism, for example associative versus dissociative adsorption of reactants and their order of adsorption, the monomer and growing intermediates which propagate could be different. When propagating reaction is terminated the product will desorb from the surface with a chance of re-adsorption, reacting with monomers and growing into longer HCs. The process conditions and nature of active sites on the catalyst surface determine the underlying propagation and termination rates, resulting the product distribution.

Stepwise polymerization (addition of single-carbon units) and chain growth reactions in FTS results in an exponential decrease in the product yield in terms of the chain length (carbon number). The fraction of a product with n^{th} carbon can mathematically be described using the Anderson–Schulz–Flory (ASF) model (equations 2.9 to 2.11) based on its relative probability of chain growth (α) [18]:

$$M_n = (1-\alpha)\alpha^{n-1} \qquad M_n\text{: Mole fraction of HC with chain length n} \qquad (2.9)$$

$$\frac{W_n}{n} = (1-\alpha)^2\alpha^{n-1} \qquad W_n\text{: weight fraction of HC with chain length n} \qquad (2.10)$$

$$\alpha = \frac{M_{n+1}}{M_n} = \frac{r_p}{r_p + r_t} < 1 \qquad r_p\text{: rate of propagation; } r_t\text{: rate of termination} \qquad (2.11)$$

$$\log(M_n) = (\log\alpha)\mathrm{n} + \log\left(\frac{1-\alpha}{\alpha}\right) \qquad (2.12)$$

According to equation 2.12, which is the logarithmic form of the ASF model (equation 2.9), mole fraction of products $[\log(M_n)]$ correlates the corresponding carbon number (n) linearly with the slope characteristics of chain prolongation probability $(\log\alpha)$. Generally, values of chain growth probability (α) for ruthenium- and cobalt-based catalysts are relatively higher than it for an iron-based catalyst. Lower partial pressure of CO (or higher H_2) would lead to limited CO coverage on the surface and lower concertation of monomers to propagate. This in turn results in higher probability of chain termination $(1-\alpha)$, lower probability of chain prolongation (α), or lower selectivity of long chain C_{5+} HCs. It is assumed that α is dependent on the FT process conditions and catalyst, but ideally independent from chain carbon number (n). Nevertheless, some experimental studies showed that there are some deviations from ASF model predicting methane, C_2, and $C_{12}-C_{14}$ for Fe, Co, and Ru based catalysts [18,19].

Three major mechanisms for FT reactions are outlined in Table 2.2. The *carbide (carbene)* mechanism which has originally been proposed by Fischer and Tropsch (1926) emphasizing on the dissociation of CO molecules into surface carbide and oxygen. then hydrogenated to H_2O and CH_2^* monomers. Further investigations suggested that the surface carbide hydrogenation might form either methylidyne or methylene monomers $(CH_x^*;\ x = 1-2)$ before propagating to long-chain HCs. Moreover, the cleaved oxygen atoms can be removed from the surface in the form of either H_2O if the CO activation occurs H-assisted, or CO_2 if it follows the unassisted pathway. The overall FT reaction to produce long-chain C_xH_y comprises of coupling/polymerization of monohydrocarbyls (CH_x^*) and other growing hydrocarbyls [16,20].

Table 2.2 Mechanisms for Fischer–Tropsch synthesis (Adopted from reference [9] with permission from the Elsevier; see Figure G.1 in Appendix G)

Surface rxn. / **Mechanism**	**Initiation** monomer formation	**Propagation** intermediates, chain growth	**Termination** product formation
Carbide	$CO_s \longrightarrow C_s + O_s$ $H_{2,s} \longrightarrow 2H_s$ $C_s + xH_s \longrightarrow CH_{x,s}$	$R_s + CH_{x,s} \longrightarrow RCH_{x,s}$ $RCH_{x,s} + (2-x)H_s \longrightarrow RCH_{2,s}$	$RCH_{2,s} + H_s \longrightarrow RCH_{3,s}$ $RCH_2CH_{2,s} \longrightarrow RCHCH_{2,s} + 2H_s$ $R_s + CO_s \longrightarrow$ Oxygenates
Enol	$H_{2,s} \longrightarrow 2H_s$ $CO_s + H_s \longrightarrow COH_s$ $COH_s + H_s \longrightarrow HCOH_s$	$RCOH_s + HCOH_s \longrightarrow RCCOH_s + H_2O$ $RCCOH_s + H_s \longrightarrow RCH_2COH_s$	$RCH_2COH_s + 4H_s \longrightarrow RCH_2CH_3 + H_2O$ $RCH_2COH_s + nH_s \longrightarrow$ Oxygenates
CO insertion	$CO_s \longrightarrow C_s + O_s$ $H_{2,s} \longrightarrow 2H_s$ $C_s + xH_s \longrightarrow CH_{x,s}$	$RCH_s + CO_s \longrightarrow RCHCO_s$ $RCHCO_s + H_s \longrightarrow RCH_2CH_s + H_2O$	$RCH_s + 2H_s \longrightarrow RCH_{3,s}$ $RCHCO_s + nH_s \longrightarrow$ Oxygenates

s: surface
R: H, CH_2, CH_3, CH_3CH_2, $CH_3CH_2CH_2$

The second main FT mechanism is the *enol or hydroxy-carbene (oxygenate)* mechanism proposed by Storch et al. in 1950s. In this pathway, CO assumed to be associatively (undissociative) chemisorbed on the active sites of the catalyst's surface, then partially hydrogenated to oxymethylene or hydroxycarbene ($HCOH^*$) species (enolic entities). These monomers can be coupled to produce water and $CHO^* - CH_3$ and propagate to form longer HCs through hydrogenation and condensation reactions. The final product distribution (alkane vs alkenes vs oxygenates) depends on the termination routes as well [9,21,22].

The third mechanism known as *carbonyl insertion* or *CO insertion* was proposed by Pichler and Shultz in the 1970's.

This mechanism assumes initiation steps similar to carbide mechanism, but direct CO insertion to the intermediates (metal-alkyl species) for chain growth [9,21,22].

Since considerable amount of alcohols and aldehydes can be formed specially with iron catalyst in HTFT, insertion of some form of oxygenate ($CO, HCO^*, HCOH^*$) species in propagation and termination steps could explain these products. Otherwise, termination step could result in formation of either α-olefin by β-hydrogen abstraction from alkyl groups or formation of paraffins by hydrogen addition to surface intermediates. Nevertheless, the reversible nature of hydrogen abstraction reaction makes the α-olefins re-adsorb and prolong in reaction with surface alkyl groups forming longer chain HCs [1,19].

Different types of monomer can be added to different chain growth intermediates and terminated in different forms of product leading to varieties of routes for FTS reaction under specific process conditions, catalysts, and reactors.

2.4 Reactors for Fischer–Tropsch synthesis

As shown in Table 2.1 the major commercial plants for FTS utilize trickle fixed-bed, fluidized bed, and slurry bubble column reactors (Figure 2.1). Fluidized reactors are normally used in the HTFT with iron catalyst. Whereas, fixed–bed and slurry bubble reactors mainly are utilized for the low–temperature FT using both iron and cobalt catalysts. Highly exothermic nature of the FT reaction (140–160 kJ/mole CO converted) makes the heat transfer efficiency be a critical aspect in designing of a reactor for the FT process [23]. Temperature rise in the FT reactor could significantly shift the product selectivity toward lighter HCs. Further, this can cause sintering in the catalyst active metal resulting a decline in the activity of the catalyst and its life time.

To achieve a better temperature control in fixed–bed FT reactors, they are designed in a multi-tublar array with steam or water as coolant in the shell side. Nonetheless, loading/unloading of the catalyst in/from these reactors is a laborious and difficult task. In the fluidized and slurry bed reactors, however, the catalyst replacement procedure is simpler and heat removal also is more efficient. Fixed-bed reactors are sometimes preferred due to their higher conversion possibility, limited catalyst loss caused by attrition, more robust structure for scale-up and different operational conditions. Fluidized bed reactor on the hand has shown superior capability to operate in higher temperature with nearly isothermal condition and lower cost of operation. As compared to fixed–bed reactors, slurry bubble reactors also exhibit better heat removal efficiency and lower pressure drop [2,16,21,24].

New emerging microchannel (microreactor) technology could address the challenges related to the smaller scale BTL, offshore GTL plants, stranded gaseous resources, associate and flaring gas monetization. The micro-structured reactors (Figure 2.2) with embedded catalyst in the micro scale channels (< 1 mm) showed superior heat and mass transfer coefficient, greater catalyst productivity (1700 $kg.m^{-3}.h^{-1}$ vs. 700 $kg.m^{-3}.h^{-1}$ in a fixed–bed reactor), lower catalyst cost, smaller facility footprint (> 10 times), modularity and lower installation/maintenance cost [25–27].

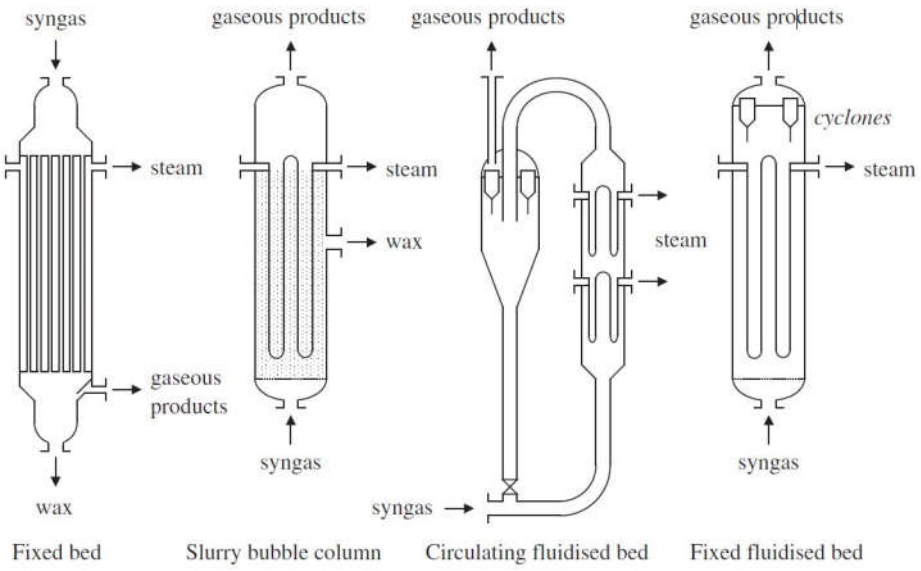

Figure 2.1 Reactors used for Fischer–Tropsch synthesis (Adopted from reference [15] with permission from the Royal Society of Chemistry; see Figure G.2 in Appendix G)

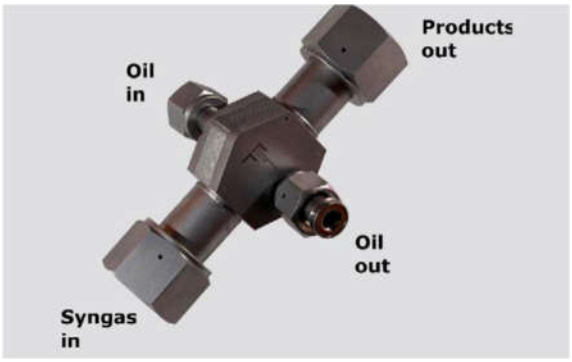

Figure 2.2 Microchannel reactor (Adopted from reference [27] with permission from the Elsevier; see Figure G.3 in Appendix G)

2.5 Active metals for the Fischer–Tropsch catalyst

In group VIII transition metals, those distinctively favoring carbon monoxide hydrogenation are Fe, Co, Ru, Ni [28]. Among them cobalt and iron are the only commercially used active metals as FT catalysts. Nickel, on the other hand, excessively favors the methanation reaction and is undesirably selective to methane formation in FT reaction conditions. Ruthenium and cobalt exhibit higher catalytic activity, heavier hydrocarbons (HCs) selectivity, and stability in low-temperature Fischer–Tropsch (LTFT: 210–240 ºC), using hydrogen enriched syngas (H_2/Co ~ 1.8–2.1). Despite the highest activity of Ru for

targeting long chain alkanes (C_{5+}), its high price and scarcity limits its industrial application, thus, leaving Co as a favorable option for heavier C_{5+} HCs synthesis [29].

Iron catalyst has higher water-gas-shift (WGS) activity, therefore is more suitable for CTL and BTL using syngas with lower H_2:CO ratio (e.g. 0.6−1.0). In contrast, cobalt performs better with higher H_2:CO ratio (e.g.1.8−2.3) syngas driven from natural gas [21,28,30]. In addition, it is less active toward WGS reaction and CO_2 production, but more selective to CH_4 and paraffinic C_{5+}. Higher intrinsic activity and better stability make the Co as a commercially preferred catalyst for FTS targeting long−chain alkanic hydrocarbons. However, understanding the catalysis, designing, and developing of more active, selective, and stable cobalt−based catalyst for FTS have been a continuing interest of research in feed-to-liquid (XTL) technology [28].

2.6 Support materials for the Fischer–Tropsch catalyst

A catalyst support (carrier) could facilitate the crystallization and stabilization of the active metal on its texture. Physicochemical and textural properties of the support material affect the metal-support interaction, crystallite size, metal dispersion, mass transfer of the reactants/products, and mechanical strength, thermal stability of the catalyst. Therefore, selecting and synthesizing of a support material with: distinct chemical composition, higher impurity, well-defined surface chemistry, appropriate pore size/volume, narrow pore size distribution is critical for designing an efficient catalyst for FTS [31,32].

2.6.1 Amorphous mesoporous metal oxide supports

The most patented and studied support materials for cobalt catalyst are conventional refractory metal oxides such as silica (SiO_2), titania (TiO_2), and alumina (Al_2O_3). Other metal oxides, such as zirconia (ZrO_2), magnesia (MgO), ceria (CeO_2), and zinc oxide (ZnO) were also examined as potential mesoporous support materials for the Co catalyst in FTS [29,33–36].

The γ-Al_2O_3 is the most commercially used support material for the cobalt-based catalyst in FTS. Enhancement of the conventional alumina's surface area along with pore volume and pore diameter enables higher loading of active metals and facilitates higher availability of active sites at equal loadings. In addition, it is crucial to optimize pore diffusional transport, which affects the activity, product selectivity, and stability of the supported cobalt catalyst in FTS [29,37]. It is believed that mesoporous materials $\left(2\ \text{nm} < d_{pore} < 50\ \text{nm}\right)$ with pore size between 10–15 nm could provide suitable texture for the formation of cobalt crystallites with so-called optimum size range of 8–10 nm for FT reaction [9,38–

40]. In relation to impact of textural characteristics on the crystallite properties, a support with larger pore sizes would result in larger cobalt crystallites, which in turn causes faster sintering, whereas, smaller pore sizes facilitate the formation of smaller ensembles, which lead to SMSI and less reducibility [29,41]. In either case, the density of cobalt active sites drops which leads to less hydrocarbon production on unit mass or surface of the dispersed cobalt atoms.

In recent years, significant researchers have been attempting to develop a novel alumina and other metal oxide supports targeting high activity, selectivity, and stability of cobalt-based catalysts in FTS [2,5,29,39]. Alvarez et al. [42] has comprehensively reviewed the synthesis methods, characterization, and applications of mesoporous alumina with various pore size distribution and different textural properties. It has also been reported by Saib et al. [43] and Khodakov et al. [44] that the different pore sizes (2-15 nm) of other mesoporous materials such as silica have a strong impact on the resulting cobalt crystallite size, its reducibility, and C_{5+} selectivity in FTS. Furthermore, the effects of pore size and crystallite phase of mesoporous alumina on the subsequent cobalt crystallite size and catalyst performance in FTS have been recently studied by a few other research groups [29,41,45–49].

2.6.2 Periodic meso-structured silica supports

Broad pore size distribution and non-uniformities in the pore structure of conventional metal oxide supports makes it hard to understand and optimize the impact of textural properties on the productivity and hydrocarbon selectivity of a catalyst used in FT reaction. This was the motivation in utilizing silica-based periodic meso-porous molecular sieves, namely MCM-48 (cubic 3D porous structure), MCM-41 (Mobil Catalytic Material number 41), SBA-15, HMS (hexagonal mesoporous silica), and SHS (Silica hollow sphere) as support materials for FT catalyst. The ordered mesoporous silica materials exhibit high surface areas, narrow pore size distributions (PSD), and large pore diameters and volumes which are tunable and advantageous for selective syngas hydrogenation. Their well-defined pore structure allows to study the effect of pore size on the catalyst (e.g. CoO_x species) physico-chemical properties (crystallite size, metal dispersion, oxidation states, reducibility, etc.) and performance (activity, selectivity, stability) in FTS [5,50–53].

2.6.3 Zeolite supports

Zeolites are well known for their shape-selective feature, which can limit the formation of products larger than their cavity diameter. Therefore, chain growth would be restricted by this feature and lead to formation of lighter hydrocarbon in FTS. In addition, the acidity of zeolites induces the secondary

cracking, isomerization (branching), oligomerization, cyclization and aromatization reactions of the main FT products. These properties were utilized in so-called modified FTS, in which a FT catalyst is mixed with a zeolite catalyst (hybrid or co-catalyst) in order to shift product distribution toward lighter hydrocarbon fuels like gasoline. For instance, faujasite zeolites (X and Y), ZSM-5, HZSM-5, MCM-22, ITQ-2, ITQ-6 have been explored for the cobalt- and iron-based catalysts in FTS [5,23,53–55].

2.6.4 Carbon supports

Carbon materials have also drawn attention as potential supports for FT catalyst. Amorphous structures such as activated and templated carbon as well as crystalline carbons namely graphite, carbon nanotubes (CNTs), carbon nanohorns (CNHs), carbon nanofibers (CNFs) were all investigated as support material for Fe, Co, and Ru based catalyst in FTS. Utilizing activated carbon (AC) as a catalyst support could be justified due to its: low price, abundance, high temperature stability in an atmosphere without oxygen, superior resistance to acidic/basic media, flexibility for tuning of its textural properties and surface chemistry. Nevertheless, presence of impurities, occurrence of significant micro-porosity, difficulties in reproduction limit its applications as a support for FT catalyst [56]. Notwithstanding, performances of promoted and unprompted Co/AC and Fe/AC catalysts for Fischer–Tropsch synthesis were explored in the literature [57–61]

Majority of porous carbons have micropores $\left(d_{pore} < 2\ nm\right)$ which are not well-suited for applications involving diffusion of large molecules, for example, as a support material in some catalytic reactions. Recently, there has been a considerable interest in developing carbons with mesoporous structure employing different synthesis methods. Ordered mesoporous carbon (OMC) or CMK family could be synthesized using an ordered mesoporous silica material (e.g. MCM-48, SBA-1, and SBA-15) as template. OMC inherits a structured pore arrangement and high surface area from the well-defined structure of the template employed during the synthesis [62]. OMC have been utilized as support material in iron and cobalt based catalyst for HC production in FTS [63–66].

Study of nano-structured materials including nanocarbons was triggered after the discovery of fullerene in 1985 and carbon nanotubes in 1991 by Iijima. Carbon nanotubes (CNTs) and nanofibers (CNFs) have merits of reproducibility and mesoporousity compared to activated carbon and carbon black if employed as a support in heterogeneous catalysis. The CNF was used to synthesize series of Co/CNF catalysts to investigate the impact of cobalt crystallite size in the range of 2.6–27 nm on the intrinsic activity of Co

in FTS. It was found that CNFs did not form mixed compounds with cobalt species and optimum cobalt size would be in the range of 6–8 nm [67].

The multiwalled carbon nanotube (MWCNT or CNT), a novel carbon-based nanomaterial, has currently intrigued researchers to use it as a promising heterogeneous catalyst support because of its exceptional properties: mesoporous texture, chemical inertness, high thermal stability and conductivity, and high mechanical strength [68,69]. The multiwalled carbon nanotubes consist of rolled-over graphene sheets in the concentric cylindrical form. The interactions of graphite basal planes and deposited metals are generally believed to be through weak van der Waals forces [70]. Moreover, the hydrophobicity of carbon nanotubes limits their application in catalysis [71]. Nonetheless, the curvature in CNTs shifts the π-electron density to exterior convex surface which may result in better adsorption sites for metal particles. Xing et al. [72], Tessonnier et al. [73], Chen et al. [74], and Pan et al. [75] have developed procedures and selectively decorated inside and outside surfaces of MWCNTs with metals to study and compare their individual influences in FT and higher alcohol synthesis. The findings reveal that when the particles are encapsulated inside the carbon nanotubes' wall, the electron-deficient inner surface of CNTs and confinement effect result in more reducible, active, selective and stable catalysts in both reactions [72–77]. Other CNT supported Fe and Co catalysts have been developed employing different preparation methods and tested in different operational conditions for their C_{5+} selectivity, activity, and stability in FTS [69,78–81].

Some of the above-mentioned supports used for FT catalysts have exhibited outstanding performances but there are still challenges need to be addressed and make them economically feasible and functional in commercial conditions and scale. The most commercially used support materials for the FT cobalt catalysts are alumina, silica, and titania. However, there is high possibility of nonreducible compound formation (e.g. aluminates and silicates) between cobalt particles and ceramic oxide supports due to the strong metal support interactions (SMSI). Therefore, the hardly reducible fraction of the cobalt in the catalyst would be loss and impact the productivity of the catalyst. To utilize higher extent of active metal in the FT catalyst, some modification in the support material, optimization in metal dispersion, and enhancement in its reducibility are essential [82,83].

2.7 Modifiers and promoters for the Fischer–Tropsch catalyst

It is well-established that the nature of carrier (support) and its textural properties, active metal precursor and its loading quantity, nature /amount of additives and catalyst preparation methods would significantly

influence the physico–chemical properties of a supported cobalt−based catalyst. These properties include cobalt dispersion, crystallite size, degree of reduction, electronic structure, number/structure of active sites, and cobalt-support interaction. Most of the mentioned characteristics of a catalyst are mainly interconnected with the last two, i.e., the strength of cobalt–support bonding and the quantity of cobalt active sites. The type of support material and promoters can directly affect these two crucial features of the active cobalt metal and indirectly modify the other physico–chemical properties and catalytic performance in FTS. Promoters for instance are the compounds that can be doped on active metal in very small quantity to enhance its catalytical performance [5,84]. These elements can function as either a structural, electronic, textural modifier or play a role of stabilizer and poison-resisting agent for the catalyst. Sometime these are modifiers which can influence the surface properties of the support, affect the crystallite size and morphology of the active metal and catalyst lifetime [28,84,85].

The structural promotion refers to influences on the cobalt−support interaction which results in higher cobalt dispersion, enhanced reducibility and stabilized Co active sites (ensemble effect) [84,86]. These might lead to an increase in the conversion/yield or a decrease in the Co particles sintering/agglomeration during the FT reaction [5,85]. It has been speculated that the electronic promoter may affect the adjacent atoms environment (ligand effect) and the active site geometry through intimate mixing with active metal [85,86]. These can induce changes on the fundamental pathways (elementary steps) of FT reaction (CO and H_2 adsorption, C_1 monomer formation, chain growth and termination) [19,87].The electronic/chemical alteration can directly affect the intrinsic site activity and selectivity of Co catalyst in FTS [28,84–86,88].

Transition metals (e.g. Ni, Cu, Mo, V, Cr, Nb, Zr, Ti) including the noble metals (e.g. Ru, Re, Ir, Pt, Pt, Pd, Rh, Os, Au, Ag), rare earth metals (e.g. Ce, La, Sc, Pr, Y), alkali and alkaline earth metals (Li, Na, K, Rb, Cs, Ca, Mg) have been studied as promoters (modifiers) for the supported cobalt catalyst in FTS [5,28,85,89–95]. Platinum, ruthenium, rhenium, iridium from noble metals and manganese, lanthanum, zirconium among transition metals are the most patented promoters for FT Co catalyst [28,96–99]. The high cost, low natural abundance, and impact of precious metals on the cobalt catalytic performance are the key factors to be considered in screening the effective 2^{nd} metal for FT catalyst. For instance, Pt is about 3 and 10 times expensive than Ru and Re, respectively, however, it is about 5 and 7 times more abundant in the nature than Ru and Re, respectively [100].

CHAPTER 3: STRUCTURAL CHARACTERIZATION OF CARBON NANOTUBES

Similar version of this chapter has been published as a research paper in the following journal:

- R.M. Abbaslou, V. Vosoughi, A. K. Dalai, "Comparison of nitrogen adsorption and transmission electron microscopy analyses for structural characterization of carbon nanotubes", Applied Surface Science (2017) 419, 817–825.

Contribution of PhD candidate

The experimental analyses, results compiling / interpretation, writing, and revising of this chapter was conducted by Vahid Vosoughi and Dr. Reza M. Abbaslou considering suggestions from Dr. Ajay Dalai.

Contribution of this chapter to the overall PhD research

In addition to studies for development of multiwalled carbon nanotube (MWCNT) supported catalysts for FTS in Chapter 4 and 5, this chapter provides interpretation of textural properties of multiwalled MWCNTs determined using high resolution transmission electron microscopy (HRTEM) and nitrogen adsorption analyses. Five types of MWCNTs with different structures were examined and the results of microscopic analyses and nitrogen adsorption method were compared. We presented some insights on the uncertainty and limitations of N_2 adsorptions analyses results obtained for the specific surface area, pore volume and average pore diameter considering the theoretical assumptions and results of HRTEM analyses.

3.1 Abstract

Carbon nanotubes (CNTs) are different from other porous substrates such as activated carbon due to their high external surfaces. This structural feature can lead in some uncertainties in the results of nitrogen adsorption analysis for characterization of CNTs. In this paper, the results of microscopic analyses and nitrogen adsorption method for characterization of carbon nanotubes were compared. Five different types of CNTs with different structures were either synthesized or purchased. The CNT samples were characterized by high resolution transmission electron microscopy (HRTEM), scanning electron microscopy (SEM) and N_2 adsorption analysis. The comparisons between the results from the microscopic analyses and N_2 adsorption showed that the total pore volume and BET surface measurements include the internal and external porosity of CNTs. Therefore, the interpretation of N_2

adsorption data required accurate TEM analysis. In addition, the evaluation of pore size distribution curves from all CNT samples in this study and several instances in the literature revealed the presence of a common peak in the range of 2–5 nm. This peak does not explain the inner pore size distribution. The presence of this common peak can be attributed to the strong adsorption of N_2 on the junction of touched and crossed nanotubes.

3.2 Introduction

Carbon nanotubes (CNTs) can be considered as one or more graphene sheets rolled up into concentric hollow cylinder. Depending on the production method, CNTs can be formed either single-walled or multi-walled with open or closed ends [101–103]. In the case of open-end nanotubes, both inner and outer surfaces of CNTs are accessible. The most important structural character of carbon nanotubes is their quasi-one-dimensional inner cavity. The high aspect ratio CNTs (i.e., length to diameter quotient ~ 100-1000) have external diameter of approximately 1 nm for single-walled structure and 3–70 nm for multi-walled structure. These structural properties, including inner and outer surfaces, distinguishes CNTs from other porous materials such as alumina and activated carbons [104–108].

This carbon allotrope with unique mechanical, physico-chemical, and optoelectronic properties have initiated a large interest and promising applications in the area of adsorption, heterogeneous catalysis, energy storage, supercapacitors, microchannel membranes, and electronic devices [69,105–107,109–111]. These potential applications are highly dependent on the chirality, length, surface features and the pore size distribution of CNTs. Consequently, several analysis techniques in the range of microscopic and macroscopic have been developed and used to characterize the structural properties of CNTs [112–117].

CNT samples are usually first examined by electron microscopy techniques which allows investigating the surface and morphology of nanotubes as well as determining the distribution of their inner and outer diameters. However, these techniques require several samples preparations and image analysis. If a CNT sample is homogenous, the characterization can be carried out analyzing a larger number of images, whereas for non-homogeneous samples, microscopic analyses will be unconvincing and thus, a macroscopic characterization technique will be required [109].

Nitrogen adsorption has been used for characterization of porous solids. This technique is able to provide valuable information about the adsorbent, including specific surface area, external surface area, micro

and meso-porosity and pore size distribution [113]. Similar to other porous materials such as activated carbon, silica, alumina and titania, CNTs have also been subjected to analysis using N_2 adsorption and the data have widely been interpreted and used in the literature [69,118–122].

There is a noticeable difference between conventional porous material and CNTs. Porous materials such as activated carbon are substrates with porous structure and their outer surfaces are assumed negligible. However, CNTs have considerable amount of external surface in addition to their internal surface. In other words, the external surface of nanotubes is even larger than their inner surface area. The other major difference between CNTs and other porous material is that the available pore volume of a CNT sample can include the summation of inner pore volume of nanotubes along with inter-tube spaces. Most of the theoretical models in gas physisorption technique, such as BET, BJH, and Langmuir employ the amount of adsorbed N_2 at different relative pressure assuming cylindrical pores with no external surfaces [113]. Therefore, applying the above-mentioned calculation models to obtain average pore size, total pore volume, and pore size distribution of CNTs may lead to inaccurate and unreliable results. There are several instances in the literature indicating the discrepancies between the results from transmission electron microscopy (TEM) and N_2 adsorption analysis [114–117].

In this paper, we have either synthesized or purchased five different CNT samples to study their structural characteristics. To elucidate the experimental data representing the textural and structural properties of the CNTs, all of the samples were analyzed using a high-resolution transmission electron microscopy (HRTEM) and nitrogen adsorption-desorption techniques. Then, results from TEM and N_2 adsorption were compared to demonstrate the suitability and limitations of N_2 adsorption technique for the interpretation of the structural properties of CNT materials. In addition, the structural characterization data from different CNT samples and imbedded discrepancies in the literature were highlighted and discussed.

3.3 Experimental

3.3.1 Material preparations

Five types of CNTs with different structures were either synthesised in our laboratories or purchased. The first CNT sample (denoted as CNT1) was prepared based on chemical vapour deposition (CVD) method. High purity, aligned multiwalled carbon nanotube films were grown on quartz substrates in a CVD reactor. In the CVD process, a solution of ferrocene in toluene was injected in a carrier gas of

Ar/H_2, into a horizontal quartz tube. Details of the synthesis procedure have been reported elsewhere [101]. The second CNT sample (denoted as CNT2) was purchased from MKnano Co. (M.K. IMPEX Canada). The third CNT sample was prepared by acid-treatment of CNT2. 10 g of CNT2 sample was treated with 500 ml of 55 wt. % of nitric acid and refluxed at 110°C for 16 h [123]. This sample denoted as CNT3. The fourth sample was purchased from Nanostructured & Amorphous Materials, Inc. This sample denoted as CNT4. The fifth sample (denoted as CNT5) was synthesized in our laboratories using anodic aluminum oxide (AAO) films along with chemical vapour deposition method. The procedure for production of CNT5 has been given elsewhere [118].

3.3.2 Material Characterizations

The structural properties of CNT samples were determined by nitrogen adsorption at 77 K using a Micromeritics ASAP 2020. Prior to each analysis, the ~ 0.2 g of samples were degassed under vacuum at 200 °C for 5 h. The specific surface area $\left[\mathrm{SSA}\left(\frac{\mathrm{m}^2}{\mathrm{g}}\right)\right]$ was determined deploying the BET (Brunauer-Emmett-Teller) method generalized based on the Langmuir adsorption theory. Plotting the linear form of BET equation allows determination of the monolayer volume $\left[\mathrm{V_m}\left(\frac{\mathrm{STP\ cm^3}}{\mathrm{g}}\right)\right]$ and BET C constant from the resulting intercept (Y) and slope (S) in the $0.05 \leq \mathrm{P/P_0} \leq 0.3$ [124–126]:

$$\frac{(P/P_0)}{V[1-(P/P_0)]} = \left(\frac{1}{V_m C}\right) + \left(\frac{C-1}{V_m C}\right).\left(\frac{P}{P_0}\right) \tag{3.1}$$

$$Y = \left(\frac{1}{V_m C}\right); S = \left(\frac{C-1}{V_m C}\right) \implies V_m = \frac{1}{S+Y} \quad ; \quad and \quad C = \frac{S}{Y} + 1 \tag{3.2}$$

$$SSA_{BET} = V_m \left(\frac{1}{22414\ \frac{STP\ cm^3}{mol.}}\right)\left(6.023 \times 10^{23}\,\frac{molec.}{mol.}\right)\left(16.2 \times 10^{-20}\,\frac{m^2}{molec.}\right) \tag{3.3}$$

The last term in equation 3.3 is the N_2 cross-sectional area.

To determine the pore volume, the isotherm data (volume adsorbed vs. relative pressure) were collected at $\mathrm{P/P0} = 0.97$ for single point approximation and pores less than 70 nm. The corresponding average pore diameter were also calculated using $4\mathrm{V/SSA_{BET}}$. For pore size distribution, BJH (Barret, Joyner, and Halenda) procedure based upon modified Kelvin model for pore filling was used. The isotherm data for BJH were collected near the saturation point $(\mathrm{P/P0} \geq 0.99)$ to assure all pores between 1.7 nm and

300 nm are filled. Due to the presence of carbon and metal blockages inside the CNT pores, fraction of pores open at both ends was assumed as zero. The total amount of adsorbed N_2 includes capillary condensation inside the pores and gradual film growth on the pore walls. The amount of condensation and film thickness are interrelated with relative pressure of adsorbate [28,29]. Kelvin model (equation 3.4) can correlate the condensation pressure and capillary radius (r_c). The adsorbed multilayer thickness (t) was predicted using the Halsey equation (equation 3.5). The pore radius (r_p) is the summation of capillary radius and film/statistical thickness ($r_p = r_c + t$) [127,129]:

$$r_c = \frac{-2\gamma V_p}{RT \ln(P/P_0)} \tag{3.4}$$

$$t = 3.54\left[\frac{-5}{(P/Po)}\right]^{1/3} \tag{3.5}$$

Where V_p is the molar gas volume adsorbed. The following properties used for N_2 in Kelvin equation [126]: $\gamma = \text{surface tension} = 8.88\ \frac{\text{dyne}}{\text{cm}}$; $\rho = \text{Molar density} = 0.02887\ \frac{\text{g}}{\text{cm}^3}$

For each CNT sample, 10 grids were prepared and at least six representative images from each grid were recorded. Then, the total number of 60−80 TEM images per sample were used for measurements and statistical evaluations. On each image, every single nanotube was marked, afterward the inner pore diameter and outer diameter of nanotubes were measured using Digital Micrograph software (version 3.11.0, Gaton Inc., 1996−2006). In addition, the accessibility of inner pore (open/closed/blocked) for every marked nanotube was recorded. In order to report the pore size distribution and the percentage of accessible inner pore (open capped pores), a population of at least 150 data points (measurements) from each sample was used.

Scanning electron microscopy characterization was conducted using Phillips SEM-505 (Edwards Vacuum Components Ltd., Sussex, England) at 300 kV in SE display mode. All the CNT samples were covered by gold in the sputter coating unit, prior to analysis.

3.4 Results and discussion

3.4.1 Transmission electron microscopy (TEM) analysis

In order to study the structure and the pore size distribution of the CNT samples, several TEM images were obtained and analyzed. Figure 3.1 shows representative images of each sample. The summary of

results from TEM analyses including inner pore accessibility, distribution of external diameter (nm), distribution of inner pore diameter, statistical average of inner pore diameter, statistical average of external pore diameter and average wall thickness are also given in Table 3.1. CNT1 sample was a non-homogenous sample and their external diameter varied from 25 to 130 nm. The internal cavities of CNT1 were already blocked during the synthesis stage. Also, the size measurement from > 60 images showed that the internal pore diameter of CNT1 were placed in an interval of 5 to 20 nm with statistical average of 9±4 nm. It should be noted that the statistical average is given in the form of average value ± the population's standard deviation.

Table 3.1 Results of TEM analysis for the CNT samples

Sample Name	Structure	Internal Dia. (nm)	External Dia. (nm)	Ave. Internal Dia. (nm)	Ave. External Dia. (nm)	Wall Thickness (nm)
CNT1	Blocked-pore	5–20	25–130	9 ± 4	42 ± 29	17 ± 14
CNT2	Closed-cap	5–9	18–30	7 ± 1	21 ± 3	7 ± 2
CNT3	Opened-cap	5–9	18–30	7 ± 1	21 ± 3	7 ± 2
CNT4	Blocked-pore	6–13	15–45	9 ± 2	30 ± 10	11 ± 5
CNT5	Opened-cap	35–70	50–90	55 ± 10	67 ± 10	6 ± 1

CNT2 sample had a narrow pore diameter distribution. Their inner pore varied from 5–9 nm with a statistical average of 7±1 nm. The external diameter distribution was also uniform ranging from 18−30 nm. Most of the CNT ends (95%) were closed, however, their inner pores were hollow (Figure 3.1). The acid treated CNT2 sample (CNT3) kept its original pore size distribution with average pore diameter of 7±1 nm. The major difference between CNT2 and CNT3 was that the acid treatment resulted in removing majority of the caps (~ 80%) as they are shown in Figure 3.1.

According to the results of TEM analysis, the external diameter of CNT4 sample varied from 15 nm to 45 nm while the distribution of inner pore diameter fell into an interval of 6–13 nm. The statistical average pore diameter for the CNT4 sample was 9±2 nm. As shown in Figure 3.1, high resolution TEM images of CNT4 sample revealed that the inner pore of the sample was not accessible. In fact, the inner cavity of CNT4 sample was blocked by graphite layers during synthesis period.

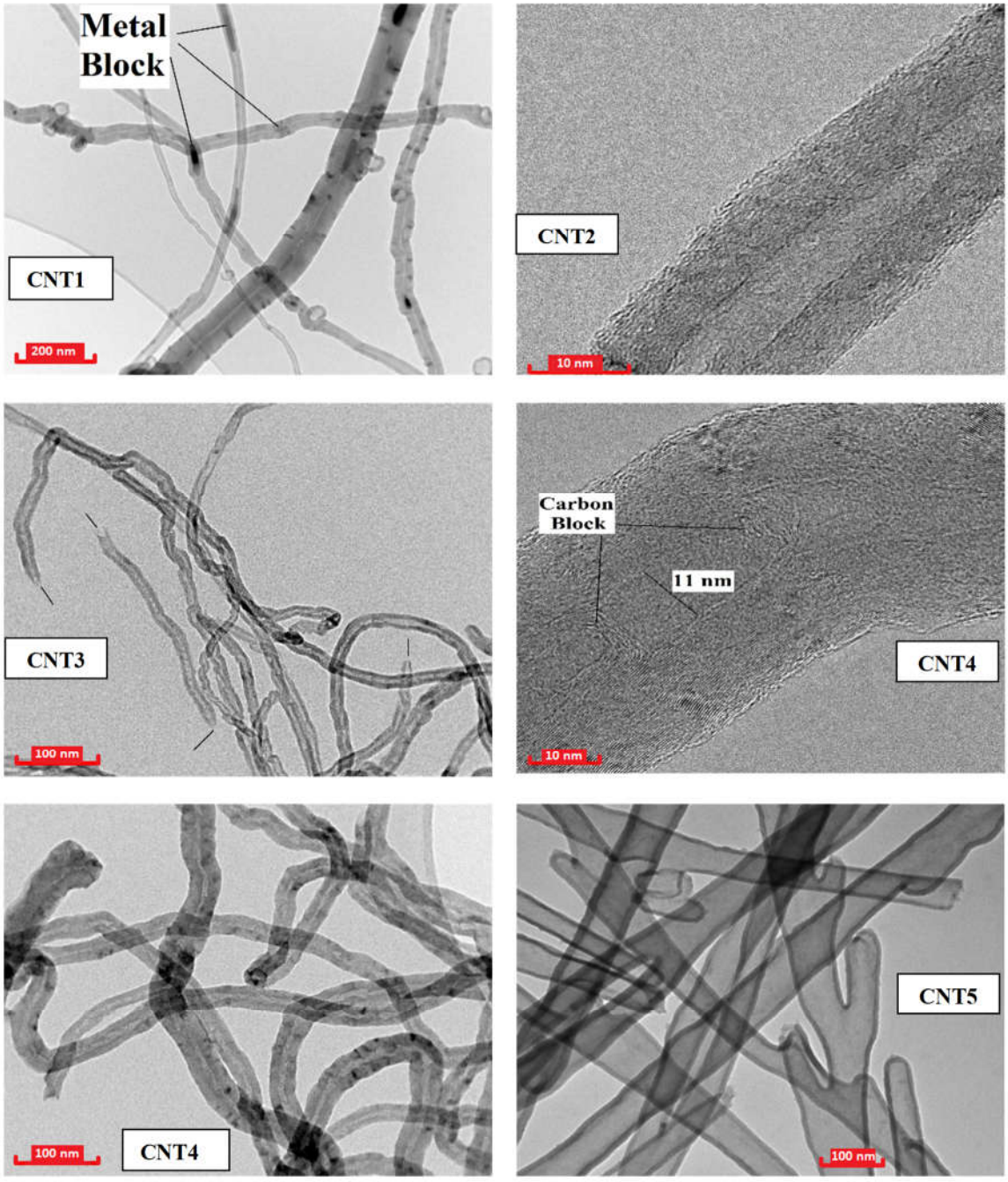

Figure 3.1 TEM images of the CNT samples showing the structure, pore diameter and accessibility of inner pore

CNT5 sample was produced using AAO precursor possessed a wide pore diameter with several “Y” branches. The outer diameter of CNT5 sample varied from 50–90 nm, as are shown in Table 3.1. The

important feature of this sample was that the inner pore diameter ranging from 35−70 nm and inner cavity was accessible from at least one end of each nanotubes.

3.4.2 Nitrogen adsorption isotherms

The nitrogen adsorption-desorption isotherms of the CNT samples studied are given in Figure 3.2. Regardless of their structure and pore size distribution, all of the CNT samples exhibited similar pattern which are composite of type III and type V adsorption isotherms, with type H3 adsorption hysteresis loop, according to IUPAC classification [125]. These are similar to typical N_2 isotherms and hysteresis for CNTs, mesoporous materials with broad pore size distribution, and aggregated plate-like pore structures [9-31]. The subsequent isotherms reflect mechanism of pore filling with N_2 for the CNT samples which can be divided into three regions. The first part exhibited a slow and gradual increase in the quantity of adsorbed N_2 which can be attributed to monolayer and multi-layer nitrogen adsorptions at low relative pressures ($0.01 \leq P/P_0 \leq 0.1$). A steep rise in N_2 uptake at very lower range of relative pressures ($P/P_0 \leq 0.01$) could be assigned to the presence of micropores in the MWCNT structure, however, there was no recorded data for this region. The second region is a slow-increasing (no-zero) slope in the middle confirming the presence of mesopores and external surface area. Its long extension within varying relative pressure of 0.1−0.8 verifies that the broad pore size distribution presents in the corresponding CNT sample. The third part comprises of a sharp rise in the amount of nitrogen condensed in the relative pressure ranging from 0.8 to 1.0.

3.4.3 BET surface area

The BET calculation obtains the sample surface area value by determining the monolayer volume of adsorbed gas from the isotherm data. The results of N_2 adsorption analysis for all five samples are given in Table 3.2.

Regarding the BET surface area, CNT1 and CNT4 samples presented lowest BET surface area. This can be attributed to the closed or blocked structure of inner cavities of these samples. In addition, CNT1 and CNT4 possessed larger diameter and thicker wall compared to that of other samples in this study which in turn leads to limited specific surface area.

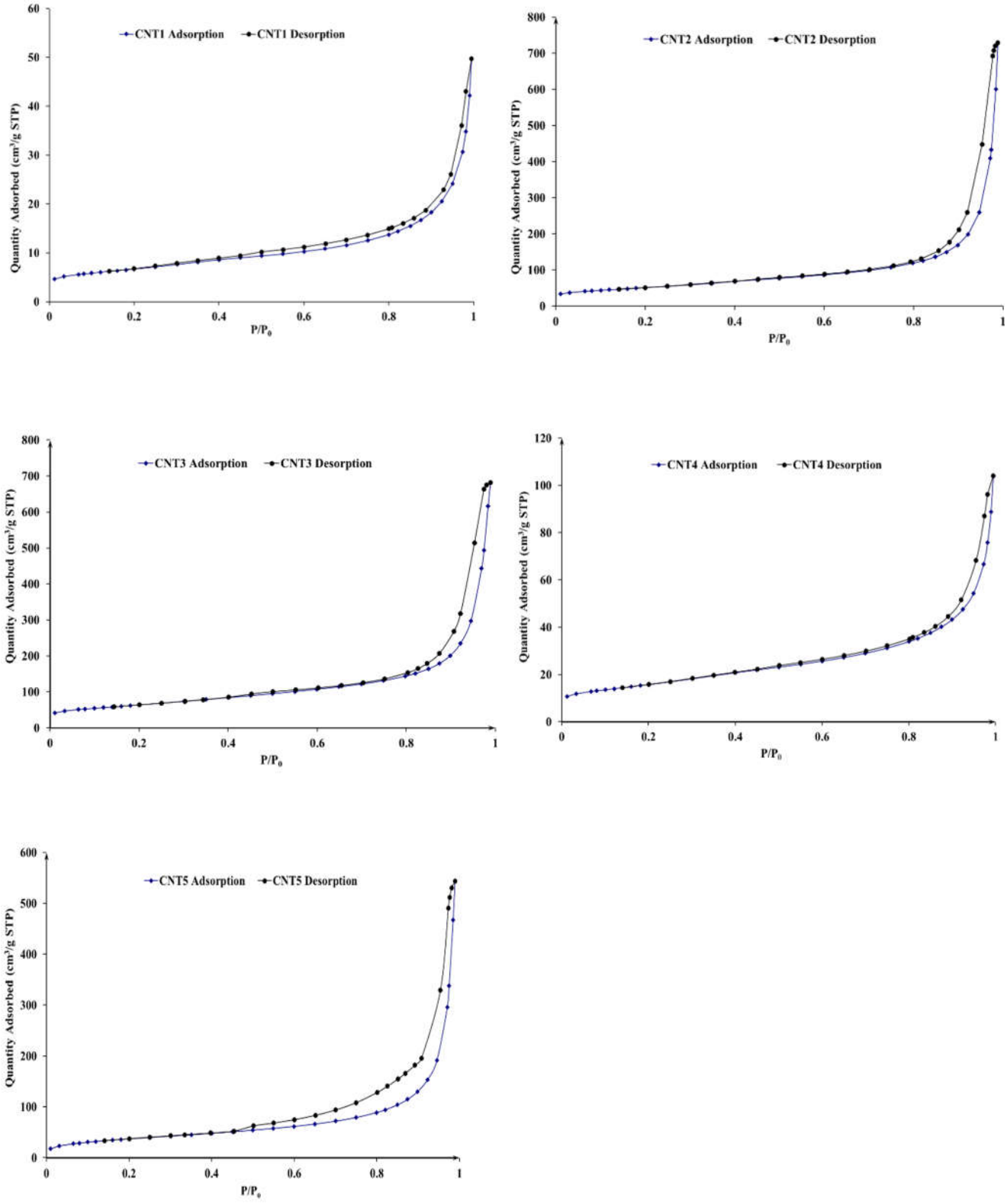

Figure 3.2 Nitrogen adsorption-desorption profiles for the CNT samples

Table 3.2 Nitrogen adsorption-desorption profiles for the CNT samples

Sample Name	BET Surface Area (m^2/g)	Average Pore Dia. (4V/A) (nm)	Total Pore Vol. (cm^3/g)
CNT1	23	8.1	0.05
CNT2	178	13.8	0.64
CNT3	229	11.9	0.69
CNT4	55	7.3	0.10
CNT5	205	10.2	0.53

As discussed in the previous section, CNT3 sample is the acid-treated version of CNT2. The TEM analysis revealed that acid treatment resulted in removing the nanotubes' caps. A theoretical calculation on the surface area of CNT2 and CNT3 samples was performed to compare the results of TEM and N_2 adsorption analyses. Supposing the n_t, n_{cl}, and n_{op} are the total number of nanotubes, the number of closed-ended, and the number of open-end nanotubes per unit mass, respectively and L is the average length of nanotubes. The percentage of open-end CNTs based on measured surface area (S) can be calculated as follows:

$$n_t = n_{cl} + n_{op} \tag{3.6}$$

$$S_{CNT2} = n_t \pi d_{out} L \tag{3.7}$$

$$S_{CNT3} = n_{op} \pi d_{out} L + n_{op} \pi d_{in} L + n_{cl} \pi d_{out} L \tag{3.8}$$

$$\frac{S_{CNT2}}{S_{CNT3}} = \frac{n_t \pi d_{out} L}{n_{op} \pi d_{out} L + n_{op} \pi d_{in} L + n_{cl} \pi d_{out} L} \tag{3.9}$$

For CNT2 sample with average $d_{out} = 21$ nm, $d_{in} = 7$ nm, $S_{CNT2} = 178$, and $S_{CNT3} = 229$ m^2/g, equation 3.9 resulted in:

$$\frac{n_{op}}{n_t} = 0.85 \tag{3.10}$$

The calculation shows that more than 85 percent of the capped nanotubes became open due to acid treatment at 110°C. This is in a good agreement with the results of TEM analysis showing that about 80%

of CNT caps have been removed. The concurrence between TEM and N_2 adsorption implies that BET analysis is reliable enough to calculate the summation of accessible inner and outer surface of nanotubes.

3.4.4 Average pore diameter

Average pore diameter is often used to calculate the average and representative pore diameter for porous substrates. Assuming that the pores are cylindrical, the average pore diameter (or pore width) is generally calculated based on 4V/A, whereas the V is specific total pore volume (single point) and A is the BET surface area. Average pore diameters (4V/A) of the CNT samples are given in Table 3.2. As can be expected, there are discrepancies among the results of TEM analysis and N_2 adsorption calculations for average pore diameter. This is due to the fact that the external surface area was higher than the internal surface for the CNT samples and the pore volume was also included the external volume of the nanotube aggregates. Therefore, the BET analysis calculation can result in inaccurate average internal pore diameter for CNTs.

3.4.5 Total pore volume

The results of total pore volume for the CNT samples are given in Table 3.2. Similar to the BET surface area, CNT1 and CNT4 had the lowest pore volume among the others. As shown in Figure 3.1, the inner pore of both CNT1 and CNT4 samples were blocked then the adsorbate did not have access to their inner cavity. Furthermore, both samples had large external diameters and thicker wall compared to other CNT samples in Table 3.1. These structural features (large outer diameter and thick nanotube wall) resulted in lower pore volumes compared to the other CNT samples examined in this study. Also, since their external pore diameters were large, their inter-tube spaces might be too big to be filled by the condensed nitrogen.

As shown in Table 3.2 and discussed in section 3.2.2, in the case of CNT3 sample, approximately 80% of nanotubes had open ends while this fraction was less than 5% for CNT2 sample. A comparison between the total pore volume of CNT2 (0.64 cm^3/g) and CNT3 (0.69 cm^3/g) showed that the pore volume corresponding to inner porosity compared to the total pore volume of these specimen were only a small portion of the measured volume (6−10 % of the total pore volume). Also, this comparison showed that the total pore volume measured by N_2 adsorption was the summation of volume of inner cavities and outer aggregated spacing of the nanotubes. In the case of CNT5, however, the inner pore was much wider than the CNT3. It is expected that a larger portion of the total pore volume belonged to the internal pore cavity.

In summary, the total pore volume of a CNT samples depends on the structural properties of the CNTs, including accessibility of inner pores, inner pore diameter and outer diameter of nanotubes. Therefore, the measured total pore volume by N_2 adsorption analysis can be used and interpreted if only the structure of nanotubes is known using a microscopy analysis.

Recently, De Lange et al. also addressed the limitations of the BJH and BET methods and details of the employed methodology namely the relative pressure range, sample quantity, inter-particle condensation, fitting methods, and test cell might negatively influence the certainty of the analyses results [128]. It is noteworthy that the proper choice of adsorptive such as krypton instead of N_2, also employing new models namely DFT instead of BJH and BET had appreciable progress on resolving the uncertainties of the conventional structural characterizations models [130].

3.4.6 Pore size distribution

The pore size distributions (PSD) of the CNT samples studied are shown in Figure 3.3. Interestingly, regardless of their different structural characteristics, all samples exhibited similar PSD patterns with a maximum in the range of 2–4 nm and another in the range of 5–130 nm. The second wide peaks are attributed to the aggregated spaces of CNT bundles. But in the case of the first sharp peak (at the range of 2-4 nm), the interpretation is not simple.

The literature review showed that there are several papers in which similar PSD profiles for different CNT samples have been reported [114–117,119–122,131–140]. These studies, including the results from characterizations of our five CNT samples, indicate that the presence of a peak at 2–4 nm is a common feature of carbon nanotubes regardless of their different structural properties.

There are number of reports in which the first peak has been attributed to the inner cavity of the CNT sample [12-15]. However, there have been discrepancies between their TEM results and their PSD curves. Zhu et al. [114] have studied hydrogen adsorption in the bundle of multiwalled CNT and characterized the CNT samples with TEM and N_2 adsorption. Their results showed that the inner cavity of their CNT sample was approximately 11 nm while there was a peak at 3–4 nm in their PSD curve.

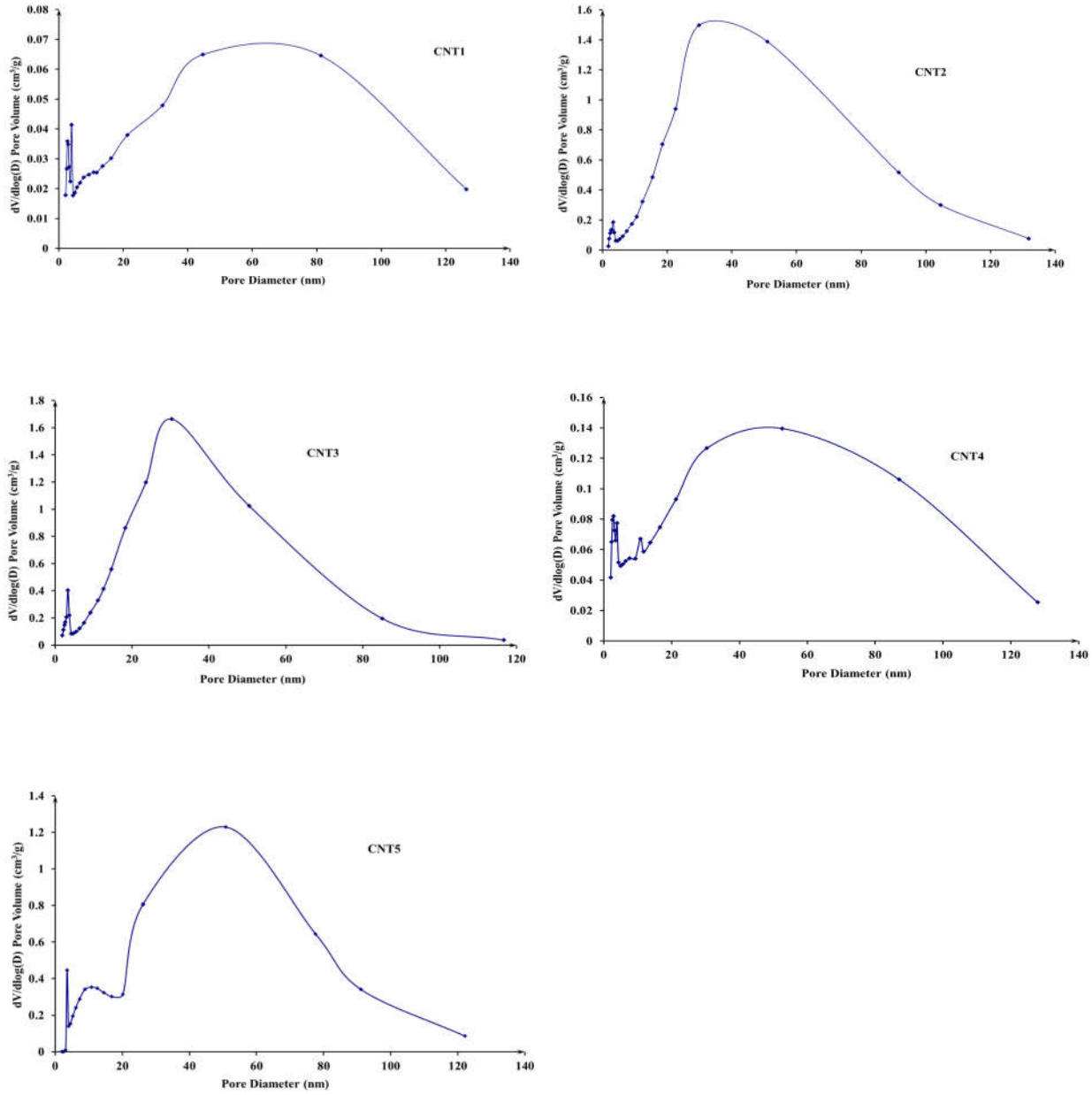

Figure 3.3 Pore size distribution curves for the CNT samples

Felenolov et al. [115] reported the characteristics of filamentous carbon (with no inner porosity) produced by methane decomposition on co-precipitated Ni/alumina and Ni-Cu/alumina catalysts. They noticed the presence of a peak at 3−4 nm and proposed that micro-roughness on the surface on monofilaments could be responsible for the peak at 2−4 nm. In another research, Shih and Li [116] examined the adsorption behaviours of volatile organic compounds (VOCs), n-hexane, benzene, trichloroethylene and acetone on two different types of multiwalled carbon nanotubes with inner pore of 7.3 and 11.2 nm. However, their

N_2 adsorption analysis and corresponding PSD curves for both CNT samples exhibited a peak at 3-4 nm. Similarly, Chiang and Wu [117] investigated and reported the adsorption of sulfur hexafluoride (SF6) on the multiwalled carbon nanotubes. The TEM images revealed that their CNT samples possessed inner pore sizes of > 10 nm. On the other hand, a sharp peak at 3−4 nm on the PSD profile was reported.

Regarding the CNT samples in this work, it is obvious that the peak at 2–4 nm on the PSD curves cannot be attributed to the inner cavities of the CNTs. As shown on Table 3.1 and Figure 3.1, the inner pore diameter of all CNT samples in this report were larger than 7 nm. Obviously, in the case of CNT1, CNT2 and CNT4 the inner hollows of the CNT samples were already blocked. Having considered the abovementioned instances and observations, it is convincing that the inner pore porosity is not responsible for the presence of the peak at 2−4 nm in the PSD profiles of the samples.

In order to study the bulk structure of CNT aggregates, CNT3 sample was analysed by scanning electron microscopy. One representative image of CNT3 sample is given in Figure 3.4. As can be seen, there are several locations where the nanotubes can meet and cross each other. This closeness can be attributed to the adherence resulting from Van der Waals forces of attractions between a pair of nanotubes. Their aggregation leads to form bundles of nanotubes including interstitial channels among nanotubes and grooves where two adjacent nanotubes meet [141]. If this is the case, as it is shown in the SEM image, strong nitrogen condensations can happen in the three-dimensional pores among transversal nanotubes as depicted in Figure 3.5. In other words, nitrogen condensations may cause two surfaces to bridge together (capillary adhesion). Let us consider a simple model for a pair of crossed nanotubes. The schematics of the model is illustrated in Figure 3.5.

If the spaces between two crossed nanotubes are filled with the condensed nitrogen and average radius of nanotubes is r, then the cross-section area can be calculated as follows:

$$A = r^2 \left[Sin(\theta) - \frac{Sin(\theta) \cdot Cos(\theta)}{2} - \frac{\theta}{2} \right] \tag{3.11}$$

where the θ [rad] angle represents the filling level of the inter-tube spacing. For the cross section of *A,* an equivalent cylindrical pore will be $d_{e-pore} = 2\sqrt{A/\pi}$. Now, for filling angle of π/4 and real nanotube diameters of 30 nm and 60 nm, d_{e-pore} will be 2.14 and 4.25 nm, respectively. These equivalent cylindrical pore diameters are in agreement with the results of N_2 adsorption. Considering the simplicity

of the model and the agreement between the measured BJH pore size distribution and the calculated pore diameters, it is quite convincing to consider the hypothesis for further investigations.

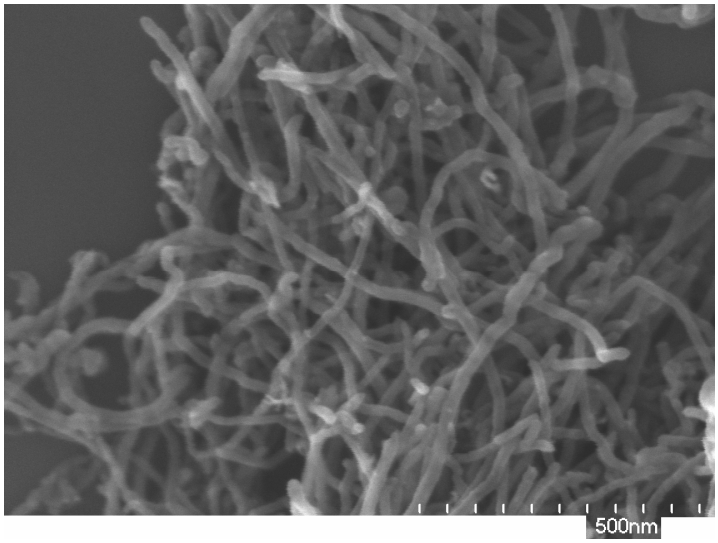

Figure 3.4 Scanning electron microscopic image of CNT3 sample.

3.5 Effects of nanotubes compression on the results of N2 adsorption analysis

In order to support the above-mentioned hypothesis, the effects of compression without addition of any binder were examined. To do so, CNT3 sample was compressed under 7 metric tonnes for 24 hours. Then the pelletized sample was analyzed using N_2 adsorption. The results including BET surface area, total pore volume, and pore volume corresponding to the pores with diameters of 2–5 nm are given in Table 3.3. The data show that the effect of compression of the BET analysis was negligible. In fact, BET calculations are independent from the compactness or alignment of CNT bundles. This is because, BET calculation is based on the monolayer coverage of nanotubes' surfaces and it is not a function of total pore volume.

The pore size distribution of CNT3 and compressed CNT3 are also presented in Figure 3.6. Comparison between PSD curves of CNT3 and compressed CNT3 sample reveals that the second peak corresponding to the spaces of aggregated nanotubes shifted from 30 nm to 18 nm. This is expected that the compression of nanotubes will result in a denser CNT bundle.

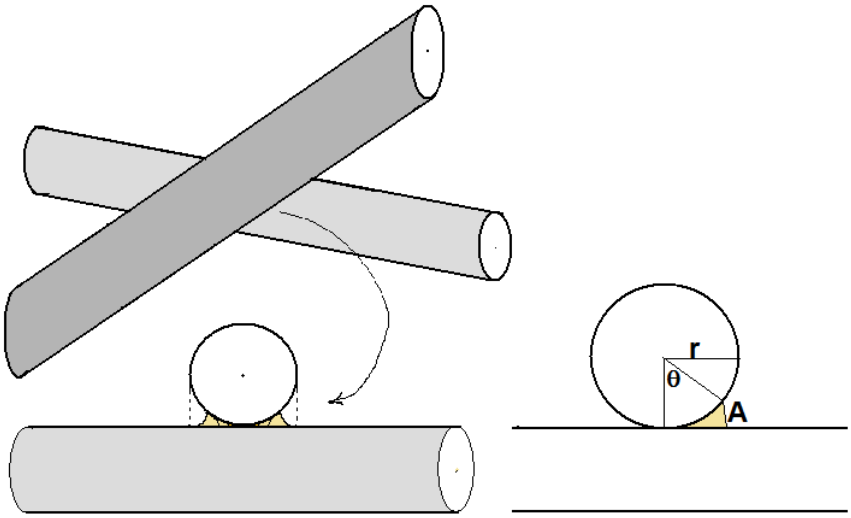

Figure 3.5 Schematic of crossed nanotubes in a bundle of CNT and the hypothesised model

Accordingly, the data for total pore volume, given in Table 3.3, shows that BJH adsorption cumulative volume decreased significantly from 1.06 to 0.66 cm^3/g. Interestingly, the compression did not change the position of the peak in the range of 2–5 nm However, the quantity of adsorbed nitrogen corresponding to the pores with diameters of 2–4 nm increased by 15%.

Table 3.3 Results of N_2 adsorption analysis for CNT3 and packed-CNT3 samples

Sample Name	**BET (m^2/g)**	**Pore Vol. (cm^3/g)**	**BJH Ads. Cum. Vol. (cm^3/g)**	**Ave. pore Dia. (nm)**	**Pore Vol. 2-5 nm (cm^3/g)**
CNT3	228.8	0.69	1.06	11.9	0.036
Compressed CNT3	229.2	0.58	0.66	10.2	0.041

The increased quantity of adsorbed nitrogen in that range can be attributed to the increase in the number of crossed and touched nanotubes in the compressed sample. This experimental observation supports the hypothesis that the nitrogen molecules can be strongly adsorbed and trapped in the transversal junction of the nanotubes, therefore they will not be desorbed unless a low relative pressure (P/P_0) is provided.

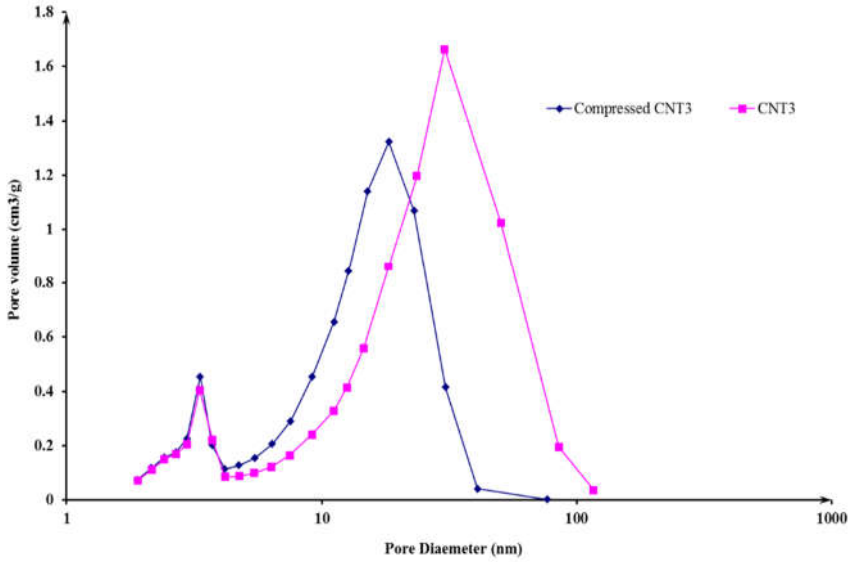

Figure 3.6 Pore size distribution curves for CNT3 and compressed CNT3 samples

3.6 Conclusions

The comparison between characterization results of the open-end and closed-end CNTs proved that the measured pore volume from N_2 adsorption technique includes both inter-nanotube spaces and internal cavities' volume (if the CNT sample comprised of open-ended nanotubes). The result of theoretical calculation revealed that the BET analysis is a reliable method to measure the summation of available internal pore surface and external surface of CNTs. Furthermore, the disagreements between the average pore size resulting from TEM and N_2 adsorption analysis indicated that the calculated average pore diameter based on N_2 adsorption analysis (4V/A) is not able to accurately predict the average internal pore width of the CNTs. Finally, it was demonstrated that the observed common sharp peak in the range of 2–4 nm on the PSD curves of CNT samples can be attributed to the strong adsorption of N_2 in the junctions of crossed and touched nanotubes.

CHAPTER 4: EFECT OF CNT PRETREATMENT ON Co/CNT CATALYST FOR FTS

A version of this chapter has been published as a research paper in the following journal and presented in the following conference and symposium:

- V. Vosoughi, S. Badoga, A. K. Dalai, N. Abatzoglou, "Effect of Pretreatment on Physicochemical Properties and Performance of Multiwalled Carbon Nanotube Supported Cobalt Catalyst for Fischer−Tropsch Synthesis", Ind. Eng. Chem. Res. (2016) 55, 6049−6059.
- V. Vosoughi, A. K. Dalai, N. Abatzoglou, "Fischer−Tropsch Synthesis: properties and performance of promoted Co/MWCNTs catalyst", 64th CSChE Conf., Oct. 19-22, 2014, Niagara Fall, Canada.
- V. Vosoughi, A.K. Dalai, "Synthesis of C_{5+} hydrocarbons through Fischer−Tropsch synthesis using multiwalled carbon nanotube supported cobalt catalyst", 23rd Canadian Symposium on Catalysis, May 11-14, 2014, Edmonton, Canada.

Contribution of PhD candidate

The experimental design, CNT treatment, catalyst preparation, characterizations, FT tests, compiling / interpretation of the results, and manuscript writing, were accomplished by Vahid Vosoughi. Dr. Sandeep Badoga assisted with the data analysis and preparing the rebuttals and revisions of the manuscript. The supervisors, Dr. Ajay Dalai and Dr. Abatzoglou, provided overall guidance and monitored the research progress.

Contribution of this chapter to the overall PhD research

After exploring textural characterization of carbon nanotubes in Chapter 3, this part of work presents insights about carbon nanotube (CNT) pre-treatment, CNT supported cobalt catalyst preparation, its application and performance for Fischer−Tropsch synthesis. The influence of different nitric acid concentrations (35, 50 and 70 wt. %) on the physico−chemical properties of multiwall carbon nanotube was investigated. Also, the corresponding cobalt catalysts were characterized by various techniques to study the impact of acid functionalization on the activity and selectivity of the prepared catalysts for Fischer−Tropsch synthesis.

4.1 Abstract

The influence of different nitric acid concentrations (35, 50, 70 wt. %) on the physicochemical properties of multiwalled carbon nanotube was investigated. 15 wt. % cobalt was impregnated on acid treated nanotubes. The corresponding catalysts were characterized by BET, XRD, Raman, SEM, TEM, TPR, CO chemisorption techniques to further study the impact of acid functionalization on textual properties, metal dispersion, crystallite size, defect generation, and reducibility of 15Co/CNT catalysts. The performance of prepared catalysts was tested for 30 % CO and 60 % H_2 with balanced Ar in a fixed bed microreactor for Fischer−Tropsch synthesis at 220 ˚C, 2 MPa, and GHSV of 3000 $cm^3 \cdot g^{-1} \cdot h^{-1}$. Pretreatment of CNTs with 70 wt. % nitric acid exhibited improved physicochemical properties of 15Co/CNT catalyst and hydrocarbon yield by 35% as compared to untreated CNT supported catalyst.

4.2 Introduction

Dwindling fossil resources, oil and gas supply security instabilities, air pollution, lessening of the flaring of associated gas, and global climate change are part of recent energy and environmental concerns. On the other hand, new discoveries of natural gas reserves, benefits from utilization of remote or stranded natural gases, and considerable improvement in carbon-containing feed-to-liquid (XTL) technologies provide further impetus for introducing alternative energy route and processes to conventional oil refining industries and products [4,142]. In the XTL integrated system, feedstock can be obtained from various carbonaceous resources and transformed into synthetic gas or syngas (hydrogen and carbon monoxide). The syngas is then catalytically converted into mixture of mainly paraffins, α-olefins, oxygenates, water, and carbon dioxide via Fischer–Tropsch synthesis (FTS). The value added hydrocarbon and oxygenate fractions are finally upgraded in order to produce sulfur and aromatic free transportation fuels and chemicals [2,143,144]. The catalyst design and understanding of FTS catalysis, along with proper process conditions and reactor type, are still the ongoing research interest of scientists and industries despite of the current acquired technological knowledge [144]. For high hydrogenation and low water−gas shift activity, high long chain alkanes selectivity, and high stability, supported cobalt is the preferred commercial catalyst as compared to Ni, Fe, and Ru in FTS [1,5]. For optimal use of fairly expensive cobalt metal, suitable support material needs to be chosen. Despite the fact that alumina, titania, and silica are widely used supports for Fischer−Tropsch commercial catalyst, there is high possibility of nonreducible compound formation (aluminates and silicates) between cobalt particles and ceramic oxide supports due to strong metal support interactions [82,83]. To overcome this issue, various other neutral supports such as activated carbon, carbon nanofibers, and carbon nanotubes have been

tested for FTS [5,23,67]. Previously in our group, Tavasoli et al., have compared the CNT supported Co catalyst with alumina supported Co catalyst for FT reaction in continuous stirred tank reactor [145]. The CNT based catalyst had shown significant increase in CO conversion as compared to alumina-based catalysts. However, both alumina and CNTs supported catalyst have shown similar stability and deactivation rate for FTS reaction [145,146]. This confirms the potential of CNTs to be tested as support material for Co catalyst, which can be used in fixed bed reactors for FTS.

Functionalization of CNTs is important and has also gained a lot of attention in an attempt to enhance its hydrophilicity and interaction with metal particles [78,79]. Functionalization of MWCNTs with nitric acid, air oxidation and ball milling has been comparatively studied for Pt/CNT catalyst for selective hydrogenation [147]. Other research group elucidated the influence of nitrogen and oxygen functionalization (with ammonia and gas phase nitric acid) of CNTs on iron based catalyst for FTS [148]. Functionalization with acid is generally considered as a wet chemical oxidation method to introduce oxygen-containing groups (hydroxyl, carbonyl, and predominantly carboxyl) on CNT walls. Furthermore, CNT pretreatment or functionalization is essential to eliminate the amorphous carbon and metal impurities, to remove the caps from tube endings, and to form some defects in CNT skeletons [149,150]. The presence of functional groups and defects on CNT walls plays the role of anchoring sites for the metal particles. This is a result of enhancement in the exchange of cations between metal and functionalized CNTs [79,151]. Consequently, the active metal dispersion in carbon supported catalyst is dependent on functionalization. This results in difference in activity of the catalysts prepared by different functionalization methods and conditions [151]. In our research group, the influence of acid treatment on CNTs as a support for Fe and Co catalysts has been investigated at room (25 ˚C) and moderate (100 ˚C) temperatures in FTS [81,103]. Trépanier et al. [81] have used 30 wt. % HNO_3 for CNT functionalization of the cobalt based catalyst. Moreover, Abbaslou et al. have patented a CNT supported iron catalyst for FTS and functionalized the CNTs with 60 wt. % nitric acid. The Fe/CNT catalyst has been tested for the period of 125 h and showed a steady state CO conversion of 84 % [152]. Zhu et al.[153] and Zhang et al. [154] have chosen nitric acid with 68 and 54 wt. % concentrations, respectively, to functionalize the CNT as a support for cobalt based catalyst in FTS.

The various functionalization conditions for treating pristine CNT influence the corresponding catalytic activity. However, to the best of our knowledge, the impact of acid concentration on properties of CNT and CNT supported Co catalysts in FTS have not been studied. The present work aims at examining the influence of different nitric acid concentrations (35, 50, and 70 wt. %) on physicochemical properties of

CNTs. The nitric acid treated CNTs were used as support material for Co catalyst. The Co/CNT catalysts were characterized using BET, XRD, CO chemisorption, TEM, Raman spectroscopy and TPR. The impact of different pretreated CNTs on cobalt dispersion, crystallite size, consequently on the activity of Co/CNT catalyst, and its selectivity to C_{5+} hydrocarbons in FT reaction was also studied.

4.3 Experimental methods

4.3.1 Support treatment and catalyst preparation

The functionalization of the carbon nanotubes was carried out by refluxing 20 g of pristine MWCNTs (95 %, 10−20 nm O.D.) in 1 L of nitric acid with different concentrations of 35, 50, and 70 wt. % for 14 h at 120 ˚C. After acid treatment, the CNTs were repeatedly rinsed with deionized (DI) water and filtered to wash off all the remaining acids. Once stable pH of solution was reached, samples were dried at 100 ˚C overnight [103]. Treated CNT batches were designated as CNT35, CNT50 and CNT70 as they were oxidized with nitric acid concentrations of 35, 50 and 70 wt. % respectively. These CNTs were used as supports for Co based catalysts. Specified amount of cobalt nitrate [Alfa Aesar $Co(NO_3)_2.6H_2O$, 99.9%], as cobalt active metal precursor, was dissolved in DI water to obtain 15 wt. % of cobalt on treated CNTs. Incipient wetness impregnation (IWI) method were applied to load the cobalt metal on CNT. The 15Co/CNTX (X = wt. % concentration of HNO_3 used for CNT pre-treatment: 35, 50, or 70 %) catalysts were first dried at 100 ˚C overnight. Then the dried catalysts were calcined with heating ramp of 1 ˚C/min and maintained at 350 ˚C for 3 h under Ar flow of 75 mL/min [81,104]. The stabilized Co/CNT catalysts were labeled as 15Co/CNT35, 15Co/CNT50 and 15Co/CNT70 based on the acid concentrations used during pre-treatment.

4.3.2 Catalyst Characterization

Nitrogen Physisorption: Micromeritics ASAP 2000 instrument was used to collect adsorption-desorption data at cryogenic temperature of liquid nitrogen, i.e. 77 K. Before the measurement, the specimens were degassed under 50 mTorr (6.7 Pa) vacuum at 200 ˚C for 4 h. Brunauer–Emmett–Teller (BET) equation was used to find out the surface area, and Barrrett–Joyner–Halenda (BJH) method was applied to calculate the specific pore volume of different CNT supports and Co/CNT catalysts [155].

CO Chemisorption: The Micromeritics ASAP 2020 chemisorption instrument was used to determine the carbon monoxide adsorption on the cobalt oxides. The catalyst was reduced at 350 ˚C for 150 min under

hydrogen flow. The reduced catalyst temperature was then decreased to 35 ˚C and kept at 1.3×10^{-5} Pa vacuum. The CO gas pulses were allowed to flow over the sample at 35 ˚C to determine the total CO uptake. The percentage metal dispersion was calculated using following equation [155]:

$$D(\%)_{Co} = \frac{1}{22414} \times \frac{V \times SF_{cal.}}{Co\ weight\ fraction/Co\ MW} \quad (4.1)$$

where D (%) is metal dispersion (%), V is the volume intercept obtained from the best line fit to the selected points of the first analysis and the repeat analysis (cm^3/g STP), and $SF_{cal.}$ is calculated stoichiometry factor (weighted average of SF for the metals in the sample) [155].

Metal dispersion can also be used to calculate the average cobalt crystallite size. All cobalt particles were assumed to be uniformly dispersed in form of spherical shape with the site density of 14.6 at/nm^2. Considering these assumptions and all cobalt particles reduced during the analysis, the following formula was obtained [47]:

$$d(Co^0)\ (nm) = \frac{96}{D(\%)_{Co}} \quad (4.2)$$

Raman Spectroscopy: Renishaw System 2000, wire version 1.3 was employed to carry out the Raman analyses of the fresh and functionalized CNTs. To determine the quality of carbon nanotubes' structure before and after acid treatment, samples were exposed to the laser excitation wavelength of 514 nm.[81]

X-ray Diffraction (XRD): Bruker Advance D8, series II, powder diffractometer was used to perform powder XRD with monochromatic CuKα radiation. The broad angle XRD analysis was carried out at 2˚/min scan rate from 10º to 90º and a step time of 2 s. Debye–Scherrer equation was employed to calculate the average crystallite thickness of Co_3O_4 particles using the half width of a chosen peak at 2θ = 36.8˚:

$$d_{XRD} = \frac{K\lambda}{\beta \cos \theta_B} \quad (4.3)$$

Where d_{XRD} is the mean diameter of crystallites (nm); K is constant value corresponding to the crystallite shape, assumed 0.98; λ (nm) is X-ray wavelength; β is full width at half max or integral breadth in radian; and $\Theta_B = 2\Theta/2$ is Bragg angle (diffraction angle). To obtain the corresponding cobalt metal (Co^0) crystallite size, the calculated thickness value multiplied by 0.75 is based on molar ratio of cobalt and oxygen in Co_3O_4 [156]:

$$d(Co^0) = 0.75 \times d(Co_3O_4) \quad (4.4)$$

Transmission Electron Microscopy (TEM): Morphology of the samples was studied from micrograph obtained from JEOL 2011 transmission electron microscope. Sample preparation was done following standard procedure [155].

Temperature Programmed Reduction (TPR): AutoChem Micromeritics 2950 HP instrument equipped with a thermal conductivity detector was employed to study the reduction behavior of catalysts prepared by differently treated CNT supports. A 20 mg CNT catalyst was placed in a high pressure stainless steel tube and was purged with hydrogen−argon mixed gas at 35 ˚C. TPR analysis was then performed by heating the sample to 750 ˚C with 10 ˚C/min ramp under 50 mL/min flow of 10 % H_2/Ar (v/v) gas mixture [155].

4.3.3 Catalyst Activity Study for Fischer−Tropsch Synthesis

The Fischer–Tropsch synthesis (FTS) was carried out in a fixed-bed microreactor with 1 cm I.D. and 50 cm length. To convert cobalt oxide particles supported on CNT to active Co^0 form in CO hydrogenation reaction, in-situ reduction was first conducted based on the following procedure. One gram of the powder catalyst was mixed with 7 g of silicon carbide with 90 mesh grit size and placed in the reactor. Ultrahigh purity (UHP) hydrogen with 30 mL/min flow rate was introduced into reactor. Then the reactor temperature was raised from room temperature to reduction temperature at 350 ˚C with 1 ˚C/min heating rate. The activation condition was maintained for 16 h at atmospheric pressure. After the catalyst reduction stage, the reactor temperature was reduced to 180 ˚C in the hydrogen gas flow. The reactor was then pressurized to the desired value of 2.07 MPa with UHP helium. While switching to syngas as a feed for the FTS reaction, the reactor temperature was also ramped up to 220 ˚C at 1 ˚C/min heating rate. The space velocity of syngas was maintained at 3000 $cm^3 \cdot g^{-1} \cdot h^{-1}$. The composition of syngas was 30 % CO, 60 % H_2, and 10 % Ar which entered through the top of the fixed-bed reactor. Argon in this mixture acts as an internal standard, which was used as a tie component in doing mass balance over the system. To control and adjust the entering gas flow rates (hydrogen and syngas), Brooks model 5850E mass flow controllers were employed. PID temperature controller was used to control the temperature of the reactor [103,157]. The reaction system was allowed to operate at steady state and then data were collected at this condition.

As the products of FTS contain heavy hydrocarbon such as wax (C_{22+}), heating tapes were used to keep the tubing after reactor at 100–120 ˚C. The products continuously entered into a hot trap (max volume of 75 mL, temperature at 100–120 ˚C) to collect C_{5+} hydrocarbons. Then the remaining products were directed to a cold condenser (max volume of 75 mL, temperature 0 ˚C) to collect water and light hydrocarbons. Finally, the cold condenser was connected to an online Shimadzu gas chromatograph (GC-2014) to analyze the noncondensable gaseous products. Two valves were located under the cold and hot condensers in order to collect liquid products [77,157]. Liquid products were analyzed using an off-line GC. CO conversion activity and C_{5+} product selectivity of the catalysts were monitored at steady state and were analyzed every 6–8 h within 50 h of time on stream.

4.4 Results and Discussion

Figure 4.1 shows the nitrogen adsorption–desorption isotherms for pristine, treated and corresponding cobalt loaded MWCNTs. All the samples unveil the typical type IV adsorption isotherms including hysteresis loop at higher relative pressure $P/P_0 \geq 0.85$, suggesting capillary condensation in mesoporous inner hollow cavities and aggregated pores of CNTs [158,159].

Textural characteristics including surface area, pore diameter, and pore volume of CNT samples are given in Table 4.1. Results from BET analysis indicate that the surface area of treated MWCNTs increased approximately by 16 %, 21 %, and 30 %, from 158 m^2/g to 184, 191, and 205 m^2/g after acid treatment with 35, 50, and 70 wt. % nitric acid, respectively.

The BJH cumulative pore size distribution also confirms that after treatment with nitric acid, pore volume of pristine CNTs considerably increases (see Figure 4.2). Also, higher acid concentration results in slightly larger CNT pores as compared to those treated at lower acid concentrations.

Functionalization of CNTs with nitric acid, for example with 70 wt. % concentration, enhanced pore volume by 34 % and pore diameter by 7 % as compared to untreated CNTs. This increase in textural properties is generally attributed to the effect of tube fragmentation, surface defects and opening of tube tips during the acid treatment [160]. However, metal loading on porous supports leads to accumulation of cobalt in narrow capillaries and hence blocks the pores which in turn reduces the surface area and pore volume but shifts the average pore diameter to higher values. After 15 wt. % cobalt loading on CNT supports, the 24–32 m^2/g drop in surface area and 0.7–1.3 nm increase in pore diameter corroborate the presence of the metal in narrow pores (see Table 4.1).

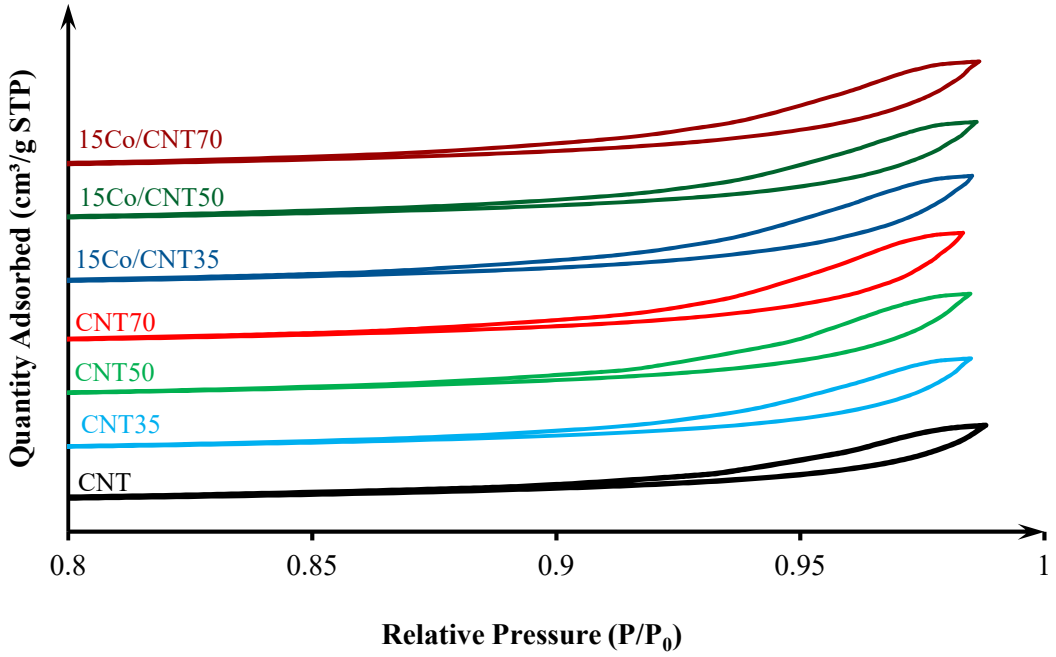

Figure 4.1 Nitrogen adsorption−desorption isotherms of pristine CNT, differently acid treated CNTs, and corresponding Co catalysts

CO chemisorption analysis (Table 4.1) on CNT supported cobalt catalysts revealed that increasing the concentration of nitric acid from 35 to 70 wt. % in treatment process leads to approximately 20 % rise in cobalt dispersion from 4.9 % to 5.9 %.

Table 4.1 Textural properties of CNT treated with different nitric acid concentrations and corresponding Co/CNT catalysts along with Co dispersion

Catalyst / Support	BET surface area (m^2/g)	Pore vol. (cm^3/g)	Pore dia. (nm)	Co dispersion (%)
CNT	158	0.52	12.3	-
CNT35	184	0.64	12.6	-
CNT50	191	0.66	12.8	-
CNT70	205	0.70	13.1	-
15Co/CNT35	156	0.60	14.2	4.9
15Co/CNT50	167	0.62	14.1	5.3
15Co/CNT70	173	0.67	13.8	5.9

It seems that higher concentration of nitric acid generates more defect sites and functionalization on tubes' walls and tips. Besides the defects, acid treatment partially removes metal residues left from CNT synthesis.

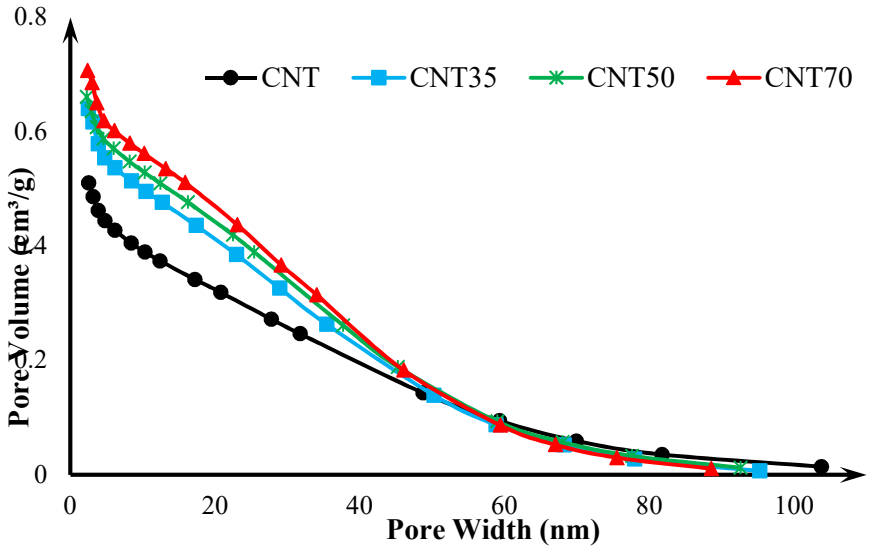

Figure 4.2 BJH desorption cumulative pore volume for pristine and differently treated CNTs

Semiquantitative X-ray florescence scanning (XRF) of pristine and treated CNTs was conducted to determine the impurities. Detected elements in pristine CNT were as follows: Mg, Al, Si, P, S, Cl, K, Ca, Co, Fe, Ni, Cu, Zn, Mo, and La each with concentration ranging from 0.01 to 0.2 wt. %. Fe and Ni were also present with 2.0 and 3.6 wt. % concentrations, respectively. After acid treatment, 30–80 % of these elements were removed. The defects and functionalized sites in CNTs facilitate cobalt anchoring and give rise to charge donation from carbon sites to depositing metal [161]. The defects generated by concentrated acid treatment on tubes were confirmed by Raman analysis as discussed below.

Table 4.2 I_D/I_G ratio after pre-treatment and cobalt loading on CNT

Support / Catalyst	CNT	CNT35	CNT50	CNT70	15Co/CNT35	15Co/CNT50	15Co/CNT70
I_D/I_G	0.64±0.04	0.87±0.05	0.96±0.03	1.08±0.04	0.79±0.06	0.99±0.04	1.1±0.06

Raman spectroscopy is an important tool to characterize C–C bond structure in carbon nanomaterial. The Raman spectra of as-received and treated CNTs and 15Co/CNTX catalysts shown in Figure 4.3 were obtained by exciting the samples with 514.5 nm laser. Two prime peaks appear in all samples: the D-

band tangential Raman modes at 1350 cm^{-1} for defect-induced carbon (disordered) and the G-band peak at 1582 cm^{-1} for hexagonal graphite (ordered carbon) [150,162].

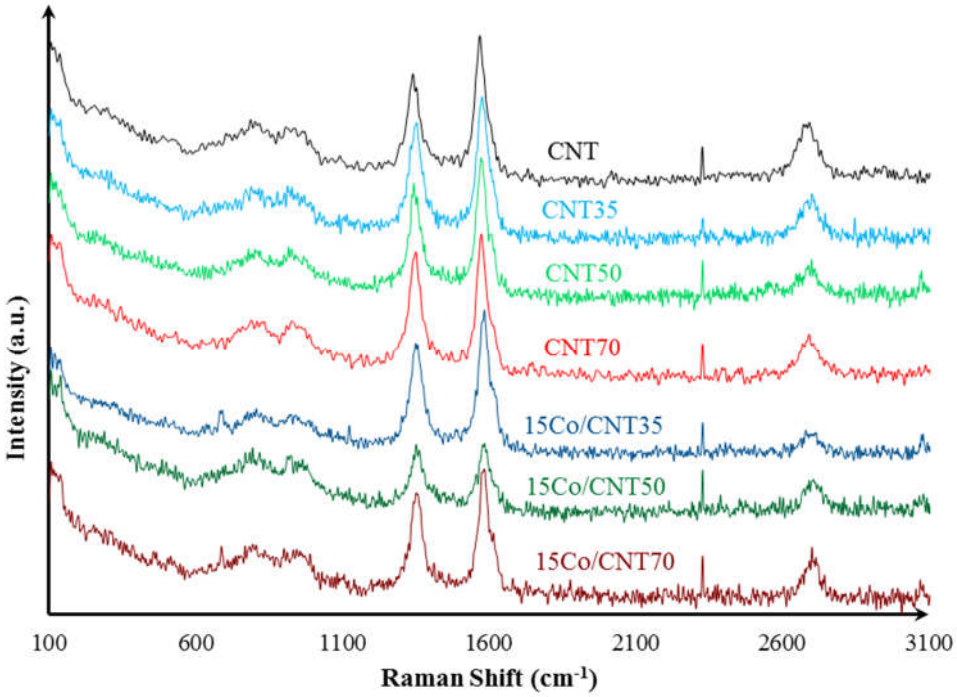

Figure 4.3 Raman spectra for CNT and 15Co/CNTX catalysts with different support treatment conditions

The area ratio of the D-band to the G-band (I_D/I_G) was used (as shown in Table 4.2) to estimate the amount of defects in CNTs wall after treatment with different nitric acid concentration [151]. The results show that the acid treatment increased the ratio of I_D/I_G from 0.68 for pristine CNT to 0.87, 0.96 and 1.08 for CNT35, CNT50 and CNT70, respectively, which indicates that higher nitric acid concentration leads to generation of more defects along the CNT surface. From the FTIR spectra also (Figure D.3 in Appendix D) it is seen that after functionalization of CNT, transmittance intensities of C=O stretch around 1680 cm^{-1}, and O–H stretch around 3440 cm^{-1} have increased [149]. This in turn is related to the formation of surface functional groups which will aid the interaction between CNT and cobalt oxide. Therefore, the higher cobalt dispersion in 15Co/CNT70 catalyst, as evidenced by CO chemisorption, can be attributed to the higher defect sites on the CNT70 support. Despite these damages in CNT skeleton, the mesoporosity of carbon tubes and their pore structure do not change significantly after acid treatment

and metal loading. This is indicated by almost identical hysteresis shapes in N_2 adsorption–desorption isotherms (Figure 4.1), similar cumulative BJH pore size distribution trend (Figure 4.2), and close I_D/I_G ratio for treated CNTs and their corresponding Co catalysts (see Figure 4.3 and Table 4.2).

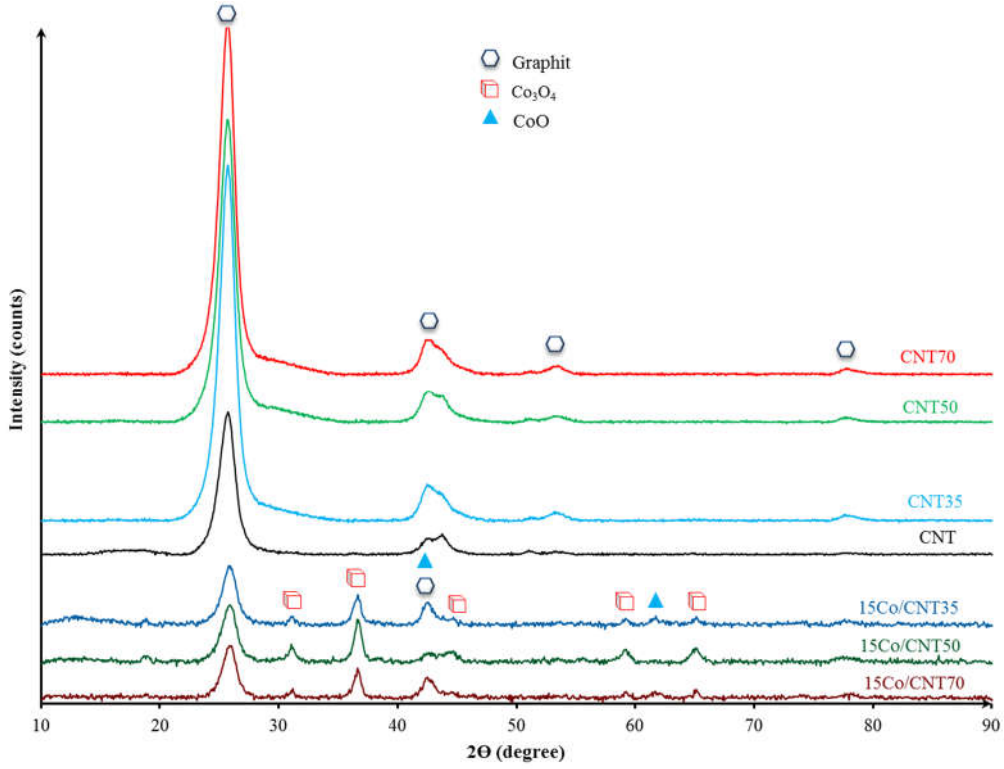

Figure 4.4 XRD patterns for CNT and 15Co/CNTX catalysts with different support treatment conditions

Figure 4.4 demonstrates XRD patterns of functionalized CNTs with different nitric acid concentrations and corresponding calcined 15Co/CNT catalysts. The peaks at 2θ of 26.3˚, 43˚, 55˚, and 77.5˚ represent those of the hexagonal graphitic structures (002), (100), (004), and (110), respectively, in carbon nanotubes, while the other peaks at 2θ of 19.0˚, 31.5˚, 36.8˚, 38, 45˚, 59.6˚, 65.5˚ in the XRD patterns are related to different crystal planes of Co_3O_4 [154,163]. The CoO peaks appear at 42.7˚ and 61.9˚ [164]. According to the XRD data, Co_3O_4 species are the dominant phase in the catalysts supported by functionalized CNTs and it has not changed by acid concentration. Therefore, the origin of cobalt species is more dependent on decomposition of cobalt nitrate on CNTs during the drying and calcination heat treatment [164]. The average Co_3O_4 crystallite size of the catalysts was calculated from Scherrer equation with the peak at 2Θ = 36.8˚ as the most intense peak relating to the (311) face of Co_3O_4 crystallites

[81,153]. Acid treatment with high HNO_3 concentrations resulted in slightly smaller cobalt crystallites as corroborated by CO chemisorption analysis (Table 4.3); The 70 wt. % HNO_3–treated CNT cobalt catalyst showed the smallest crystallite size of 11 nm as compared to 12.1 nm shown by 35 wt. % HNO_3-treated CNT cobalt catalyst.

Table 4.3 Co_3O_4 crystallite size from XRD and Co^0 size from CO chemisorption analysis

Catalyst/Support	d_{XRD} (nm)	$d_{CO\ Chem.}$ (nm)
15Co/CNT35	12.1	19.3
15Co/CNT50	11.7	18.1
15Co/CNT70	11.0	16.5
Used 15Co/CNT35	37.5	-
Used 15Co/CNT50	35.2	-
Used 15Co/CNT70	32.6	-

The HRTEM images of pristine CNTs, treated CNTs and 15Co/CNTX catalyst are also demonstrated in Figure 4.5. There was no distinguishable difference among TEM micrographs of CNT35, CNT50, and CNT70; however, three different magnifications of pristine CNTs, treated CNTs, and their corresponding catalysts have been illustrated. The closed tips of pristine CNTs, the removed caps in treated tubes and situated cobalt oxide particles inside and outside the tube walls are visible in the micrographs. Due to capillary force induced from carbon nanotubes during the impregnation, metal solution can easily fill the inner cavities of tubes. In addition, acid treatment enhances the hydrophilicity of tubes, leading to easier accessibility of metal cations to anchor to the active sites [165]. Since we have used the total pore volume of CNT as amount of the required solution for the incipient wetness impregnation, cobalt solution mainly fills inner pores (internal surfaces) and some of the aggravated outer pores among tubes (external surfaces). This procedure results in mixed distribution of particles on inside and outside surfaces of tubes (see Figure 4.5, bottom row). It was interpreted that the darker particles on central channel of tubes are particles located outside the tubes and particles with lighter color are located inside tubes. The demonstrated particles by an arrow in Figure 4.5 (bottom row) are only to put emphasis on those large particles outside the tubes and small particles inside the tubes. For the particles larger than the size of inner diameter of tubes it is clear that they are situated on external surfaces. The encapsulated particles inside the tubes, are rather small and uniform in size range of 2–5 nm range, conforming tubes' inner

diameters, whereas particle in outer surface have grown in large range of size 1–30 nm due to lack of restriction (see Figure 4.5).

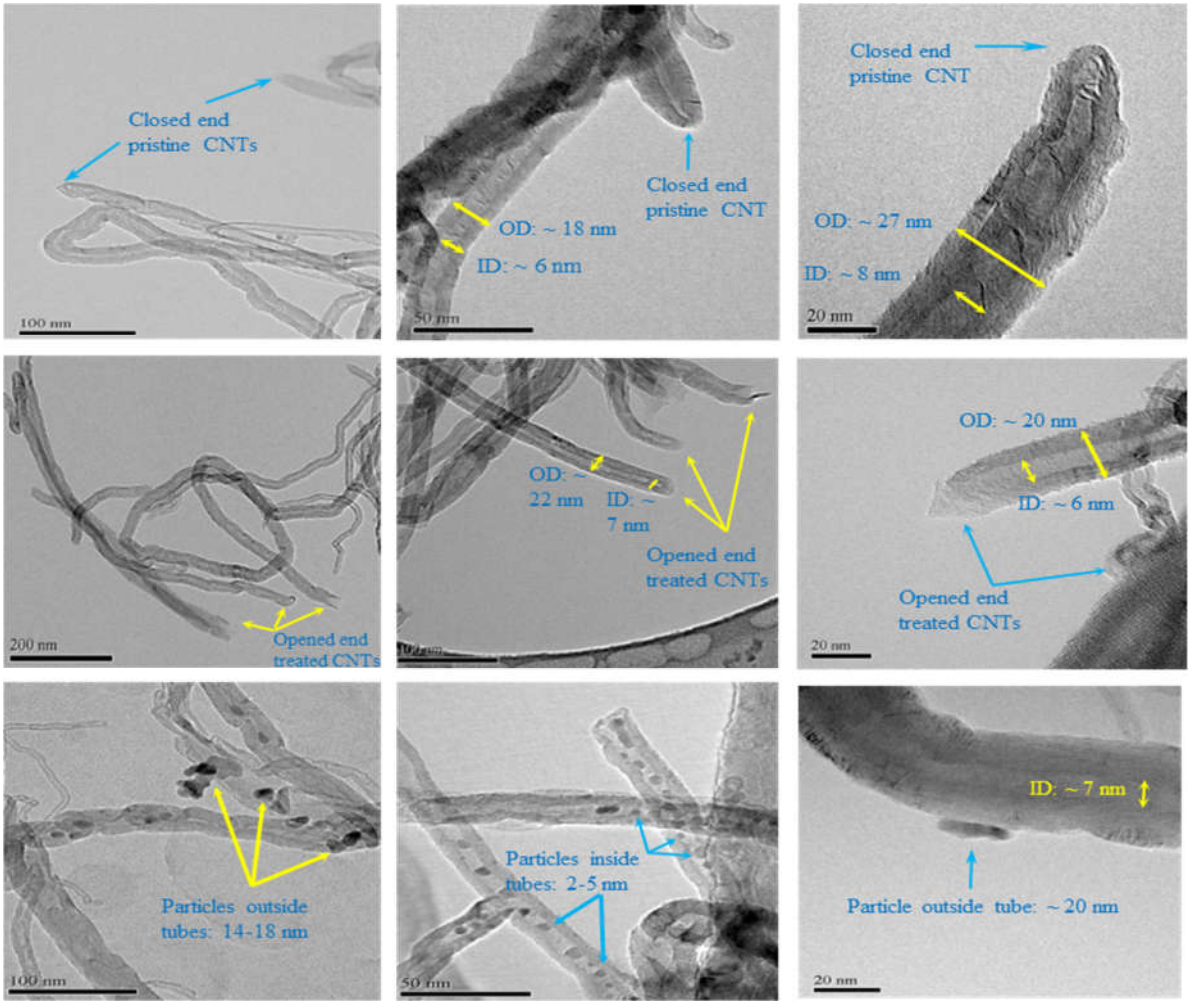

Figure 4.5 HRTEM images of pristine CNTs (top row), treated CNTs (middle row), and 15Co/CNTX catalysts (bottom row)

The TPR patterns and reducibility of calcined 15Co/CNTX catalysts are shown in Figure 4.6. Various peaks in TPR spectra represent the presence of different cobalt species formed during the catalyst preparation [5]. TPR profiles for all catalysts exhibit two main peaks. Typically, the main low temperature peak (250–270 ˚C) ascribes the reduction of Co_3O_4 to CoO; however, the larger Co_3O_4 particles may start reducing even at lower temperatures (180–250 ˚C). The high temperature peak (300–500 ˚C) is mainly assigned to the second step of reduction from CoO to Co^0. Nevertheless, reduction of larger CoO species to Co^0 or decomposition of uncalcined cobalt nitrates entrapped in pores can also comprise or overlap a fraction of the low temperature peaks [166,167].

Possible gasification of carbon support can overlap with second peak and broaden it at the higher temperatures of 650 ˚C [168]. The metallic cobalt may catalyze the methane formation through hydrogenation of carbon nanotubes [164]. The reduction temperature for 15Co/CNT70 catalyst is 476 ˚C which is 8 and 5 ˚C lower than that for cobalt oxide supported on CNT35 and CNT50, respectively. The amount of H_2 consumption calculated by determining the area under curve for 15Co/CNT70, 15Co/CNT50, and 15Co/CNT35 catalysts are 160.1, 151.9, and 136.1 cm^3/g, respectively. Slightly lower reduction temperature and higher reducibility of cobalt catalyst on CNT support treated with 70 wt. % acid could be attributed to the uniform distribution of cobalt oxide particles during the calcination. This result substantiates better dispersion of cobalt particle (from H_2 chemisorption analysis) on highly defected and oxygenated support. It should be noted that TPR analysis were conducted in gas mixture of 10 vol % H_2 and balanced Ar, while the reduction for FT reaction was performed in ultrahigh pure (UHP) hydrogen. Partial pressure of H_2 can affect extent of cobalt reduction; therefore the TPR results can only be used as a qualitative and comparative study [169].

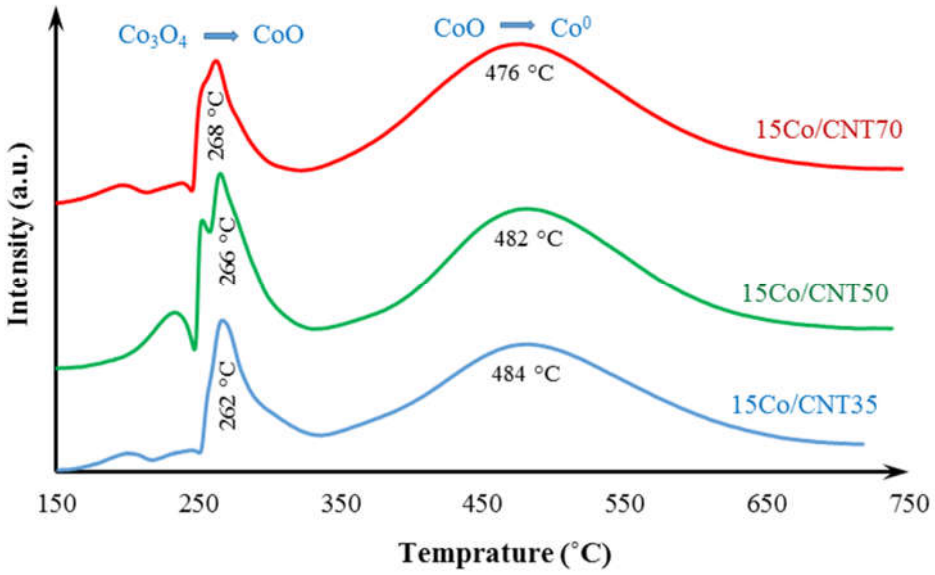

Figure 4.6 Temperature-programmed reduction profiles for 15Co/CNTX catalysts with different treatment condition of CNTs

Analyzing outlet gas from reactor via online GC was started after 6 h of continuous FT reaction run. The operation conditions were kept constant for the catalysts during 50 h of activity test and were as following: 2.07 MPa, 220 ˚C, and 1200 h^{-1}. The concentrations of unconverted CO, produced CO_2, CH_4,

and C_2 to C_4 hydrocarbons (HCs) plus nonreactive Ar were recorded and compiled to CO conversion (%), and C_{5+} selectivities in 8-hour intervals. Figure 4.7 illustrates changes in CO conversion activity of all catalysts over time. The profiles for CH_4 and C_{5+} selectivity with time-on-stream (TOS) are also provided in Figure D.2 of Appendix D. We also conducted FTS with cobalt catalyst supported on pristine CNT (without treatment) for better understanding of nitric acid treatment impact on the Co/CNT catalysts' performance. Table 4.4 summarizes the performance of catalysts in terms of CO conversion (%), HC yield (FTS rate), and product selectivity (for methane, carbon dioxide, light and heavy HCs). The TOS for reasonably stable activity of the catalysts to acquire the results was ~ 20 h.

Activity versus TOS for cobalt catalysts with treated CNT support shows that CO conversion drops almost 25 % within the initial 20 h run for the FT reaction. The observed CO conversion efficiency for 15Co/CNT70, 15Co/CNT50, and 15Co/CNT35 catalysts began with 41.6, 39, and 37 %, then almost leveled at 30.1 %, 27.5 %, and 25.2 %, respectively. Doubling the acid concentration, from 35 to 70 wt. %, for the CNT support treatment resulted in an approximately 5 % rise in CO conversions of 15Co/CNT catalyst (e.g., from 37 % to 41.6 % at TOS = 6 h). Activity test for 15Co/CNT catalyst without support treatment starts with 32 % CO conversion and reaches 22 % after 20 h of run. The activity loss for 15Co/CNTX catalysts is considerably less as compared to 45 % for 15Co/CNT counterpart at TOS of 20 h. A glance at Figure 4.7 reveals that the cobalt catalysts with CNT supports treated with different concentrations of nitric acid are more stable and lose less activity. The stability of the catalysts with treated supports may be attributed to the extent of functional groups, defects, and strength of cobalt that anchors with support.

The decline in the activity of catalysts was possibly caused by one or more of the following deactivation mechanisms in the cobalt active sites: (1) sintering and cobalt migration, (2) cobalt carbide formation, (3) cobalt oxidation in the presence of water (FT by-product), (4) carbon deposition and carburization, (5) surface reconstruction, (6) poisoning [170], and (7) decline in reactant and product adsorption / desorption rate due to the formation of heavy HCs (C_{20+}) inside the CNT pores. Due to the weak interaction of Co–CNT, presence of large particles (> 20 nm) in the aggregated pores of inter-particles, amorphous carbonaceous impurities in CNT, and water production during FTS reactions, the first four mechanisms play crucial roles in the instability of Co/CNT catalysts. The XRD analysis of spent catalysts (Table 4.3) shows that sintering of cobalt crystallites occurred within the reaction and they have been enlarged by almost 3 times their original size after being used for more than 2 days. All main deactivation

mechanisms lead to decrease in active cobalt surface availability for adsorbed $CO+H_2$ species in the FT reaction.

Table 4.4 Activity, Selectivity, and Productivity of 15Co/CNT and 15Co/CNTX Catalysts in FTS at 220 ˚C, 2.07 MPa, 1200 h^{-1}, and TOS = 20 h

Catalysts	**15Co/CNT**	**15Co/CNT35**	**15Co/CNT50**	**15Co/CNT70**
CO Conversion (%)	22.0	25.2	27.5	30.1
FTS rate $\left(g_{HC}.g_{cat}^{-1}.h^{-1}\right)$	0.17	0.20	0.21	0.23
α	0.83	0.81	0.79	0.75
CH_4 (%)	6.4	7.8	8.1	9.5
CO_2 (%)	1.0	1.2	1.7	2.5
C_2-C_4 (%)	2.4	3.1	4.5	6.8
C_{5+} (%)	90.2	87.9	85.7	81.2
$\frac{C_{2-4}^{=}}{C_{2-4}^{-}}$ **ratio**	0.67	0.62	0.54	0.45

* error: ± 3%

FTS rate is defined as gram of hydrocarbons produced per unit time (hour) and unit catalyst mass (g) [171]. As shown in Table 4.4, the functionalized CNT with 70 wt. % nitric acid, as a support of 15 wt. % cobalt catalyst resulted in 0.03 and 0.06 $g_{HC}.g_{cat}^{-1}.h^{-1}$ increase in hydrocarbon yield as compared to that of 35 wt. % nitric acid treated and untreated catalysts, respectively. The results show that there is 35.3 % increase in hydrocarbon yield with 70 % nitric acid treatment for CNT as compared to no nitric acid treatment for 15 wt. % Co/CNT catalyst.

The selectivities of catalysts toward methane, carbon dioxide, light hydrocarbons ($C_2+C_3+C_4$), and heavy hydrocarbons (C_{5+}), are presented in Table 4.4. It is seen that treatment of support with higher concentration of nitric acid shows termination of hydrocarbon chain. As shown in Table 4.4, 15Co/CNT70 is somewhat less selective to C_{5+} HCs (81.2 %) and slightly more selective to methane (9.5 %) as compared to 15Co/CNT50 and 15Co/CNT35. At the same time, cobalt catalyst using untreated CNT support exhibits the minimum methane (6.4 %) and the maximum C_{5+} (90.2 %) selectivities as compared to cobalt catalysts using treated CNT supports. The profiles for CH_4 and C_{5+} selectivity over TOS are also provided in Appendix D (see Figure D.1). It was observed that within 50 h time-on-stream

the activity of 15Co/CNTX catalysts decreases (~ 11 %) whereas the C_{5+} selectivity (~8 %) increases and CH_4 selectivity decreases (~ 6 %).

The catalyst characterization results confirm that treatment and functionalization of CNTs with higher nitric acid concentration enhanced the textural properties of the CNTs. This also increased the functional groups and defects on CNTs as compared to CNTs treated with low acid concentration. These in turn lead to slightly higher cobalt dispersion, smaller crystallite size, and higher extent of reduction. This implies that slightly higher number of Co^0 sites are accessible for adsorption of H_2 and CO reactants in the case of 70 wt. % HNO_3-treated support [172]. This results in higher CO conversion and hydrocarbon yield among other catalysts in this study; therefore, the catalytic performance of 15Co/CNT70 catalyst is slightly better. Although the 15Co/CNT70 catalyst showed the lowest chain growth probabilities (α) of 0.75, lowest C_{5+} selectivity of 81.2 %, and highest methane selectivity of 9.5 %. Bezemer et al. had shown in their work that the decrease in C_{5+} selectivity (from 85 to 51 wt. %) was observed with reduction in the cobalt particle size (from 16 to 2.6 nm) [67]. This could be due to the difference in cobalt site density.[37] Similarly, in our case, the lower C_{5+} selectivity in 15Co/CNT70 catalyst could be due to the smaller cobalt crystallite size. Shimura et al. [48] compared 18 types of different phase of alumina supported cobalt catalysts with varying CO conversion ranging from 22 to 61 % with C_{5+} and CH_4 selectivity ranging from 78 to 90 % and 2 to 9%, respectively. The results indicate that the nature of support has large impact on the activity and product selectivity.

The reported values for HC selectivity in Table 4.4 were calculated including CO_2 product. The Co/CNT catalysts tested by some other researchers also exhibited rather lower selectivity values for CH_4 and C_2−C_4, ranging 5−10 % and 3.5−6 %, respectively [154,173,174]. The relatively higher selectivity of methane by 15Co/CNT70 as compared to the counterpart catalysts suggests the slightly higher presence of dissociated hydrogen which is capable of hydrogenating the formed carbon species to methane [67]. This can be ascribed to increased hydrogenation ability of CNT supports after treatment with strong acid concentrations. Olefin to paraffin ratio is another parameter to differentiate the catalysts' selectivity. It is assumed that the olefin to paraffin ratio $\left(\frac{C_{2-4}^{=}}{C_{2-4}^{-}}\right)$ in light hydrocarbon range and in heavy hydrocarbons product distribution are the same. After hydrogenation is initiated to form CH, CH_2, and CH_3 intermediates, longer chain hydrocarbons are propagated to form through coupling, until the chain termination occurs [95]. Olefin to paraffin ratio has decreased from 0.62 to 0.45 for the catalysts prepared, using 35 to 70 wt. % nitric acid, respectively for CNT pre-treatment. This can be ascribed to effective

participation of unsaturated HCs in the re-adsorption on active sites [175,176]. Therefore, functionalization of CNT support with higher concentration of nitric acid leads to more active sites and higher hydrocarbon yield.

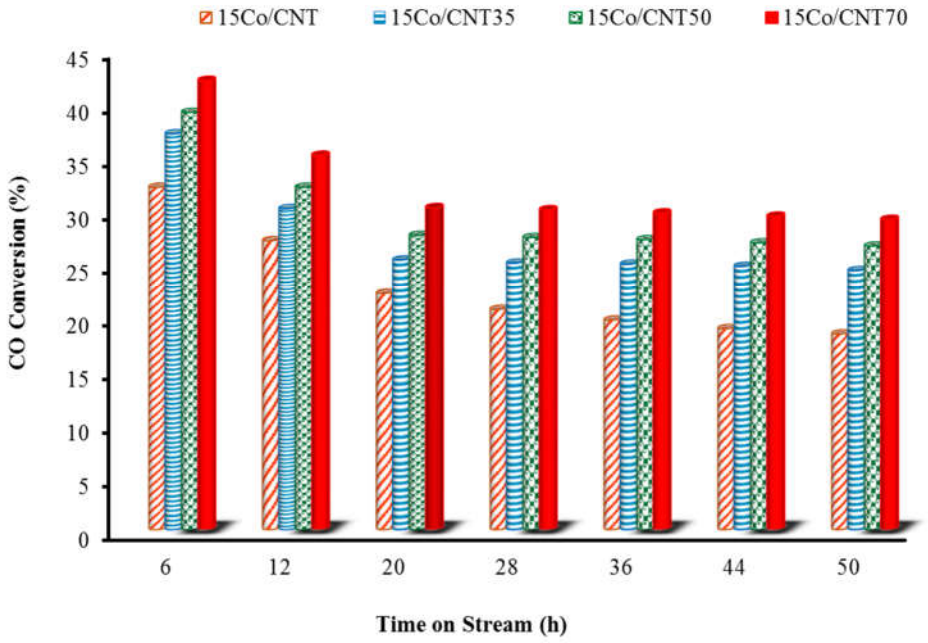

Figure 4.7 CO conversion for 15Co/CNT and 15Co/CNTX catalysts at 220 ˚C, 2.07 MPa, and 1200 h^{-1}

4.5 Conclusions

Functionalization of CNTs with higher nitric acid concentration enhanced the textural properties of the CNTs as compared to untreated CNTs. Higher concentration of HNO_3 (70 wt. %) resulted in the creation of more defects on CNTs walls (I_D/I_G = 1.1) and more anchoring sites for cobalt metals; leading to a slightly higher dispersion of metal (5.9 % vs 4.9 % and 3 %) and thus CO conversion. The harshest condition for CNT functionalization, 70 wt. % HNO_3, leads to decrease in cobalt crystallite size according to XRD, which was also in agreement with crystallite size calculated from CO chemisorption. The change in nitric acid concentrations from 35 to 70 wt. % slightly increased the reducibility and decreased the reduction temperature of cobalt oxide nanoparticle as confirmed by the TPR analysis of 15Co/CNTX catalysts. Selectivity study for prepared catalysts reveals that the cobalt catalyst supported on CNTs treated with lower concentration nitric acid shows lower tendency to produce undesired methane and higher tendency to desired C_{5+} products. This positive feature can be negated by lower CO conversion

activity and HC yield. In general, pre-treatment of CNTs with higher concentration of nitric acid had positive influence on textural properties of support and characteristics of cobalt catalysts. As a result, severe treatment of CNT support enhanced the catalytic performance of cobalt catalysts in FTS, in terms of CO conversion and hydrocarbon yield as compared to moderately, slightly, and untreated CNT correspondent catalysts.

CHAPTER 5: BINDER AND PELLET SHAPE IMPACT ON THE Fe/CNT CATALYST FOR FTS

A version of this chapter has been published as a research paper in the following journal:

- S. Badoga, V. Vosoughi, A. K. Dalai, "Performance of promoted Iron/CNT catalyst for Fischer–Tropsch Synthesis: Influence of pellet shapes and binder loading", Fuel & Energy (2017) 31, 12633–12644.

Contribution of PhD candidate

The CNT treatment, catalyst preparation, characterizations of physico-chemical properties, and FT tests were conducted by Vahid Vosoughi. Dr. Badoga performed mechanical tests on the pelletized catalysts and wrote the manuscript. Revising the manuscript was done by Vahid Vosoughi. The interpretation of the results was conducted by Vahid Vosoughi and Dr. Badoga. Dr. Ajay Dalai supervised the work and reviewed the manuscript.

Contribution of this chapter to the overall PhD research

Studies on Co/CNT catalysts showed that there are some limitations (e.g. losing long term activity and issues with sintering) to be considered for scale-up and commercial purposes, however, Fe/CNT catalyst works in our group has unveiled more promising features of this catalyst to be examined for large scale FT applications. Therefore, this part of research work focused on synthesizing and pelletizing the promoted iron catalysts supported on multiwalled carbon nanotubes and examining them for FTS. Cylindrical and spherical shapes of Fe/CNT catalysts were prepared using varying loadings of the binder. The physico-chemical and mechanical properties of all pelletized catalysts were characterized, and their catalytic performance was tested in the FT reaction.

5.1 Abstract

Instead of powder, catalyst pellets are preferred in a fixed-bed reactor for Fischer–Tropsch synthesis (FTS). In this research, promoted iron catalysts supported on carbon nanotubes (CNT) was pelletized in two different shapes (spherical and cylindrical) using different bentonite loadings (10–20 wt. %). The pellets were tested for mechanical strength using single pellet and bulk crushing test methods (ASTM D 4179, 6175, and 7084). The spherical pellets were found to sustain higher crushing strength as compared to cylindrical pellets. However, both spherical and cylindrical Fe/CNT pellets with 20 wt.% bentonite

loading were found to be mechanically stronger than commercial alumina spherical pellets, suggesting their suitability in fixed bed reactors. The pellets were characterized to determine the change in active metal dispersion and ease in reducibility based on their shape and binder content using CO chemisorption, XRD and H_2–TPR. The cylindrical shaped pelleted catalysts were found to be easy to reduce as compared to spherical shaped pelleted catalysts. All pellets were tested for FTS in a fixed bed reactor at 270 ℃ and 2.07 MPa with syngas (H_2/CO = 2.0) flowing at rate of 60ml/min. 20 wt.% bentonite loaded Fe/CNT pellet was found to be stable with highest CO conversion and C_{5+} selectivity among all pelleted catalysts. The decline in CO conversion in pelleted Fe/CNT catalyst containing 10–15 wt % bentonite loading could be due to the structural instability of these materials during reaction. The internal mass transfer calculations estimated severe diffusional limitations in spherical pellet catalysts resulting in sharp decline in their FTS activity. Hence, cylindrical pelleted catalyst containing 20 wt. % bentonite was found to be best performing among the series and its performance for FTS was optimized for temperature, pressure and GSHV using Taguchi method.

5.2 Introduction

The major contributing factor for global warming are greenhouse gases such as CO_2 and CH_4 which are emitted from the combustion of fossil fuels. In 2015, 399 ppm of CO_2 was recorded in atmosphere[177]. The serious climatic concerns such as sea level, heat waves, droughts, etc., arising from global warming are the driving forces for production and utilization of carbon dioxide neutral biofuels. Biofuels can be produced from biomass including vegetable oil, algae, municipal solid waste, woody biomass, grasses, non-edible oils, and agricultural by-products. One of the processes to produce liquid fuels from biomass is via gasification to produce syngas (mixture of CO and H_2) followed by its conversion to liquid fuels via Fischer-Tropsch synthesis (FTS). The syngas is catalytically converted to mixture of hydrocarbons C_1–C_{60} (paraffins, olefins, and oxygenates) via FTS. The FTS reactions are complex, however reactions 5.1 and 5.2 are desirable [178], whereas the water gas shift (WGS) reaction is the major side reaction (equation 5.3).

$$(2n+1)\,H_2 + n\,CO \longrightarrow C_nH_{2n+2} + n\,H_2O \quad (5.1)$$

$$2n\,H_2 + n\,CO \longrightarrow C_nH_{2n} + n\,H_2O \quad (5.2)$$

$$CO + H_2O \longrightarrow CO_2 + H_2 \quad (5.3)$$

Most widely used metals for the FTS are iron and cobalt. The iron based catalysts show high water gas shift (WGS see equation 5.3) activity, therefore, it is preferred to be used for conversion of hydrogen lean synthesis gas ($H_2/CO < 1.8$), typically derived from coal and biomass [5]. The WGS reaction results in the production of hydrogen which is building block of hydrocarbons. Iron catalyst is more selective towards production of olefins and oxygenates as compared to paraffins. However, the hydrocarbon selectivity can be varied with temperature [38]. The high temperature FTS (280–340 °C) results in lower chain hydrocarbons C_1–C_{15} and is mainly utilized for the production of gasoline and low molecular weight olefins. The low temperature FTS (< 280 °C) leads to increase in selectivity towards high molecular weight paraffins and waxes[38]. Studies showed that iron catalysts are prone to faster deactivation as compared to cobalt based catalyst and show higher CO_2 selectivity[38]. The Co catalyzed FTS reaction shows higher selectivity for paraffins and heavy molecular weight waxes as compared to iron catalyst and exhibit higher hydrocarbon productivity per unit mass of the catalyst [5,38]. However, the lower price and abundance of iron, and as well as its compatibility for hydrogen deficient syngas makes it as highly attractive option for biomass driven route for liquid fuel production.

The catalyst performance is a back bone for the economy of the FTS process. Therefore, development of catalyst with improved hydrocarbon yield is the focus of FTS research. This can be achieved by using appropriate promotors and support materials. Most commonly used promoters for iron catalyst are Mn, K and Cu. Copper helps in increasing the reduction of iron oxide, manganese plays a role in stabilizing the activity and reducing CH_4 selectivity [179]. Potassium enhances the adsorption of CO and H_2 on active sites [180]. Various support materials including Al_2O_3, silica, SBA-15, TiO_2, ZrO_2 and carbon nanotubes (CNT) have been tested for FTS and significant improvements in the activity were observed as compared to unsupported Fe catalyst [181–184]. Recently, a patent from our group suggested the role of CNT supported iron catalyst, promoted with Mo, K and Cu related to the improvement in FTS [185]. The FTS activity also depends on the synergy between catalyst and type of reactor. High temperature FTS reactions are typically performed in fluidized bed or circulating bed reactors, whereas, for low temperature reactions, fixed-bed, slurry bubble column or slurry stirred tank reactors are preferred [5,186].

The catalyst pellets are preferred in fixed−bed reactors for efficient handling and product separation. The catalyst activity is also dependent on the shape and type of the pellet [38,187]. Yang et al. [188] have studied the effects of two pellet sizes, pellet A 0.5 cm ID and 0.5 cm length, and Pellet B was $1/4^{th}$ of Pellet A. They observed that larger pellet size, pellet A gives higher CO conversion and C_{5+} selectivity.

However, the chain growth probability (α) was higher for Pellet B. Lower α for larger pellet was attributed to the diffusional-limitation of long chain hydrocarbon products from large pellets[188]. Brunner et al. [187] have reported the effects of catalyst shapes on the FTS activity attained in a trickle bed reactor. They illustrated the difference in catalyst effectiveness, void fraction and heat transfer for trilobes, hollow cylinder, cylinder and spherical pellet shape and concluded that trilobes or hollow cylindrical shapes performed better in FTS. Further, various studies have been reported on the mass transfer limitations and modelling of catalyst pellets for FTS [189,190]. It is noteworthy that, the desired shapes and sizes of the catalyst pellet for FTS depend on the type of reactors being used for FTS. Typically, the catalyst particle size for fluidized and slurry reactor is <100 μm [191]. However, for fixed bed reactor, the spherical pellet is typically 0.1–0.7 cm, cylindrical pellet is 0.3–1.3 cm diameter with L/D ratio of 3–4 [191].

This work is designed with the aim of studying the effects of catalyst pelletization on FTS activity. The CNT supported Fe catalyst promoted with K, Mo and Cu, inspired by the recent patent [185] from our group was synthesized and pelletized in two different shapes, cylindrical and spherical, using different binder loadings. Bentonite clay was used as a binder and each pelleted catalyst was tested for the Fischer–Tropsch synthesis at 270 °C and 2.07 MPa. The syngas (H_2/CO = 2.0) flow rate used was 60 ml. g_{cat}^{-1}. min^{-1}. The FTS activity was measured in terms of CO conversions and hydrocarbon selectivity. The pelleted catalysts were tested for the effects of bentonite loading on their mechanical strengths using ASTM D 4179, 6175, and 7084 methods. The catalysts were characterized using BET, X-ray diffraction, CO-chemisorption and H_2-TPR to correlate the physico-chemical properties to the FTS performance. The pelletized catalysts were tested for the absence of internal mass transfer limitations, and the liquid hydrocarbon product was analyzed quantitatively. The pellet catalyst with cylindrical shape containing 20 wt. % bentonite loading was found to be the best performing catalyst with suitable mechanical properties, and its process conditions were optimized for the best catalytic performance.

5.3 Experimental

5.3.1 Materials

Multiwalled carbon nanotubes (MWCNTs) (OD: 10–20nm and ID: 5–10nm) were purchased from US Nanomaterials Inc. Iron(III) nitrate nanohydrate, $Fe(NO_3)_3.9H_2O$, copper(II) nitrate trihydrate, $(Cu(NO_3)_2.3H_2O$, potassium nitrate, KNO_3, ammonium heptamolybdate tetrahydrate,

$(NH_4)_6Mo_7O_{24}.4H_2O$ were purchased from Sigma–Aldrich, Edmonton, Canada. 70 % (v/v) HNO_3 and bentonite was purchased from Fischer–Scientific, Saskatoon, Canada.

5.3.2 Carbon nanotube functionalization and catalyst synthesis

The carbon nanotubes were treated with HNO_3 to create functional groups and defects on its surface, which would serve as anchoring sites for active metals during catalyst preparation. In addition, acid treatment process increases the surface area of CNT by opening the ends of the nanotubes. In a typical functionalization process, 10g of pristine CNT was added to 1 L of 60 wt. % HNO_3 solution. The mixture was heated at 115 °C under reflux for 18 h. Then the treated CNTs were filtered and washed with excess of deionized water until the pH stabilized. Further, the treated CNTs were dried overnight at 80 °C, the resultant material is named as functionalized CNTs.

The catalyst was synthesized using procedure adopted from the work conducted by Reza et al. (2010) [192]. 30 wt. % iron and 0.5 wt. % copper was impregnated on the functionalized CNT via incipient wetness impregnation method, using $Fe(NO_3)_3.9H_2O$ and $Cu(NO_3)_2.3H_2O$ as precursors. The resulting material was dried at 120 °C for 12 h. Following this, 1 wt. % potassium and 0.5 wt. % molybdenum were impregnated using KNO_3 and $(NH_4)_6Mo_7O_{24}.4H_2O$ as precursors. The material was then dried at 120 °C for 12 h and calcined at 400 °C for 3 h under the flow of argon with ramp rate of 1 °C/min to produce powder 0.5Mo-1K-0.5Cu-30Fe/CNT catalyst.

5.3.3 Catalyst pelletization

The powder 0.5Mo-1K-0.5Cu-30Fe/CNT catalyst was pelletized using bentonite as a binder. Three different bentonite loadings of 10, 15, and 20 wt. % were used to determine the effect of bentonite loading on the catalyst activity and mechanical strength of the pellets. The Caleva Multi Lab Extruder was used to pelletize the powder catalyst containing bentonite. Two different shapes of pellets, spherical (2–4 mm diameter) and cylindrical (1 mm diameter and 12–15 mm length) were synthesized and are shown in Figure 5.1. The pellets were dried at room temperature. Therefore, 3 types of spherical pellets and 3 types of cylindrical pellets using 10, 15 and 20 wt. % bentonite loadings were produced. Consequently, the spherical pellet catalysts were named as 10S, 15S, and 20S, and the cylindrical pellet catalysts were named as 10C, 15C, and 20C.

Spherical extrudates
(2-4 mm D)

Cylindrical extrudates
(1 mm D & 12-15 mm L)

Figure 5.1 Spherical and cylindrical MoKCuFe/CNT catalyst pellets

5.3.4 Characterization

5.3.4.1 Textural properties of fresh and spent catalysts

The powder MoKCuFe/CNT catalyst and pellet catalysts (10S, 15S, 20S, 10C, 15C and 20C) were characterized in oxide form to determine the textural, chemical and physical properties. The textural properties including the surface area, pore volume and pore diameter were determined using Micromeritics ASAP 2020 analyzer. The surface area was calculated by adopting multi-point Brunauer–Emmett–Teller (BET) method, whereas Barrett, Joyner, Halenda (BJH) method was used for calculating the pore size distribution. The dispersion and crystalline phase of active metals on the surface of CNT in calcined catalysts was determined using X–ray diffraction (XRD). The powder XRD experiments was conducted in Bruker Advance D8 series II, powder diffractometer. The scan was performed from 2θ = 10−80◦ utilizing Cu Kα radiation. The percentage metal dispersion in each catalyst was determined from the amount of CO uptake calculated during CO chemisorption, which was done using Micrometrics ASAP2020 Chemi analyzer. The ease in active metal (iron) reducibility in all the catalysts in this study was determined using hydrogen- temperature programmed reduction (TPR) performed in Micromeritics Autochem 2950 HP. The spent pelleted catalysts were also studied using BET, BJH and XRD to determine the physico–chemical changes in the pellet catalysts after reaction. The details on the

methodology to perform characterizations including XRD, BET, CO–chemisorption and H_2–TPR are discussed in previous work from our group [193].

5.3.4.2 Mechanical properties of the catalyst pellet

The synthesized catalyst pellets 10C, 15C, 20C, 10S, 15S and 20S were tested to determine their mechanical strengths using single pellet crushing strength (ASTM D 4179 method), and bulk crushing strength methods (ASTM D 6175 method). The texture analyzer instrument was used to perform the single pellet crushing test. This instrument estimates the amount of force (N) a pellet can hold before it collapses. The crushing strength, σ (kPa) for spherical and cylindrical pellet was then calculated using equations 5.4 and 5.5, respectively [194].

$$\sigma_S = \frac{2.8 * Force\ (N)}{\Pi * D^2} \tag{5.4}$$

$$\sigma_C = \frac{2 * Force\ (N)}{\Pi * T * L} \tag{5.5}$$

where, D is the diameter of sphere, T is the diameter/thickness of cylinder and L is the length of cylinder. The crushing strength was determined for 15 pellets of each kind and the average value is reported.

Bulk crushing strength was measured using Instron material testing machine by following ASTM D 7084 method. The bulk crushing strength test determines the amount of pressure required to break the pellets to produce 1.0% fines. The pellets were dried at 120 °C for 12 h before this test. 1g of pellets were taken in a die and three different loads 100N, 200N and 300N were applied. The amount of fines produced were measured, and the graph corresponding to crushing pressure versus percentage fines produced is drawn for each kind of pellet to calculate the pressure required to break the pellets to produce 1% fines.

5.3.5 Catalytic evaluation for Fischer–Tropsch synthesis

Fischer–Tropsch reaction over MoKCuFe/CNT catalyst was carried out in a fixed bed flow reactor operating at 270 °C and 2.07 MPa, with syngas (H_2/CO = 2.0) flowrate of 60 ml/min. The experimental setup consists of gas inlet system containing set of brooks mass flow controllers, a furnace with controller to heat the reactor, hot and cold condensers at the outlet of reactor, and back pressure regulator to maintain the pressure in the system. The outlet gas from the reactor system was sent to online GC for analysis. The liquid products were collected from the condensers and characterized. The reactor is a tube type with 1 cm I.D and 50 cm length.

The catalyst is loaded in the reactor using a loading procedure. Based on the temperature profile in the reactor, a reaction zone is defined. The top and bottom portion of the reaction zone was filled by stacking 3 mm glass beads, followed by 16 mesh silica carbide (SiC), 46 mesh SiC, then 60 mesh and 90 mesh SiC materials. In the reaction zone, 1g of catalyst diluted with 7 ml of 90 mesh SiC was loaded. After reactor loading, the catalyst was reduced in situ at 380 °C under the flow of hydrogen at 30 ml/min for 16 h. After reduction, the temperature was reduced to reaction temperature (270 °C) and system was pressurized to 2.07 MPa with helium. The hydrogen was switched with syngas to start the FT process. After 10h of reaction, the tail gas was analyzed with GC for determining CO conversion and hydrocarbon selectivity. The reaction was carried out for 80h. The best performing pelletized catalyst was optimized for process conditions including temperature, pressure and gas hourly space velocity (GHSV). Set of 9 FT experiments were performed using 3-level, 3×3 Taguchi method with varying temperature from 260 to 280 °C, pressure from 1.72 to 3.10 MPa, and GHSV from 1600 to 3200 h^{-1}.

5.4 Results and Discussion

5.4.1. N_2 adsorption–desorption analysis for oxide catalysts

The surface area, pore size and pore volume for pellet and powder materials were determined using BET analysis. Figure 5.2 shows the adsorption isotherms for functionalized CNT, powder and pelleted MoKCuFe/CNT catalysts (all in oxide state). Each material showed adsorption-desorption hysteresis loop, which is characteristic of type IV isotherm. The hysteresis corresponds to capillary condensation of nitrogen inside meso-pores. The shape of hysteresis loop is between type H1 and H3 [195]; H1 because the adsorption and desorption branches are almost vertical and parallel, and H3 because the capillary condensation is taking place at high P/P_0. It also signifies wide range in pore size distribution. Typically, the isotherm with this shape and type indicates the presence of plate–like particles of slit shaped pores [196]. In this work it could be attributed to long and cylindrical nanotubes with openings at end, defects on circumference (due to functionalization with HNO_3), and randomly oriented transversal structure. As expected from BET isotherm analysis, the broad pore size distribution was observed for all materials (see Figure 5.2).

The reduction in amount of nitrogen adsorbed in powder MoKCuFe/CNT catalyst as compared to the functionalized CNT as seen in isotherms (see Figure 5.2) is due to the filling of pores with active metals including iron, molybdenum, copper and potassium oxides.

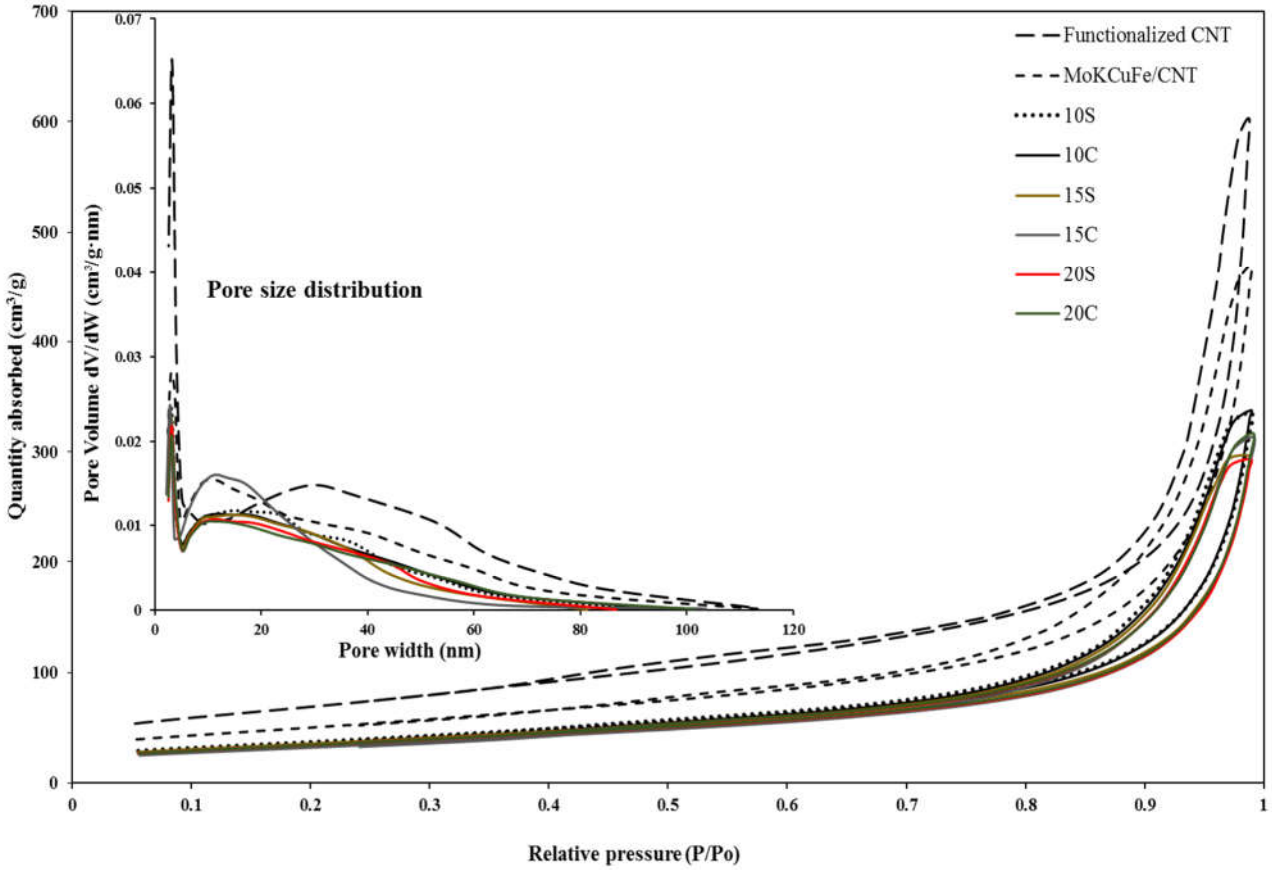

Figure 5.2 N_2 adsorption–desorption isotherms and pore size distribution of powder and pelletized catalysts

Further, the reduction in quantity of nitrogen adsorbed in pelletized catalysts is due to the addition of bentonite. Table 5.1 represents the surface area, pore size and pore volume for each material. The surface area of functionalized CNT was reduced from 240 m^2/g to 175 m^2/g on addition of active metals (as discussed above). It was observed, that with addition of 10, 15 and 20 wt. % bentonite, the surface area decreased from 180 m^2/g to 135, 123 and 115 m^2/g, respectively. However, the decrease in pore volume depends on the shape of pellet. For 10S, 15S and 20S materials, the decrease in pore volume was 28, 36 and 39 %, respectively, whereas for 10C, 15C and 20C materials the decrease in pore volume was 24, 30 and 34 %, respectively.

Therefore, it can be concluded form the BET analysis that the cylindrical shaped pellet showed better textural properties as compared to spherical pellets. It can also be noticed from Table 5.1 that with increase in the bentonite loading the density of pellet also increased.

Table 5.1 Textural properties and CO chemisorption results for the MoKCuFe/CNT powder and pelleted catalysts.

Materials	Surface area (m^2/g)	Pore volume (cm^3/g)	Pore diameter (nm)	Density (g/cm^3)	CO chemisorption	
					CO uptake (µmol/g)	% Metal Dispersion
Functionalized CNT	240	0.84	14.5	0.63	-	-
MoKCuFe/CNT	175	0.66	14.7	0.77	153	2.8
10S	135	0.47	14.1	0.87	131	2.6
10C	132	0.50	14.5	0.86	132	2.6
15S	123	0.42	13.2	0.91	113	2.5
15C	125	0.46	12.8	0.89	118	2.6
20S	115	0.40	13.8	0.96	103	2.4
20C	117	0.43	14.7	0.93	109	2.6

Porosity (φ, a dimensionless parameter) is defined as the product of pore volume (cm^3/g) and pellet density (g/cm^3). It can be seen from N_2 adsorption desorption analysis (see Table 5.1) that at each bentonite loading, the cylindrical pellets have higher pore volume and also higher porosity than corresponding spherical pellet. This could be due to the inherent difference between the shapes (cylindrical and spherical) leading to difference in accessibility of pores, as the surface area of cylinder is larger than that of a sphere.

5.4.2 X–ray diffraction for oxide catalysts

The powder wide angle XRD patterns for all materials are shown in Figure 5.3. The catalysts MoKCuFe/CNT, 10S, 10C, 15S, 15C, 20S and 20C show the peaks at same 2θ, however, there are differences in intensities. This signifies the different crystallite size in each catalyst. The peaks at 2θ = 23.9° and 26° is due to the graphitic structure of carbon nano-tubes [192]. The peaks at 2θ = 33°, 40.8°, 49.3°, correspond to the presence of Fe_2O_3, and the peaks at 2θ = 19.8°, 30°, 35.4°, 54°, 57°, 62.5° and 64° represent the presence of Fe_3O_4 [197–199]. The Scherrer's equation 5.6 [155] was employed to find the crystallite size for Fe_3O_4 and Fe_2O_3 using most intense peak at 2θ =35.4° and 33°, respectively.

$$d_p = \frac{0.89 * \lambda}{B * Cos(\theta)} \tag{5.6}$$

where d_p is crystallite diameter, B is the difference in angles at full width at half max, and $\lambda = 1.54$ Å is the wavelength. The calculated crystallite sizes for Fe_3O_4 and Fe_2O_3 present in each catalyst are shown in Table 5.2. It was observed that the crystallite size increased slightly with addition of bentonite as in case of 15B and 20B catalysts.

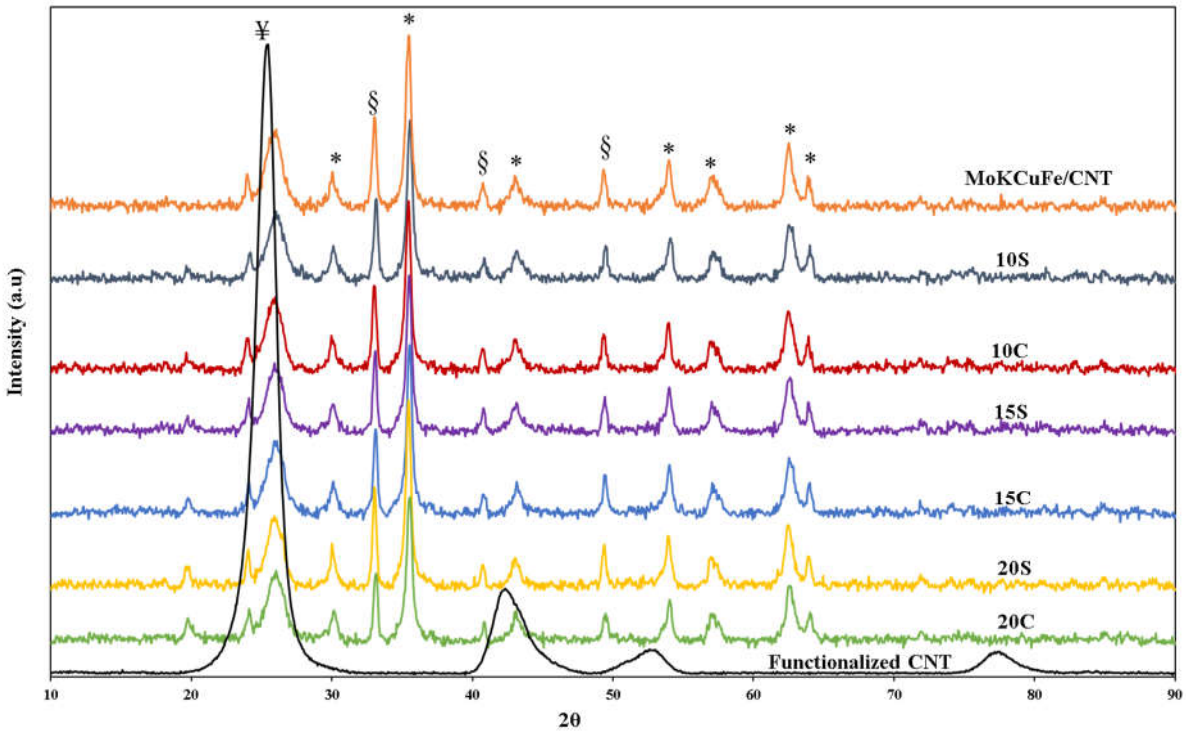

Figure 5.3 XRD patterns for powder and pelletized catalysts. ¥ = graphitic structure of CNT, § = Fe_2O_3, and * = Fe_3O_4

Table 5.2 Iron oxide crystallite size from XRD analysis

Catalysts	Fe_3O_4 crystallite size (nm)	Fe_2O_3 crystallite size (nm)
MoKCuFe/CNT	18.4	20.5
10S	18.0	21.0
10C	18.3	22.8
15S	18.1	26.4
15C	19.2	24.1
20S	19.9	26.4
20C	17.9	22.1

5.4.3 CO chemisorption

The percentage metal (iron) dispersion in all the pelleted catalysts was determined using CO chemisorption. The amount of CO adsorbed and percentage metal dispersion are shown in Table 5.1. The data for powder MoKCuFe/CNT catalysts with no bentonite is also shown in Table 5.1. Similar to XRD, it was observed during chemisorption analysis that with addition of bentonite the amount of CO adsorbed decreases, resulting in lowering the metal dispersion from 2.8% (in MoKCuFe/CNT) to 2.4 % (in 20S) (by 14 %) for spherical pellets. However, the decline in metal dispersion was only ~ 7 % for the cylindrical pellets. This could be due to the blocking of small pores on addition of bentonite. The pores size distribution shown in Figure 5.2 confirms the decline in pore volume at lower pore diameter range (< 5 nm) on addition of bentonite.

5.4.4 H_2–Temperature programmed reduction

The ease in reducibility of active metals is very important step during the activation of catalyst. Therefore, to determine the influence of bentonite and pellet shape on the reducibility of iron in MoKCuFe/CNT catalyst, the H_2–TPR studies were performed. The H_2–TPR profiles for each pelletized catalyst and MoKCuFe/CNT powder catalyst (without bentonite) are shown in Figure 5.4. The reduction of iron oxides presents in catalysts with hydrogen flow at temperature below 570 °C occurs in two steps. First step is the reduction of hematite (Fe_2O_3) to magnetite (Fe_3O_4) followed by reduction of magnetite to metallic iron.[200] These authors have indicated that below 570 °C, the reduction of magnetite to metallic iron proceeds via the formation of wustite (FeO). However, the wustite is found to be unstable in these conditions and quickly reduces to metallic iron. It is known that at higher reduction temperature (> 570 °C) the wustite (FeO) is detectable and reduces at temperature above 600 °C [201,202].

The TPR profile of each catalyst shows two distinct peaks. The lower temperature peak, at 390 °C for MoKCuFe/CNT catalyst without binder is due to reduction of Fe_2O_3 (hematite) to Fe_3O_4 (magnetite) and the second broad peak centered at 580 °C corresponds to the reduction of Fe_3O_4 to FeO to metallic Fe [199]. The TPR profiles for bentonite loaded materials shows that the first stage of reduction took place at lower temperature as compared to the powder catalyst without binder. The first reduction peak for pellet catalysts are at 250–300 °C and the second peak is at 10–20 °C lower temperature than that shown by binder free catalyst. The reduction temperature decreased as the bigger particles are easy to reduce, because of less metal support interactions.

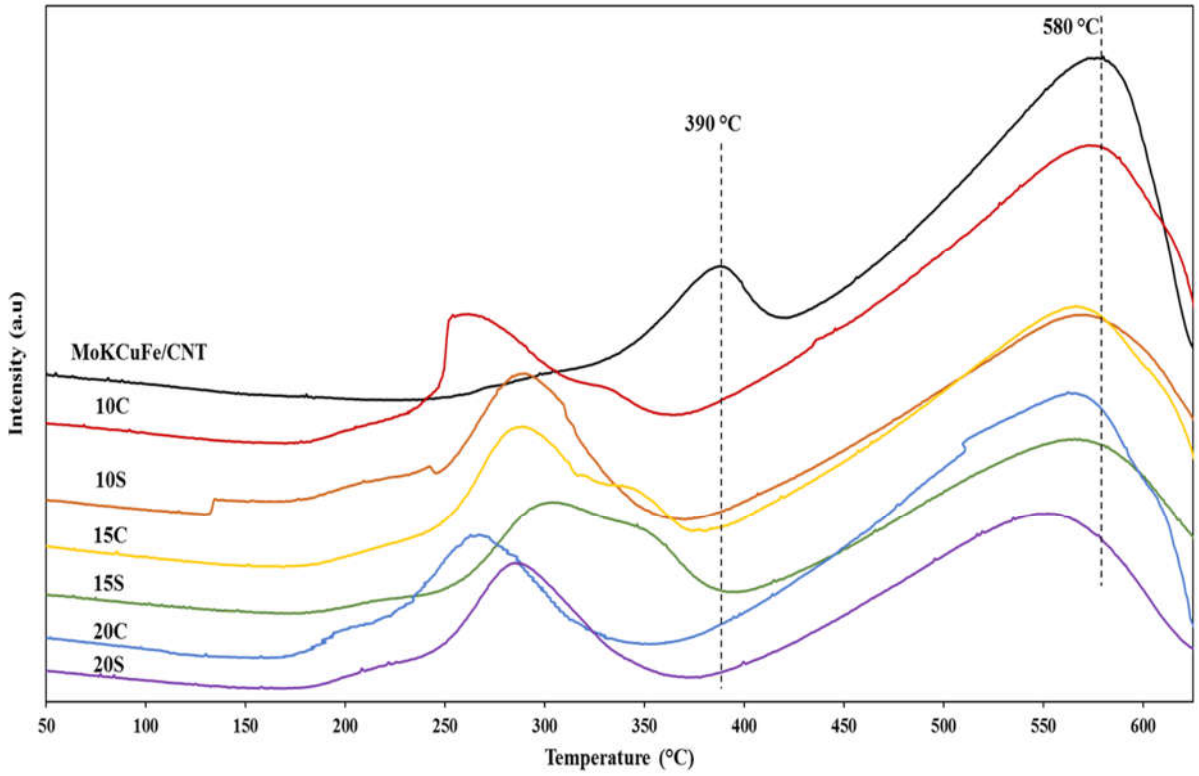

Figure 5.4 H_2–TPR profile for powder and pelletized catalysts

TPR profiles for pelleted catalysts indicates the same with reduction of Fe_2O_3 at 290 °C (10S), 260 °C (10C), 300 °C (15S), 280 °C (15C), 280 °C (20S), and 265 °C (20C). The broadness of the first reduction peak (at lower temperatures) can be attributed to presence of various metals (Mo, K, Cu and Fe) and their effects on reducibility. It was also observed during H_2-TPR analysis that the reduction of Fe_2O_3 in cylindrically shaped pellet catalysts occurs at 10-15 °C lower than that in spherically shaped counterpart pellet catalyst. This could be due to the difference in effective diffusivity of hydrogen in the pores of spherical and cylindrical pellets. It was observed during BET analysis (see Table 5.1) that the cylindrical shaped pellets have slightly higher porosity and hence higher effective diffusivity. Therefore, it can be concluded that cylindrical shaped pelleted catalysts are easy to reduce as compared to spherically shaped pelletized catalysts.

5.4.5 Mechanical properties of pellets

5.4.5.1 Single Pellet crushing strength test

The texture analyzer was used to calculate the single pellet crushing strength using ASTM D 4179 and 6175 methods. Figure 5.5 shows the schematic representation of determining crushing strength using

texture analyzer. Bottom plate was stationary, and the load was applied from the top plate. The analyzer was connected to a computer through software, which gives the value of load, which a pellet could stand before it collapses.

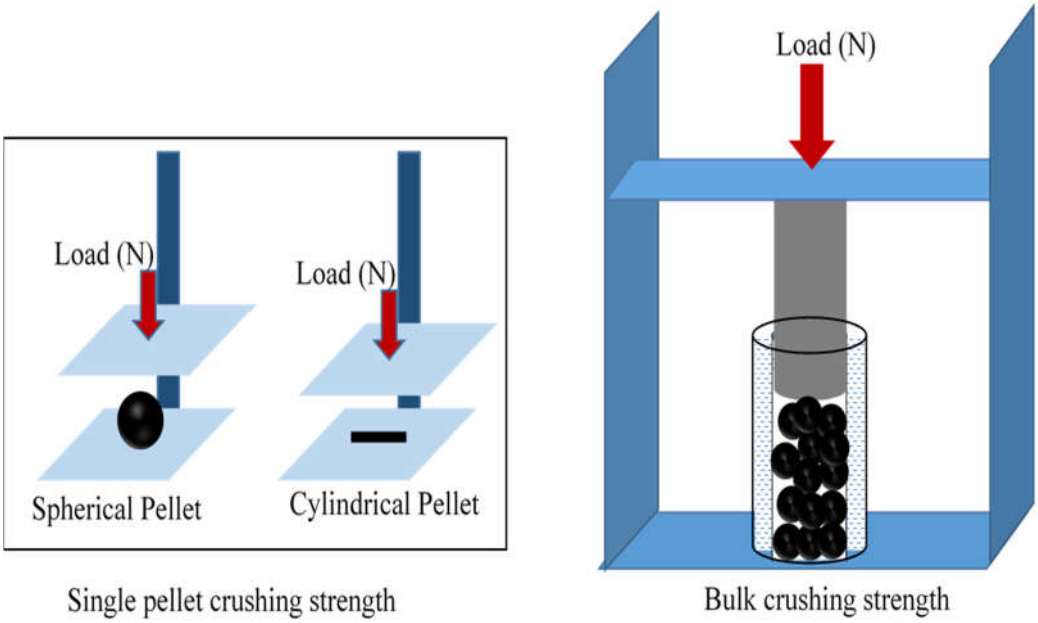

Figure 5.5 Schematic representation for determining mechanical strength

Using equations 5.4 and 5.5 the crushing strength for all the 6 pellets was determined and shown in Table 5.3. It can be observed from the table that with increasing the bentonite loading from 10 to 20 wt. % the mechanical strength of the catalyst pellet also increases. However, at each loading the crushing strength of cylindrical pellet is lower than that shown by spherical pellet. The strength of 20S catalyst pellet is highest among all 6 pelleted catalysts and is found to 6 % and 20 % higher than that of 15S and 10S catalyst pellets, respectively.

5.4.5.2 Bulk crushing strength test

Figure 5.5 shows the schematic representation of bulk crushing strength. 1g of pellets was filled in Quarter inch (ID) cylindrical die, which was attached to Instron material testing machine. Three different loads were applied to fresh catalyst pellets. After each load the corresponding amount of fines produced due to bulk crushing of pellets was recorded.

The data for all 6 pellet catalysts are shown in Table 5.4. The plot of crushing pressure versus fines produced by breaking of pellets is shown in Figure 5.6.

Table 5.3 Single pellet crushing strength

Catalyst pellet	Crushing strength σ (kPa)
10C	408
10S	525
15C	478
15S	620
20C	530
20S	660

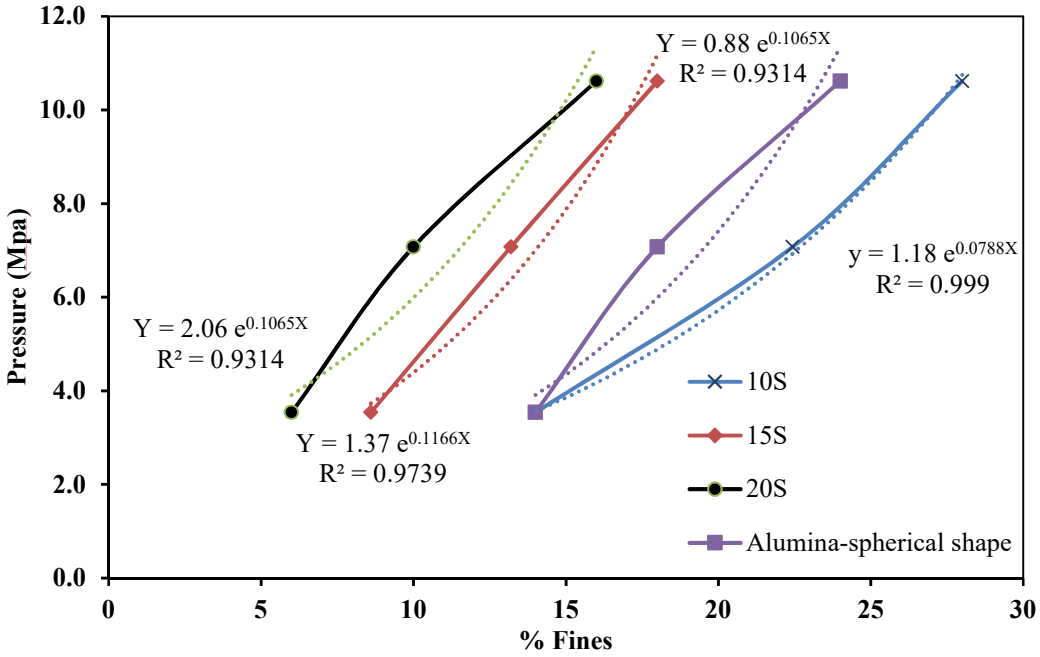

Figure 5.6 Relationship between crushing pressure and percentage fines produced during bulk crushing strength test.

The curve fitting was used to extrapolate the data to find the pressure required to break the pellets to produce 1 % fines. The data for each pellet is shown in Table 5.5. Similar to single pellet crushing strength test, it was observed from this analysis (see Table 5.3) that the increase in bentonite loading results in increasing the pellet strength. For comparison the bulk crushing strength of alumina spherical pellets (3-4 mm dia) was also determined. The catalyst pellets 20C and 20S showed the maximum bulk crushing strength of 2.3 MPa and 1.55 MPa among all the pelleted catalysts including alumina pellets.

Table 5.4 Amount of fines produced during bulk crushing test of pellets

Load (N)	Pressure (Mpa)	% fines formed on crushing						
		10S	15S	20S	10C	15C	20C	Alumina-spherical shape
100	3.5	14	9	6	22	14	10	14
200	7.1	22	13	10	26	19	18	18
300	10.6	28	18	16	30	24	22	24

These values are also higher than the bulk crushing strength for alumina pellets reported in literature [203]. Therefore, it can be concluded from the mechanical strength testing that MoKCuFe/CNT catalyst pellets weather cylindrical or spherical with 20 wt % bentonite loading possess higher mechanical strength than the conventional alumina pellet and are suitable for commercial applications.

Table 5.5 Bulk crushing strength test results for pellets

Catalyst pellets	Pressure (MPa) required to crush the pellets to produce 1.0% fines
10S	1.28
15S	1.54
20S	2.30
10C	0.35
15C	0.92
20C	1.55
Alumina-spherical shape	0.98

5.4.6 Catalyst testing for Fischer–Tropsch synthesis

All catalysts were tested for Fischer–Tropsch synthesis in a fixed bed reactor using 60 ml/min of Syngas ($H_2/CO = 2.0$) at 270 °C and 2.07 kPa. The outlet liquid and gas were separated, and the gas was analyzed in an online GC to determine the CO conversion and hydrocarbon selectivity. The liquid product was tested to determine the boiling point distribution using simulated distillation. The results of outlet gas analysis for each catalyst are shown in Tables 5.6 and 5.7.

Table 5.6 shows the initial CO conversion and hydrocarbon selectivity at 10^{th} hour of time on stream. The powder MoKCuFe/CNT catalyst exhibited the highest CO conversion of 93.7 % with maximum selectivity for C_{5+} hydrocarbon (85.4 %). The addition of bentonite results in lowering the FTS activity, and with increase in bentonite loading there is decline in initial FTS activity. The CO conversion follows

the order MoKCuFe/CNT > 10C ≈ 10S > 15C ≈ 15S > 20C ≈ 20S. The decline in initial FTS activity with increasing bentonite loading could be due to the lower amount of iron present in these catalysts.

Table 5.6 FTS activity of powder and pellet catalysts after 10 h time on stream. Reaction conditions: 270 °C, 2.07 MPa, 60 ml. g_{cat}^{-1}. min^{-1} syngas flow (H_2/CO = 2.0).

Catalyst	CO conversion (mole %)	CO conversion (mole%)/ % of Fe in catalyst	CO_2 Selectivity	Hydrocarbon selectivity (%)		
				CH_4	C_2-C_4	C_{5+}
MoKCuFe/CNT	93.7	3.12	42.9	7.3	7.3	85.4
10S	90.0	3.33	41.9	6.7	11.2	82.1
10C	91.0	3.37	43.5	7.8	11.9	80.2
15S	89.4	3.51	44.2	8.7	12.8	78.5
15C	89.0	3.49	43.5	7.9	11.8	80.2
20S	86.3	3.60	43.8	9.1	10.5	80.4
20C	87.6	3.65	47.9	10.1	17.8	72.1

The CO conversion per percent of iron present in catalyst (see Table 5.6) indicates that the catalyst with higher bentonite loading shows higher conversion per percent of iron. This could be related to the ease in reduction of the iron oxides in these catalysts during activation, which results in the higher extent of reduction and formation of more number of active sites. It was evident from the H_2–TPR analysis (see Figure 5.4) that addition of bentonite promotes the reduction of hematite and magnetic to metallic iron at lower temperatures as compared to that shown by bentonite free catalyst.

With increasing time on stream, CO conversion was declined in each catalyst before it stabilizes (see Table 5.7 and Figure 5.7). However, the catalysts with 10% and 15% bentonite loading showed maximum decline in CO conversion. For catalyst 10S the CO conversion decreased from 90% to 42% in 70 h.

However, for 10C catalyst CO conversion declined to 62 % from 91% in 70 h. The CO conversion activity for each catalyst follows the order: MoKCuFe/CNT > 20C ≥ 20S > 15C > 10C > 15S > 10S. There was more decline in FTS activity of 10 wt. % bentonite loaded catalyst in comparison to 20 wt. % bentonite loaded catalyst, and higher activity of cylindrical pellet in comparison to spherical pellet of same material is explained based on the spent catalyst analysis.

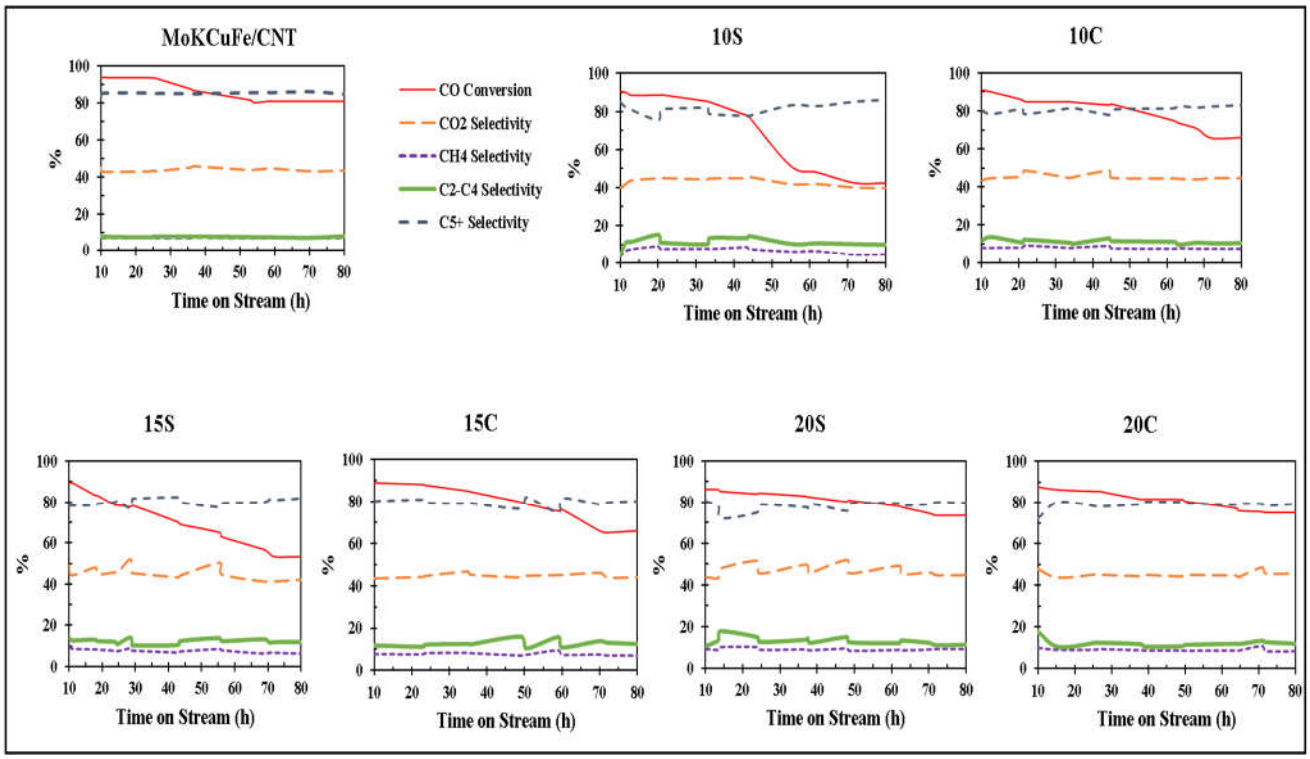

Figure 5.7 Time on stream FTS activity data for powder and pellet catalysts

Table 5.7 FTS activity of powder and pellet catalysts after 70 h time on stream. Reaction conditions: 270 °C, 2.07 MPa, 60 ml. g_{cat}^{-1}. min^{-1} syngas flow ($H_2/CO = 2.0$).

Catalyst	CO conversion (mole %)	CO conversion (mole %)/ % of Fe in catalyst	CO_2 Selectivity	Hydrocarbon selectivity (%)		
				CH_4	C_2-C_4	C_{5+}
MoKCuFe/CNT	80.9	2.70	43.3	7.2	7.9	84.9
10S	42.4	1.57	39.8	4.9	10.0	85.1
10C	65.7	2.43	44.6	7.3	10.5	82.3
15S	53.2	2.09	41.1	6.9	11.9	81.2
15C	65.2	2.56	43.9	7.3	13.1	79.6
20S	73.6	3.07	45.7	8.5	12.8	78.6
20C	75.1	3.13	44.7	9.2	11.0	79.8

It can be seen that the least decline in hydrocarbon production rate was observed in 20C pelleted catalyst. Figure 5.8 shows the boiling point distribution of hydrocarbon liquid produced by each catalyst. It can be observed from Figure 5.8 that the catalysts containing 10 wt. % and 15 wt. % bentonite produced

more amount of short chain hydrocarbons. However, catalyst 20C and 20S relatively produced more amount of long chain hydrocarbons, which closely matches the boiling product distribution of powder MoKCuFe/CNT catalyst.

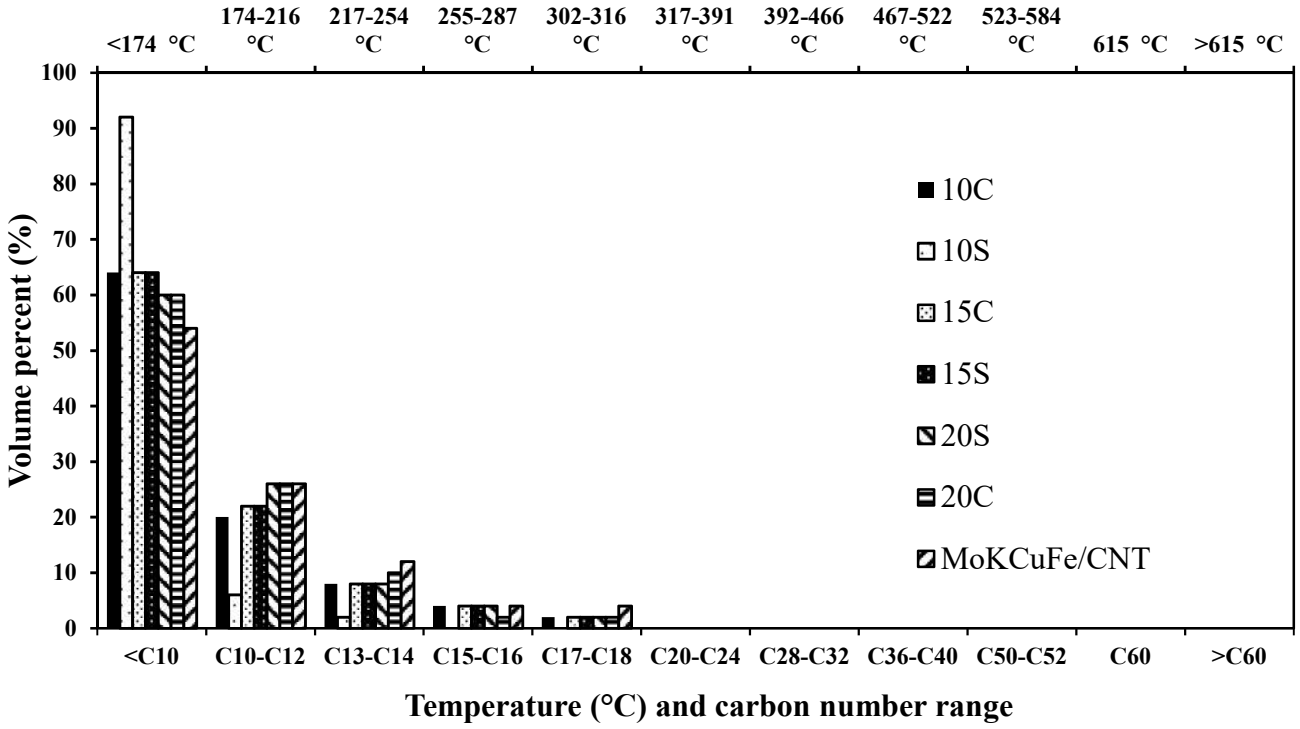

Figure 5.8 Boiling point distribution of hydrocarbon liquid produced by powder and pelleted catalysts

Table 5.8 Liquid hydrocarbon production rate using CNT supported Fe catalysts (powder and pellet). Reaction condition: 270 °C, 2.07 MPa, 60 ml. g_{cat}^{-1}. min^{-1} syngas flow (H_2/CO = 2.0).

Catalyst	Liquid hydrocarbons $(g_{HC} \cdot g_{cat}^{-1} \cdot h^{-1})$	Liquid hydrocarbons $(g_{HC} \cdot g_{iron}^{-1} \cdot h^{-1})$
MoKCuFe/CNT	0.25	0.83
10S	0.12	0.44
10C	0.15	0.56
15S	0.14	0.55
15C	0.17	0.67
20S	0.18	0.75
20C	0.20	0.83

The catalyst 20C was found to be the best performing catalyst among all pelletized catalysts, therefore the optimization of temperature, pressure and GSHV was performed. Taguchi method with 3 factors design of experiment was performed with three levels of temperatures (260, 270, and 280 °C), pressures (1.72, 2.41, 3.10 MPa), and GHSVs (1600, 2400, 3200 h^{-1}). Table 5.9 shows the design of experiments and FTS activity and selectivity data at each condition. It can be observed from Table 5.9 that with increase in temperature the CO conversion increases however the C_{5+} selectivity decreases. Decrease in GSHV resulted in increasing conversion however, it affected the liquid production rate. The increase in pressure results in slight increase in CO conversion and C_{5+} selectivity. Therefore, 270 °C and 2.07–3.10 MPa were found to be optimum for higher C_{5+} selectivity.

Table 5.9 Taguchi DOE and FTS activity data and process parameter optimization for 20C catalyst.

Temperature (°C)	Pressure (MPa)	GSHV (h^{-1})	CO Conversion (mole %)	CO_2 Selectivity (%)	HC selectivity (%)		
					CH_4	C_2-C_4	C_{5+}
260	1.72	1600	55	42.5	1.0	19.0	80.0
260	2.41	2400	53	45.0	1.0	16.0	83.0
260	3.10	3200	50	47.7	7.6	18.5	73.9
270	1.72	2400	72	50.4	9.1	20.5	70.4
270	2.41	3200	76	44.2	7.8	11.0	81.2
270	3.10	1600	85	40.3	9.3	10.1	80.6
280	1.72	3200	73	42.9	6.0	14.7	77.3
280	2.41	1600	88	45.2	11.0	18.5	70.5
280	3.10	2400	85	43	11.2	15.7	73.1

5.4.7 N_2 adsorption-desorption analysis for spent catalysts

The N_2 adsorption desorption analysis was performed for spent catalyst and the surface area, pore volume and pore diameter for each spent pelleted catalyst are shown in Table 5.10. The percentage decline in pore volume as compared to fresh catalyst was also reported in Table 5.10. It was observed that the catalysts 10C and 10S showed ~ 35 % decline in pore volume followed by catalyst 15C and 15S showing 27 % decline. The catalysts 20C and 20S showed the least decline in surface area and pore volume among all catalysts. The decline in textural properties could be related to the change in FT activity. Catalyst 10S showed largest decline in pore volume which resulted in largest decline in CO conversion. The decline

in pore volume follows the order 10S > 15S > 20S and the decline in FTS activity also follows the same order (see Table 5.7). Therefore, it can be concluded from BET analysis of spent catalyst that the catalyst pellets containing 10 wt. % and 15 wt. % are not stable to retain the textural properties during reaction. This could be due to less density and high porosity of the 10S, 10C, 15S and 15C materials. It was observed that the order of decline in pore volume follows the order of increasing porosity (or decreasing density) (see Table 5.1).

Table 5.10 Textural properties of spent pelleted catalysts

Catalyst	Surface area (m^2/g)	Pore volume (cm^3/g)	Pore diameter (nm)	Pore volume of fresh catalyst (cm^3/g)	% age difference in pore volume
10S spent	79	0.33	20	0.47	30
10C spent	75	0.34	27	0.50	32
15S spent	79	0.33	20	0.42	21
15C spent	79	0.36	23.2	0.46	22
20S spent	95	0.37	16	0.40	8
20S spent	98	0.4	16.5	0.43	7

During FTS reaction, the small pores present in above mentioned pelleted catalysts contributing to the higher porosity and higher initial reaction rate, might be filled due to the formation of liquid hydrocarbon hence, result in lowering the activity. The increase in average pore size indicates the absence of small pores in spent 10S, 10C, 15S and 15C pellet catalysts.

5.4.8 Internal Mass-transfer limitations

The effectiveness factor η was calculated to determine if the reaction is kinetic or mass transfer limited. If η is > 0.95 the reaction is kinetic controlling otherwise it is diffusion controlled. Following equations were used to determine η [204,205].

$$R_{CO} = -\eta k C_{CO} \tag{5.7}$$

$$\phi = \sqrt{\frac{ka^2}{D_{eff}}} \tag{5.8}$$

For sphere,

$$\eta = \frac{1}{\phi}\left[\frac{1}{tanh3\phi} - \frac{1}{3\phi}\right] \quad (5.9)$$

For cylinder,

$$\eta = \frac{tanh\phi}{\phi} \quad (5.10)$$

where, R_{CO} is the rate of CO conversion mol.cm^{-3}.s^{-1}, ϕ is Thiele modulus and a is characteristic length

$$a = \frac{Volume_{sphere/cylinder}}{Surface\ area_{sphere/cylinder}} \quad (5.11)$$

For sphere the value of a = 0.05833 cm and for cylinder a = 0.024 cm.

The binary diffusivity D of CO and H_2 in fresh catalyst was estimated using Chapman–Enskog theory [206].

$$D_{CO-H_2} = \frac{0.00186 * T^{3/2}}{P * \sigma_{CO-H_2} * \Omega}\left(\frac{1}{M_{Co}} + \frac{1}{M_{H_2}}\right)^{1/2} \quad (5.12)$$

$$\sigma_{CO-H_2} = \frac{1}{2}\left(\sigma_{CO} + \sigma_{H_2}\right) \quad (5.13)$$

The value of collision diameter σ_{CO-H_2} was estimated as 3.245 Å, Ω was estimated as 0.79, P and T are reaction pressure 2.07 MPa and temperature (543 °C). Hence, the value of D_{CO-H_2} was calculated and found to be 0.02877 cm^2/s.

The catalyst pores were estimated to be filled due to the production of hydrocarbon liquid during FTS reaction. Therefore, the diffusivity of CO and H_2 in pores filled with liquid was estimated using equations 5.14 and 5.15 [207].

$$D_{CO} = 5.584\ X\ 10^{-7}\ exp\left(-\frac{1786.29}{T}\right) \quad (5.14)$$

$$D_{H_2} = 1.085\ X\ 10^{-6}\ exp\left(-\frac{1624.63}{T}\right) \quad (5.15)$$

The D_{CO} was calculated to be 2.08×10^{-4} cm^2/s and D_{H_2} was calculated to be 4.56×10^{-4} cm^2/s. The effective diffusivity, D_{eff} was calculated using following correlation (equation 5.16) [205]

$$D_{eff} = \frac{D_{CO-H_2} * \varphi * 0.8}{\tau} \quad (5.16)$$

Where, φ is porosity and τ is tortuosity (assumed value for τ = 4.0)

The value of D_{eff} was calculated from equations 5.12 and 5.16, also solving equations 5.7 to 5.10 results in finding the value of effectiveness factor η at initial reaction rate (10 h) for all the pelleted catalysts. The values for η are shown in Table 5.11. It was observed that for initial reaction rate the value of η was greater than 0.95 for all catalysts indicating that the reaction is kinetic limited. However, as the FTS reaction progresses the pores were assumed to be filled with liquid hydrocarbon. Therefore, in order to evaluate the η for steady state reaction the diffusivity of CO and H_2 in pores filled with liquid was estimated from equations 5.14 and 5.15. The effective diffusivity was then calculated (equation 5.16) using the porosity calculated from the pore volume of spent catalyst and shown in Table 5.12. It was observed that the porosity follows the order 20C > 20S > 15C > 15S > 10C > 10S and hence the effective diffusivity also follows the same order. This implies that the diffusion of CO and H_2 in 20 S and 20 C is faster than other pelleted catalysts.

Table 5.11 Effectiveness factor at initial reaction rate for all pelleted catalysts.

Catalyst	Rate (mol.cm^{-3}.s^{-1}) @ TOS = 10 h	Porosity (φ)	Effective diffusivity (D_{eff})	Thiele modulus (ϕ)	Effectiveness factor (η)
10 S	9.7E-06	0.41	2.09E-03	0.30	0.95
10 C	9.6E-06	0.43	2.20E-03	0.14	0.99
15 S	1.0E-05	0.38	1.96E-03	0.32	0.95
15 C	9.7E-06	0.41	2.10E-03	0.15	0.99
20 S	1.0E-05	0.38	1.97E-03	0.32	0.95
20 C	1.0E-05	0.40	2.05E-03	0.15	0.99

Again, using the reaction rate data from Table 5.12, and solving for equations 5.7 to 5.10 the effectiveness factor was calculated for all pelleted catalyst at 70 h TOS and reported in Table 5.12. It can be observed that for all spherical pellet catalysts the value of η is very low in the range of 0.19 to 0.25 indicating that the reaction is severely mass transfer limited. However, the reaction was not severely mass transfer controlling for the cylindrical pelleted catalyst as the value of η were found be in the range of 0.66−0.69. Therefore, it can be concluded that the large decline in FTS activity of spherical pellet catalyst as compared to cylindrical pellet catalyst as shown in Table 5.7 and Figure 5.7 is due to severe internal mass transfer limitations in spherical pellet catalyst.

Table 5.12 Effectiveness factor at steady state reaction for all pelleted catalysts.

Catalyst	Rate (mol.cm^{-3}.s^{-1}) @ TOS = 70 h	Porosity (φ)	Effective diffusivity (D_{eff})	Thiele modulus (ϕ)	Effectiveness factor (η)
10 S	4.50E-06	0.29	2.58E-05	3.5	0.25
10 C	6.92E-06	0.29	2.63E-05	1.3	0.66
15 S	5.92E-06	0.30	2.70E-05	4.3	0.21
15 C	7.10E-06	0.32	2.88E-05	1.2	0.69
20 S	8.65E-06	0.36	3.28E-05	5.1	0.19
20 C	8.56E-06	0.39	3.52E-05	1.2	0.69

5.5 Conclusion

In this work, the CNT supported MoKCu promoted Fe catalyst was synthesized and utilized for Fischer-Tropsch synthesis. The catalyst was pelletized into spherical and cylindrical pellets using bentonite as binder. Three different loadings of bentonite 10, 15 and 20 wt. % were used and mechanical strength of different pellets was determined. Single pellet and bulk crushing strength tests were performed following ASTM D 4179, 6175 and 7084 methods. Spherical pellets are found to be mechanically stronger than cylindrical pellets for any given loading of bentonite. Additionally, with increasing the bentonite loading the mechanical strength increased and 20 wt. % bentonite loaded pellets showed the maximum single pellet crushing strength of 660 kPa. Bulk crushing strength test revealed that the strength of cylinder and spherical pellet containing 20 wt. % bentonite is higher than the corresponding strength for alumina spherical pellets. All pelleted catalysts were characterized to determine textural and chemical properties. It was observed from XRD and CO chemisorption analysis that the iron dispersion decreased by ~ 7−15 % with bentonite loading. The H_2−TPR studies concluded that on addition of bentonite the reduction of iron oxide species was faster. It was also observed that cylindrical shaped pelleted catalysts are easy to reduce as compared to spherical shaped pelleted catalysts. The FTS activity test showed that the pelletized catalysts both spherical and cylindrical containing 20 wt. % bentonite maintained the highest activity. However, sharp decline in CO conversion for pelletized catalyst containing 10 and 15 wt. % bentonite was observed, which could be related to change in textural properties due to their high porosity and less density. Large decline in FTS activity of spherical pellet catalysts (containing 10 and 15 wt. % bentonite) as compared to cylindrical could be assigned to the presence of severe mass transfer limitations in former particles as evident from the η value of around 0.2. The cylindrical pellets containing 20 wt. %

bentonite were the best performing catalyst among all studied, and 270 °C and 2.07−3.10 MPa were found to be optimum for higher CO conversion and C_{5+} selectivity.

CHAPTER 6: MESOPOROUS ALUMINA SUPPORTED Co CATALYST FOR FTS

Similar version of this chapter has been published as a research paper in the following journal and presented in the following conference:

- V. Vosoughi, S. Badoga, A.K. Dalai, N. Abatzoglou, "Modification of mesoporous alumina as a support for Co-based catalyst in Fischer-Tropsch Synthesis", Fuel Proc. Tech. (2017) 162, 55-65.
- V. Vosoughi, Ajay. K. Dalai, N. Abatzoglou, "Fischer-Tropsch Synthesis: stable mesoporous alumina supported cobalt catalyst", 66th CSChE Conf., Oct. 16-19, 2016, Quebec City, Canada.

Contribution of PhD candidate

The experimental design, mesoporous alumina synthesis, catalyst preparation, characterizations, FT tests, compiling / interpretation of the results, and manuscript writing were performed by Vahid Vosoughi. Optimization of the process conditions was conducted by Dr. Sandeep Badoga. Rebuttals for the manuscript was prepared with the assistance and suggestions of Dr. Badoga. This study and the writing was accomplished based on the suggestions and supervision of Drs. Ajay Dalai and Dr. Abatzoglou.

Contribution of this chapter to the overall PhD research

Having examined the carbon nanotube supported Co and Fe catalysts for Fischer-Tropsch synthesis in Chapters 4 and 5, in this part of work, mesoporous alumina (m-Al_2O_3) is used as a support material for development of Co-based catalyst for FTS. This chapter provides some insights on the instability and modification of mesoporous alumina with higher textural properties during the preparation of Co-based catalysts. The influence of different solvents (water, ethanol, and acetone) during the impregnation of cobalt on the physico-chemical properties of mesoporous alumina was investigated. Also, the corresponding cobalt catalysts were characterized by various techniques to study their properties and performance for Fischer-Tropsch Synthesis. The stable mesoporous alumina supported Co catalyst prepared using ethanol as solvent showed higher CO conversion activity and hydrocarbon yield as compared to that shown by γ-Al_2O_3 supported Co catalyst.

6.1 Abstract

The high surface area, large pore volume and pore diameter mesoporous alumina was synthesized using pluronic F127 as a structure-directing agent. This material was employed as a support for the cobalt catalyst in Fischer-Tropsch Synthesis (FTS). During the catalyst synthesis, impregnation of cobalt nitrate aqueous solution caused a collapse in the structure and a drastic decline in the textural properties of the mesoporous alumina. Organic solvents such as acetone and ethanol were employed instead to realize their impact on the corresponding cobalt catalysts stability. The synthesized catalysts were characterized using BET, XRD, TEM, TPR, and H_2 chemisorption. The catalysts prepared using organic solvents were found to retain the textural properties of the mesoporous alumina. The process conditions including temperature, pressure, and GHSV were optimized adopting Taghuchi experimental design. Then, all catalysts were tested in FTS utilizing syngas with H_2/CO ratio 2.0, at optimized conditions of 230 ºC, 2.76 MPa, and GHSV of 900 h^{-1}. The Co/γ-Al_2O_3 catalyst was also synthesized and tested in FTS for the comparison study. The physico-chemical properties of the synthesized catalysts were correlated with their performances in FTS. The mesoporous alumina supported cobalt catalyst using ethanol as a solvent in its preparation was found to be the most stable in the series and it showed 8.3% higher CO conversion, 3.3% higher C_{5+} selectivity, and 2.7 % lower CH_4 selectivity as compared to those shown by Co/γ-Al_2O_3 catalyst. Higher cobalt loadings of 22.5 and 30 wt. % were also prepared using ethanol solvent and examined in FTS. Doubling the cobalt content from 15 to 30 wt. % of the catalyst resulted in stable catalyst with 23 % increase in the hydrocarbon yield and 4 % improve in C_{5+} selectivity.

6.2 Introduction

Different carbonaceous feedstocks (coal, natural gas, biomass, wastes, oil residues) can be thermally transformed into carbon monoxide and hydrogen mixture which is called synthetic gas or syngas. Then, the intermediate product (syngas) can be catalytically converted to sulfur– and aromatic–free transportation fuels, and value added hydrocarbons deploying Fischer–Tropsch synthesis (FTS) [1–4]. Cobalt is the most active metals for FTS catalyst with higher selectivity for long chain paraffinic hydrocarbons. Optimizing the usage of high price cobalt and enhancing the physico–chemical properties of the supported cobalt catalyst for FTS are crucial aspects of designing an efficient catalyst with higher liquid hydrocarbon productivity and selectivity [2,5,6].

Specific surface area, pore size distribution, and the surface chemistry of the support material on the one hand, drying procedure, solvent evaporation rate, precursor decomposition rate, and calcination condition

during the catalyst preparation on the other hand would affect the affinity of cobalt with the support [44]. As a result, the dispersion, crystallite size, and reducibility of cobalt species (CoO_x) in the catalyst would vary. For example, weakly interacting support develops larger cobalt crystallites with lower dispersion, which need lower reduction temperature to form Co^0 metals. Conversely, strong metal-support interaction (SMSI) results in smaller cobalt species with higher dispersion that requires higher temperature to reduce them to Co^0. Thus, moderate support-cobalt precursor interaction favors optimum dispersion of cobalt crystallites [19]. These physico-chemical properties namely cobalt dispersion, crystallite size, and ease of reduction lead to different type and number of Co^0 active sites during the catalyst reduction. The active adsorption sites for CO + H_2 reactants and intermediate species during the FT reaction have significant impact on the catalytic performance of the cobalt catalyst [5,7,8]. In general, the crucial factors of the cobalt catalyst design for FTS would be (i) support material with appropriate physico-chemical and textural properties, (ii) method of catalyst preparation (including precursor type, loading, drying, calcination and reduction procedures), and (iii) optimum operational conditions in favor of higher CO conversion and C_{5+} selectivity [208].

In relation to impact of textural characteristics on the crystallite properties, a support with larger pore sizes would result in larger cobalt crystallites, which in turn causes faster sintering, whereas, smaller pore sizes facilitate the formation of smaller ensembles, which lead to SMSI and less reducibility [41]. In either case, the density of cobalt active sites drops which leads to less hydrocarbon production on unit mass or surface of the dispersed cobalt atoms.

In recent years, significant researchers have attempted to develop a novel alumina and other metal oxide supports targeting high activity, selectivity, and stability of cobalt-based catalysts in FTS [2,5,39]. The most patented and studied support materials for cobalt catalyst are conventional refractory metal oxides such as silica (SiO_2), titania (TiO_2), and alumina (Al_2O_3). The γ-Al_2O_3 is the most commercially used support material for the cobalt-based catalyst in FTS. Enhancement of the conventional alumina's surface area along with pore volume and pore diameter enables higher loading of active metals and facilitates higher availability of active sites at equal loadings. In addition, it is crucial to optimize pore diffusional transport, which affects the activity, product selectivity, and stability of the supported cobalt catalyst in FTS [37]. It is believed that mesoporous materials with pore size between 10 and 15 nm could provide suitable texture for the formation of cobalt crystallites with so-called optimum size range of 8-10 nm for FT reaction [9,38–40]. The effects of pore size and crystallite phase of mesoporous alumina on the

subsequent cobalt crystallite size and catalyst performance in FTS have been recently studied by a few other research groups [41,45–49].

The *main* interest in the synthesis of mesoporous alumina is to improve the textural properties and tunability of pore diameter concerning its application [209–212]. Templating method, using nonionic triple-block co-polymers such as P123 and F127 is a successful route to synthesize high surface area and large pore diameter mesoporous alumina [42]. These directing agents exhibited effective meso-structural ordering properties, and amphiphilic character. They are also commercially inexpensive and readily biodegradable [213]. However, aiming at synthesizing moderately large pore diameter with high surface area could cause the support material to be more susceptible to instability in the pore structure. We observed that wet impregnation of cobalt on the synthesized mesoporous alumina during the catalyst preparation led to a collapse in some pores of the support material. This induces a decline in the textural properties of the catalyst namely surface area, pore diameter, and pore volume.

Therefore, one of the main challenges of synthesizing an ordered support material with higher surface area, larger pore diameter and pore volume is the stability of its structure. To the best of our knowledge, limited works have been reported on addressing and resolving the instability of the synthesized mesoporous alumina, especially for catalytic application. In this study, aqueous and organic solvents (ethanol and acetone) were used for impregnation of the cobalt precursor during the catalyst preparation. All synthesized catalysts were characterized to determine their stability and then were examined for their activity and products selectivity in FTS using syngas with H_2/CO ratio of 2.0. Catalysts prepared using organic solvents, were found to retain the textural properties of synthesized mesoporous alumina. The operational conditions (temperature, pressure and flow rate) for FT reaction using synthesized mesoporous alumina supported cobalt catalysts were also optimized in this work. Moreover, as a baseline for comparison, the γ-alumina supported cobalt catalyst was synthesized, characterized, and tested for FT reaction in a fixed bed reactor. To investigate more on the synthesized mesoporous alumina as a support the impact of higher loadings of cobalt on the corresponding catalysts was also assessed.

6.3 Experimental methods

6.3.1 Materials

Pluronic F127 $(EO)_{106}(PO)_{70}(EO)_{106}$ as a structure-directing agent and aluminum isopropoxide $Al(O\text{-}i\text{-}Pr)_3$ as an alumina support precursor were purchased from Sigma–Aldrich, Oakville, Canada. Cobalt

nitrate $Co(NO_3)_2.6H_2O$, 99.9% as an active metal precursor, and γ-Al_2O_3 as a commercial support were purchased from Alfa Aesar, Tewksbury, United States. Anhydrous ethanol, isopropanol, and acetone as solvents were purchased from Fisher Scientific, Ottawa, Canada.

6.3.2 Support synthesis

The synthesis procedure of the desired mesoporous alumina material was adapted from literature [209,214]. The molar ratio of materials was used based on the following relation: 1.0 $Al(iPro)_3$: 0.01 F127: 8.0 EtOH: 6.0 iPrOH: 4.0 H_2O. 40 g of aluminum isopropoxide was dissolved in the mixture of ethanol and isopropanol solution in beaker A at 50 ºC with rigorous stirring for an hour. In beaker B, 27 g of non-ionic F127 copolymer was dissolved in the ethanol and isopropanol solution at 50 ºC under stirring condition for half an hour. Following the dissolution of polymer, limited amount of water was added dropwise to the beaker B to hydrolyze the aluminum alkoxide. The dissolved aluminum isopropoxide solution from beaker A was gradually added into beaker B. The resultant white suspension was stirred at low RPM at 50 ºC for 4 h. Subsequently, the suspension was kept at room temperature for 24 h for further aging. The gel type solution was then kept for hydrothermal treatment at 80 ºC for 24 h followed by 150 ºC for 24 h. The resulting material was washed with anhydrous ethanol, filtered and dried. Finally, the dried powder was calcined at 600 ºC for 6 h with heating rate of 0.5 ºC/min to remove the organic soft template.

6.3.3 Catalyst preparation

To synthesize the mesoporous alumina (m-Al_2O_3) supported cobalt catalyst, the specified amount of cobalt nitrate was dissolved in three different solvents namely ethanol (E), acetone (A) and water (W). Incipient wetness impregnation (IWI) method was employed to fill the pores with 15 wt.% of cobalt loading on the mesoporous alumina. Subsequently, the alumina supported cobalt catalysts were dried in vacuum oven at 50-70 °C for 12 h and later calcined at 400 °C for 3 h with ramp rate of 1°C/min. The catalysts were named as yCo(X)/m-Al_2O_3, where y represents the cobalt loading in weight percentage: 15, 22.5, 30; X denotes the solvent used for dissolving the cobalt precursor: A, E, and W. Commercially available γ-Al_2O_3 support was also used to prepare the 15Co(E)/γ-Al_2O_3 counterpart catalyst, following the same preparation procedure to compare its performance with m-Al_2O_3 supported cobalt catalysts.

6.3.4 Catalyst characterization

Nitrogen physisorption: The Micromeritics ASAP 2020 instrument was employed to determine the adsorption-desorption amount of N_2 at cryogenic temperature of 77 K. The samples were degassed under

50 mTorr (6.7 Pa) vacuum at 200 ºC for 4 h, prior to the analysis. Brunauer-Emmett-Teller (BET) equation was used to calculate the specific surface area. To estimate the specific pore volume and pore diameter of the specimen the Barrett-Joyner-Halenda (BJH) method was applied [69,155].

H_2 chemisorption: The Micromeritics ASAP 2020 chemisorption instrument was used to estimate the amount of hydrogen adsorption on the metal atoms. A catalyst sample was first reduced with hydrogen at 400 ºC for 150 min. The temperature was then reduced to 35 ºC and kept the reduced catalyst under 1.3×10^{-5} Pa vacuum condition. To determine the H_2 adsorption uptake on the atomic metal the H_2 gas flow was introduced to pass through the sample at 35 ºC [69,155]. Fraction of available metallic active phase (Co^0) in the surface (D) has been estimated according to the hydrogen uptake in the chemisorption. It is assumed that the stoichiometry of H:Co adsorption is 1:1 and all the cobalt species in the sample are reduced to Co^0 atoms [46,215]:

$$D\% = \frac{measured\ Co^0 atoms\ on\ the\ surface}{Total\ Co^0\ atoms\ in\ the\ sample} \times 100 \tag{6.1}$$

Temperature programmed reduction (TPR): The reduction behavior of the active metal oxides were studied using the AutoChem Micromeritics 2950 HP instrument equipped with a thermal conductivity detector. A 40 mg of the catalyst was placed in the stainless steel U-shaped sample holder and was purged with helium gas at 100 ºC. The sample was then cooled down to 35 ºC and then the TPR analysis was conducted by heating the sample with 10 ºC/min ramp to 800 ºC under 50 mL/min flow of 10% H_2/N_2 (v/v) gas mixture [69,155]. Degree of reduction (DOR) was determined and employed for estimating the amount of reduced cobalt atoms in the sample. Then, the corrected dispersion of Co atoms can be calculated based upon the amount of reduced cobalt atoms [46,215]:

$$D_{corr.}\% = \frac{measured\ Co^0 atoms\ on\ the\ surface}{Reduced\ Co^0\ atoms\ in\ the\ sample} \times 100 = \frac{D\%}{DOR} \tag{6.2}$$

In addition, the cobalt crystallites have been deemed to be in spherical shape with a site density of 14.6 atoms/nm^2. The Co^0 cluster size was calculated based upon the corrected cobalt dispersion [46,215]:

$$d_{chem.}^{Co^0} = \frac{96}{D_{corr.}\%} = \frac{96}{D\%} \times DOR \tag{6.3}$$

X-ray diffraction (XRD): The Bruker Advance D8, series II, Powder diffractometer with monochromatic Cu Kα radiation was used to carry out powder XRD of the samples. The broad angle XRD was measured at 2º/min scan rate from 10º to 90º and a step time of 2 s. To calculate the average thickness of the cobalt

oxide crystallites, the Debye–Scherrer equation was employed using the half width of the characteristic peak at 2θ = 36.8º:

$$d_{XRD}^{Co_3O_4} = \frac{K\lambda}{\beta \cos\theta} \times \frac{180}{\pi} \quad (6.4)$$

Where, $d_{XRD}^{Co_3O_4}$ is the mean diameter of crystallites (nm); *K* is a constant corresponding to the crystallite shape assumed 0.89; $\lambda = 0.154$ (nm) is X-ray wavelength; β is full-width at half-max (FWHM) or integral breadth in radian; and $\Theta_B = 2\Theta/2$ is Bragg angle (diffraction angle) [43,154].

Transmission electron microscopy (TEM): To examine the morphology of the samples through their micrographs, the JEOL 2011 transmission electron microscope was used. The standard sample preparation was followed to carry out the analysis [153].

6.3.5 Catalyst performance study for Fischer-Tropsch Synthesis

A fixed-bed micro reactor with 1 cm I.D. and 50 cm length was used to conduct the Fischer–Tropsch Synthesis (FTS). Top and bottom part of the reaction zone in the tubular reactor was filled with four different silicon carbides (SiC) in the size order of fine to coarse and glass beads at the ends. The reaction zone comprised of 1 g powder catalyst diluted with 7 g of 90–120 mesh SiC. Before introducing the syngas to the reactor, as a feed for FT reaction, in-situ reduction was carried out. To reduce the calcined catalysts, ultra-high purity (UHP) hydrogen was introduced at atmospheric pressure with 30 ml/min flow rate. The reactor temperature was increased with 1 ºC/min rate and maintained at 400 ºC for 18 h during the reduction. After the activation stage, the reactor temperature was ramped down to 180 ºC and the system was pressurized to 2.07 MPa with UHP helium. Then, the H_2 and He in-flow were closed, and the reactor inlet flow was switched to syngas, and the reactor temperature was slowly increased to the reaction temperature (220–240 ºC), at 0.5 ºC/min heating rate. The syngas was introduced at the space velocity of 900 h^{-1}. The composition of syngas was 30% CO, 10% Ar balanced with H_2. The outlet flowrate of the syngas and mass balance over the reaction was estimated using argon as a tie component. To regulate the flow rate of entering gases (hydrogen and syngas) to desired values, Brooks mass flow controllers (model 5850E) were utilized. To achieve the desired reaction temperature a PID controller was employed. The reaction system was left for 8–12 h of operation to be stabilized before starting data acquisition [100,155].

The C_{5+} hydrocarbons (HCs) including C_{22+} waxes were collected in a hot trap at 80 ºC. The remaining gaseous products entered into cold condenser set at 0 ºC to collect the water and part of light hydrocarbons. The residual gases (CO, CO_2, C_1–C_4, Ar) were introduced to an online gas chromatograph (Shimadzu GC–2014) instrument to analyze the mixture composition [69,77,157]. Liquid products were separately distilled and analyzed in an off-line GC instrument. Catalytic performance of the catalysts was examined at every 8 h intermittent for 80-150 h time-on-stream.

6.3.6 Experimental design for optimization of operational conditions

Minitab 17 software was used to determine the design of experiments and preliminary screening of the operational conditions for the mesoporous alumina supported cobalt catalysts in this study: 15Co(A)/m-Al_2O_3, 15Co(E)/m-Al_2O_3, and 15Co(W)/m-Al_2O_3. The impact of input variables namely pressure (P), temperature (T) and gas hourly space velocity (GHSV) on out variables (responses) of CO conversion and selectivity was investigated. Taguchi method with 3 factors at 3 levels (two degrees of freedom) was used to design the experiments (see Table E.2 in Appendix E). Nine different experiments based on the Taguchi design were performed for each catalyst. The chosen three levels for T were 220, 230 and 240 °C; for P were 1.38, 2.07 and 2.76 MPa; and for GHSV were 600, 900 and 1200 h^{-1}.

6.4 Result and discussion

6.4.1 Characterization

Textural properties of synthesized mesoporous alumina, γ-Al_2O_3, and their corresponding cobalt-based catalysts are given in Table 6.1. If only the support texture contributes to the measured surface area, after loading 15 wt. % cobalt, which is equivalent of ~ 20 wt. % of Co_3O_4, the resultant calcined catalysts are expected to possess ~ 80% of the pristine alumina surface area if the structural deformation and pore blockage are not significant. After preparing of the 15Co(A)/m-Al_2O_3 and 15Co(E)/m-Al_2O_3 catalysts, the specific surface area of the support decreased by 18.8 and 16.6%, from 410 to 342 and 333 m^2/g, respectively, which is close to theoretical prediction. Besides, during the cobalt impregnation the pore volume of mesoporous alumina drops from 1.6 cm^3/g to ~ 1.3 cm^3/g. This is due to the partial filling of the pores with impregnated cobalt species. The pore diameter was observed to slightly drop from 11.8 to ~ 11.3 nm for catalysts prepared by ethanol and acetone solvents, respectively, whereas using water as solvent in preparation of 15Co(W)/m-Al_2O_3 catalyst significantly reduced the textural property of the support. The surface area underwent 30% decrease from 410 to 287 m^2/g indicating of substantial decline in the porosity. Furthermore, the pore volume decreased from 1.6 to 0.5 cm^3/g, and pore diameter from

11.8 to 5.3 nm. These imply that the synthesized mesoporous alumina material is vulnerable to structural alteration in the presence of water solvent, which shows better stability with organic solvents. This fact has also been evidenced by distortion in the hysteresis of nitrogen adsorption–desorption isotherm for the 15Co(W)/m-Al_2O_3 catalyst as shown in Figure 6.1. The distinct loss in texture of support material during the impregnation can be ascribed to rehydroxylation or hydrolysis of Al_2O_3 while interacting with H_2O [216]. It might be also attributed to partial particle sintering and amorphous phase formation of alumina while exposed to aqueous solutions [217,218]. A few other studies have also observed similar instability of mesoporous alumina during wet impregnation with aqueous solutions [196,219].

Table 6.1 Textural properties of synthesized m-Al_2O_3 and corresponding Co catalysts prepared with different solvents and Co loadings

Catalyst/Support	BET surface area[a] (m^2/g)	Pore vol.[b] (cm^3/g)	Pore dia.[c] (nm)
m-Al_2O_3	410	1.6	11.8
γ-Al_2O_3	282	0.79	7.7
15Co/γ-Al_2O_3	221	0.57	7.5
15Co(W)/m-Al_2O_3	287	0.51	5.3
15Co(A)/m-Al_2O_3	342	1.35	11.3
15Co(E)/m-Al_2O_3	333	1.30	11.4
22.5Co(E)/m-Al_2O_3	301	1.15	11.6
30Co(E)/m-Al_2O_3	274	1.03	11.0

[a.] BET (error: 3%)
[b.] BJH desorption (error: 2.5%)
[c.] BJH desorption (error: 1.5%)

Increasing the cobalt loadings to 22.5 and 30 wt. % in the catalyst prepared using ethanol as solvent decreases the surface area to 301 and 274 m^2/g, and pore volume to 1.15 and 1.03 cm^3/g, respectively. This verifies that the synthesized mesoporous alumina can still be stable in higher content of the cobalt loadings.

All the samples reveal the typical type-IV(a) adsorption isotherms, suggesting the meso-structure, and occurrence of capillary condensation in the pores' cavity and aggregated inter-particle spaces [125,220]. The capillary condensation occurs due to irreversibility between adsorption and desorption of liquid nitrogen on pore walls [221]. This finding corroborates XRD and HRTEM analyses results, which is discussed later in this paper.

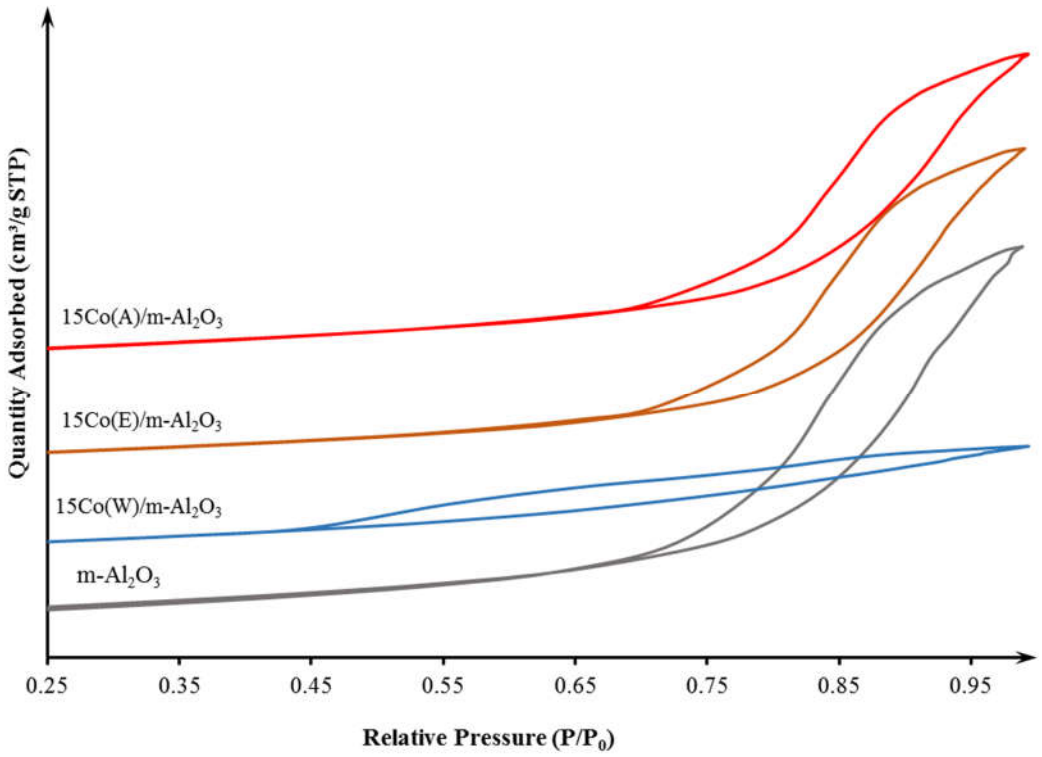

Figure 6.1 Nitrogen adsorption-desorption isotherms of mesoporous alumina, and corresponding prepared Co catalysts using different solvents

The isotherms for mesoporous alumina and catalysts 15Co(A)/m-Al_2O_3 and 15Co(E)/m-Al_2O_3 exhibits the same sized H1 & H3 composite hysteresis loop at higher relative pressure, implying the slit-shape pores or plate-like particles [125,220]. The hysteresis loop for 15Co(W)/m-Al_2O_3 catalyst is apparently H3 & H4 composite type with noticeable uptake at lower relative pressure of 0.45. This might be associated with filling of micropores or aggregated meso-pores generated during the collapse and dissolution of γ-alumina in the water. There is proportional correlation between N_2 Adsorption capacity and pore volume [220]. For the synthesized alumina and corresponding cobalt catalysts prepared by organic solvents, N_2 uptake was in the range of 800–1000 cm^3/g STP, whereas, for the cobalt catalyst prepared with water solvent, it was ~ 330 cm^3/g STP.

The pore size distribution (PSD) curves of all samples are shown in Fiure 6.2. The results for average pore size and specific pore volume were determined using the Barrett-Joyner-Halenda (BJH) desorption method, as shown in Table 6.1.

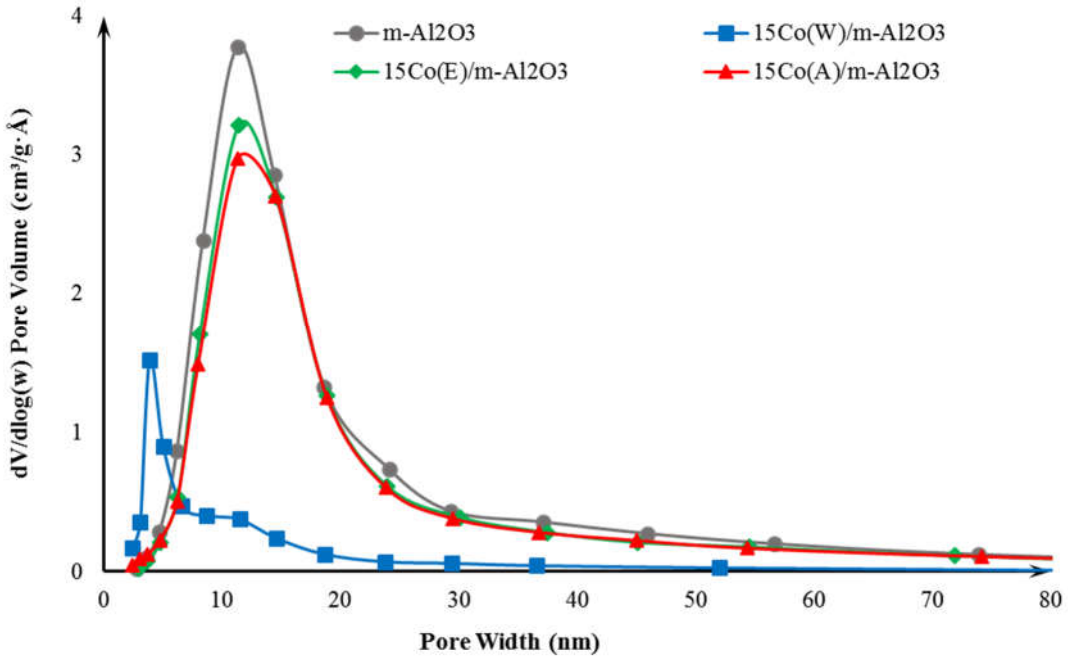

Figure 6.2 Pore size distribution of mesoporous alumina, and corresponding prepared Co catalysts using different solvents

The broad range of pore distribution for 15Co(A)/m-Al_2O_3 and 15Co(E)/m-Al_2O_3 catalysts (~ 2–30 nm) can be attributed to disordered structure of mesoporous alumina, and the irregular shapes of inter-crystallite voids which are randomly stacked, while the PSD for 15Co(W)/m-Al_2O_3 catalyst became narrower (~ 2–10 nm) after agglomeration of loosely piled nanoparticles [222,223] or possible collapse in some pore walls after interacting with water. However, the synthesized mesoporous alumina and corresponding cobalt catalysts exhibited mono-modal pore distributions.

Dispersion of cobalt based on the total cobalt content (D%) in the Co/Al_2O_3 catalysts was obtained through H_2 chemisorption analysis and it was corrected ($D_{corr.}$ %) considering the extent of reduction of the cobalt oxides (see Table 6.2). The degree of reduction (DOR) for each catalyst was estimated based upon the ratio of consumed H_2 during the TPR analysis over the stoichiometric H_2 required to reduce all Co_3O_4 molecules to Co^0 atoms.

Despite the fact that 15Co(W)/m-Al_2O_3 catalyst showed 4-7% higher reducibility as compared to 15Co(A)/Al_2O_3 and 15Co(E)/m-Al_2O_3, it resulted in lower cobalt dispersion of 6.1%, as compared to 7.1 and 7.9%, shown by 15Co(A)/Al_2O_3 and 15Co(E)/m-Al_2O_3 catalysts, respectively.

Different interaction of organic and aqueous solutions with the mesoporous alumina surface during the catalyst preparation steps resulted in distinct catalyst textures, which in turn led to different cobalt interaction and dispersion on the surface. The high corrected Co dispersion of 7.9 and 7.1 % were achieved by 15Co(E)/m-Al_2O_3 and 15Co(A)/m-Al_2O_3 catalysts, respectively, and the lowest 6.1 % was acquired in the series by 15Co(W)/m-Al_2O_3. The higher dispersion of the former catalysts could be associated with limited dissolution of alumina and textural distortion in presence of organic solvents during the catalyst preparation. The interaction of cobalt cations in organic and aqueous solvents with different alumina active sites and hydroxyl groups on the surface have not comprehensively been discussed in the literature [224].

Table 6.2 Co dispersion, degree of reduction, and crystallite size of Co/m-Al_2O_3 prepared with different solvents and Co loadings

Catalyst/Support	**$D_{tot.}$ (%)[a]**	**DOR (%)[b]**	**$D_{corr.}$ (%)[c]**	**$d_{Chem}^{Co^0}$ (nm)[d]**	**$d_{XRD}^{Co_3O_4}$ (nm)[e]**
15Co(W)/m-Al_2O_3	4.1	67.6	6.1	15.8	13.1
15Co(E)/m-Al_2O_3	4.8	60.8	7.9	12.2	10.5
15Co(A)/m-Al_2O_3	4.5	63.6	7.1	13.6	12.2
15Co/γ-Al_2O_3	3.8	60.0	6.5	14.8	10.1
22.5Co(E)/m-Al_2O_3	5.2	68.9	7.5	12.7	11.7
30Co(E)/m-Al_2O_3	5.7	79.7	7.2	13.4	13.1

[a] Dispersion of total cobalt atoms; from H_2 chemisorption (error: 1.5%)
[b] Degree of reduction (error: 2%)
[c] Corrected dispersion based on the reduced cobalt atoms
[d] $d_{chem.}^{Co^0} = \frac{96}{D_{corr.}\%}$
[e] $d_{XRD}^{Co^0} = 0.75 \times d_{XRD}^{Co_3O_4}$; (error: 1.3%)

Doubling the cobalt loading from 15 to 30 wt. % increased the reducibility from 60.8 to 79.7 % whereas the corrected cobalt dispersion dropped from 7.9 to 7.2 %, respectively. This can be ascribed to bigger clusters of cobalt species and their less interaction with support surface.

Figure 6.3 shows the TPR patterns and reducibility of the calcined catalysts. Reduction temperature of the catalysts could be correlated with cobalt oxide crystallite size, and its interaction with alumina support [46,169]. Generally, TPR spectra for supported cobalt based catalyst exhibits two predominant peaks, the first one appears in temperature range of 250–300 ºC and the second peak at 300–500 ºC limit, ascribing to two-stage reduction of $Co_3O_4 \longrightarrow CoO \longrightarrow Co^0$, respectively [5,166,225]. In this study, TPR

patterns of all catalysts comprise of two peaks: the low temperature reduction of 15Co(X)/m-Al_2O_3 series and 15Co(E)/γ-Al_2O_3 extend between 260 ºC and 330 ºC, the high temperature peak appears in the broad range of 320–620 ºC. For 22.5Co(E)/m-Al_2O_3 and 30Co(E)/m-Al_2O_3 catalysts the Co_3O_4 to CoO reduction stage starts even at lower temperature of 230 ºC. This could be attributed to possible uncalcined cobalt nitrate decomposition and larger Co_3O_4 cluster reduction. The extension of CoO to Co^0 reduction stage from ~ 320 to ~ 620 ºC can be associated with wide size range of cobalt species and their different metal-support interaction. Small cobalt oxides, and Co atoms that dissolve in alumina lattice forming cobalt aluminate species can strongly bound with support and turn into hardly reducible species [5,166,225].

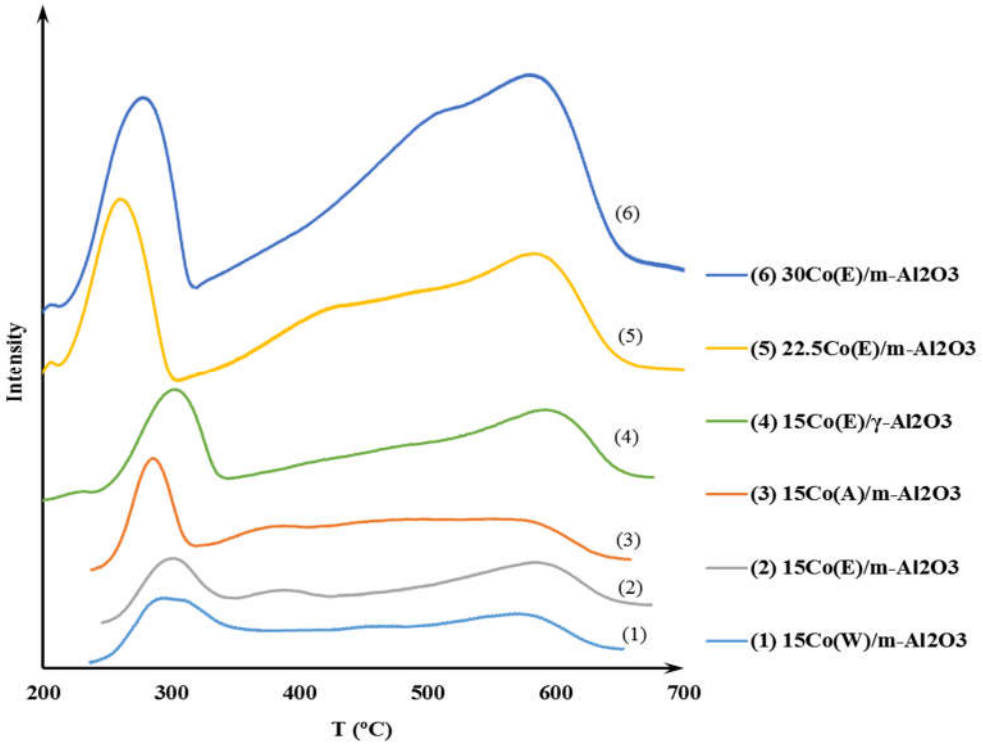

Figure 6.3 Temperature-programmed reduction profile for mesoporous alumina supported Co catalysts prepared by different solvents and varied cobalt loadings

According to the first peaks maxima in TPR profile, the reduction temperature for 15Co(A)/m-Al_2O_3, 15Co(E)/m-Al_2O_3, and 15Co(W)/m-Al_2O_3 catalysts appeared as 286, 298, and 313 ºC, respectively. It was confirmed from N_2 adsorption, PSD, and XRD that the cobalt catalysts prepared by organic solvents exhibit quite similar characteristics. Slightly higher reduction temperature for alumina supported cobalt catalyst prepared by ethanol (15Co(E)/m-Al_2O_3) as compared to the catalyst prepared by acetone

(15Co(A)/m-Al_2O_3) can be assigned to its higher dispersion, and smaller crystallite size of cobalt. However, higher reduction temperature of cobalt catalyst (15–27 ºC) prepared by aqueous solvent as compared to other two counterpart catalysts, could be explained by interaction of cobalt and alumina during the impregnation, drying, and calcination resulting in the formation of cobalt aluminate. Possible hydrolysis of mesoporous alumina with water during the catalyst preparation could facilitate the incorporation of Co^{3+} in Al^{3+} matrix and results in formation of cobalt aluminate compound, which reduces at high temperature [5,169,216,226].

Figure 6.4 demonstrates wide-angle XRD patterns of the synthesized mesoporous alumina and corresponding calcined catalysts prepared with organic and aqueous solvents. Different diffraction peaks for the γ-Al_2O_3 and Co_3O_4 phases appeared. The peaks at 2θ of 37º, 39º, 46º, and 66º of the support material, represent the cubic structures (311), (222), (400), and (440) planes' reflection, respectively [227,228]. Guzman-Castillo et al. [229] reported that the transition from bohemite to γ-Al_2O_3 occurs in the range of 380–580 °C during the calcination, however, possible presence of unchanged bohemite phase has appeared at 2θ of 28–30º. Moreover, the γ-alumina has been described as a defect spinel structure that can be characterized by oxygen atoms in cubic closed-packed sites, with tetrahedrally and octahedrally coordinated aluminum cations in the lattice [216,228]. The relatively broad peaks could be a result of highly disordered structure of alumina platelets forming the pores [5,220,228].

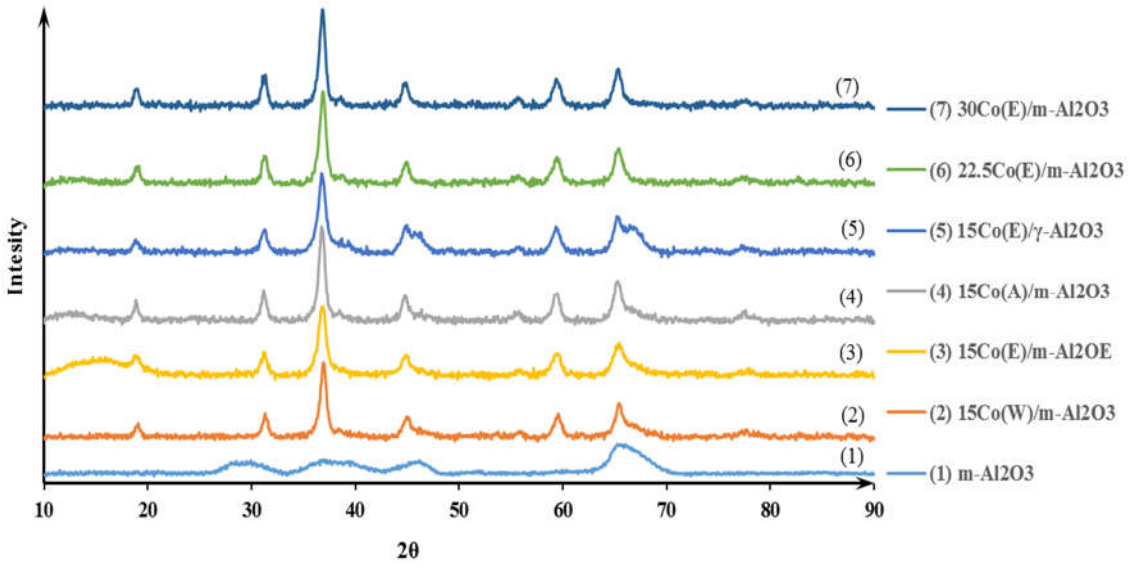

Figure 6.4 XRD patterns for mesoporous alumina, yCo(X)/m-Al_2O_3, and 15Co(E)/γ-Al_2O_3 catalysts using different solvents and varying cobalt loading

As in the catalyst diffractograms, the peaks appeared at 2θ of 19.0º, 31.5º, 36.8º, 38º, 45º, 59.6º, 65.5º are related to different crystallite planes of Co_3O_4 [212]. According to the XRD patterns, the catalysts did not show the CoO peaks appear at 42.7º and 61.9º, therefore, Co_3O_4 species seem to be the only crystallite phase of cobalt oxide in the calcined catalysts supported by mesoporous Al_2O_3 [230]. Also, all peaks representing γ-Al_2O_3 phase either disappeared or overlapped with cobalt oxide peaks in XRD patterns of all catalysts. Scherrer equation was used to calculate the volumetric average crystallite size at 2θ = 36.8º as a main intense peak signifying the (311) face of Co_3O_4 crystallites in alumina supported cobalt catalyst. It is noteworthy that the crystallite size was estimated using FWHM for β (angular breadth). Catalysts prepared with organic solvents resulted in smaller cobalt crystallites as supported by H_2 chemisorption analysis (Table 6.2). The 15Co(E)/Al_2O_3, 15Co(A)/Al_2O_3 catalysts showed crystallite size of 10.5, and 12.2 nm, respectively, as compared to 13.1 nm shown by 15Co(W)/Al_2O_3-W catalyst. Considering the average pore diameter of 5.3 nm in 15Co(W)/m-Al_2O_3 catalyst and the average Co_3O_4 crystallites size of 13.1 nm, cobalt oxides in the catalyst must be deposited mostly in the outside of the pores.

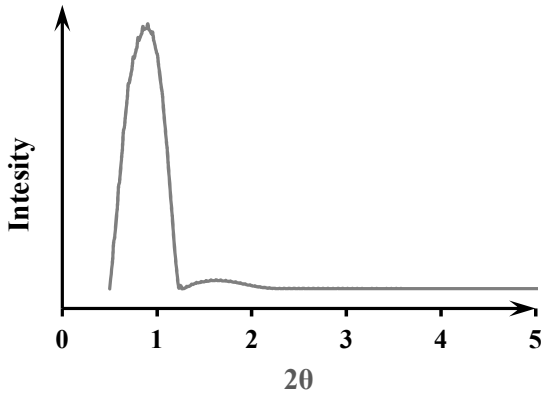

Figure 6.5 Typical low-angle XRD pattern for mesoporous alumina and yCo(X)/m-Al_2O_3 catalysts prepared by different organic and aqueous solvents

Low angle XRD analysis exhibited similar peaks for mesoporous alumina and the corresponding catalyst samples. A typical diffraction shown in Figure 6.5 exhibits one intense peak at 1º, and one weak but broad peak at 1.7º. The first peak could correspond to (100) plane scattering, and the second peak would be overlapped reflection of (110) and (200) planes of 2-d hexagonal space group (p6mm). These signify the presence of ordered meso-structure in synthesized alumina and alumina supported cobalt catalysts prepared by ethanol, acetone, and water solvents [213,231]. Due to the presence of water during the alumina synthesis procedure (H_2O:Al = 4), partial disorder in the structure of mesoporous alumina and

supported cobalt catalysts are expected [196]. The inter-lattice distance between (100) planes (d_{100}) of 15.7 nm was calculated using the Bragg equation.

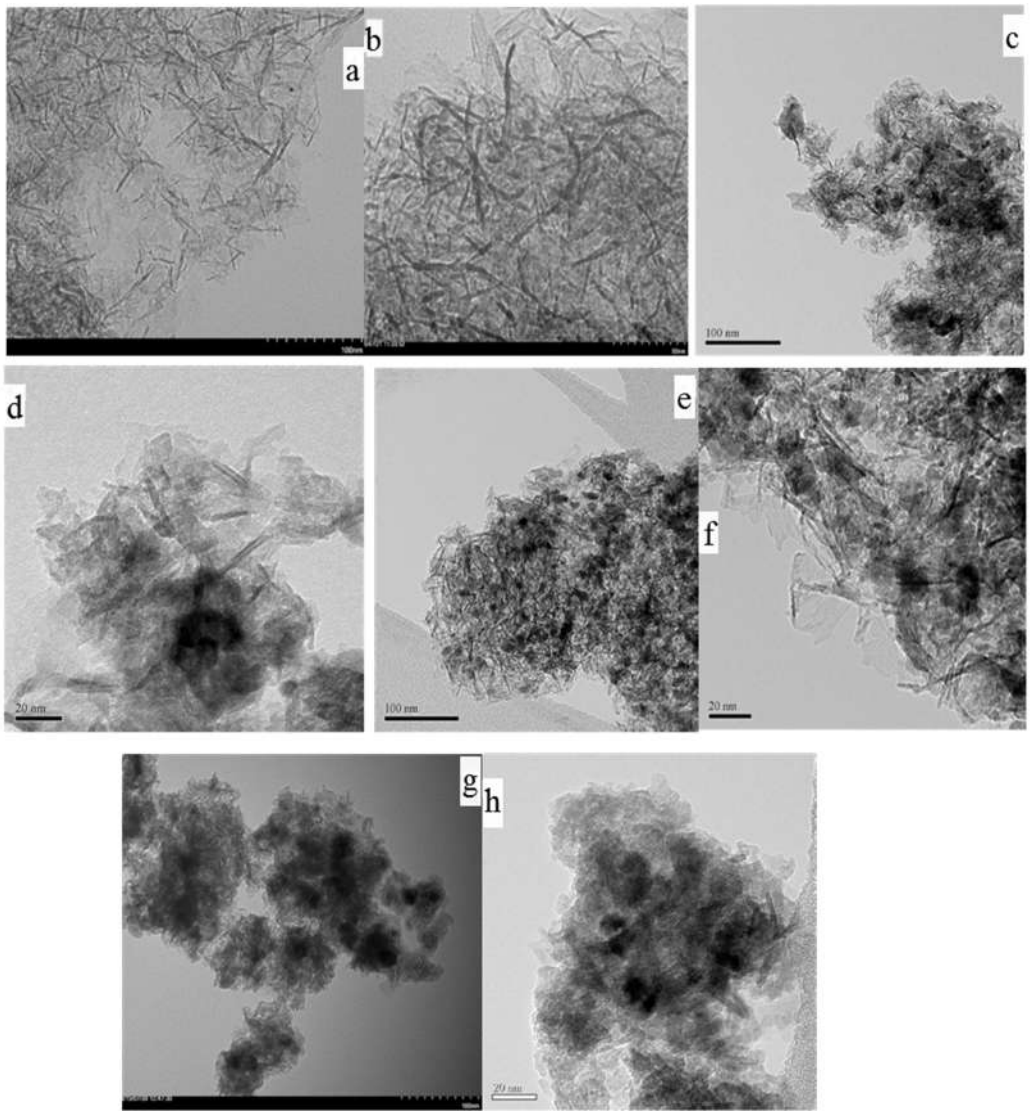

Figure 6.6 HRTEM images of (a,b) synthesized mesoporous Al_2O_3, and (c,d) 15Co(A)/m-Al_2O_3, (e,f) 15Co(E)/m-Al_2O_3, (g,h) 15Co(W)/m-Al_2O_3 catalysts

The HRTEM images of mesoporous Al_2O_3, and corresponding cobalt catalysts prepared by organic and aqueous solutions are demonstrated in Figure 6.6. To illustrate more detailed morphology of the surface, two different magnifications from each sample have been shown. The platelet and slit-like nature of the synthesized mesoporous alumina are visible in these micrographs. According to the HRTEM images, the catalysts prepared with organic solvents confirm well dispersion of cobalt on the surface. It is apparent from micrographs that 15Co(A)/m-Al_2O_3, 15Co(E)/m-Al_2O_3 catalysts retain support's initial structure to

the most part as compared to distorted alumina structure in 15Co(W)/m-Al_2O_3 catalyst. As shown in Figures 6.6g and 6.6h, the slit-like or lath-like shape of the alumina support has deformed to higher degree in 15Co(W)/m-Al_2O_3 catalyst which corroborates the decline in textural properties of BET and hysteresis deformation of N_2 adsorption-desorption analysis.

6.4.2 Fischer–Tropsch synthesis

The Fischer–Tropsch reactions employing the alumina supported cobalt catalysts were carried out in a fixed bed reactor. The H_2/CO ratio of 2.0 was used and the reactions were performed at 230 °C, 2.76 MPa and 900 h^{-1} gas hourly space velocity (GHSV). To obtain the CO_2, CH_4, C_2–C_4, C_{5+} selectivities, all the catalysts were examined at similar CO conversion of ~ 50 % and 230 °C, 2.76 MPa conditions. As shown in Table 6.3, activity and selectivities of the catalysts have been reported in 100–150 h time-on-stream (TOS) after reaching a steady-state condition. The performance for γ-Al_2O_3 supported cobalt catalyst is also presented for comparison with those of mesoporous alumina supported catalysts.

Table 6.3 FTS activity of the Co/m-Al_2O_3 catalysts prepared by different solvents and loadings at 900 h^{-1}, and their selectivities at 50 % CO conversion (230 ˚C and 2.76 MPa)

Catalyst	TOS (h)	GHSV (h^{-1})	CO Conversion (%)	Yield ($g_{HC} \cdot g_{cat}^{-1} \cdot h^{-1}$)	Selectivity (%)			
					CO_2	CH_4	C_2-C_4	C_{5+}
15Co(E)/m-Al_2O_3	100	900	61.3	0.186	2.9	14.4	2.8	82.8
	115	1190	50.8	0.214	2.5	15.1	3.0	81.9
15Co(A)/m-Al_2O_3	100	900	57.6	0.179	2.5	15.2	3.2	81.6
	120	1150	50.5	0.184	2.3	15.9	3.1	81.0
15Co(W)/m-Al_2O_3	100	900	39.3	0.113	2.0	13.7	1.7	84.6
	120	505	49.3	0.093	2.7	12.3	2.2	85.5
15Co/γ-Al_2O_3	120	900	53.0	0.153	1.5	16.7	3.9	79.4
	135	1000	49.5	0.156	1.4	17.0	4.0	79.0
22.5Co(E)/m-Al_2O_3	100	900	65.5	0.202	3.1	14.2	2.7	83.0
	115	1510	50.7	0.241	2.0	12.8	3.1	84.1
30Co(E)/m-Al_2O_3	120	900	74.5	0.228	3.6	13.2	2.9	83.9
	150	1720	50.3	0.284	1.5	10.4	3.4	86.2

The mesoporous alumina supported cobalt catalyst prepared by ethanol shows the highest CO conversion of 61.3% and hydrocarbon productivity of 0.186 $g_{HC}.g^{-1}_{cat}.h^{-1}$ among the 15Co(X)/m-Al_2O_3 and 15Co(E)/γ-Al_2O_3 series. The CO conversion and hydrocarbon yield shown by 15Co(E)/m-Al_2O_3 catalyst are 8.3% and 21%, respectively, higher as compared to that shown by commercial γ-Al_2O_3 catalyst. Moreover, 15Co(E)/m-Al_2O_3 catalyst exhibited 3.7%, and 25% higher CO conversion activity as compared to 15Co(A)/m-Al_2O_3 and 15Co(W)/m-Al_2O_3 catalysts, respectively. This confirms that the stable mesoporous alumina supported catalyst (15Co(E)/m-Al_2O_3) exhibits higher FT performance as compared to γ-alumina supported cobalt catalyst.

Increasing the cobalt loading by 50 and 100 % (from 15 to 22.5 % and 30 wt. %, respectively), improved the CO conversion from 61.3 to 65 % and 74.5 %, in addition, the HC yield from 0.186 to 0.202 and 0.228 $g_{HC}.g^{-1}_{cat}.h^{-1}$, respectively.

According to the findings of Iglesia and coworker [19,37], cobalt site-time-yield (STY) is independent of the relatively large crystallites. The intrinsic activity (TOF) for the catalysts were in the range of 1.6 $\times10^{-2}$ – 2.4 $\times10^{-2}$ s^{-1}, which unveils the structural-insensitivity of cobalt crystallite in FT reaction [232]. Further, to evaluate the importance of internal diffusion as rate-limiting steps in the pores, Weisz–Prater criterion were applied:

$$C_{WP} = \frac{-r'_A(obs).\rho_c.R^2}{D_e.C_{A,s}} = \frac{\text{Chemical reaction rate}}{\text{Molecular diffusion rate}} \quad (6.5)$$

Substituting the values for reaction rate $[-r'_A(obs)]$, catalyst density (ρ_c), catalyst particle radius (R), effective diffusivity (D_e), and concentration $(C_{A,s})$ revealed $C_{WP} \ll 1$ which can be translated into kinetics as controlling step of FT reaction rate for these catalysts [205].

All 15Co(X)/m-Al_2O_3 catalysts exhibited higher C_{5+} and lower CH_4 selectivities as compared to γ-alumina supported cobalt catalyst. Moreover, cobalt loading showed positive impact on increasing C_{5+} and lowering CH_4 selectivities. Higher cobalt loading of 30 wt. % happened to produce the lowest CH_4 (10.4 %) and highest C_{5+} (86.2 %) selectivities. This can be attributed to higher CO hydrogenation activity (74.5 %) of 30Co(E)/m-Al_2O_3 catalyst as compared to the rest of catalysts in the series [47]. The carbon dioxide and methane selectivity in this work, as the least undesired products, were in the range of 1.4–2.7 % and 12.3–17 %, respectively, for 15Co(X)/m-Al_2O_3 and 15Co(E)/γ-Al_2O_3 catalysts at 230 °C

and 50 % CO conversion. However, at lower reaction temperature the carbon dioxide and methane selectivity declined. For example, the CO_2 and CH_4 selectivity in the mentioned condition for 15Co(E)/m-Al_2O_3 catalyst are 2.5 % and 15.1 %, respectively. Nonetheless, the selectivity drops to 2.0% and 7.8% for CO_2 and CH_4, respectively, at 1.38 MPa, 220 °C, GHSV = 600 h^{-1}. It has also been reported in literature that above 225 °C, the CH_4 selectivity of Co catalyst in FTS considerably increase from ~ 8 % to ~ 16 % [233]. For further comparison, the methane and CO_2 selectivity of other research works on cobalt catalyst are presented in Appendix E (see Table E.1, [72, 234–237]).

As reported in the literature [233], the linearity between C_1 and C_{5+} selectivities in FTS were observed for alumina supported cobalt catalysts $\left(S_{C_{5+}}\% = 97.3 - 1.02S_{CH_4}\%;\ R^2 = 0.97\right)$. As it is known: $S_{C_{5+}} = 1 - \left(S_{C_1} + S_{C_{2-4}}\right)$, then the maximum selectivity for long chain HCs will be achieved when the methane and other light HCs are at their minimum. It is hard to directly correlate the slightly higher C_{5+} selectivity of 15Co(W)/m-Al_2O_3 catalyst in 15Co(X)/m-Al_2O_3 and 15Co(E)/γ-Al_2O_3 series to its higher crystallite size, however it might be associated with different active sites and rate limiting elementary reactions on the surface [41].

Comparison of the physico-chemical characteristic data of mesoporous alumina supported cobalt catalysts, prepared by organic and aqueous solvents, provides the evidence to explain the similarity of 15Co(A)/m-Al_2O_3 and 15Co(E)/m-Al_2O_3 catalysts and their better performance as compared to 15Co(W)/m-Al_2O_3 catalyst. The latter showed instability in mesoporous alumina structure during the cobalt impregnation, which resulted in higher cobalt crystallite size, lower cobalt dispersion, consequently limited active sites for CO hydrogenation [232]. As a result, activity of 15Co(W)/m-Al_2O_3 catalyst in terms of CO conversion, as well HC yield was considerably lower than its counterpart catalysts prepared by organic solvents. Despite the fact that the average pore size, crystallite size, dispersion and reducibility of the 15Co(W)/m-Al_2O_3 catalyst were considerably different from its counterparts, the difference in C_{5+} selectivity was not significant and light hydrocarbon selectivity was close in the range of 2.3–4%. It is noteworthy that 15Co(E)/m-Al_2O_3 catalyst slightly outperformed 15Co(A)/m-Al_2O_3 catalyst in terms of activity, which can be justified possessing higher dispersion and more number of active sites for CO hydrogenation.

6.4.3 Optimization studies

For mesoporous alumina supported Co catalysts, the interactions of process parameters including, temperature pressure and GHSV and their effect on CO conversion and C_{5+} selectivity were studied using

Taguchi L9 (3×3) orthogonal array matrix. The Taguchi design of experiment (DOE) for three levels of temperatures (220, 230 and 240 °C), pressures (1.38, 2.07 and 2.76 MPa), and GHSVs (600, 900 and 1200 h^{-1}) was developed based on factorial design using MiniTab 17 (see Table 6.5). The experiments were conducted based on the Taguchi design to determine the optimized CO conversion and C_{5+} selectivity and the results for 15Co(E)/m-Al_2O_3 catalyst are shown in Table 6.4. The results were statistically analyzed to specify the significance of input variables on responses using analysis of variance (ANOVA). Consequently, the DOE led to preliminary screening of process conditions for optimum catalyst performance of the synthesized catalysts. The Taguchi analysis for 15Co(E)/m-Al_2O_3 is shown here and the analysis for 15Co(A)/m-Al_2O_3 and 15Co(W)/m-Al_2O_3 are presented in Appendix E (See Tables E.2 to E.7 and Figures E.1 to E.4). The effect of individual process parameter on CO conversion and C_{5+} selectivity is determined from main effect plots for means, which were created using MiniTab 17 software. It was observed from Figure 6.7 that with increase in temperature the CO conversion increases and does vice versa with GHSV. Their simultaneous effects might be canceled out relatively.

Table 6.4 Experimental design, CO conversion and C_{5+} selectivity for 15Co(E)/m-Al_2O_3 catalyst

Temperature (°C)	Pressure (MPa)	GHSV (h^{-1})	CO Conversion (%)	C_{5+}Selectivity (%)
220	1.38	600	51	85.2
220	2.07	900	47	85
220	2.76	1200	42	84.6
230	1.38	900	61	82.6
230	2.07	1200	58	82.3
230	2.76	600	68	83.4
240	1.38	1200	70	79.5
240	2.07	600	77	80.3
240	2.76	900	73	80.6

Pressure change has no significant effect on CO conversion, however, the C_{5+} selectivity increases with increase in pressure (see Figures 6.7 and 6.8). Also, with increase in temperature, C_{5+} selectivity decreases (see Figure 6.8).

Table 6.5 ANOVA data on CO conversion for 15Co(E)/m-Al_2O_3 catalyst

Source	DF	Adj. SS	Adj. MS	F-Value	P-Value
Temperature	2	1077.56	538.778	255.21	0.004
Pressure	2	0.22	0.111	0.05	0.95
GHSV	2	113.56	56.778	26.89	0.036
Residual	2	4.22	2.111		
Total	8	1195.56			

Table 6.6 ANOVA data on C_{5+} selectivity for 15Co(E)/m-Al_2O_3 catalyst

Source	DF	Adj. SS	Adj. MS	F-Value	P-Value
Temperature	2	34.6689	17.3344	557.18	0.002
Pressure	2	0.3089	0.1544	4.96	0.168
GHSV	2	1.1089	0.5544	17.82	0.053
Residual	2	0.0622	0.0311		
Total	8	36.1489			

The ANOVA analysis for the design of experiments for CO conversion and C_{5+} selectivity is presented in Tables 6.5 and 6.6. The P-value less than 0.05 indicates the 95 % confidence to reject the null hypothesis (that the process parameters such as temperature, pressure and GHSV have no influence on CO conversion and C_{5+} selectivity). It is shown in Table 6.5 that the P-value for temperature and GSHV is less than 0.05, indicating that these both parameters have significant effect on CO conversion and the effect of temperature was more dominant. The P-values of ANOVA analysis for C_{5+} selectivity are 0.002, 0.168, and 0.053 for temperature, pressure, and GHSV, respectively. This also indicates that comparatively the temperature has major effect on C_{5+} selectivity.

In order to determine the optimum operating conditions, the interaction between parameters is studied. As observed, the FT reaction at 240 °C gives higher CO conversion and lower C_{5+} selectivity as compared to reaction at 230 °C, however, operating at high temperature compromises the catalyst life. The lower GHSV gives higher conversion, however, this would result in lower production rates. Therefore, the optimum operating conditions determined are 230 °C, 2.76 MPa (400 psi), and 900 h^{-1} for 15Co(X)/m-Al_2O_3 catalysts.

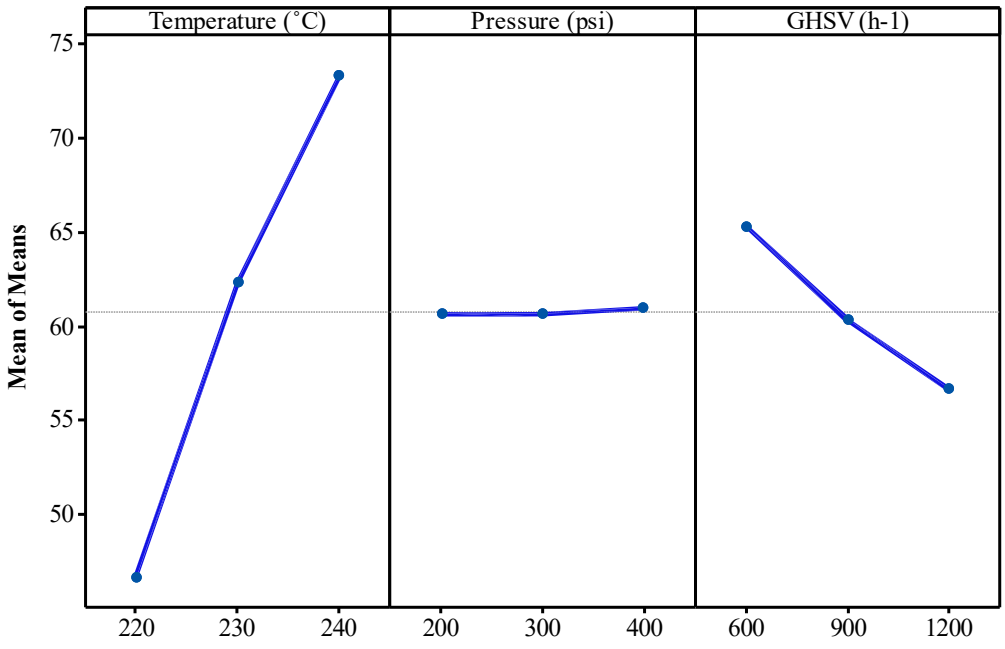

Figure 6.7 Main effect plot means of CO conversion (%) for 15Co(E)/m-Al_2O_3 catalyst

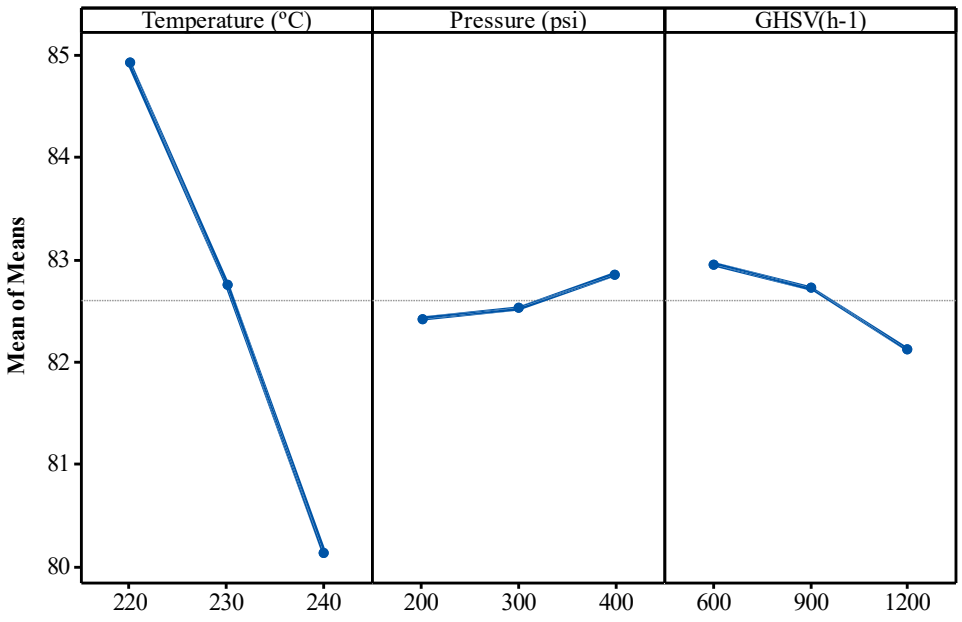

Figure 6.8 Main effect plot means of C_{5+} selectivity (%) for 15Co(E)/m-Al_2O_3 catalyst

Similarly, for catalysts 15Co(A)/m-Al_2O_3 and 15Co(W)/m-Al_2O_3, i.e., main effect plots for mean and ANOVA analysis were created, and it was observed that temperature has major effect on CO conversion

and C_{5+} selectivity (see Tables 6.5 and 6.6). The optimum operating conditions for these two catalysts are similar to that for 15Co(E)/m-Al_2O_3 catalyst.

Based on the design of experiments the linear regression model was developed (equations 6.6 to 6.11) to determine the CO conversion and C_{5+} selectivity for process parameters in the range of 220–240 °C, 1.38–2.76 MPa (200-400 psi) and 600–1200 h^{-1}.

For Catalyst 15Co(E)/m-Al_2O_3:

$$\text{CO Conversion (\%)} = -233.4 + 1.3333\ T + 0.0017\ P - 0.0144\ GHSV\ ;\ R^2 = 0.97 \quad (6.6)$$

$$C_{5+}\ \text{Selectivity (\%)} = 138.4 - 0.2400T + 0.0022\ P - 0.0014\ GHSV\ ;\ R^2 = 0.98 \quad (6.7)$$

For Catalyst 15Co(A)/m-Al_2O_3:

$$\text{CO Conversion (\%)} = -275.5 + 1.5000\ T + 0.0033\ P - 0.0172\ GHSV\ ;\ R^2 = 0.98 \quad (6.8)$$

$$C_{5+}\ \text{Selectivity (\%)} = 135.1 - 0.2267\ T + 0.0010\ P - 0.0019\ GHSV\ ;\ R^2 = 0.98 \quad (6.9)$$

For Catalyst 15Co(W)/m-Al_2O_3:

$$\text{CO Conversion (\%)} = -238.2 + 1.2667\ T + 0.0050\ P - 0.0172\ GHSV\ ;\ R^2 = 0.99 \quad (6.10)$$

$$C_{5+}\ \text{Selectivity (\%)} = 141.3 - 0.2417\ T + 0.0012\ P - 0.0017\ GHSV\ ;\ R^2 = 0.99 \quad (6.11)$$

It should be noted that the values in the ANOVA Tables and equations 6.6 to 6.11 are calculated based on units °C, psi, and h^{-1} for T, P and GHSV, respectively.

There are still areas of improvement for mesoporous alumina supported catalyst including synthesis method, cobalt catalyst preparation, especially, solvent impact on the cobalt cation solvation. Robust experimental design also can be performed including extensive operational condition, feed composition, and cobalt loading to further improvement in optimization of the developed catalyst for Fischer-Tropsch reaction.

6.5 Conclusions

Substituting the ethanol and acetone as alternative solvents for water during the impregnation of cobalt, resolved the sensitivity and instability of the synthesized mesoporous alumina, which was otherwise observed during the metal impregnation using aqueous solvent. The prepared cobalt catalysts with

organic solvents exhibited well-retained textural properties of the alumina support as compared to the cobalt catalyst prepared by demineralized water as observed from BET and HRTEM analyses. Also, the performances of the 15Co(E)/m-Al_2O_3 and 15Co(A)/m-Al_2O_3 catalysts, as prepared by ethanol and acetone, respectively, in terms of CO conversion activity and productivity were considerably higher than those of 15Co(W)/m-Al_2O_3, corroborating with the cobalt dispersion, and crystallite size results obtained from H_2 chemisorption, TPR analysis, and XRD. Moreover, the mesoporous alumina supported cobalt catalyst prepared by ethanol showed 8.3% higher CO conversions, 18% higher HC yields, and 2.6% lower CH_4 selectivities as compared to that shown by the γ-Al_2O_3 supported cobalt catalyst. The synthesized mesoporous alumina with high surface area and large pores exhibited favorable qualities to be a promising support material for even higher loadings of cobalt catalyst. The corresponding catalysts also revealed an improved catalytic performance in FTS. For instance, increasing the cobalt loading from15 to 30 wt. % on the mesoposrous alumina, enhanced the selectivity of the desired C_{5+} hydrocarbons by 4.3% and suppressed the undesired methane selectivity by 4.8%.

CHAPTER 7: MESO-ALUMINA MOFIDICATION USING TRANSITION METALS AND CHELATING AGENTS

This chapter is under preparation to be sent for publication as research paper titled:

- V. Vosoughi1, A.K. Dalai, N. Abatzoglou, "Mesoporous alumina supported cobalt catalyst for Fischer-Tropsch synthesis: effects of support modification and cobalt chelation".

Contribution of the PhD candidate

The experimental design, methodology, support synthesis, catalyst preparation, characterizations, FT tests, compiling / interpretation of the results, and writing of this chapter were conducted by Vahid Vosoughi. This study and the writing was accomplished based upon the suggestions and supervision from Drs Ajay Dalai and Nicholas Abatzoglou.

Contribution of this chapter to the overall PhD research

In chapter 6, mesoporous alumina (m-Al_2O_3) with high surface area, large pore diameter and volume was successfully synthesized. Then the organic solvents namely ethanol was examined to stabilize its structure during the cobalt catalyst preparation with varying loadings. Testing the developed Co/m-Al_2O_3 catalyst in FTS exhibited promising activity and C_{5+} selectivity as compared to one prepared by commercial alumina support (Co/γ-Al_2O_3). In pursuit of further development for the Co/m-Al_2O_3 catalyst for FTS, this chapter provides the result of studies on the modification of the support (m-Al_2O_3) and the active metal (Co). The synthesized m-Al_2O_3 was modified with two loading levels of lanthanum and cerium, then the corresponding cobalt catalysts were prepared. Other series of modified cobalt catalysts were prepared using NTA and EDTA chelating agents. The corresponding catalyst were characterized and tested for the FT reaction under optimized operational conditions obtained from our earlier study in Chapter 6. The main objective was to examine further improvement of the performance of Co/m-Al_2O_3 catalyst in FTS by changing the interaction and dispersion of Co on the mesoporous alumina support.

7.1 Abstract

The mesoporous alumina (m-Al_2O_3) as support for the cobalt based catalyst was modified by cerium and lanthanum as transition metals. Ce and La were added on m-Al_2O_3 in two loading levels of 5 and 10 wt. % then dried and calcined before adding 15 wt. % Co. The corresponding catalysts were examined for Fischer-Tropsch synthesis at 230 ˚C, 2.76 MPa, and 900 h^{-1} syngas with $H_2/CO = 2$. The physico-

chemical properties of the corresponding catalysts and activity test showed that 5 wt. % La-modified Co/m-Al_2O_3 catalyst outperformed in the series. Further, within the preparation of Co/m-Al_2O_3 and Co/γ-Al_2O_3 catalysts NTA and EDTA as chelating agents were utilized to study their modifying impact on the properties of chelated catalysts, also the performance of catalysts in the FTS. The 15CoNTA/γ-Al_2O_3 showed higher dispersion (1 to 2.3 absolute percentage) and higher CO conversion (~ 8 to 20 absolute percentage) as compared to EDTA-chelated and m-Al_2O_3 supported counterpart catalysts.

7.1 Introduction

It is well-established that addition of second metals in a small quantity as promoters to Co supported catalysts can notably impact the Co-support interaction, CoO_x reducibility, thereby the catalyst performance in FT reaction. As mentioned in chapter 2 (section 2.7), noble metals, alkali/rare earth/transition metal oxides could play the role of promoter/modifier for Co based FT catalysts. Optimizing the interaction between cobalt species and the support, thus enhancing the reducibility of cobalt species could influence the number of Co^0 active sites, which increases the activity, selectivity and stability of the catalyst.

Modification of the support material could alter the surface properties in favour of suitable metal-support interaction (MSI). Zirconia modification of silica and alumina supports for Co based catalyst in FTS was examined and resulted in higher activity and selectivity towards higher hydrocarbons (HCs) [238,239]. Silica doped alumina with varying concentrations of SiO_2 was investigated to control the Lewis and Bronsted acid sites on the support for FTS Co catalyst. To stabilize titania and alumina as supports for cobalt in FTS, and prevent their dissolution in the slurry bed red reactor, silica modification of the supports was tested and reported to be successfully effective [224]. La_2O_3 and CeO_2 are well-known stabilizers for the alumina supported catalysts in high temperature reactions due to their capability to scavenge deposited carbons [240]. The promotional impact of La and Ce from rare earth metal group with different loadings on silica, titania and alumina supported cobalt catalysts for CO hydrogenation reaction have been studied by some other groups [241–243].

The presence of some of the organic compounds (e.g. glycine, citric acid, saccharose) or chelating agents (CAs) could result in formation of different complexes with Co that could impact the Co dispersion during the catalyst preparation. Using EDTA, NTA, and CyDTA (trans-1,2-diaminocyclohexane-N,N,N′,N′-tetra-acetic) as chelating agents with cobalt nitrate solution resulted in different complex formation constants. The Co/SiO_2 catalyst which was prepared using NTA with moderate complex formation constant (affinity to Co^{2+}) exhibited higher activity in FTS [244]. Donation of two or more

pairs of electrons on a CA to cobalt cations leads to formation of ligands (dentates) between them. The chelated cobalt nitrate complexes can uniformly decompose during the drying and calcination stages of catalyst preparation to release cobalt ions, which can favor the Co dispersion [245].

In this work, La and Ce with two loadings as modifiers was selected and the corresponding catalyst were tested in FTS. Further, in view of improving the cobalt dispersion and reducibility, NTA and EDTA chelating agents were also added in the solution of cobalt nitrate before impregnating on the mesoporous alumina support. Chelating effects of these additives on physico-chemical properties of the mesoporous alumina supported cobalt catalysts and their performance in FTS were examined and compared with chelated Co catalysts supported on γ-alumina as a comparison basis.

7.2 Experimental

7.2.1 Support and catalyst preparation

The similar method presented in experimental section of chapter 6 for synthesis of mesoporous alumina (m-Al_2O_3) support was utilized in this phase of work. Specific amounts of $La(NO_3)_3 \cdot 6H_2O$ and $Ce(NO_3)_3.6H_2O$ as precursors of La and Ce were dissolved in ethanol and the resulting solutions were first impregnated on the mesoporous alumina support. After drying and calcination lanthanum or cerium modified alumina supports were impregnated with $Co(NO_3)_3 \cdot 6H_2O$ solution followed by drying and calcination to obtain the 15Co-xCe/m-Al_2O_3 and 15Co-xLa/m-Al_2O_3 catalysts (x: 5, 10 wt. % equivalent to 16 and 30 % molar ratio of modifier to cobalt).

To prepare the chelated Co/m-Al_2O_3 catalysts, cobalt was loaded in two steps. The first 7.5 wt. % of Co dissolved in ethanol and impregnated on the support, dried at 60 ºC in the vacuum oven, then calcined at 400 ºC for 3 h. In the next step, additional 7.5 wt. % Co along with one of the chelating agents (CA/Co = 0.5 molar ratio) was dissolved in 28 % ammonia solution, then loaded, dried and calcined at the same conditions.

7.2.2 Characterization

Physico-chemical properties of the modified and chelated Co/m-Al_2O_3 catalysts were measured employing N_2 adsorption, H_2 Chemisorption, TPR, and XRD techniques, which were explained in chapters 6.

7.2.3 Activity test of the catalyst for the Fischer–Tropsch synthesis.

The catalysts were examined in fixed bed reactor for FTS with similar procedure for the loading, start-up, data acquisition as explained in chapter 6. Also, the optimized process conditions obtained in chapter 6 (230 ˚C, 2.76 MPa, and 900 h^{-1}) for the activity test were chosen in this work to run FT reactions. The selectivity data for the catalysts were collected at activity level of ~ 50% CO conversion in FTS.

7.4 Results and discussion

7.4.1 Characterization results

The textural properties of La- and Ce-modified supports, corresponding 15Co/m-Al_2O_3 catalysts, as well as chelated Co catalysts supported on both mesoporous and γ alumina supports are shown in Table 7.1. After modification of m-Al_2O_3 support with 5 and 10 wt. % Ce, 40–60 (m^2/g) and 0.1–0.24 (cm^3/g) decline in the surface area and pore volume took place, respectively. The textural properties of the mesoporous alumina support are provided in Chapter 6 (see Table 6.1).

Table 7.1 Textural properties of La/Ce–modified m-Al_2O_3, corresponding catalysts, and NTA/EDTA-chelated Co catalysts supported on m-Al_2O_3 and γ-Al_2O_3

Catalyst	BET surface area (m^2/g)	Pore vol. (cm^3/g)	Pore dia. (nm)
5Ce/m-Al_2O_3	373	1.50	11.7
10Ce/m-Al_2O_3	351	1.36	11.6
5La/m-Al_2O_3	365	1.43	11.7
10La/m-Al_2O_3	335	1.28	11.5
15Co5Ce/m-Al_2O_3	276	1.15	11.5
15Co10Ce/m-Al_2O_3	256	1.02	11.3
15Co5La/m-Al_2O_3	265	1.08	11.4
15Co10La/m-Al_2O_3	244	0.92	11.1
15CoEDTA/m-Al_2O_3	349	1.27	10.3
15CoNTA/m-Al_2O_3	333	1.21	10.7
15CoEDTA/γ-Al_2O_3	216	0.58	7.8
15CoNTA/γ-Al_2O_3	223	0.58	7.5

Modification with lanthanum exhibited slightly higher decline in the texture of the support and corresponding catalysts. Moreover, EDTA-chelated 15Co/m-Al_2O_3 catalyst also showed 15% decrease in the surface area (SA) and 33% decrease in the pore volume (PV) of the mesoporous alumina. The

decline in textural properties for the NTA-chelated 15Co/m-Al_2O_3 catalyst were ~ 18 % and ~ 24% for the SA and PV, respectively.

As discussed before in chapter 6, the fraction of surface cobalt out of total loaded cobalt ($D_{total\ Co}$ % = D %) was obtained using H_2 chemisorption analysis assuming H/Co stochiometric ratio of 1. The fraction of surface Co out of the reduced cobalt atoms ($D_{reduced\ Co}$ % = $D_{corr.}$ %) were also obtained after correcting the apparent Co dispersion (D%). These can be estimated by dividing the dispersion over degree of reduction (DOR). Using the H_2 uptake from TPR analysis and diving by the stoichiometric H_2 required to reduce the total content of Co would result in the DOR. As shown in Table 7.2, increasing the loadings of La and Ce as a support modifier, from 5 to 10 wt. %, resulted in small decreases in apparent dispersion and the degree of reduction of the relating catalysts. If these results are compared with dispersion and reducibility of unmodified 15Co/m-Al_2O_3 (4.8% and 60.8%, respectively as shown in Table 6.2), it can be concluded that except the 15Co5La/m-Al_2O_3 catalyst, others in the series exhibited slightly lower dispersion and less reducibility. This can be attributed to interaction of La and Ce with Co in higher loadings of the modifiers (> 0.1) which could negatively impact its promotional effects. However, the impact of Ce and La on the activity and selectivity of Co catalyst may depend on the their concertation (molar ratio), and preparation method [246,247].

Table 7.2 Dispersion and Co crystallite size of La/Ce-modified and NTA/EDTA-chelated Co catalysts supported on m-Al_2O_3 and γ-Al_2O_3

Catalyst/Support	**D (%)**	**DOR (%)**	$D_{corr.}$ **(%)**	**Co^0 size (nm)**	**Co_3O_4 Crystallite size (nm) from XRD**
15Co5Ce/m-Al_2O_3	4.4	53.4	8.2	11.7	12.5
15Co10Ce/m-Al_2O_3	4.2	46.7	9.0	10.7	11.8
15Co5La/m-Al_2O_3	5.0	57.9	8.6	11.1	12.4
15Co10La/m-Al_2O_3	4.6	50.0	9.2	10.4	10.3
15CoEDTA/m-Al_2O_3	2.3	45.4	5.1	18.9	12.5
15CoNTA/m-Al_2O_3	3.6	41.5	8.7	11.1	10.9
15CoEDTA/γ-Al_2O_3	3.1	56.1	5.5	17.4	13.1
15CoNTA/γ-Al_2O_3	4.6	50.5	9.1	10.5	10.1

The TPR profiles of all modified and chelated cobalt catalysts are shown in Figures 7.1 and 7.2, respectively. The first reduction temperature in TPR profile increased from 285 to 291.5 ºC and 292 to

304 ºC for Ce and La-modified Co catalysts, respectively, indicating higher interaction of cobalt and modifiers with increasing their loading (see Figure 7.1).

Addition of chelating agents to the solution of Co precursor before impregnation on the support material could affect the deposition, decomposition, and dispersion of the cobalt phases, thereby the number of cobalt active sites and performance of the catalyst in FT reaction [248–250].

Cobalt dispersion and crystallite size analysis, reported in Table 7.2, confirm that the NTA resulted in higher dispersion and smaller crystallite size as compared to EDTA on both m-Al_2O_3 and γ-Al_2O_3 supported cobalt catalyst. It is believed that the addition of chelating agents could lead to formation of stable complexes with Co^{2+} and controlling decomposition of the cobalt complexes during the thermal treatment and calcination [248].

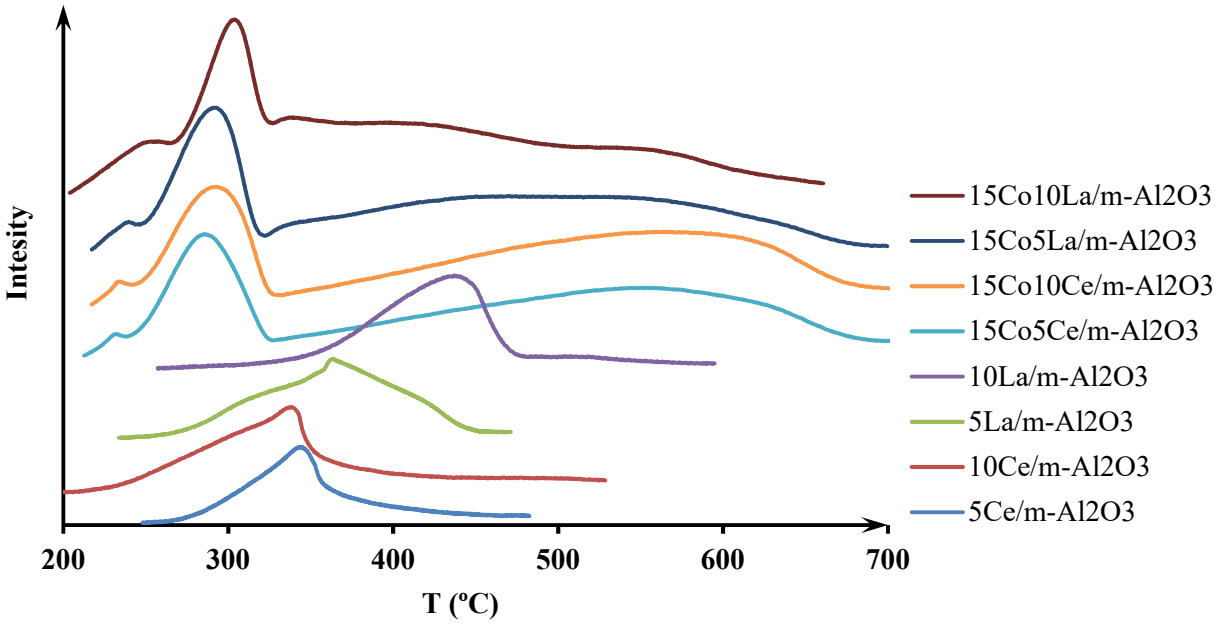

Figure 7.1 Temperature-programmed reduction profiles for La/Ce -modified mesoporous alumina as a support for cobalt catalysts

The mechanism of EDTA and NTA Co^{2+} complexes' decomposition has not been explained in detail in the literature. Strong chelation of cobalt with EDTA can be attributed to higher numbers of short chain carboxylic groups and nitrogen atoms as compared to NTA counterpart which resulted in lower dispersion of cobalt and interaction with alumina support.

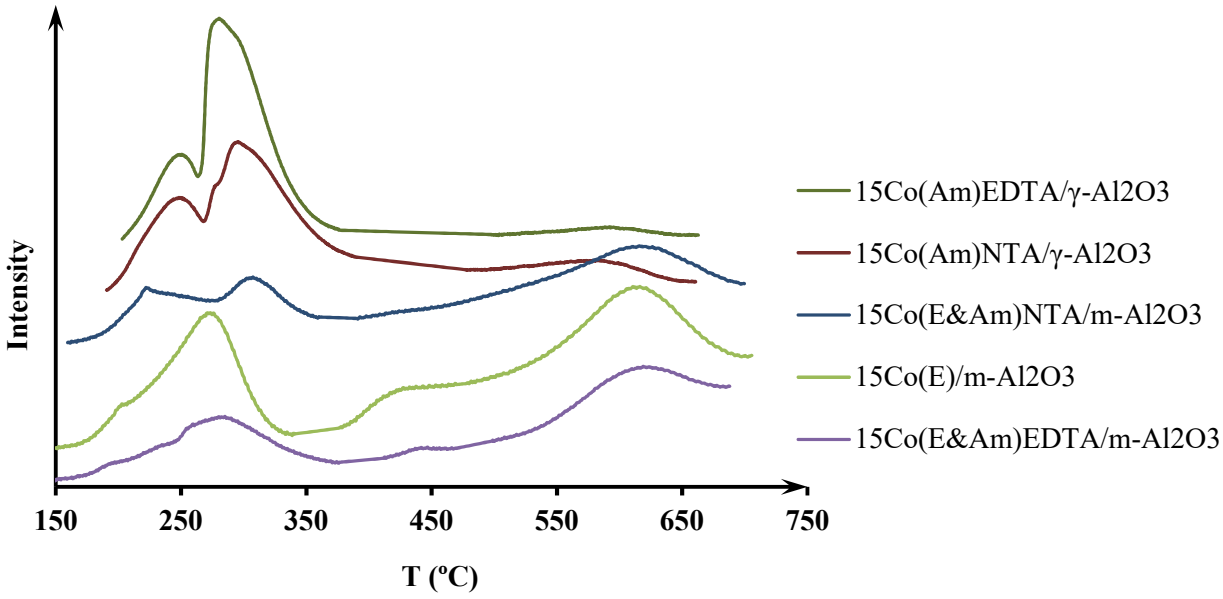

Figure 7.2 Temperature-programmed reduction profiles for mesoporous/γ-alumina supported cobalt catalysts chelated with NTA and EDTA

XRD pattern of modified mesoporous alumina support with Ce and La shows (Figure 7.3) that only 10Ce/m-Al_2O_3 exhibits some diffraction peaks corresponding CeO_2. The peaks occurred at 28.6°, 33.1°, 47.6°, and 56.5 ° can be attributed to diffraction from different planes of the cerium oxide species. Lack of diffraction peaks for lanthanum and cerium oxides in 5Ce/m-Al_2O_3, 5La/m-Al_2O_3, and 10La/m-Al_2O_3 spectra indicates of fine dispersion of La and Ce on the surface. The low intensity peaks at 2θ = 37.2°, 45.8°, and 66.7° correspond to γ-Al_2O_3 phase [240,251].

The XRD patterns of chelated mesoporous and γ alumina supported cobalt catalysts are shown in Figure 7.4. The peaks corresponding to Co_3O_4 diffractions take places at 2θ: 19.0º, 31.5º, 36.8º, 38º, 45º, 59.6º, 65.5º. Addition of CA had no significant impact on the spectra of the catalyst. However, NTA-Chelated cobalt catalysts supported on both mesoporous and γ-alumina revealed smaller crystallites size as compared to their EDTA-chelated counterparts. The calculated crystallite size from XRD analysis corroborates with those obtained from H_2 chemisorption (See Table 7.2).

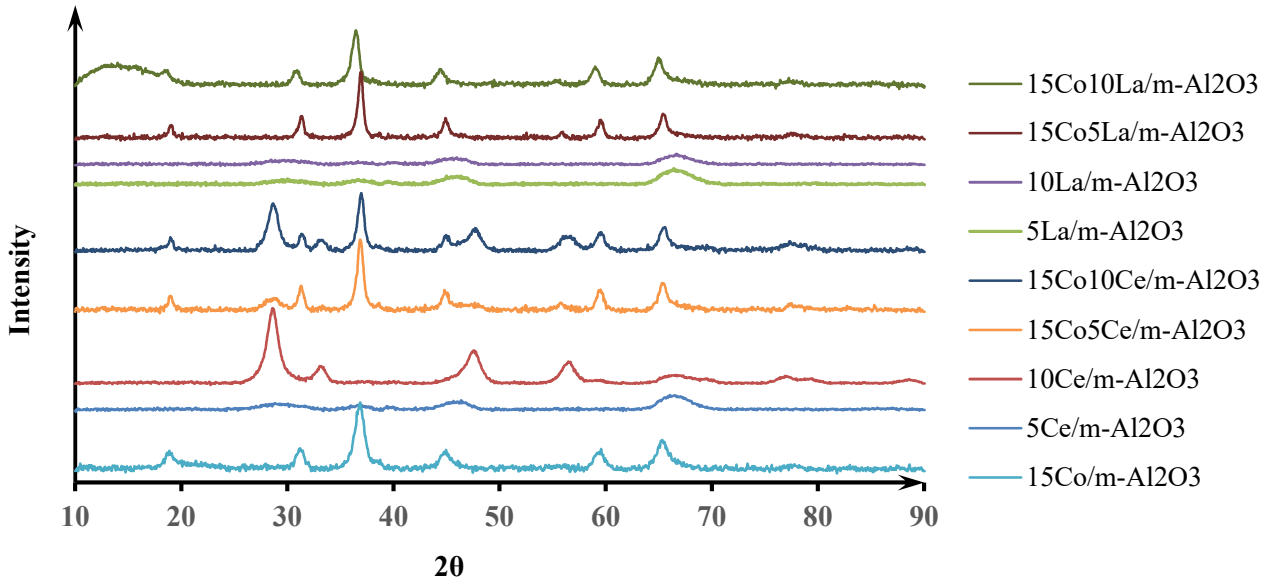

Figure 7.3 XRD patterns for the Ce- and La-modified m-Al_2O_3 and corresponding Co catalysts

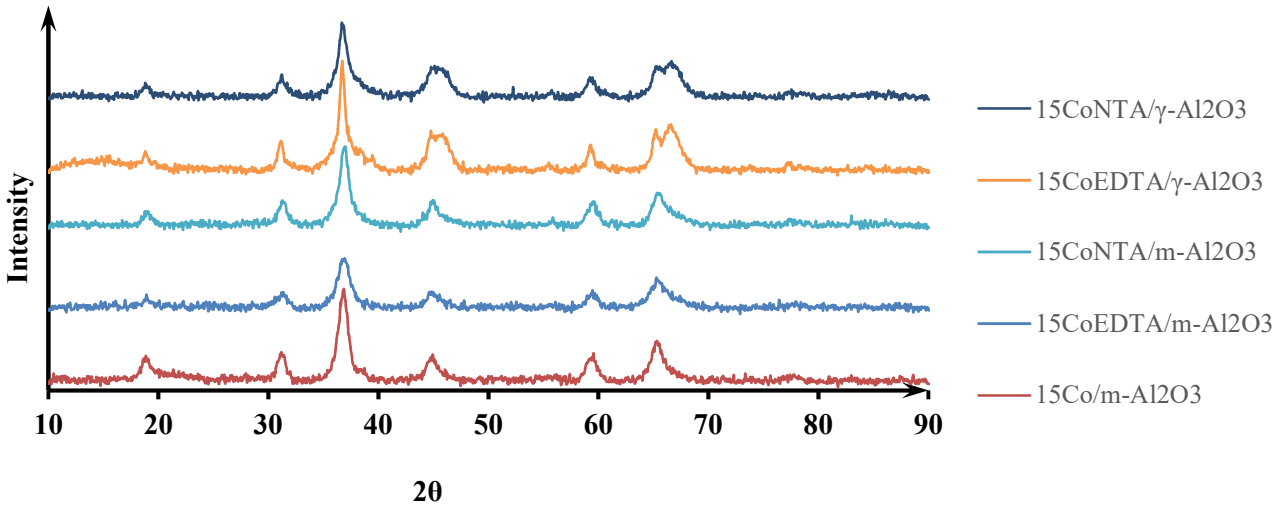

Figure 7.4 XRD patterns for the NTA- and EDTA-chelated cobalt catalysts supported on the mesoporous and γ alumina

7.4.2 Activity and selectivity results

As shown in Table 7.3, modification of mesoporous alumina with higher amount of Ce and La significantly drops the CO conversion and HC yield of the corresponding catalyst. The higher activity of

Co supported on m-Al_2O_3 modified by La can be assigned to higher cobalt active sites accessibility and reducibility, which was evidenced from H_2 chemisorption and TPR analyses.

Also, higher selectivities of CO_2, CH_4, and C_2 to C_4 hydrocarbons for 15Co-xLa/m-Al_2O_3 as compared to 15Co-xCe/m-Al_2O_3 catalysts reveal that La has more promoting effect towards WGS reaction and lighter HCs synthesis than Ce. Moreover, higher loading of each modifier blocks the H_2 chemisorption and concentration of active intermediates leading to methane but favors C_2-C_4 and C_{5+} hydrocarbons. This phenomenon might be attributed to the strong association of Co active sites by La/Ce at higher loading of modifiers [242,243,252].

Table 7.3 FTS activities of the La/Ce-modified & NTA/EDTA-chelated 15Co/m-Al_2O_3 catalysts at 900 h^{-1}, and their selectivity at 50 % CO conversion (230 ˚C, 2.76 MPa)

Catalyst	TOS (h)	GHSV (h^{-1})	CO Conversion (%)	Yield ($g_{HC}.g_{cat}^{-1}.h^{-1}$)	Selectivity (%)			
					CO_2	CH_4	C_2-C_4	C_{5+}
15Co-5Ce/m-Al_2O_3	120	900	52.3	0.162	2.7	13.1	2.4	84.5
	135	850	49.7	0.155	2.9	15.2	2.2	82.6
15Co-10Ce/m-Al_2O_3	85	900	28.3	0.089	1.4	8.2	3.8	88.0
	100	510	49.3	0.091	3.5	10.8	2.8	86.4
15Co-5La/m-Al_2O_3	100	900	64.5	0.197	3.4	16.0	3.2	80.8
	120	1390	49.0	0.210	3.9	15.3	2.9	81.8
15Co-10La/m-Al_2O_3	85	900	45.0	0.136	5.0	14.1	4.3	81.6
	100	890	48.9	0.131	5.3	13.6	4.1	82.3
15CoEDTA/m-Al_2O_3	85	900	46.2	0.144	1.8	14.5	3.0	82.5
	100	810	49.5	0.149	1.6	14.8	3.2	82.0
15CoNTA/m-Al_2O_3	85	900	57.5	0.178	2.4	17.5	3.7	78.8
	100	1180	49.2	0.177	3.2	17.1	3.3	79.7
15CoEDTA/γ-Al_2O_3	100	900	54.5	0.169	1.4	13.4	3.4	83.2
	115	1160	50.2	0.173	1.3	13.3	3.2	83.5
15CoNTA/γ-Al_2O_3	100	900	65.8	0.206	2.3	17.3	3.9	78.2
	115	1425	50.5	0.197	2.1	17.8	4.7	77.5

It is evident that the deposition of cobalt species during the catalyst preparation, as well as the cobalt dispersion and the number of active sites could be affected in presence of the chelating agent molecules in the reduced catalysts (Figure 7.4 and Table 7.2). Interestingly, EDTA with higher affinity to Co^{2+} was less effective for enhancing the CO conversion activity, HC yield and C_{5+} selectivity than the NTA-assisted Co catalysts (see Table 7.3). For instance, 15CoNTA/m-Al_2O_3 and 15CoNTA/γ-Al_2O_3 exhibited almost 11% more CO conversions as compared to 15CoEDTA/m-Al_2O_3 and 15Co-EDTA/γ-Al_2O_3

catalysts. NTA and EDTA chelating agents suppressed the CO conversion activity of cobalt on mesoporous alumina support by 3.8 and 15.1 %, respectively. However, CA-assisted cobalt catalysts on γ-alumina enhanced the CO conversion by 1.5 and 12.5 % due to EDTA and NTA incorporation, respectively. NTA with smaller complex formation constant (log K_{NTA} = 10.3 and log K_{EDTA} = 16.4) is better candidate to modify the γ-Al_2O_3 supported cobalt catalysts performance [253,254]. It is noteworthy that the stronger interaction of EDTA with Co^{2+} during the catalyst preparation results in poor metal dispersion and reducibility of both mesoporous and γ-Al_2O_3 supported catalysts. These findings are corroborated with cobalt dispersion and reducibility of the corresponding catalysts (shown in Table 7.2).

7.5 Conclusions

Increasing the loadings of La and Ce from 5 to 10 wt. % as m-Al_2O_3 modifiers led to higher reduction temperature, lower dispersion of Co and lower catalytic activities of the corresponding Co/m-Al_2O_3 catalysts in FTS. However, La with lower loading of 5 wt. % slightly favored the corrected Co dispersion (from 7.9 to 8.6 %) in 15Co/m-Al_2O_3 catalyst. This resulted in increasing the CO conversion to 65 % as compared to 61 % in 15Co/m-Al_2O_3 catalyst without modifiers (see Table 6.3 in chapter 6). Ce with higher loading (10 %) was less effective modifier for FTS.

Chelation of cobalt using NTA with lower affinity to Co^{2+} during the preparation of both 15Co/m-Al_2O_3 catalyst showed higher CO conversion, HC yield, and C_{5+} selectivity as compared to EDTA-assisted Co catalysts. Also, γ-Al_2O_3 supported cobalt catalysts with both EDTA and NTA chelating agents exhibited better catalytic performance for FTS as compared to chelated cobalt catalysts supported on m-Al_2O_3. NTA-chelation enhanced the apparent dispersion of 15Co/γ-Al_2O_3 catalyst (see Table 6.3 in chapter 6) from 3.8 to 4.6 %. This resulted in 32 % increase in the HC yield of 15CoNTA/γ-Al_2O_3 as compared to same catalyst without chelation.

CHAPTER 8: PROMOTED Co CATALYST SUPPORTED ON MESO-Al_2O_3 FOR FTS

A version of this chapter has been published as a research paper in the following journal:

- V. Vosoughi1, A.K. Dalai, N. Abatzoglou, Y. Hu, "Performances of promoted cobalt catalysts supported on mesoporous alumina for Fischer−Tropsch synthesis", Appl. Catal. A: Gen., 2017, 547, 155-163.

Contribution of the PhD candidate

The experimental design, mesoporous alumina synthesis, catalyst preparation, characterizations, FT tests, compiling / interpretation of the results, and manuscript writing were conducted by Vahid Vosoughi. Dr. Yongfeng Hu carried out the EXAFS test in SXRMB beamline at Canadian Light Source facility. This study and the writing was accomplished based on the suggestions and supervision of Drs. Ajay Dalai and Nicholas Abatzoglou.

Contribution of this chapter to the overall PhD research

Having examined the stability of mesoporous alumina supported Co catalyst and addition of modifiers and chelating agents in Chapters 6 and 7, in this part of work we attempted a to develop optimum Co/m-Al_2O_3 catalyst through addition of promoters. The main objective of this study was to develop efficient mesoporous alumina supported Co catalyst for Fischer−Tropsch synthesis targeting heavier hydrocarbons. This work investigated the effects of different promoters (Ru, Re, Pt, Ir, Mn, Y) on the physico−chemical properties of cobalt catalyst supported on the synthesized mesoporous alumina material. The catalysts were characterized utilizing N_2 adsorption, TPR, H_2 Chemisorption, XRD, XANES techniques. Further, the promoted catalysts were examined for their activity and C_{5+} selectivity in Fischer−Tropsch synthesis at industrially relevant conditions.

8.1 Abstract

Noble metals (Ru, Re, Pt, Ir) and transition metals (Mn, Y) with their atomic ratio of 0.01 to cobalt were used as promoters on the cobalt catalyst supported on mesoporous alumina. The cobalt loading was 15 wt. % and all catalysts were tested for Fischer−Tropsch synthesis in a fixed-bed reactor. The process conditions for activity test were: 230 ˚C and 2.76 MPa, GHSV = 900 h^{-1}, and $\frac{H_2}{CO} = 2.0$. The selectivity

test for the promoted and unpromoted catalysts was performed at CO conversion ~ 50 % by adjusting the syngas flowrate. Addition of promoters increased the cobalt dispersion on mesoporous alumina support. The highest increase in dispersion from 4.7% to 7.6% resulted from addition of Ru. Promoters positively impacted the cobalt dispersion in the decreasing order of: Ru < Re < Pt < Ir < Mn < Y. The reduction temperature for all promoted catalysts were shifted to lower temperature. The maximum decrease in temperature happened with platinum by $\Delta T \sim -150\ ^{\circ}C$ for 1st reduction temperature and $\Delta T \sim -270\ ^{\circ}C$ for 2nd reduction temperature. The reducibility of the CoO_x species on mesoporous alumina was extensively improved by noble metals addition and modestly enhanced by Mn and Y. Significant increase in CO conversion and C_{5+} of the promoted catalysts were observed. CO conversion was increased from ~ 60 % to ~ 86, 84, 82, 80 % as a result of Ru, Re, Ir, and Pt addition. Addition of Ru and Re promoters favored the heavy molecular weight hydrocarbons' (C_{5+}) selectivity and improved it from 81.7 % to 84.2 and 83.1 %, respectively.

8.2 Introduction

It is crucial to develop alternative (non-crude oil-based) and environmentally sound routes to produce transportation fuels and hydrocarbon−based specialty products. Fischer−Tropsch synthesis (FTS) and associated technologies such as gas-to-liquid (GTL), coal-to-liquid (CTL), biomass-to-liquid (BTL), currently seem to be promising options to synthesize the value added liquid hydrocarbons (HCs) [2,4]. FTS potentially can convert the syngas to light hydrocarbons (C_1−C_4), premium middle distillate cuts (naphtha, jet fuel, diesel), and heavier solid waxes (C_{22+}). Aside from the impact of feed composition, reactor type, and operational conditions on productivity and product distribution of FTS, the catalyst characteristics including the support material, active metal, additive, and preparation method are crucial for the better catalysts' performance [4,144]. Among group VIII transition metals, iron and cobalt distinctively favor carbon monoxide hydrogenation and are commercially used in FT catalysts. Iron catalyst has higher water-gas-shift (WGS) activity, therefore is more suitable for CTL and BTL with lower H_2:CO ratio (even 0.6−1.0) syngas. In contrast, cobalt performs better with higher H_2:CO ratio (e.g.1.8−2.3) syngas driven from natural gas [21,30]. In addition, it is less active toward WGS reaction and CO_2 production, but more selective to CH_4 and paraffinic C_{5+}. Higher intrinsic activity and better stability make the Co as a commercially preferred catalyst for FTS targeting long−chain alkanic hydrocarbons. However, understanding the catalysis, designing, and developing of more active, selective, and stable cobalt−based catalyst for FTS have been a continuing interest of research in feed-to-liquid (XTL) technology [39,255,256].

It is well-established that the nature of carrier (support) and its textural properties, active metal precursor and its loading quantity, nature/amount of additives and catalyst preparation methods would significantly influence the physico-chemical properties of a supported cobalt−based catalyst. These properties include cobalt dispersion, crystallite size, degree of reduction, electronic structure, number/structure of active sites, and cobalt-support interaction. Most of the mentioned characteristics of a catalyst are mainly interconnected with the last two, i.e., the strength of cobalt-support bonding and the quantity of cobalt active sites. The type of support material and promoters can directly affect these two crucial features of the active cobalt metal and indirectly modify the other physico-chemical properties and catalytic performance in FTS. Promoters for instance are the compounds that can be doped on active metal at very small quantity to enhance its catalytical performance [5,84]. These elements can function as either a structural, electronic, textural modifier or play a role of stabilizer and poison-resisting agent for the catalyst. These modifiers can influence the surface properties of the support, affect the crystallite size and morphology of the active metal and catalyst lifetime [84,85].

The structural promotion refers to influences on the cobalt−support interaction which results in higher cobalt dispersion, enhanced reducibility and stabilized Co active sites (ensemble effect) [84,86]. These might lead to an increase in the conversion/yield or a decrease in the Co particles sintering/agglomeration during the FT reaction [5,85]. It has been speculated that the electronic promoter may affect the adjacent atoms environment (ligand effect) and the active site geometry through intimate mixing with active metal [85,86]. These can induce changes on the fundamental pathways (elementary steps) of FT reaction (CO and H_2 adsorption, C_1 monomer formation, chain growth and termination) [19,87].The electronic/chemical alteration can directly affect the intrinsic site activity and selectivity of Co catalyst in FTS [84–86,88].

Platinum, ruthenium, rhenium, iridium from noble metals and manganese, lanthanum, zirconium among transition metals are the most patented promoters for FT Co catalyst [96–99]. The high cost, low natural abundance, and impact of precious metals on the cobalt catalytic performance are the key factors to be considered in screening the effective 2^{nd} metal for FT catalyst. For instance, Pt is about 3 times expensive than Ru but 5 times more abundant. Re is ~ 7 times more scarcer than Pt but quite an inexpensive option (~ 10 times cheaper than Pt) [100].

Some of the parameters, which can significantly influence the promotional effect of the elements on Co-supported FT catalyst are: (1) the nature of support surface and its textural properties, (2) cobalt and promoter loading, (3) preparation method of the promoted cobalt catalyst, and (4) FTS process condition.

All of these variables affect the number of active sites, their stability, and cobalt-support interaction which make it difficult to compare the impact of a promoter solely on the performance of cobalt catalyst in FT reaction [5,85]. The promotional mechanism of the second metal added to Co catalyst for FTS have not been elucidated comprehensively. However, transition metals and their oxides are generally added to ensure the selectivity for heavier hydrocarbons and stability of the cobalt catalyst [5,9]. The noble metals are also well−known for their considerable improvement in the reducibility and dispersion of cobalt catalysts supported on SiO_2 [236,257], TiO_2 [258,259], Al_2O_3 [215,260].

In our earlier work, discussed in chapter 6, the mesoporous alumina was synthesized with high surface area (> 400 m^2/g) and large pore diameter (> 10 nm), also was loaded with Co for FTS favoring C_{5+} HC. The objective of this work was to continue development of the mesoporous alumina supported cobalt catalyst for FTS via addition of the 2nd metal as promoter. Since the higher cobalt dispersion and extent of reduction (> 80%) are beneficial for HCs yield and selectivity, their improvement via employing promoter metals was explored on the synthesized mesoporous alumina support. In this regard, the commercially used noble metals (Ru, Re, Pt, Ir) with 1% molar ratio of promoter to Co were chosen in this study. The same concentration level of manganese (Mn) and yttrium (Y) from transition metals were also examined. There is a limited research in the literature studying the promotional effect of Y on Co based catalyst in FTS. The impact of adding the transition and noble metals on physico−chemical properties of the cobalt catalyst using mesoporous alumina support were investigated employing in-depth characterization. Further, all corresponding promoted cobalt-based catalysts were tested for their activity and selectivity performance for Fischer−Tropsch synthesis in a fixed−bed reaction system.

8.3 Experimental methods

8.3.1 Materials

For the mesoporous alumina support synthesis, aluminum isopropoxide $Al(O\text{-}i\text{-}Pr)_3$ as a precursor of alumina, and pluronic F127 $[(EO)_{106}(PO)_{70}(EO)_{106}]$ as a structure-directing agent were purchased from Sigma–Aldrich, Oakville, Canada. Also, anhydrous ethanol and isopropanol as solvents used were procured from Fisher Scientific, Ottawa, Canada. The following active and promoter metal precursors were purchased from Alfa Aesar, Tewksbury, United States: cobalt nitrate [$Co(NO_3)_2.6H_2O$, 99.9%], Mmanganese (II) nitrate hydrate [$Mn(NO_3)_2.xH_2O$, 99.999%], rhenium (VII) oxide [R_2O_7, 99.99%], ruthenium (III) nitrosyl nitrate [$Ru(NO)(NO_3)_2$, 99.9%], platinum (IV) nitrate solution [PtN_4O_{12}, Pt 15%

w/w], yttrium (III) nitrate hexahydrate [$Y(NO_3)_3.6H_2O$, 99.9%], Iridium (III) chloride hydrate [$IrCl_3.xH_2O$, 99.9%].

8.3.2 Support synthesis

Non-ionic templating sol-gel method was adopted to synthesize the mesoporous alumina (m-Al_2O_3) as a support material. In this method, aluminum alkoxide (e.g. aluminium isopropoxide) is hydrolyzed in the presence of a long chain structure-directing agent. This template was triblock copolymer surfactant, Pluronic F127, with a hydrophilic poly ethylene oxide (PPO) connected to two hydrophilic poly ethylene oxide (PEO) chains [42]. Employing this templating agent, with appropriate ratios of precursor and solvents secure the high specific surface area (>300 m^2/g) and pore volume (>1 cm^3/g) with mesoporous structure. These polymers are relatively non−toxic, biodegradable, inexpensive, and commercially available compounds. Moreover, employing different ratio of H_2O/Al in the synthesis provides the flexibility of tuning the pore diameter [209,214]. The moderately large pore diameter of 10-15 nm was targeted during the synthesis procedure to meet the recommended properties for cobalt catalyst in FTS [39,40]. The chosen molar ratio of the precursors and solvents for this synthesis was 1.0 Al(o-i-Pr)$_3$: 0.01 F127: 8.0 EtOH: 6.0 iPrOH: 4.0 H_2O. Aluminum iso-propoxide and non-ionic F127 copolymer were separately dissolved in the mixture of ethanol and isopropanol at 50 ºC. Appropriate amount of water was introduced into the polymer solution before adding the aluminum iso-propoxide solution into it. Following the 4 h stirring of the suspension at 50 ºC, it was aged at room temperature for 24 h. The resulting gel was treated at two thermal stages of 80 ºC and 150 ºC for 24 h each. The thickened gel was then filtered, dried and calcined at 600 ºC for 6 h. Further details of the synthesis procedure for the mesoporous alumina support have been explained elsewhere [35,37-38].

8.3.3 Catalyst preparation

To prepare the promoted cobalt catalysts, incipient wetness impregnation (IWI) method was employed to fill the pores of the support. The required amount of cobalt precursor to secure 15 wt. % of Co loading on the catalyst along with promoter precursor were dissolved in the anhydrous ethanol for co−impregnation on the dried mesoporous alumina support. The atomic ratio of the added promoter metals to cobalt metal was 0.01 which is equivalent to 0.27, 0.5, 0.52, 0.28, 0.15, 0.24 wt. % of Ru, Re, Pt, Ir, Mn, and Y in the catalyst, respectively. All catalysts were vacuum dried in 60 °C for 12 h and then calcined at 400 °C for 3 hours.

8.3.4 Catalyst Characterization

Nitrogen physisorption: The adsorption and desorption amount of nitrogen at cryogenic temperature of 77 K was measured using Micromeritics ASAP 2020 instrument. To strip all possible volatile content, about 0.2 g of the samples was vacuum heated first at 50 mTorr (6.7 Pa) and 200 ºC for 4 hours. The specific surface area and pore dimensions were calculated using the Brunauer-Emmett-Teller (BET) and Barrett-Joyner-Halenda (BJH) method [69,155].

H_2 chemisorption: The hydrogen adsorption amount to estimate the number of cobalt atoms available on the surface was measured using chemisorption (ASAP 2020 instrument). 0.1 g of the calcined catalysts was first reduced by hydrogen at 400 ºC for 150 min then cooled down to 35 ºC under 1.3×10^{-5} Pa vacuum. Then the hydrogen gas was introduced on sample to determine the H_2 uptake and cobalt atoms accordingly, assuming H:Co stoichiometry of 1:1 for chemisorption [46,69,155].

$$\mathrm{D} = \frac{\text{measured } \mathrm{Co^0} \text{ atoms on the surface}}{\text{total } \mathrm{Co^0} \text{ atoms in the sample}} \tag{8.1}$$

Where D is the fraction of available cobalt atoms (Co^0) in the surface available for chemisorption out of the whole cobalt available in the sample [46,215].

Temperature programmed reduction (TPR): To study the impact of promoter on reducibility of the mesoporous supported cobalt catalysts AutoChem Micromeritics 2950 HP instrument was used, which is equipped with a thermal conductivity detector. Prior to the analysis, the catalyst samples were degassed first at 100 ºC, then 35 ºC by introducing the helium gas into the stainless steel U−shaped sample holder. Reduction profiles of the catalysts were acquired by increasing the temperature with 10 ºC/min ramping steps to 800 ºC. This reduction behaviour was obtained under 50 mL/min flow of 10 % H_2/N_2 (v/v) gas and recorded using the thermal conductivity of the outlet gas via a detector [153]. Degree of reduction (DOR) for the catalysts was calculated by taking the ratio of the consumed H_2 for reduction from TPR analysis over the required stochiometric H_2 to reduce all cobalt oxides (Co_3O_4) to metallic Co. Then, the dispersion of Co atoms was corrected by associating it with the extent of reduced cobalt atoms [46,215]:

$$\mathrm{D_{corr.}}\% = \frac{\text{measured } \mathrm{Co^0} \text{ atoms on the surface}}{\text{Reduced } \mathrm{Co^0} \text{ atoms in the sample}} \times 100 = \frac{\mathrm{D}\ \%}{\mathrm{DOR}} \tag{8.2}$$

In order to calculate the Co^0 crystallite size based on the Co dispersion amount, the cobalt clusters were assumed to be in spherical shape with a site density of 14.6 atoms/nm^2 [46,215]:

$$d_{chem.}^{Co^0} = \frac{96}{D_{corr.}\,\%} = \frac{96}{D\,\%} \times DOR \tag{8.3}$$

X−ray diffraction (XRD): To carry out the powder XRD analysis for the catalysts, the Bruker Advance D8, series II, diffractometer with monochromatic Cu Kα radiation was used. The operating voltage and current were 40 kV and 40 mA, respectively. The broad angle XRD from 10 to 90º was achieved at 2º/min scan rate and 2 s step time. To estimate the mean diameter of the cobalt oxide crystallites, Debye–Scherrer equation was applied at 2θ = 36.8º:

$$d_{XRD}^{Co_3O_4} = \frac{K\lambda}{\beta \cos\theta} \times \frac{180}{\pi} \tag{8.4}$$

Where, $d_{XRD}^{Co_3O_4}$ is the average thickness of crystallites (nm); K is assumed 0.89 as shape factor constant for sphere crystallites; λ is X−ray wavelength = 0.154 (nm); β is broadening at half-max intensity (full width at half maximum) in degree; and $\theta_B = 2\theta/2$ is Bragg angle (diffraction angle) [43,154].

Transmission electron microscopy (TEM): To examine the morphology of the samples through their micrographs, the JEOL 2011 transmission electron microscope was used. The standard sample preparation was followed to carry out the analysis [69,155].

X−ray absorption near−edge structure (XANES) spectroscopy: The Co K−edge, XANES of the promoted and unpromoted cobalt catalyst supported on mesoporous alumina were obtained at the Soft X−ray Microanalysis Beamline (SXRMB) of the Canadian Light Source with medium energy range of 1.7–10 keV. To acquire the scan for X-ray spectra the monochromator equipped with double−crystal silicon (1 1 1) was utilized. Double−sided conductive carbon tape was used to disperse the sample on it. The data for XANES spectrum was collected in two modes: total electron yield by measuring the sample drain current; and partial fluorescence yield using Si(Li) drift detector. The XANES spectra were corrected with background subtraction and normalized to the incident photon flux and to unity using polynomials.

8.3.4 Catalyst performance study for Fischer-Tropsch Synthesis

Fischer–Tropsch reaction was carried out in the fixed−bed micro reactor with 1 cm internal diameter and 50 cm length. To ensure uniform mass flow and heat transfer across the reactor, five different layers of silicon carbides (SiC) from coarse to fine toward the reaction zone were used. Moreover, for each run, one gram of the powder catalyst was diluted with 7 g of SiC (90 mesh). Prior to FT reaction, in-situ

reduction occurred using ultra−high purity (UHP) hydrogen. To reduce the catalyst, the reactor temperature was raised with 1 ºC/min step to 400 ºC and maintained for 18 h under 30 ml/min flow of H_2 and atmospheric pressure. Following the reduction, the reactor was cooled down to 180 ºC and pressurized to 2.76 MPa, and the inlet gas was switched to syngas (H_2:60%, CO:30%, Ar: 10%). After syngas introduction, the reactor temperature was gradually raised to 230 ºC with heating ramp of 0.5 ºC/min. Brook mass flow controller and PID temperature controller were used to adjust the flow and temperature to desired values for FT reaction. The products were first passed through a container wrapped with heating tape and maintained at about 100 ºC to collect heavy HCs and waxes in liquid form. The lighter products and water are condensed in cold trap which was maintained at around 0 ºC. The non−condensable reactant and product gas mixture (CO, Ar, CO_2, C_1−C_4) was analyzed through gas chromatograph (Shimadzu GC−2014) in 8 h intervals, otherwise sent to exhaust gas line [69,77,157]. Liquid hydrocarbons were collected from the hot and cold traps and analyzed via an off−line GC.

After doing mass balance over the argon as a non−reactive component in the reaction, following equations were used to estimate the activity and selectivity the catalyst in FTS:

$$\text{CO conversion percentage: } \mathrm{CO_{conv.}}\% = \frac{\text{Mole } \mathrm{CO_{in}} - \text{Mole } \mathrm{CO_{out}}}{\text{Mole } \mathrm{CO_{in}}} \times 100 \tag{8.5}$$

$$\text{Selectivity of } \mathrm{CO_2}\text{: } \mathrm{S_{CO_2}}\% = \frac{\text{Mole } \mathrm{CO_{2,out}}}{\text{Mole } \mathrm{CO_{in}} - \text{Mole } \mathrm{CO_{out}}} \times 100 \tag{8.6}$$

$$\text{Selectivity of light HCs } (n = 1, 2, 3, 4)\text{: } \mathrm{S_{C_n}}\% = \frac{\text{Mole } \mathrm{C_n} \times 100}{\text{Mole } \mathrm{CO_{in}} - \text{Mole } \mathrm{CO_{out}} - \text{Mole } \mathrm{CO_{2,out}}} \tag{8.7}$$

$$\text{Selectivity of long} - \text{chain HCs (n} \geq 5\text{): } \mathrm{S_{C_{5+}}}\% = 1 - \left(\mathrm{S_{C_1}} + \mathrm{S_{C_2}} + \mathrm{S_{C_3}} + \mathrm{S_{C_4}}\right) \tag{8.8}$$

8.4 Result and Discussion

8.4.1 Characterization

As shown in Table 8.1, co−impregnation of cobalt along with different promoters had rather similar impact on the textural properties of the mesoporous alumina. Deposition of cobalt oxides during the calcination partially fills the porosity of the support. The 15 wt. % Co^0 loading in the calcined catalysts is equivalent to the presence of ~ 20 wt. % Co_3O_4. If the contribution of cobalt oxides in the surface area is neglected, it is expected that after the catalysts are prepared and calcined, the support would lose around 20% of its specific surface area (SSA). The unpromoted and all promoted catalysts revealed the

SSA in 310−330 m^2/g limit which shows 18.5−23% decrease in the SSA of the support (405 m^2/g), conforming the expected decline. Pore volume of all catalysts dropped from 1.55 to 1.11−1.28 cm^3/g. However, no considerable changes were observed for pore diameter of corresponding catalyst considering the experimental error of ±0.2 nm. The mesoporous alumina support exhibited the pore diameter of 11.8 nm and the corresponding unpromoted and promoted catalysts showed the average pore diameter between 11.3−12.0 nm.

Table 8.1 Textural properties of mesoporous alumina supported Co catalysts with different promoters

Catalyst/Support	BET surface area (m^2/g)	BJH Pore volume (cm^3/g)	Pore diameter (nm)
mAl_2O_3	405	1.55	11.8
Co/mAl_2O_3	330	1.28	11.4
$CoRu/mAl_2O_3$	310	1.11	11.5
$CoRe/mAl_2O_3$	315	1.16	11.3
$CoPt/mAl_2O_3$	322	1.19	12.0
$CoIr/mAl_2O_3$	313	1.22	11.9
$CoMn/mAl_2O_3$	311	1.13	11.8
CoY/mAl_2O_3	317	1.20	12.0

To study the impact of added promoters on dispersion of the cobalt catalysts supported on mesoporous alumina, H_2 chemisorption was preferred over the CO chemisorption [261] due to the difficulty in determining the number of chemisorbed CO atoms on a Co atom (stoichiometry of CO:Co ~ 1−2) [262,263]. H_2 chemisorption results shown in Table 8.2 indicate that the promotion with noble metals (Ru, Re, Pt, Ir) led to higher cobalt dispersion (D%) than transition metals (Mn and Y). The highest increase in apparent dispersion of Co in the Co/mAl_2O_3 catalyst was obtained by the addition of Ru and Re promoters, changing the Co dispersion from 4.8% to 7.6% and 7.1%, respectively. The order of improvement in dispersion of Co because of using different promoters is as follows: Ru > Re > Pt > Ir > Mn > Y; the transition metals only slightly improved the Co apparent dispersion (from 4.8 to ~ 5.3%). The interaction of promoters with Co, support and their location is complicated. Using aberrated−corrected scanning transmission electron microscopy, Shannon et al. found that the isolated atoms of the Re, Pt, and Ir were present on the Co surface, whereas the Ru appeared in patches but all connected with Co particles [264]. However, it is believed that the presence of promoter during the oxidation treatment (calcination) facilitates the nucleation of cobalt oxide crystallites and crystallization

sites. Therefore, the probability of the smaller cobalt crystallite formation increases which results in the enhancement of the cobalt dispersion and active site density [82].

Temperature programmed reduction (TPR) profiles in Figure 8.1 present the reduction behavior of unprompted and promoted Co/mAl_2O_3 catalysts. It is evident that the noble metals considerably shifted the reduction temperature to lower degrees, while the transition metals impact on reducibility were not significant. It is well-established for the supported cobalt that at least two prevailing peaks appear on its TPR profile. The first peak represents reduction of Co (II, III) to Co (II) crystallites, $Co_3O_4 \longrightarrow CoO$, which reportedly occurs in range of 200−300 ºC. The second peak signifies reduction of Co (II) to zero valance cobalt, $CoO \longrightarrow Co^0$, which might take places within 400−500 ºC [169,265]. In this work, the first and second reduction peaks of unpromoted Co/mAl_2O_3 appeared at 260−330 ºC and relatively broad range of 350−620 ºC, respectively. The calcination temperature and cobalt-alumina interaction could underlie the location of the reduction peaks [169]. The broad-ranging reduction stage of $CoO \longrightarrow Co^0$ can be attributed to the reduction of two different cobalt species which starts at lower temperatures and extends to the higher temperatures due to: (1) the reduction of strongly bonded Co_3O_4 to the support, and (2) the reduction of strongly bonded CoO to the support or those cobalt ions which could be embedded in the alumina lattice and formed hardly reducible species [5,169].

All promoters used in this work increased the cobalt reducibility for the mesoporous alumina supported cobalt catalyst and shifted either both or one of the occurring reduction ranges to lower temperature. As illustrated in Figure 8.1, the first maxima of reduction were shifted from 300 ºC to 186, 296, 146, 188, 220, 229 ºC and the second maxima from 592 ºC to 325, 352, 333, 345, 567, 574 ºC, as a result of adding Ru, Re, Pt, Ir, Mn, Y promoters, respectively. The first stage of reduction ($Co_3O_4 \rightarrow CoO$) seems to be facilitated more with noble metals (i.e. $\Delta T = 112-154$ ºC) than with Mn and Y transition metals (i.e. $\Delta T = 71-80$ ºC). However, Re was almost ineffective on shifting the maxima for the first stage of the reduction which concurred with findings of other research groups [85,266]. It is believed that the rhenium oxide itself reduces at higher temperature (~ 350 ºC) that may be the reason why the first reduction stage of the cobalt was not facilitated much by rhenium [5,266]. Regarding the second peak of reduction, all noble metals exhibited considerable impact on shifting the maxima of $CoO \rightarrow Co^0$ stage to lower temperatures (i.e. $\Delta T = 140-270$ ºC) forming distinct narrow peak as compared to unprompted Co/mAl_2O_3 catalyst, whereas the Mn and Y lowered the second peak reduction temperature only by 25 and 18 ºC, respectively. The corresponding surface area for the main peaks was also estimated using deconvolution of the reduction profiles and presented in Table F.3 in Appendix F.

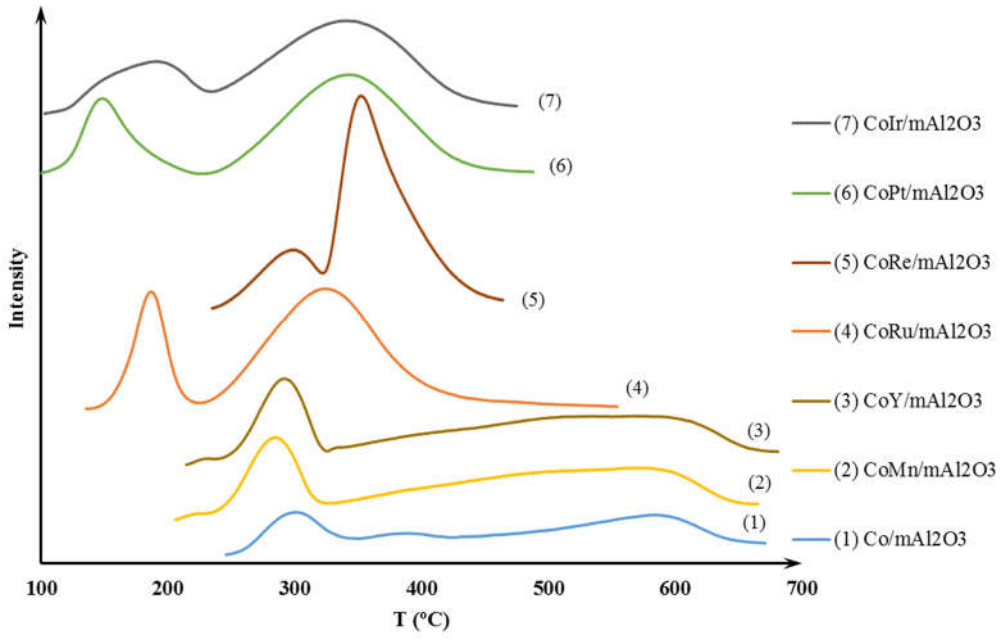

Figure 8.1 Temperature−programmed profile for mesoporous alumina supported Co catalysts with different noble and transient metal promoters

Despite the fact that the conditions for TPR analysis were not the same as the condition for in-situ reduction of the catalyst before FT reaction in terms of purity of hydrogen (10% vs UHP), reduction temperature (35 to 700 ºC vs 400 ºC), and duration (2−3 h vs 18 h), the measured H_2 uptake and estimated DOR could be used as basis for comparison. To estimate the stochiometric amount of H_2, it is assumed that all Co_3O_4 were converted to Co^0 following reactions (8.9) and (810) [166]:

$$Co_3O_4 + H_2 \rightarrow 3CoO + H_2O \tag{8.9}$$

$$3CoO + 3H_2 \rightarrow 3Co^0 + 3H_2O \tag{8.10}$$

As it is presented in Table 8.2, addition of the noble and transition metals to Co improved the reducibility of the corresponding mesoporous alumina supported cobalt catalysts. Structural contribution of the added promoters on the cobalt dispersion and its reducibility was in the same order of enhancement (Y < Mn < Re < Pt < Ru < Ir). It was observed that the 2nd metals (noble) added to the Co/mAl_2O_3 catalyst in 1% molar ratio level, considerably facilitated the reduction of the catalyst. Degree of reduction (DOR) for unpromoted catalyst was enhanced from ~ 61% to ~ 82, 84, 85, and 87% by addition of Re, Pt, Ru, and

Ir promoters, respectively. The same order of reducibility for the fresh calcined Co/alumina catalysts was reported in other study [90]. Mn and Y also improved the extent of reduction for the corresponding promoted catalysts by absolute percentage increase of 10 and 13, respectively, as compared to the unpromoted counterpart catalyst (Co/mAl_2O_3). As it is evidenced, at equal ratio of the promoter to cobalt atoms, the noble metals are much more effective promoters than transition metals by lessening the catalyst reduction temperature, thereby, (i) facilitating the reduction of hardly−reducible small cobalt crystallites interacting strongly with the support, and (ii) increasing the number of Co^0 active sites on the surface [5,233].

Table 8.2 Dispersion and Co crystallize size of $Co/m\text{-}Al_2O_3$ catalysts with different promoters

Catalyst	D (%)	DOR (%)	$D_{corr.}$ (%)	$d^{Co^0}_{chem.}$ (nm)	$d^{Co_3O_4}_{XRD}$ (nm)	$d^{Co^0}_{XRD}$ (nm)
Co/mAl_2O_3	4.7	60.9	7.8	12.0	10.8	8.1
$CoRu/mAl_2O_3$	7.6	84.5	9.0	10.7	10.4	7.8
$CoRe/mAl_2O_3$	7.1	81.5	8.7	11.0	11.1	8.3
$CoPt/mAl_2O_3$	6.9	83.7	8.2	11.7	11.5	8.6
$CoIr/mAl_2O_3$	6.6	86.9	7.6	12.6	11.8	8.9
$CoMn/mAl_2O_3$	5.2	70.5	7.4	13.0	13.2	9.9
CoY/mAl_2O_3	5.4	74.3	7.2	13.4	13.5	10.1

The ease of reductions could be associated with rapid dissociation of hydrogen molecules on the noble metal surface and following diffusion of hydrogen atoms (spillover) to neighboring cobalt oxide species [82,267]. Different electronic properties of transition metals (as substrates) exhibit different affinity toward adsorbed atoms or molecules (adsorbates).

Iglesia et al. [268] unveiled formation of Ru−Co oxides species and bimetallic alloying during the calcination and catalyst activation, respectively, using x-ray adsorption spectroscopy (XAS). Formation of RuO_x, which is easily-reducible and can be mobile and bond with CoO_x, assists the reduction of CoO_x ensembles during H_2 activation of the catalyst (structural promotion) as well [232]. The chemisorption model, the d−band theory, developed by Hammer and Nørskov [269] also successfully explains the different reactivity of transition metals toward gaseous adsorbates (e.g. H_2). As one moves from the bottom right to top left through the d−block metals of periodic table, the contribution of unpaired d-

electrons to surface bonding of adsorbate increases. This can be related to the degree of filling (d_f) in the d−band states of metals where it becomes more depopulated as one shifts to the earlier transition metals in the left which results in formation of stronger chemisorption bonds (e.g. $d_f^{Pt} = 0.9$ and $d_f^{Y} = 0.2$) [269]. Appropriate chemisorption strength favoring the hydrogen spillover and facilitating the cobalt oxide reduction, follows the Sabatier principle and demonstrates volcano type trend among transition metals. The later elements on the right column of transition metals (e.g. Ag, Au) show poor dissociative chemisorption and the earlier elements (e.g. Zr, Sc) on the left columns of transition metals form strong bond that hydrogen atoms cannot desorb easily after adsorption, whereas the noble metals behave in between [269,270].

Apparent dispersion increased by ~ 2−3 absolute % (from 4.7% to 6.6−7.6%) owing to addition of the noble metals to cobalt in 1% molar ratio of promoter (Table 8.2), whereas Mn and Y had insignificant impact on increasing the fraction of cobalt atoms available on the surface (from 4.7 to 5.2 and 5.4, respectively). This might be associated with strong interaction of H_2 with Mn and Y which become difficult for dissociated H atoms to desorb, spill over, and reduce the neighboring CoO_x species to metallic Co. During the reduction, the MnO_x and YO_x species remain in their oxidic form while they adsorb the reducing hydrogen strongly. As mentioned above, the promoter loading level and catalyst preparation method can affect the MnO_x and YO_x species location in the catalyst to be either on the CoO_x surface or alumina support. As reviewed by Morales et al [85], Mn could aid the dispersion of cobalt if it is bound with the support. Considering the fact that all cobalt species after reduction may not be in form of Co^0 and still remain in oxidised form, degree of reduction needs to be taken into account. After calculating the DOR, the apparent dispersion of the catalysts was corrected ($D_{corr.}$%) as shown in Table 8.2. According to the equation 8.2, the bigger the degree of reduction (DOR → 1), the smaller difference would be between the apparent cobalt dispersion and the corrected dispersion value (D% → $D_{corr.}$%). The higher dispersion of cobalt could be translated to more available cobalt surface area and active sites for the CO hydrogenation in FTS. The average surface Co^0 crystallite diameter ($d_{chem.}^{Co^0}$) was also corrected based on the percentage of the Co atoms which are present in the reduced form. As shown in equation 8.3, the higher metal dispersion results in smaller crystallite of the cobalt metal. The Ru exhibited the highest impact on improving the dispersion of Co/mAl_2O_3 which resulted in the smallest Co^0 size of 10.7 nm. The catalyst with the lowest corrected dispersion (D_Y% = 7.2) led to the largest average Co^0 crystalline diameter of 13.4 nm. Given that the average surface diameter of the Co^0 crystallites for unpromoted catalyst was estimated of 12.5±0.5 nm, addition of one atom promoter for every 100 atoms

of the cobalt did not noticeably change the $d^{Co^0}_{chem.}$ for the promoted catalysts. This could be related to strongly interacting Co particles with the alumina support.

HRTEM images (Figure 8.2) also confirm the analogy among unpromoted and promoted cobalt catalysts. These micrographs do not reveal information about the doped promoters position whether they interacted with cobalt surface or segregated on the support. However, the images from calcined catalysts exhibited well distribution of cobalt crystallites on the mesoporous alumina support. Mn-promoted catalyst exhibited somewhat more coalescence of Co particles with rather bigger sizes. The EDAX mapping for unpromoted and two promoted catalysts were appended in Figure F.2 of Appendix F identifying the present Co and Al elements.

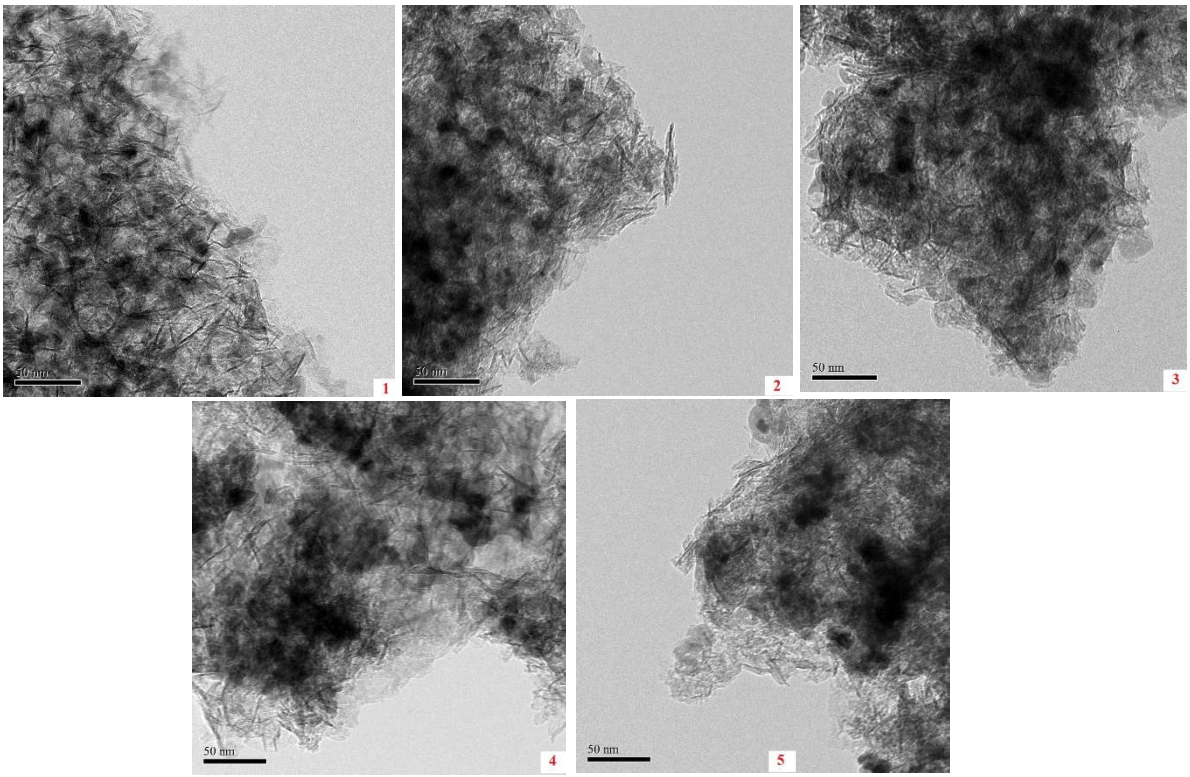

Figure 8.2 HRTEM images of (1) Co/mAl_2O_3, (2) $CoRu/mAl_2O_3$, (3) $CoRe/mAl_2O_3$, (4) $CoPt/mAl_2O_3$, (5) $CoMn/mAl_2O_3$.

The wide-angle XRD patterns of the unpromoted and promoted cobalt catalysts supported on the mesoporous alumina as well as the spectra for the powder CoO and Co_3O_4 are demonstrated in Figure 8.3. The corresponding XRD spectra for the synthesized alumina was discussed in chapter 6. The reflections from (311), (222), (400), and (440) planes in γ-Al_2O_3 cubic structure appear at 2θ: 37º, 39º,

46º, and 66º respectively [227,228]. CoO and Co_3O_4 are the main possible cobalt oxides would present in a supported and calcined cobalt catalysts. Diffraction peaks at 42.7º and 61.9º, which represent the CoO, were not distinguished for all the unpromoted and promoted cobalt catalysts supported on the mAl_2O_3, whereas the Co(II, III) was the prevalent cobalt oxide phase in the series as evidenced by reflections from different planes of Co_3O_4 at 2θ of 19.0º, 31.5º, 36.8º, 38º, 45º, 59.6º, 65.5º [212].

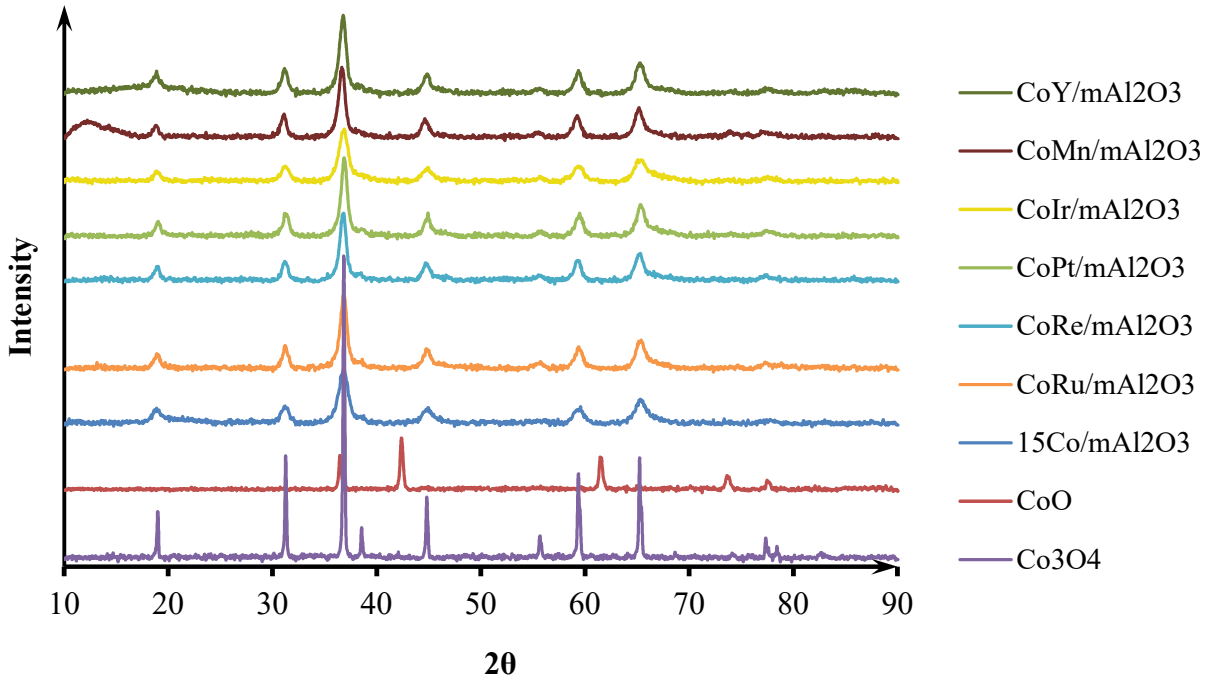

Figure 8.3 XRD patterns for unprompted and promoted cobalt catalyst supported on the mesoporous alumina

The XRD patterns were also used to estimate the Co_3O_4 crystallite size in the catalyst employing the equation 8.4. FWHM method for estimation of angular breadth (β) was applied at 2θ = 36.8º, the most intense peak of Co_3O_4 phase representing (311) face of crystallites, to obtain the average width of cobalt oxide crystallites in the catalysts. As the results shown in Table 8.2, the crystallite size ($d_{XRD}^{Co_3O_4}$) of promoted cobalt catalysts from XRD analysis also verifies that the noble metal addition did not notably influence the cobalt oxide size on mesoporous alumina (−0.4 to +1.0 nm change from 10.8 nm). However, doping Mn and Y resulted slightly more change in the cobalt oxide crystallite size as compared to noble metals, increasing it from 10.8 nm to 13.2 and 13.5, respectively. The increase in the crystallite size might be attributed to weakening of the Co−support interaction which in turn causes the migration of

smaller atoms toward larger cobalt crystallites. In the case of manganese, deposition of MnO_2 on CoO_x and formation of $Co_{3-x}Mn_xO_4$ ($0 < x < 1.4$) spinels have been also evidenced [85].

The XRD results of Co_3O_4 width were multiplied by coefficient of 0.75 to estimate the Co^0 size ($d_{XRD}^{Co^0}$) presented in Table 8.2. The Co^0 size trend estimated from XRD corroborate with the findings of the H_2 chemisorption analysis. Nonetheless, the crystallite size of Co^0 approximated from chemisorption analysis, for the corresponding catalysts, are considerably larger. The difference in the average Co^0 size determined using two methods could be ascribed to: (i) enlargement of cobalt ensembles during the reduction in H_2 chemisorption analysis and (ii) inaccessibility of noticeable amount of the present metal for H_2 chemisorption.

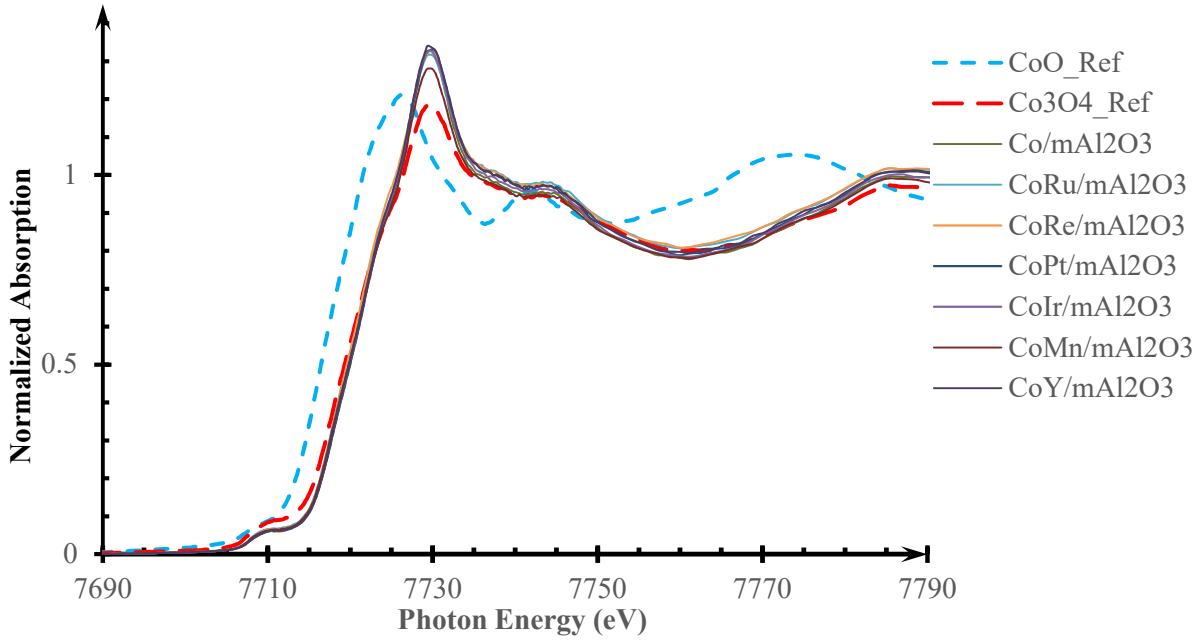

Figure 8.4 XANES spectra for Co^0 (dotted line), CoO (small−dashed), Co_3O_4 (large−dashed), unprompted and promoted cobalt catalysts (solid lines) supported on the mesoporous alumina

The Co K-edge normalized XANES spectra of unpromoted and promoted cobalt catalysts supported on the mesoporous alumina are shown in Figure 8.4. The reference spectra for cobalt oxide II (CoO) and cobalt oxide II & III (Co_3O_4) standards are also shown in Figure 8.4. The intense peak or edge jump occurs at ~ 7730 eV owing to the dipole allowed 1s to 4p electronic transition. The edge jump for CoO is 4eV lower than that of Co_3O_4. This is due to the higher oxidation state of cobalt in Co_3O_4 as it requires higher energy to pull out additional electron. The XANES spectra for all calcined cobalt catalysts were

fitted using linear curve fitting with Co^{2+} (CoO) and $Co^{+2,+3}$ (Co_3O_4) references and it resulted in the presence of > 99 % Co_3O_4. The fitting data for the XANES spectra, obtained from Athena software were provided in Table F.1 in Appendix F. This corroborates with XRD results showing the prevalence of the Co (II, III) phase in all catalysts.

8.4.2 Fischer-Tropsch synthesis

The promoted cobalt catalysts supported on the mesoporous alumina were tested in commercial condition of 230 °C and 2.76 MPa with H_2/CO ratio of 2. To compare the CO conversion activity (%) and productivity ($g_{HC}.g_{cat}^{-1}.h^{-1}$) of all promoted cobalt catalysts, the FT reaction was performed at the same gas hourly space velocity (GHSV) of 900 h^{-1}. The operating conditions used in this research were based on the optimization study discussed in chapter 6. Moreover, the selectivity of all catalysts for main products (CO_2, CH_4, C_2−C_4, C_{5+}) was evaluated at similar CO conversion of ~ 50 % by adjusting the syngas inflow. As shown in Table 8.3, the catalysts performance data was acquired for 100−140 h of time-on-stream (TOS) and reaching the stable condition.

Promotional effect of noble metals (NMs) on the CO conversion (%) and mass−based activity of mesoporous alumina supported cobalt catalyst in FTS is substantial. Without promotion, the Co/mAl_2O_3 catalyst converted ~ 60 % of inlet carbon monoxide to CO_2 and hydrocarbons, whereas addition of NMs resulted in 20−26 absolute % increase in the converted CO and reached to 80.2, 81.6, 84.1, and 86.3 % for Ir, Pt, Re, and Ru, respectively. It is generally accepted that promoting with NMs (i) improves the extent of reduction, and (ii) enhances the active metal dispersion [21]. The first two factors lead to higher active site density and the latter may contribute to boost the intrinsic activity of the active sites [21]. Higher accessible cobalt atoms for the adsorbed reactants, and rapid reactions of adsorbates on the surface sites consequently convert more of CO+H_2 reactants to products. It is noteworthy that not all ensemble of cobalt atoms could be an active site for the FT reaction, nonetheless, active site density is proportional to the number of surface atoms [271].

Considerable improvements in CoO_x reducibility and cobalt dispersion were evidenced in this study for the promoted catalysts with NMs. Even though, iridium resulted in higher reducibility among the NMs (~ 87 %), ruthenium with highest reduced cobalt dispersion (9 %) exhibited the highest CO conversion (86.3 %) and hydrocarbon yield, 0.258 $g_{HC}.g_{cat}^{-1}.h^{-1}$.

Table 8.3 FTS activity of 15Co/m-Al_2O_3 catalysts with different promoters at 900 h^{-1}, and their selectivity at ~ 50 % CO conversion (230 ˚C, 2.76 MPa)

Catalyst	TOS (h)	GHSV (h^{-1})	CO Conversion (%)	Yield ($g_{HC} \cdot g_{cat}^{-1} \cdot h^{-1}$)	Selectivity (%)			
					CO_2	CH_4	C_2–C_4	C_{5+}
Co/mAl_2O_3	100	900	60.2	0.185	2.8	14.8	2.6	82.6
	115	1190	49.4	0.189	2.4	15.4	2.9	81.7
CoRu/mAl_2O_3	115	900	86.3	0.258	5.9	15.4	2.2	82.3
	125	2265	50.6	0.358	1.5	12.5	3.3	84.2
CoRe/mAl_2O_3	125	900	84.1	0.247	7.6	16.5	2.8	80.7
	140	2250	49.9	0.340	2.6	13.8	3.1	83.1
CoPt/mAl_2O_3	120	900	81.6	0.239	9.6	17.1	3.3	79.6
	135	2130	50.0	0.319	3.8	15.8	3.5	80.7
CoIr/mAl_2O_3	120	900	80.2	0.228	8.0	19.1	4.1	76.8
	135	2020	50.3	0.305	3.3	17.0	4.5	78.5
CoMn/mAl_2O_3	115	900	62.8	0.193	3.3	14.5	3.3	82.2
	125	1250	51.2	0.196	2.6	14.0	3.5	82.5
CoY/mAl_2O_3	120	900	61.1	0.189	3.5	18.3	2.2	79.4
	135	1210	50.4	0.193	2.3	17.0	2.9	80.1

Obviously, the order of activity in the catalysts follows the fraction of the available surface cobalt (Co^0 dispersion). Nevertheless, in the case of unpromoted and Ir–promoted Co/mAl_2O_3 catalysts with similar cobalt dispersion (~ 7.6 %), it is the greater extent of reduction in CoIr/mAl_2O_3 (~ 87 vs. ~ 61 %) which might have contributed to its higher CO conversion activity (~ 80 vs. ~ 60 %). The catalytic surface has a dynamic nature where active sites undergo reconstruction during the CO+H_2 adsorption, reaction, and intermediates' desorption [21]. The promoters interact with support (structural) and cobalt (electronical) which may benefit maintaining the initial reducibility, active sites density, or improving their resistance to deactivation and sintering during the surface atomic rearrangement [21]. It is hard to distinguish the promoters precise impact on the electronic and structural properties and consequently the catalyst performance. However, more in-depth spectroscopic and in–situ characterization techniques are required to understand dynamic change on the composition and morphology of the surface [85,272].

Addition of manganese and yttrium, in 1 % molar ratio concentration with respect to cobalt, on mesoporous alumina supported cobalt catalyst raised the reducibility by ~ 10 and 14 %, respectively, while the cobalt dispersion was dropped to some extent (from 7.7 to 7.2 %). This trade-off between reducibility increase and dispersion decrease resulted in rather unchanged CO conversion in FTS (from 60.2 to 61.1 %). The marginal improvement in performance of Mn−promoted cobalt catalyst in FTS at lower loading of promoter (Mn/Co = 0.01) has already been reported [273]. Regarding yttrium promotional effect in other research work, 1 wt. % Y was added to 20 wt. % cobalt catalyst supported on the θ-Al_2O_3. TPR, H_2 chemisorption, and XRD characterization showed insignificant changes in the physico-chemical properties, along with negligible variation in FTS activity and selectivity of the catalyst [91]. It is noteworthy that the extent to which the promoter can modify the cobalt catalytic features and performance depends on promoter loading, Co loading. loading sequence, support nature, catalyst preparation method, calcination and reduction treatments [85].

The addition of promoter metal can contribute to cobalt performance via increasing the number of available cobalt sites (textural/structural), enhancing the specific rate of FTS per surface site (electronic/chemical), or altering the reactants concentration at vicinity of active sites and affecting the product selectivity (synergistic) [19,85]. The estimated cobalt site-time-yield (STY) for the promoted catalysts were in the range of $2.1 \times 10^{-2} - 4.0 \times 10^{-2}$ s^{-1} as compared to 1.7×10^{-2} s^{-1} for unpromoted cobalt catalyst. These values for turn over frequency (TOF) are in good agreement with reported TOF data for alumina supported cobalt catalysts in other works [21,271]. It has been rationalized that the small increase in the magnitude of the specific rate of FTS per surface site could be assigned to maintaining the active cobalt sites free from deactivating carbon and oxygen atoms during the FTS reaction [85,268]. The slight changes in the site−based activity of promoted cobalt catalyst in this work would be still consistent with structural−insensitivity assumption of cobalt crystallite size above 6−10 nm in FT reaction [9,19,67,271].

The selectivity of promoted catalysts for FTs products is presented in Table 8.3. The Ru-promoted cobalt catalyst exhibited the highest C_{5+} selectivity of 84.2 % as compared to 81.7 % in unpromoted Co/mAl_2O_3 counterpart at the similar CO conversion level of ~ 50 %. Ruthenium itself is very active catalyst for long chain hydrocarbons (C_{5+}) as compared to other NMs (Re, Pt, Ir) which are not active for CO dissociation [215]. Rhenium also exhibited beneficial impact on C_{5+} selectivity by increasing it to 83.1 %, whereas, Pt and Ir adversely acted. Platinum−promoted cobalt catalyst slightly decreased the C_{5+} selectivity to 80.7, while the iridium lowered it to 78.5%. The promotional effect of manganese on long chain hydrocarbon was marginally positive, while, the yttrium dropped it to 80.1%. As shown in Table 8.3, the

$CoRu/mAl_2O_3$ catalyst with highest selectivity toward long−chain hydrocarbons showed the lowest selectivity (12.5%) to methane product, conversely the $CoIr/mAl_2O_3$ was the most selective catalyst for CH_4 (17%) while being the least selective to C_{5+} cuts. This signifies that the methanation and chain growth compete on the common C_1 monomer thus, less selectivity to heavier hydrocarbons indicates higher chain termination probability on the corresponding catalysts [233].

Utilization of microkinetics and in-situ X-ray adsorption techniques such as EXAFS would be crucial to understand underlying reasons for the activity and selectivity of differently promoted cobalt catalyst during the FT reaction. As a result, associative/dissociative H_2 and CO adsorption (C_1 monomer formation), oxygen desorption (H_2O and CO_2 formation), monomers coupling (chain growth), and hydrogen addition / abstraction to / from C_xH_y intermediates on differently coordinated active sites could be understood [19,87]. The higher activity and productivity of Ru can be assigned to its ability to decelerate the cobalt active site deactivation by inhibiting carbon deposition, slowing down formation of non-active cobalt aluminate, and facilitating oxygen removal from the surface [5,232]. Tsubaki et al. speculated that the higher activity of the Ru-added Co catalyst is attributed to the bridge-adsorbed CO which is more active (easily dissociate) than linear−adsorbed CO [236]. It can be observed that the enhancement of CO conversion in the promoted catalysts (Figure F.1 in Appendix F.) can be mainly correlated with the increase in Co dispersion. The increase in cobalt site atoms on the surface not only contributes to enhancement of the catalyst activity, it also shifts the selectivity toward the higher C_{5+} HCs. As a result, CH_4 selectivity decreases due to increased probability in α-olefin re-adsorption [232].

Source of CO_2 product could be the result of water-gas-shift (WGS) ($CO + H_2O \rightarrow CO_2 + H_2$) reaction and Boudouard reaction ($C + CO \rightarrow CO_2$). Platinum- and iridium-promoted cobalt catalysts increased the CO_2 selectivity from 2.4 to 3.8 and 3.3 %, respectively (at ~ 50% CO conversion), whereas the Ru-added catalyst decreased it to 1.5%. The other promoters did not have significant impact on CO_2 selectivity.

Deactivation pattern of the promoted catalysts was also explored to evaluate the effects of different promoters used at the same atomic ratio on the stability of the Co/mAl_2O_3 catalysts in FT. The time-on-stream data for CO conversion (%) and selectivities of the promoted catalysts were provided in Table F.2 in Appendix F. Comparison of different promoters in terms of stability revealed that the Pt- and Ir-promoted catalysts lost the highest average % of the CO conversion by ~ 0.13 and ~ 0.1 $\frac{\%}{h}$, respectively, in the last 50 h of the time-on-stream. Re, Ru, Mn, and Y lost approximately by 0.06, 0.08, 0.06, and

$0.05\ \frac{\%}{h}$, respectively. This evidenced that the transition metals, Re, and Ru promoted catalysts exhibit more stability compared to Ir and Pt promoted cobalt catalysts supported on the mesoporous alumina. It is speculated that with reduction facilitating promoters, more number of small cobalt oxides, strongly interacting with support, are reduced during the catalyst activation. However, these small reduced cobalt crystallites are highly prone to reoxidation in presence of water during the FT reaction [170]. The findings of this work confirm the different deactivation hindrance of the promoter elements on the chosen level of concentrations and operation conditions. Re from noble metals and the used transition metals exhibit better stability as compared to the counterpart promoters in this study.

In summary, during the promoter screening for the cobalt catalyst all the advantages and disadvantages need be addressed separately for individual elements. For instance, platinum is the more naturally available, highly reducing, moderately active, selective and stable, but very expensive option among the noble metals for FTS Co catalyst, whereas rhenium is naturally scarce element, highly C_{5+} selective, productive, and stable, with quite reasonable price among the noble metals. Ruthenium is moderately high price and very scarce element worldwide, however, according to the results of this work, ruthenium is the most active and C_{5+} selective, moderately stable, highly reducing and dispersing promoter for the cobalt catalyst.

8.5 Conclusions

Addition of Ru, Re, Pt, Ir noble metals (NMs) in mesoporous alumina supported cobalt catalysts $\left(\frac{\text{NM}}{\text{Co}} = \frac{1\ \text{atom}}{100\ \text{atom}}\right)$ significantly increased the cobalt dispersion, and degree of reduction. The impact of NMs on the cobalt crystallite size was not substantial. This was confirmed by calculation of Co^0 size from H_2 chemisorption and XRD analyses. Addition of Mn and Y transition metals in the same atomic ratio (1 %) resulted in mild increase in the Co apparent dispersion and extent of reduction. Prevalent Co-oxide species in all oxidized catalysts was Co_3O_4 which is confirmed by XRD and XANES analyses. After testing all catalysts in the fixed-bed Fischer-Tropsch reactor, the NM-promoted Co/mAl_2O_3 catalysts unveiled a noticeable raise (absolute percentage of ~ 20−27 %) in CO conversion and hydrocarbon productivity. The selectivity of desired C_{5+} products increased as result of Ru and Re addition to cobalt catalyst from 81.7 % to 84.2 and 83.1 %, respectively. In addition, the selectivity of undesired CH_4 product dropped from 15.4% for unpromoted cobalt catalyst to 12.5 and 13.8 %, respectively, for $CoRu/mAl_2O_3$ and $CoRe/mAl_2O_3$ catalysts in FTS. The Pt and Mn exhibited slightly positive impact on the C_{5+} and CH_4 selectivity, whereas Ir and Y adversely affected the product

selectivities. Ru was the most effective option among the promoters added to mAl_2O_3 supported Co catalyst for enhancing the activity and C_{5+} selectivity, while, the employed transition metals exhibited to be more efficient promoters to slow down the catalyst deactivation. Moreover, noble metals could affect the stability of cobalt catalysts in considerably different manner. In this study, Re-promoted catalyst disclosed rather low loss in CO conversion (~ 0.06%/h), comparable to Mn- and Y-promoted Co catalysts in FTS.

CHAPTER 9: CONCLUSIONS AND RECOMMENDATIONS

9.1 Conclusions

The main objectives of this work were to (i) develop multiwalled carbon nanotube (MWCNT) and mesoporous alumina (mAl_2O_3) supported catalysts, and (ii) investigate some of the parameters affecting the performance of Co/CNT, Fe/CNT and Co/mAl_2O_3 catalysts for conversion of syngas into transportation fuels range of hydrocarbons. MWCNTs as a support material were functionalized using different concentrations of nitric acid and corresponding Co based catalysts were examined in the Fischer-Tropsch synthesis (FTS). Further, the functionalized MWCNT were used as support material for iron-based catalyst and the impact of binder loading and pellet shape on the performance of the pelletized Fe/CNT catalysts were studied in FTS. Textual properties of MWCNTs were characterized using nitrogen adsorption and microscopic analyses and the results were compared and discrepancies were discussed. Moreover, mAl_2O_3 was synthesized and used for the Co based catalysts in FTS. In this regard, the impact of organic and aqueous solvents on the structural stability of mesoporous alumina during the catalyst preparation, as well as, the effects of Co loading, promoters, chelating agents, support modifiers on the physico-chemical properties and performance of the corresponding Co/mAl_2O_3 catalysts were investigated for Fischer-Tropsch reaction. The overall conclusions from each phase of this research are summarized below.

- Treatment of CNT support with higher nitric acid concentration (70 wt. %) enhanced the physico-chemical properties (textural, cobalt dispersion and reducibility) and performance of Co catalyst in FTS, in terms of CO conversion and hydrocarbon yield as compared to untreated CNT catalyst.
- Addition of 20 wt. % (as compared to 10 and 15 wt. %) bentonite clay as a binder to promoted Fe/CNT catalyst resulted in maximum bulk crushing strength. The cylindrical pellets were fairly stable with 78% CO conversion and 82 % C_{5+} selectivity as compared to its spherical counterpart catalyst.
- The organic solvents such as ethanol and acetone can significantly retain the textural properties of the mesoposrous alumina support during catalyst preparation. Further, with these solvents, doubling the loading of cobalt from 15 to 30 wt. % on mesoporous alumina increased the HC productivity by 25 %, CO conversion by 13% and C_{5+} selectivity by 4%.
- Among La and Ce, as mesoporous alumina modifiers, La with lower loading (5%) favored the physico-chemical properties of the 15Co/m-Al_2O_3 catalyst and its performance in FTS.
- γ-Al_2O_3 exhibited properties to be a more appropriate support for chelated cobalt catalyst in FTS, especially for chelation with NTA as compared to the mesoporous alumina (m-Al_2O_3).

- Noble metals as promoters for cobalt catalyst in FTS proved to be very efficient candidates to lower the reduction temperature, rise the reducibility and enhance the density of active sites to a great extent as compared to transition metals. These resulted in higher steady-state activity and productivity at similar GHSV.
- Addition of noble metals especially Ru and Re were the optimum option for developing Co/m-Al_2O_3 catalyst in FTS as compared to other promoters and modifiers.

9.2 Recommendations for the future research work

- The loadings of Ce and La modifiers on mesoporous alumina support need to be optimized for the cobalt-based catalysts in FTS.
- Effects of zirconia, titania, silica and manganese oxide as modifiers for mesoporous Al_2O_3 supported Co catalysts need to be studied for FT process.
- Loading of Ru and Re promoters on Co/m-Al_2O_3 catalysts need to be optimized for FTS.
- Palletization of optimum promoted Co/m-Al_2O_3 catalyst for pilot plant scale production along with technoeconomic and life cycle analysis need to be studied.

REFERENCES

[1] M.E. Dry, The Fischer-Tropsch process: 1950-2000, Catal. Today. 71 (2002) 227–241.

[2] A. Steynberg, M.E. Dry, Introduction to Fischer-Tropsch technology, in: Fischer-Tropsch Technol., Elsevier Science & Technology Books, 2004: pp. 1–63.

[3] A.C. Vosloo, Fischer–Tropsch: a futuristic view, Fuel Process. Technol. 71 (2001) 149–155.

[4] P.M. Maitlis, A. de Klerk, What is Fischer–Tropsch?, in: Greener Fischer-Tropsch Process. Fuels Feed., Wiley-VCH Verlag & Co. KgaA, 2013: pp. 1–15.

[5] A.Y. Khodakov, W. Chu, P. Fongarland, Advances in the development of novel cobalt Fischer-Tropsch catalysts for synthesis of long-chain hydrocarbons and clean fuels, Chem. Rev. 107 (2007) 1692–1744.

[6] Z. Wang, Z. Yan, C. Liu, D.W. Goodman, Surface Science Studies on Cobalt Fischer-Tropsch Catalysts, ChemCatChem. 3 (2011) 551–559.

[7] J. Zhang, J. Chen, J. Ren, Y. Sun, Chemical treatment of γ-Al2O3 and its influence on the properties of Co-based catalysts for Fischer-Tropsch synthesis, Appl. Catal. A Gen. 243 (2003) 121–133.

[8] S.K. Beaumont, Recent developments in the application of nanomaterials to understanding molecular level processes in cobalt catalysed Fischer–Tropsch synthesis, Phys. Chem. Chem. Phys. 16 (2014) 5034.

[9] J. van de Loosdrecht, F.G. Botes, I.M. Ciobica, A. Ferreira, P. Gibson, D.J. Moodley, A.M. Saib, J.L. Visagie, C.J. Weststrate, J.W. Niemantsverdriet, Fischer–Tropsch Synthesis: Catalysts and Chemistry, in: Compr. Inorg. Chem. II, 2013: pp. 525–557.

[10] S. Cornot-Gandolphe, China's Coal Market – Can Beijing Tame "King Coal"?, 2014.

[11] J. Xu, Y. Yang, Y.W. Li, Recent development in converting coal to clean fuels in China, Fuel. 152 (2015) 122–130.

[12] Advancing towards U.S. Dept. of Agriculture Loan Guarantee, (2017). http://www.velocys.com/press/nr/nr170619.php.

[13] Alberta Energy Regulator Approval to Build Canada's First Commercial Gas to Liquids Plant, (2017). http://mailchi.mp/7c756dc15218/expander-energy-inc.

[14] E. van Steen, H. Schulz, Polymerisation kinetics of the Fischer–Tropsch CO hydrogenation using iron and cobalt based catalysts, Appl. Catal. A Gen. 186 (1999) 309–320. http:

[15] A. de Klerk, E. Furimsky, Catalysis in the Refining of Fischer-Tropsch Syncrude, The Royal Society of Chemistry, 2010.

[16] P.M. Maitlis, A. de Klerk, Greener Fischer-Tropsch Processes for Fuels and Feedstocks, WILEY-VCH Verlag GmbH & Co. KGaA, 2013.

[17] I.C. Yates, C.N. Satterfield, Intrinsic Kinetics of the Fischer-Tropsch Synthesis on a Cobalt Catalyst, Energy & Fuels. 5 (1991) 168–173.

[18] H. Schulz, K. Beck, E. Erich, Mechanism of the Fischer Tropsch process, in: Stud. Surf. Sci.

Catal., 1988: pp. 457–471.

[19] E. Iglesia, Design, synthesis, and use of cobalt-based Fischer-Tropsch synthesis catalysts, Appl. Catal. A Gen. 161 (1997) 59–78.

[20] M. Ojeda, R. Nabar, A.U. Nilekar, A. Ishikawa, M. Mavrikakis, E. Iglesia, CO activation pathways and the mechanism of Fischer-Tropsch synthesis, J. Catal. 272 (2010) 287–297.

[21] C.H. Bartholomew, R.J. Farrauto, Hydrogen production and synthesis gas reactions, Wiley Online Library, 2006.

[22] E. de Smit, B.M. Weckhuysen, The renaissance of iron-based Fischer–Tropsch synthesis: on the multifaceted catalyst deactivation behaviour, Chem. Soc. Rev. 37 (2008) 2758.

[23] Q. Zhang, J. Kang, Y. Wang, Development of Novel Catalysts for Fischer-Tropsch Synthesis: Tuning the Product Selectivity, ChemCatChem. 2 (2010) 1030–1058.

[24] M.E. Dry, The Fischer-Tropsch process: 1950-2000, in: Catal. Today, 2002: pp. 227–241.

[25] S.R. Deshmukh, A.L.Y. Tonkovich, K.T. Jarosch, L. Schrader, S.P. Fitzgerald, D.R. Kilanowski, J.J. Lerou, T.J. Mazanec, Scale-up of microchannel reactors for Fischer-Tropsch synthesis, in: Ind. Eng. Chem. Res., 2010: pp. 10883–10888.

[26] J.J. Lerou, A.L. Tonkovich, L. Silva, S. Perry, J. McDaniel, Microchannel reactor architecture enables greener processes, Chem. Eng. Sci. 65 (2010) 380–385.

[27] R. Myrstad, S. Eri, P. Pfeifer, E. Rytter, A. Holmen, Fischer-Tropsch synthesis in a microstructured reactor, Catal. Today. 147 (2009).

[28] V. Vosoughi, A.K. Dalai, N. Abatzoglou, Y. Hu, Performances of promoted cobalt catalysts supported on mesoporous alumina for Fischer-Tropsch synthesis, Appl. Catal. A Gen. 547 (2017). doi:10.1016/j.apcata.2017.08.032.

[29] V. Vosoughi, S. Badoga, A.K. Dalai, N. Abatzoglou, Modification of mesoporous alumina as a support for cobalt-based catalyst in Fischer-Tropsch synthesis, Fuel Process. Technol. 162 (2017) 55–65.

[30] A.P. Vogel, B. Van Dyk, A.M. Saib, GTL using efficient cobalt Fischer-Tropsch catalysts, Catal. Today. 259 (2015) 323–330.

[31] J. Regalbuto, Catalyst Preparation : Science and Engineering, 2006.

[32] D.B. Bukur, X. Lang, D. Mukesh, W.H. Zimmerman, M.P. Rosynek, C. Lii, Binder / Support Effects on the Activity and Selectivity of Iron Catalysts in the Fischer-Tropsch Synthesis, Ind. Eng. Chem. Res. 29 (1990) 1588–1599.

[33] C.H. Bartholomew, R.C. Reuel, Cobalt-Support Interactions: Their Effects on Adsorption and CO Hydrogenation Activity and Selectivity Properties, Ind. Eng. Chem. Prod. Res. Dev. 24 (1985) 56–61.

[34] Z. Pan, D.B. Bukur, Fischer-Tropsch synthesis on Co/ZnO catalyst - Effect of pretreatment procedure, Appl. Catal. A Gen. 404 (2011) 74–80.

[35] M.K. Gnanamani, M.C. Ribeiro, W. Ma, W.D. Shafer, G. Jacobs, U.M. Graham, B.H. Davis, Fischer-Tropsch synthesis: Metal-support interfacial contact governs oxygenates selectivity over CeO2 supported Pt-Co catalysts, Appl. Catal. A Gen. 393 (2011) 17–23.

[36] R.P. Marin, S.A. Kondrat, T.E. Davies, D.J. Morgan, D.I. Enache, G.B. Combes, S.H. Taylor, J.K. Bartley, G.J. Hutchings, Novel cobalt zinc oxide Fischer-Tropsch catalysts synthesised using supercritical anti-solvent precipitation, Catal. Sci. Technol. 4 (2014) 1970–1978.

[37] E. Iglesia, S.L. Soled, J.E. Baumgartner, S.C. Reyes, Synthesis and Catalytic Properties of Eggshell Cobalt Catalysts for the Fischer-Tropsch Synthesis, J. Catal. 153 (1995) 108–122.

[38] H. Jahangiri, J. Bennett, P. Mahjoubi, K. Wilson, S. Gu, A review of advanced catalyst development for Fischer-Tropsch synthesis of hydrocarbons from biomass derived syn-gas, Catal. Sci. Technol. 4 (2014) 2210–2229.

[39] R. Luque, A.R. de la Osa, J.M. Campelo, A.A. Romero, J.L. Valverde, P. Sanchez, Design and development of catalysts for Biomass-To-Liquid-Fischer–Tropsch (BTL-FT) processes for biofuels production, Energy Environ. Sci. 5 (2012) 5186.

[40] E. van Steen, M. Claeys, Fischer-Tropsch Catalysts for the Biomass-to-Liquid (BTL)-Process, Chem. Eng. Technol. 31 (2008) 655–666.

[41] Ø. Borg, P.D.C. Dietzel, A.I. Spjelkavik, E.Z. Tveten, J.C. Walmsley, S. Diplas, S. Eri, A. Holmen, E. Rytter, Fischer-Tropsch synthesis: Cobalt particle size and support effects on intrinsic activity and product distribution, J. Catal. 259 (2008) 161–164.

[42] C. Márquez-Alvarez, N. Žilková, J. Pérez-Pariente, J. Čejka, Synthesis, Characterization and Catalytic Applications of Organized Mesoporous Aluminas, Catal. Rev. 50 (2008) 222–286.

[43] a. M. Saib, M. Claeys, E. van Steen, Silica supported cobalt Fischer–Tropsch catalysts: effect of pore diameter of support, Catal. Today. 71 (2002) 395–402.

[44] A.Y. Khodakov, A. Griboval-Constant, R. Bechara, V.L. Zholobenko, Pore Size Effects in Fischer Tropsch Synthesis over Cobalt-Supported Mesoporous Silicas, J. Catal. 206 (2002) 230–241.

[45] S. Storsæter, B. Tøtdal, J.C. Walmsley, B.S. Tanem, A. Holmen, Characterization of alumina-, silica-, and titania-supported cobalt Fischer-Tropsch catalysts, J. Catal. 236 (2005) 139–152.

[46] S. Rane, Ø. Borg, J. Yang, E. Rytter, A. Holmen, Effect of alumina phases on hydrocarbon selectivity in Fischer-Tropsch synthesis, Appl. Catal. A Gen. 388 (2010) 160–167.

[47] Ø. Borg, S. Eri, E.A. Blekkan, S. Storsater, H. Wigum, E. Rytter, A. Holmen, Fischer–Tropsch synthesis over γ-alumina-supported cobalt catalysts: Effect of support variables, J. Catal. 248 (2007) 89–100.

[48] K. Shimura, T. Miyazawa, T. Hanaoka, S. Hirata, Fischer-Tropsch synthesis over alumina supported cobalt catalyst: Effect of crystal phase and pore structure of alumina support, J. Mol. Catal. A Chem. 394 (2014) 22–32.

[49] A. Martínez, G. Prieto, J. Rollán, Nanofibrous γ-Al2O3 as support for Co-based Fischer-Tropsch catalysts: Pondering the relevance of diffusional and dispersion effects on catalytic performance, J. Catal. 263 (2009) 292–305.

[50] A.Y. Khodakov, A. Griboval-Constant, R. Bechara, F. Villain, Pore-size control of cobalt dispersion and reducibility in mesoporous silicas, J. Phys. Chem. B. 105 (2001) 9805–9811. doi:10.1021/jp011989u.

[51] J.-S. Jung, S.W. Kim, D.J. Moon, Fischer–Tropsch Synthesis over cobalt based catalyst

supported on different mesoporous silica, Catal. Today. 185 (2012) 168–174.

[52] L.F.F.P.G. Bragana, M. Ojeda, J.L.G. Fierro, M.I.P. Da Silva, Bimetallic Co-Fe nanocrystals deposited on SBA-15 and HMS mesoporous silicas as catalysts for Fischer-Tropsch synthesis, Appl. Catal. A Gen. 423–424 (2012) 146–153.

[53] A. Martínez, G. Prieto, The application of zeolites and periodic mesoporous silicas in the catalytic conversion of synthesis gas, Top. Catal. 52 (2009) 75–90.

[54] S.H. Kang, J.H. Ryu, J.H. Kim, P.S. Sai Prasad, J.W. Bae, J.Y. Cheon, K.W. Jun, ZSM-5 supported cobalt catalyst for the direct production of gasoline range hydrocarbons by Fischer-Tropsch synthesis, Catal. Letters. 141 (2011) 1464–1471.

[55] P. Concepción, C. López, A. Martínez, V.F. Puntes, Characterization and catalytic properties of cobalt supported on delaminated ITQ-6 and ITQ-2 zeolites for the Fischer-Tropsch synthesis reaction, J. Catal. 228 (2004) 321–332.

[56] Y. Yang, K. Chiang, N. Burke, Porous carbon-supported catalysts for energy and environmental applications: A short review, Catal. Today. 178 (2011) 197–205.

[57] V. Calvino-Casilda, A.J. Lopez-Peinado, C.J. Duran-Valle, R.M. Martin-Aranda, Last decade of research on activated carbons as catalytic support in chemical processes, Catal. Rev. - Sci. Eng. 52 (2010) 325–380.

[58] W. Ma, E.L. Kugler, D.B. Dadyburjor, Effect of Mo loading and support type on hydrocarbons and oxygenates produced over Fe-Mo-Cu-K catalysts supported on activated carbons, Stud. Surf. Sci. Catal. 163 (2007) 125–140.

[59] W.P. Ma, Y.J. Ding, L.W. Lin, Fischer-Tropsch synthesis over activated-carbon-supported cobalt catalysts: Effect of Co loading and promoters on catalyst performance, Ind. Eng. Chem. Res. 43 (2004) 2391–2398.

[60] W. Ma, E.L. Kugler, D.B. Dadyburjor, Potassium effects on activated-carbon-supported iron catalysts for Fischer-Tropsch synthesis, Energy and Fuels. 21 (2007) 1832–1842.

[61] Y. Pei, S. Jian, Y. Chen, C. Wang, Synthesis of higher alcohols by the Fischer–Tropsch reaction over activated carbon supported CoCuMn catalysts, RSC Adv. 5 (2015) 76330–76336. doi:10.1039/C5RA10804G.

[62] B.R. Ryoo, S.H. Joo, M. Kruk, M. Jaroniec, Ordered Mesoporous Carbons, Adv. Mater. 13 (2001) 677–681.

[63] Y. Yang, L. Jia, Y. Meng, B. Hou, D. Li, Y. Sun, Fischer-Tropsch synthesis over ordered mesoporous carbon supported cobalt catalysts: The role of amount of carbon precursor in catalytic performance, Catal. Letters. 142 (2012) 195–204.

[64] K. Xiong, J. Li, K. Liew, X. Zhan, Preparation and characterization of stable Ru nanoparticles embedded on the ordered mesoporous carbon material for applications in Fischer-Tropsch synthesis, Appl. Catal. A Gen. 389 (2010) 173–178.

[65] M. Oschatz, W.S. Lamme, J. Xie, A.I. Dugulan, K.P. de Jong, Ordered Mesoporous Materials as Supports for Stable Iron Catalysts in the Fischer–Tropsch Synthesis of Lower Olefins, ChemCatChem. 8 (2016) 2846–2852.

[66] K.-S. Ha, G. Kwak, K.-W. Jun, J. Hwang, J. Lee, Ordered mesoporous carbon nanochannel

reactors for high-performance Fischer–Tropsch synthesis, Chem. Commun. 49 (2013) 5141.

[67] G.L. Bezemer, J.H. Bitter, H.P.C.E. Kuipers, H. Oosterbeek, J.E. Holewijn, X. Xu, F. Kapteijn, A.J. Van Diilen, K.P. De Jong, Cobalt particle size effects in the Fischer-Tropsch reaction studied with carbon nanofiber supported catalysts, J. Am. Chem. Soc. 128 (2006) 3956–3964.

[68] P. Serp, E. Castillejos, Catalysis in carbon nanotubes, ChemCatChem. 2 (2010) 41–47.

[69] V. Vosoughi, S. Badoga, A.K. Dalai, N. Abatzoglou, Effect of Pretreatment on Physicochemical Properties and Performance of Multiwalled Carbon Nanotube Supported Cobalt Catalyst for Fischer-Tropsch Synthesis, Ind. Eng. Chem. Res. 55 (2016) 6049–6059.

[70] H. Dai, Carbon nanotubes: Opportunities and challenges, Surf. Sci. 500 (2002) 218–241.

[71] S. Kundu, Y. Wang, W. Xia, M. Muhler, Thermal stability and reducibility of oxygen-containing functional groups on multiwalled carbon nanotube surfaces: A quantitative high-resolution xps and TPD/TPR study, J. Phys. Chem. C. 112 (2008) 16869–16878.

[72] C. Xing, G. Yang, D. Wang, C. Zeng, Y. Jin, R. Yang, Y. Suehiro, N. Tsubaki, Controllable encapsulation of cobalt clusters inside carbon nanotubes as effective catalysts for Fischer-Tropsch synthesis, Catal. Today. 215 (2013) 24–28.

[73] J.-P. Tessonnier, O. Ersen, G. Weinberg, C. Pham-Huu, D.S. Su, R. Schlogl, Selective deposition of metal nanoparticles inside or outside multiwalled carbon nanotubes, ACS Nano. 3 (2009) 2081–2089.

[74] W. Chen, Z. Fan, X. Pan, X. Bao, Effect of confinement in carbon nanotubes on the activity of Fischer-Tropsch iron catalyst, J. Am. Chem. Soc. 130 (2008) 9414–9419.

[75] X. Pan, X. Bao, The effects of confinement inside carbon nanotubes on catalysis, Acc. Chem. Res. 44 (2011) 553–562.

[76] A.N. Khlobystov, Carbon nanotubes: From nano test tube to nano-reactor, ACS Nano. 5 (2011) 9306–9312.

[77] R.M.M. Abbaslou, A. Tavassoli, J. Soltan, A.K. Dalai, Iron catalysts supported on carbon nanotubes for Fischer-Tropsch synthesis: Effect of catalytic site position, Appl. Catal. A Gen. 367 (2009) 47–52.

[78] K.A.S. Fernando, Y. Lin, Y.P. Sun, High aqueous solubility of functionalized single-walled carbon nanotubes, Langmuir. 20 (2004) 4777–4778.

[79] N. Karousis, N. Tagmatarchis, D. Tasis, Current Progress on the Chemical Modification of Carbon Nanotubes, Chem. Rev. 110 (2010) 5366–5397.

[80] R.M.M. Abbaslou, A. Tavassoli, J. Soltan, A.K. Dalai, Iron catalysts supported on carbon nanotubes for Fischer-Tropsch synthesis: Effect of catalytic site position, Appl. Catal. A Gen. 367 (2009) 47–52.

[81] M. Trépanier, A. Tavasoli, A.K. Dalai, N. Abatzoglou, Fischer–Tropsch synthesis over carbon nanotubes supported cobalt catalysts in a fixed bed reactor: Influence of acid treatment, Fuel Process. Technol. 90 (2009) 367–374.

[82] F. Diehl, A.Y. Khodakov, Promotion of Cobalt Fischer-Tropsch catalysts with noble metals: A review, Oil Gas Sci. Technol. 64 (2009) 11–24.

[83] J.P. den Breejen, J.R.A. Sietsma, H. Friedrich, J.H. Bitter, K.P. de Jong, Design of supported cobalt catalysts with maximum activity for the Fischer-Tropsch synthesis, J. Catal. 270 (2010) 146–152.

[84] B. Cornils, W.A. Herrmann, C. Wong, H. Zanthoff, R. Eds, Catalysis from A to Z, 2007.

[85] B.Y.F. Morales, B.M. Weckhuysen, Promotion Effects in Co-based Fischer–Tropsch Catalysis, in: J. J. Spivey and K. M. Dooley (Ed.), Catalysis, RSC Publishing, 2006: pp. 1–40.

[86] B.E. Koel, J. Kim, Promoters and Poisons, in: Handb. Heterog. Catal., 2nd Ed., Wiley-VCH Verlag GmbH & Co. KGaA., 2008: pp. 1593–1624.

[87] C.J. Weststrate, P. van Helden, J.W. Niemantsverdriet, Reflections on the Fischer-Tropsch synthesis: Mechanistic issues from a surface science perspective, Catal. Today. 275 (2016) 100–110.

[88] I. Chorkendorff, J.W. Niemantsverdriet, Concepts of Modern Catalysis and Kinetics, 2003.

[89] E. Rytter, N.E. Tsakoumis, A. Holmen, On the selectivity to higher hydrocarbons in Co-based Fischer–Tropsch synthesis, Catal. Today. 261 (2016) 3–16.

[90] T. Jermwongratanachai, G. Jacobs, W.D. Shafer, V.R.R. Pendyala, W. Ma, M.K. Gnanamani, S. Hopps, G.A. Thomas, B. Kitiyanan, S. Khalid, B.H. Davis, Fischer–Tropsch synthesis: TPR and XANES analysis of the impact of simulated regeneration cycles on the reducibility of Co/alumina catalysts with different promoters (Pt, Ru, Re, Ag, Au, Rh, Ir), Catal. Today. 228 (2014) 15–21.

[91] K. Shimura, T. Miyazawa, T. Hanaoka, S. Hirata, Fischer-Tropsch synthesis over alumina supported cobalt catalyst: Effect of promoter addition, Appl. Catal. A Gen. 494 (2015) 1–11.

[92] O.L. Eliseev, M. V. Tsapkina, O.S. Dement'eva, P.E. Davydov, a. V. Kazakov, a. L. Lapidus, Promotion of cobalt catalysts for the Fischer-Tropsch synthesis with alkali metals, Kinet. Catal. 54 (2013) 207–212. htt.

[93] H. Ming, B.G. Baker, M. Jasieniak, Characterization of cobalt Fischer-Tropsch catalysts. 2. Rare earth-promoted cobalt-silica gel catalysts prepared by wet impregnation, Appl. Catal. A Gen. 381 (2010) 216–225.

[94] J.H. Den Otter, S.R. Nijveld, K.P. De Jong, Synergistic Promotion of Co/SiO2 Fischer-Tropsch Catalysts by Niobia and Platinum, ACS Catal. 6 (2016) 1616–1623.

[95] J. Cheng, P. Hu, P. Ellis, S. French, G. Kelly, C.M. Lok, A DFT study of the chain growth probability in Fischer-Tropsch synthesis, J. Catal. 257 (2008) 221–228.

[96] S.W.T. Price, D.J. Martin, A.D. Parsons, W.A. Sławiński, A. Vamvakeros, S.J. Keylock, A.M. Beale, J.F.W. Mosselmans, Chemical imaging of Fischer-Tropsch catalysts under operating conditions, Sci. Adv. 3 (2017).

[97] J.L. Casci, C.M. Lok, M.D. Shannon, Fischer-Tropsch catalysis: The basis for an emerging industry with origins in the early 20th Century, Catal. Today. 145 (2009) 38–44.

[98] R. Oukaci, A.H. Singleton, J.G. Goodwin, Comparison of patented Co F–T catalysts using fixed-bed and slurry bubble column reactors, Appl. Catal. A Gen. 186 (1999) 129–144.

[99] E. Rytter, A. Holmen, Deactivation and Regeneration of Commercial Type Fischer-Tropsch Co-

Catalysts—A Mini-Review, Catalysts. 5 (2015) 478–499.

[100] F. Diehl and A. Y. Khodakov, Promotion of Cobalt Fischer-Tropsch Catalysts with Noble Metals: a Review, Oil Gas Sci. Technol. 64 (2009) 11–24.

[101] R.M. Malek Abbaslou, J. Soltan, A.K. Dalai, The effects of carbon concentration in the precursor gas on the quality and quantity of carbon nanotubes synthesized by CVD method, Appl. Catal. A. 372 (2010) 147–152.

[102] G.D. Ado Jorio, M.S. Dresselhaus, Carbon nanotubes: Advanced topics in the synthesis, structure, properties and applications, 2008.

[103] R.M. Malek Abbaslou, A. Tavasoli, A.K. Dalai, Effect of pre-treatment on physico-chemical properties and stability of carbon nanotubes supported iron Fischer–Tropsch catalysts, Appl. Catal. A Gen. 355 (2009) 33–41.

[104] R.M. Malek Abbaslou, J. Soltan, A.K. Dalai, Iron catalyst supported on carbon nanotubes for Fischer-Tropsch synthesis: Effects of Mo promotion, Fuel. 90 (2011) 1139–1144.

[105] R.H. Baughman, A. a Zakhidov, W. a de Heer, Carbon nanotubes--the route toward applications., Science. 297 (2002) 787–792.

[106] P. Serp, M. Corrias, P. Kalck, Carbon nanotubes and nanofibers in catalysis, Appl. Catal. A Gen. 253 (2003) 337–358.

[107] M. Trojanowicz, Analytical applications of carbon nanotubes: a review, TrAC - Trends Anal. Chem. 25 (2006) 480–489.

[108] Z. Li, Z. Pan, S. Dai, Nitrogen adsorption characterization of aligned multiwalled carbon nanotubes and their acid modification, J. Colloid Interface Sci. 277 (2004) 35–42.

[109] W.A. de Heer, A. Châtelain, D. Ugarte, A Carbon Nanotube Field-Emission Electron Source, Science (80-.). 270 (1995) 1179–1180.

[110] Y. Yao, C. Ma, J. Wang, W. Qiao, L. Ling, D. Long, Rational design of high-surface-area carbon nanotube/microporous carbon core-shell nanocomposites for supercapacitor electrodes, ACS Appl. Mater. Interfaces. 7 (2015) 4817–4825.

[111] K.M. Marr, B. Chen, E.J. Mootz, J. Geder, M. Pruessner, B.J. Melde, R.R. Vanfleet, I.L. Medintz, B.D. Iverson, J.C. Claussen, High Aspect Ratio Carbon Nanotube Membranes Decorated with Pt Nanoparticle Urchins for Micro Underwater Vehicle Propulsion via H 2 O 2 Decomposition, ACS Nano. 9 (2015) 7791–7803.

[112] C. Gommes, S. Blacher, N. Dupont-Pavlovsky, C. Bossuot, M. Lamy, A. Brasseur, D. Marguillier, A. Fonseca, E. McRae, J.B. Nagy, J.P. Pirard, Comparison of different methods for characterizing multi-walled carbon nanotubes, in: Colloids Surfaces A Physicochem. Eng. Asp., 2004: pp. 155–164.

[113] K. Kaneko, Determination of pore size and pore size distribution. 1. Adsorbents and catalysts, J. Memb. Sci. 96 (1994) 59–89.

[114] H. Zhu, A. Cao, X. Li, C. Xu, Z. Mao, D. Ruan, J. Liang, D. Wu, Hydrogen adsorption in bundles of well-aligned carbon nanotubes at room temperature, Appl. Surf. Sci. 178 (2001) 50–55.

[115] V.B. Fenelonov, A.Y. Derevyankin, L.G. Okkel, L.B. Avdeeva, V.I. Zaikovskii, E.M. Moroz, A.N. Salanov, N. a. Rudina, V. a. Likholobov, S.K. Shaikhutdinov, Structure and texture of filamentous carbons produced by methane decomposition on NI and NI-CU catalysts, Carbon N. Y. 35 (1997) 1129–1140.

[116] Y. Shih, M. Li, Adsorption of selected volatile organic vapors on multiwall carbon nanotubes., J. Hazard. Mater. 154 (2008) 21–28.

[117] Y.-C. Chiang, P.-Y. Wu, Adsorption equilibrium of sulfur hexafluoride on multi-walled carbon nanotubes., J. Hazard. Mater. 178 (2010) 729–738.

[118] R.M.M. Abbaslou, J. Soltan, A.K. Dalai, Effects of nanotubes pore size on the catalytic performances of iron catalysts supported on carbon nanotubes for Fischer–Tropsch synthesis, Appl. Catal. A Gen. 379 (2010) 129–134.

[119] L.J. Kennedy, J.J. Vijaya, G. Sekaran, J. Joseph, J.D. Rani, J. Pragasam, Bulk preparation and characterization of mesoporous carbon nanotubes by catalytic decomposition of cyclohexane on sol-gel prepared Ni-Mo-Mg oxide catalyst, Mater. Lett. 60 (2006) 3735–3740.

[120] C. Lu, H. Chiu, Adsorption of zinc(II) from water with purified carbon nanotubes, Chem. Eng. Sci. 61 (2006) 1138–1145.

[121] P.X. Hou, Q.H. Yang, S. Bai, S.T. Xu, M. Liu, H.M. Cheng, Bulk storage capacity of hydrogen in purified multiwalled carbon nanotubes, J. Phys. Chem. B. 106 (2002) 963–966.

[122] R.Q. Long, R.T. Yang, Carbon nanotubes as a superior sorbent for nitrogen oxides, Ind. Eng. Chem. Res. 40 (2001) 4288–4291.

[123] R.M. Malek Abbaslou, A. Tavasoli, A.K. Dalai, Effect of pre-treatment on physico-chemical properties and stability of carbon nanotubes supported iron Fischer-Tropsch catalysts, Appl. Catal. A Gen. 355 (2009) 33–41.

[124] C.H. Bartholomew, R.J. Farrauto, Catalyst Characterization and Selection, in: Fundam. Ind. Catal. Process., John Wiley & Sons, Inc., 2005: pp. 118–196.

[125] M. Thommes, K. Kaneko, A. V. Neimark, J.P. Olivier, F. Rodriguez-Reinoso, J. Rouquerol, K.S.W. Sing, Physisorption of gases, with special reference to the evaluation of surface area and pore size distribution (IUPAC Technical Report), Pure Appl. Chem. 87 (2015) 1051–1069.

[126] ASAP 2020 Accelerated Surface Area and Porosimetry System (Operator's Manual), V4.01, Micromeritics Instrument Corporation, 2011.

[127] T. Miyata, A. Endo, T. Ohmori, T. Akiya, M. Nakaiwa, Evaluation of pore size distribution in boundary region of micropore and mesopore using gas adsorption method, J. Colloid Interface Sci. 262 (2003) 116–125.

[128] M.F. De Lange, T.J.H. Vlugt, J. Gascon, F. Kapteijn, Adsorptive characterization of porous solids: Error analysis guides the way, Microporous Mesoporous Mater. 200 (2014) 199–215.

[129] P. Klobes, K. Meyer, R.G. Munro, Porosity and specific surface area measurements for solid materials, Porosity Specif. Surf. Area Meas. (2006) 11–40.

[130] K.A. Cychosz, R. Guillet-Nicolas, J. García-Martínez, M. Thommes, Recent advances in the textural characterization of hierarchically structured nanoporous materials, Chem. Soc. Rev. 46 (2017) 389–414.

[131] P.X. Hou, S.T. Xu, Z. Ying, Q.H. Yang, C. Liu, H.M. Cheng, Hydrogen adsorption/desorption behavior of multi-walled carbon nanotubes with different diameters, Carbon N. Y. 41 (2003) 2471–2476.

[132] E. Ruckenstein, Y.H. Hu, Catalytic preparation of narrow pore size distribution mesoporous carbon, Carbon N. Y. 36 (1998) 269–275.

[133] D.Y. Kim, C.M. Yang, Y.S. Park, K.K. Kim, S.Y. Jeong, J.H. Han, Y.H. Lee, Characterization of thin multi-walled carbon nanotubes synthesized by catalytic chemical vapor deposition, Chem. Phys. Lett. 413 (2005) 135–141.

[134] Y.-H. Li, Y. Zhu, Y. Zhao, D. Wu, Z. Luan, Different morphologies of carbon nanotubes effect on the lead removal from aqueous solution, Diam. Relat. Mater. 15 (2006) 90–94.

[135] A. Kukovecz, T. Kanyo, Z. Konya, I. Kiricsi, Long-time low-impact ball milling of multi-wall carbon nanotubes, Carbon N. Y. 43 (2005) 994–1000.

[136] Y.H. Hu, E. Ruckenstein, Pore size distribution of single-walled carbon nanotubes, Ind. Eng. Chem. Res. 43 (2004) 708–711.

[137] L. Li, F. Li, C. Liu, H.-M.H. Cheng, Synthesis and characterization of double-walled carbon nanotubes from multi-walled carbon nanotubes by hydrogen-arc discharge, Carbon N. Y. 43 (2005) 623–629.

[138] P. Ciambelli, D. Sannino, M. Sarno, A. Fonseca, J.B. Nagy, Selective formation of carbon nanotubes over Co-modified beta zeolite by CCVD, Carbon N. Y. 43 (2005) 631–640.

[139] Q.F. Hou, X.C. Lu, X.D. Liu, B.X. Hu, J.Q. Cui, J. Shen, The surface fractal investigation on carbon nanotubes modified by the adsorption of poly(acrylic acid), Surf. Coatings Technol. 190 (2005) 394–399.

[140] M. Ge, K. Sattler, Bundles of carbon nanotubes generated by vapor-phase growth, Appl. Phys. Lett. 64 (1994) 710–711.

[141] X. Ren, C. Chen, M. Nagatsu, X. Wang, Carbon nanotubes as adsorbents in environmental pollution management: A review, Chem. Eng. J. 170 (2011) 395–410.

[142] A.C. Vosloo, Fischer-Tropsch: A futuristic view, Fuel Process. Technol. 71 (2001) 149–155.

[143] H. Schulz, Short history and present trends of Fischer–Tropsch synthesis, Appl. Catal. A Gen. 186 (1999) 3–12.

[144] A. de Klerk, Fischer–Tropsch Facilities at a Glance, in: Fischer-Tropsch Refin., Wiley-VCH Verlag & Co. KgaA, 2011: pp. 1–19.

[145] A. Tavasoli, R.M.M. Abbaslou, M. Trepanier, A.K. Dalai, Fischer-Tropsch synthesis over cobalt catalyst supported on carbon nanotubes in a slurry reactor, Appl. Catal. A Gen. 345 (2008) 134–142.

[146] A. Tavasoli, R.M. Malek Abbaslou, A.K. Dalai, Deactivation behavior of ruthenium promoted Co/γ-Al2O3 catalysts in Fischer-Tropsch synthesis, Appl. Catal. A Gen. 346 (2008) 58–64.

[147] A. Solhy, B.F. Machado, J. Beausoleil, Y. Kihn, F. Gonçalves, M.F.R. Pereira, J.J.M. Órfão, J.L. Figueiredo, J.L. Faria, P. Serp, MWCNT activation and its influence on the catalytic performance of Pt/MWCNT catalysts for selective hydrogenation, Carbon N. Y. 46 (2008)

1194–1207.

[148] H.J. Schulte, B. Graf, W. Xia, M. Muhler, Nitrogen- and Oxygen-Functionalized Multiwalled Carbon Nanotubes Used as Support in Iron-Catalyzed, High-Temperature Fischer-Tropsch Synthesis, ChemCatChem. 4 (2012) 350–355.

[149] F. Avilés, J.V. Cauich-Rodríguez, L. Moo-Tah, A. May-Pat, R. Vargas-Coronado, Evaluation of mild acid oxidation treatments for MWCNT functionalization, Carbon N. Y. 47 (2009) 2970–2975.

[150] V. Datsyuk, M. Kalyva, K. Papagelis, J. Parthenios, D. Tasis, A. Siokou, I. Kallitsis, C. Galiotis, Chemical oxidation of multiwalled carbon nanotubes, Carbon N. Y. 46 (2008) 833–840.

[151] M. a. M. Motchelaho, H. Xiong, M. Moyo, L.L. Jewell, N.J. Coville, Effect of acid treatment on the surface of multiwalled carbon nanotubes prepared from Fe–Co supported on CaCO3: Correlation with Fischer–Tropsch catalyst activity, J. Mol. Catal. A Chem. 335 (2011) 189–198.

[152] R. Abbaslou, A. Dalai, Promoted iron catalysts supported on carbon nanotubes for fischer-tropsch synthesis, U.S. patent 20130116350 A1, 2013.

[153] Y. Zhu, Y. Ye, S. Zhang, M.E. Leong, F. Tao, Synthesis and catalysis of location-specific cobalt nanoparticles supported by multiwall carbon nanotubes for Fischer-Tropsch synthesis, Langmuir. 28 (2012) 8275–8280.

[154] H. Zhang, W. Chu, C. Zou, Z. Huang, Z. Ye, L. Zhu, Promotion Effects of Platinum and Ruthenium on Carbon Nanotube Supported Cobalt Catalysts for Fischer–Tropsch Synthesis, Catal. Letters. 141 (2010) 438–444.

[155] S. Badoga, K.C. Mouli, K.K. Soni, A.K. Dalai, J. Adjaye, Beneficial influence of EDTA on the structure and catalytic properties of sulfided NiMo/SBA-15 catalysts for hydrotreating of light gas oil, Appl. Catal. B Environ. 125 (2012) 67–84.

[156] D. Schanke, Study of Pt-Promoted Cobalt CO Hydrogenation Catalysts, J. Catal. 156 (1995) 85–95.

[157] M. Trépanier, A.K. Dalai, N. Abatzoglou, Synthesis of CNT-supported cobalt nanoparticle catalysts using a microemulsion technique: Role of nanoparticle size on reducibility, activity and selectivity in Fischer–Tropsch reactions, Appl. Catal. A Gen. 374 (2010) 79–86.

[158] Q. Ma, D. Wang, M. Wu, T. Zhao, Y. Yoneyama, N. Tsubaki, Effect of catalytic site position: Nickel nanocatalyst selectively loaded inside or outside carbon nanotubes for methane dry reforming, Fuel. 108 (2013) 430–438.

[159] Q.H. Yang, P.X. Hou, S. Bai, M.Z. Wang, H.M. Cheng, Adsorption and capillarity of nitrogen in aggregated multi-walled carbon nanotubes, Chem. Phys. Lett. 345 (2001) 18–24.

[160] Y.H. Li, S. Wang, Z. Luan, J. Ding, C. Xu, D. Wu, Adsorption of cadmium(II) from aqueous solution by surface oxidized carbon nanotubes, Carbon N. Y. 41 (2003) 1057–1062.

[161] J. Zhu, A. Holmen, D. Chen, Carbon Nanomaterials in Catalysis: Proton Affinity, Chemical and Electronic Properties, and their Catalytic Consequences, ChemCatChem. 5 (2013) 378–401.

[162] P. Delhaes, M. Couzi, M. Trinquecoste, J. Dentzer, H. Hamidou, C. Vix-Guterl, A comparison between Raman spectroscopy and surface characterizations of multiwall carbon nanotubes, Carbon N. Y. 44 (2006) 3005–3013.

[163] W. Li, C. Liang, W. Zhou, J. Qiu, G. Sun, Q. Xin, Preparation and Characterization of Multiwalled Carbon Nanotube-Supported Platinum for Cathode Catalysts of Direct Methanol Fuel Cells, J. Phys. Chem. B. 107 (2003) 6292–6299.

[164] H. Zhang, C. Lancelot, W. Chu, J. Hong, A.Y. Khodakov, P. a. Chernavskii, J. Zheng, D. Tong, The nature of cobalt species in carbon nanotubes and their catalytic performance in Fischer–Tropsch reaction, J. Mater. Chem. 19 (2009) 9241.

[165] F. Rodríguez-reinoso, The role of carbon materials in heterogeneous catalysis, Carbon N. Y. 36 (1998) 159–175.

[166] H.-Y. Lin, Y.-W. Chen, The mechanism of reduction of cobalt by hydrogen, Mater. Chem. Phys. 85 (2004) 171–175.

[167] B. Ernst, A. Bensaddik, L. Hilaire, P. Chaumette, A. Kiennemann, Study on a cobalt silica catalyst during reduction and Fischer–Tropsch reaction: In situ EXAFS compared to XPS and XRD, Catal. Today. 39 (1998) 329–341.

[168] E. Van Steen, F.F. Prinsloo, Comparison of preparation methods for carbon nanotubes supported iron Fischer – Tropsch catalysts, 71 (2002) 327–334.

[169] W. Chu, P.A. Chernavskii, L. Gengembre, G.A. Pankina, P. Fongarland, A.Y. Khodakov, Cobalt species in promoted cobalt alumina-supported Fischer-Tropsch catalysts, J. Catal. 252 (2007) 215–230.

[170] N.E. Tsakoumis, M. Rønning, Ø. Borg, E. Rytter, A. Holmen, Deactivation of cobalt based Fischer–Tropsch catalysts: A review, Catal. Today. 154 (2010) 162–182.

[171] M.C. Bahome, L.L. Jewell, D. Hildebrandt, D. Glasser, N.J. Coville, Fischer-Tropsch synthesis over iron catalysts supported on carbon nanotubes, Appl. Catal. A Gen. 287 (2005) 60–67.

[172] E. van Steen, F.F. Prinsloo, Comparison of preparation methods for carbon nanotubes supported iron Fischer–Tropsch catalysts, Catal. Today. 71 (2002) 327–334.

[173] A. Tavasoli, M. Trépanier, R.M. Malek Abbaslou, A.K. Dalai, N. Abatzoglou, Fischer-Tropsch synthesis on mono- and bimetallic Co and Fe catalysts supported on carbon nanotubes, Fuel Process. Technol. 90 (2009) 1486–1494.

[174] T.O. Eschemann, W.S. Lamme, R.L. Manchester, T.E. Parmentier, A. Cognigni, M. Rønning, K.P. de Jong, Effect of support surface treatment on the synthesis, structure, and performance of Co/CNT Fischer–Tropsch catalysts, J. Catal. 328 (2015) 130–138.

[175] X. Liu, X. Li, K. Fujimoto, Effective control of carbon number distribution during Fischer-Tropsch synthesis over supported cobalt catalyst, Catal. Commun. 8 (2007) 1329–1335.

[176] Q. Zhang, J. Kang, Y. Wang, Development of Novel Catalysts for Fischer-Tropsch Synthesis: Tuning the Product Selectivity, ChemCatChem. 2 (2010) 1030–1058.

[177] T.R. Karl, J.M. Melillo, T.C. Peterson, Global Climate Change Impacts in the United States, 2009.

[178] S.S. Ail, S. Dasappa, Biomass to liquid transportation fuel via Fischer Tropsch synthesis - Technology review and current scenario, Renew. Sustain. Energy Rev. 58 (2016) 267–286.

[179] H. Wang, Y. Yang, J. Xu, H. Wang, M. Ding, Y. Li, Study of bimetallic interactions and

promoter effects of FeZn, FeMn and FeCr Fischer-Tropsch synthesis catalysts, J. Mol. Catal. A Chem. 326 (2010) 29–40.

[180] Y. Yang, H. Xiang, Y. Xu, L. Bai, Y. Li, Effect of potassium promoter on precipitated iron-manganese catalyst for Fischer – Tropsch synthesis, Appl. Catal. A Gen. 266 (2004) 181–194.

[181] A. Mosayebi, M.A. Mehrpouya, R. Abedini, The development of new comprehensive kinetic modeling for Fischer-Tropsch synthesis process over Co-Ru/gamma-Al2O3 nano-catalyst in a fixed-bed reactor, Chem. Eng. J. 286 (2016) 416–426.

[182] Z. Li, R. Liu, Y. Xu, X. Ma, Enhanced Fischer-Tropsch synthesis performance of iron-based catalysts supported on nitric acid treated N-doped CNTs, Appl. Surf. Sci. 347 (2015) 643–650.

[183] L.A. Cano, A.A. Garcia Blanco, G. Lener, S.G. Marchetti, K. Sapag, Effect of the support and promoters in Fischer-Tropsch synthesis using supported Fe catalysts, Catal. Today. 282 (2017) 204–213.

[184] M. Al-Dossary, J.L.G. Fierro, Effect of high-temperature pre-reduction in Fischer-Tropsch synthesis on Fe/ZrO2 catalysts, Appl. Catal. A Gen. 499 (2015) 109–117.

[185] R. Abbaslou, A.K. Dalai, Promoted iron catalysts supported on carbon nanotubes for fischer-tropsch synthesis, US20130116350 A1, 2013.

[186] B.H. Davis, Overview of reactors for liquid phase Fischer – Tropsch synthesis, Catal. Today. 71 (2002) 249–300.

[187] K.M. Brunner, H.D. Perez, R.P.S. Peguin, J.C. Duncan, L.D. Harrison, C.H. Bartholomew, W.C. Hecker, Effects of particle size and shape on the performance of a trickle fixed-bed recycle reactor for fischer-tropsch synthesis, Ind. Eng. Chem. Res. 54 (2015) 2902–2909.

[188] J.H. Yang, H.J. Kim, D.H. Chun, H.T. Lee, J.C. Hong, H. Jung, J. Il Yang, Mass transfer limitations on fixed-bed reactor for Fischer-Tropsch synthesis, Fuel Process. Technol. 91 (2010) 285–289.

[189] Y.-N. Wang, Y.-Y. Xu, H.-W. Xiang, Y.-W. Li, B.-J. Zhang, Modeling of Catalyst Pellets for Fischer-Tropsch Synthesis, Ind. Eng. Chem. Res. 40 (2001) 4324–4335. doi:10.1021/ie010080v.

[190] A. Nanduri, P.L. Mills, Comparison of Diffusion Flux Models for Fischer-Tropsch Synthesis, in: 2015 COMSOL Conf. Bost., 2015: pp. 1–7.

[191] N.O. Elbashir, B. Bao, M.M. El-halwagi, An Approach to the Design of Advanced Fischer-Tropsch Reactor for Operation in Near-Critical and Supercritical Phase Media, Adv. Gas Process. 1 (2009) 423–433.

[192] R. Abbaslou, Iron catalyst supported on carbon nanotubes for Fischer-Tropsch synthesis: experimental and kinetic study, University of Saskatchewan, 2010.

[193] V. Vosoughi, S. Badoga, A.K. Dalai, N. Abatzoglou, Effect of Pretreatment on Physicochemical Properties and Performance of Multiwalled Carbon Nanotube Supported Cobalt Catalyst for Fischer-Tropsch Synthesis, Ind. Eng. Chem. Res. 55 (2016) 6049–6059.

[194] Y. Li, D. Wu, J. Zhang, L. Chang, D. Wu, Z. Fang, Y. Shi, Measurement and statistics of single pellet mechanical strength of differently shaped catalysts, Powder Technol. 113 (2000) 176–184.

[195] K.S.W. Sing;, D.H. Everett;, Reporting physisorptin data for gas/solid systems with special

reference to the determination of surface Area and porosity, Pure Appl. Chem. 57 (1985) 603–619.

[196] S. Badoga, R. V. Sharma, A.K. Dalai, J. Adjaye, Synthesis and characterization of mesoporous aluminas with different pore sizes: Application in NiMo supported catalyst for hydrotreating of heavy gas oil, Appl. Catal. A Gen. 489 (2015) 86–97.

[197] Y. Lu, Q. Yan, J. Han, B. Cao, J. Street, F. Yu, Fischer–Tropsch synthesis of olefin-rich liquid hydrocarbons from biomass-derived syngas over carbon-encapsulated iron carbide/iron nanoparticles catalyst, Fuel. 193 (2017) 369–384.

[198] K. Sudsakorn, J.G. Goodwin, A.A. Adeyiga, Effect of activation method on Fe FTS catalysts: Investigation at the site level using SSITKA, J. Catal. 213 (2003) 204–210.

[199] M.G.A. Cruz, F.A.N. Fernandes, A.C. Oliveira, J.M. Filho, A.C. Oliveira, A.F. Campos, E. Padron-Hernandez, E. Rodriguez-Castellon, Effect of the calcination temperatures of the Fe-based catalysts supported on polystyrene mesoporous carbon for FTS Synthesis, Catal. Today. 282 (2016) 174–184.

[200] M.J. Tiernan, P. a Barnes, G.M.B. Parkes, Reduction of Iron Oxide Catalysts: The Investigation of Kinetic Parameters Using Rate Perturbation and Linear Heating Thermoanalytical Techniques, J. Phys. Chem. B. 105 (2001) 220–228.

[201] W.K. Jozwiak, E. Kaczmarek, T.P. Maniecki, W. Ignaczak, W. Maniukiewicz, Reduction behavior of iron oxides in hydrogen and carbon monoxide atmospheres, Appl. Catal. A Gen. 326 (2007) 17–27.

[202] L.S. Ferreira, J.O. Trierweiler, Modeling and simulation of the polymeric nanocapsule formation process, IFAC Proc. Vol. 7 (2009) 405–410.

[203] E. David, Mechanical strength and reliability of the porous materials used as adsorbents/ catalysts and the new development trends, Arch. Mater. Sci. Eng. 73 (2015) 5–17.

[204] R.J.D. Mark E. Davis, Effects of Transport Limitations on Rates of Solid-Catalyzed Reactions, McGraw-Hill, 2013.

[205] H.S. Fogler, Elements of chemical reaction engineering, Fourth Ed., Prentice Hall PTR, 2006.

[206] W. He, W. Lu, J.H. Dickerson, Gas transport in solid oxide fuel cells, Springer, 2014. doi:10.1007/978-3-319-09737-4.

[207] W. Jianmin, S. Qiwen, Z. Zongsen, P. Lifeng, Diffusion and Reaction Model of Catalyst Pellets for Fischer-Tropsch Synthesis, China Pet. Process. Petrochemical Technol. 15 (2013) 77–86.

[208] A.R. De La Osa, A. De Lucas, A. Romero, J.L. Valverde, P. Sánchez, Influence of the catalytic support on the industrial Fischer-Tropsch synthetic diesel production, Catal. Today. 176 (2011) 298–302.

[209] C. Lesaint, W.R. Glomm, yvind Borg, S. Eri, E. Rytter, G. ye, Synthesis and characterization of mesoporous alumina with large pore size and their performance in Fischer-Tropsch synthesis, Appl. Catal. A Gen. 351 (2008) 131–135.

[210] J.C. Ray, K.S. You, J.W. Ahn, W.S. Ahn, Mesoporous alumina (I): Comparison of synthesis schemes using anionic, cationic, and non-ionic surfactants, Microporous Mesoporous Mater. 100 (2007) 183–190.

[211] K.M.S. Khalil, Formation of mesoporous alumina via hydrolysis of modified aluminum isopropoxide in presence of CTAB cationic surfactant, Appl. Surf. Sci. 255 (2008) 2874–2878.

[212] D. Merino, I. Pérez-Miqueo, O. Sanz, M. Montes, On the Way to a More Open Porous Network of a Co–Re/Al2O3 Catalyst for Fischer–Tropsch Synthesis: Pore Size and Particle Size Effects on Its Performance, Top. Catal. (2015) 1–12.

[213] D. Zhao, J. Feng, Q. Huo, N. Melosh, G.H. Fredrickson, B.F. Chmelka, G.D. Stucky, Triblock Copolymer Syntheses of Mesoporous Silica with Periodic 50 to 300 Angstrom Pores, Science (80-.). 279 (1998) 548–552.

[214] Z. Shan, J.C. Jansen, W. Zhou, T. Maschmeyer, A1-TUD-1, stable mesoporous aluminas with high surface areas, Appl. Catal. A Gen. 254 (2003) 339–343.

[215] W. Ma, G. Jacobs, R.A. Keogh, D.B. Bukur, B.H. Davis, Fischer–Tropsch synthesis: Effect of Pd, Pt, Re, and Ru noble metal promoters on the activity and selectivity of a 25%Co/Al2O3 catalyst, Appl. Catal. A Gen. 437 (2012) 1–9.

[216] M. Trueba, S.P. Trasatti, γ-alumina as a support for catalysts: A review of fundamental aspects, Eur. J. Inorg. Chem. (2005) 3393–3403.

[217] A. Mino, C. Lancelot, P. Blanchard, C. Lamonier, L. Rouleau, M. Roy-Auberger, S. Royer, E. Payen, Potential of templated mesoporous aluminas as supports for HDS CoMo catalysts, New J. Chem. 40 (2016) 4258–4268.

[218] G. Lefèvre, M. Duc, P. Lepeut, R. Caplain, M. Fédoroff, Hydration of γ-alumina in water and its effects on surface reactivity, Langmuir. 18 (2002) 7530–7537.

[219] N. Bejenaru, C. Lancelot, P. Blanchard, C. Lamonier, L. Rouleau, E. Payen, F. Dumeignil, S. Royer, Synthesis, characterization, and catalytic performances of novel CoMo hydrodesulfurization catalysts supported on mesoporous aluminas, Chem. Mater. 21 (2009) 522–533.

[220] B. Huang, C.H. Bartholomew, S.J. Smith, B.F. Woodfield, Facile solvent-deficient synthesis of mesoporous γ-alumina with controlled pore structures, Microporous Mesoporous Mater. 165 (2013) 70–78.

[221] J.C. Groen, L.A.. Peffer, J. Pérez-Ramírez, Pore size determination in modified micro- and mesoporous materials. Pitfalls and limitations in gas adsorption data analysis, Microporous Mesoporous Mater. 60 (2003) 1–17.

[222] H.Y. Zhu, J.D. Riches, J.C. Barry, γ-Alumina nanofibers prepared from aluminum hydrate with poly(ethylene oxide) surfactant, Chem. Mater. 14 (2002) 2086–2093.

[223] B. Huang, C.H. Bartholomew, B.F. Woodfield, Facile synthesis of mesoporous γ-alumina with tunable pore size: The effects of water to aluminum molar ratio in hydrolysis of aluminum alkoxides, Microporous Mesoporous Mater. 183 (2014) 37–47.

[224] S. Barradas, E.A. Caricato, P.J. van Berge, J. van de Loosdrecht, Support modification of cobalt based slurry phase Fischer-Tropsch catalysts, in: Stud. Surf. Sci. Catal., 2000: pp. 55–65.

[225] C.W. Tang, C. Bin Wang, S.H. Chien, Characterization of cobalt oxides studied by FT-IR, Raman, TPR and TG-MS, Thermochim. Acta. 473 (2008) 68–73.

[226] A.Y. Khodakov, Fischer-Tropsch synthesis: Relations between structure of cobalt catalysts and

their catalytic performance, Catal. Today. 144 (2009) 251–257.

[227] H. Romar, A.H. Lillebø, P. Tynjälä, T. Hu, A. Holmen, E.A. Blekkan, U. Lassi, Characterisation and Catalytic Fischer-Tropsch Activity of Co-Ru and Co-Re Catalysts Supported on γ-Al2O3, TiO2 and SiC, Top. Catal. 58 (2015) 887–895.

[228] R.-S. Zhou, R.L. Snyder, Structures and transformation mechanisms of the η, γ, and θ transition aluminas, Acta Crystallogr. Sect. B. 47 (1991) 617–630.

[229] M.L. Guzman-Castillo, F. Hernandez-Beltran, J.J. Fripiat, A. Rodriquez-Hernandez, R.G. De Leon, J. Navarrete-Bolanos, A. Tobon-Cervantes, X. Bokhimi, Physicochemical properties of aluminas obtained from different aluminum salts, in: Catal. Today, 2005: pp. 874–878.

[230] C.W. Tang, C. Bin Wang, S.H. Chien, Characterization of cobalt oxides studied by FT-IR, Raman, TPR and TG-MS, Thermochim. Acta. 473 (2008) 68–73.

[231] L.B. Sun, W.H. Tian, X.Q. Liu, Magnesia-incorporated mesoporous alumina with crystalline frameworks: A solid strong base derived from direct synthesis, J. Phys. Chem. C. 113 (2009) 19172–19178.

[232] E. Iglesia, Design, synthesis, and use of cobalt-based Fischer-Tropsch synthesis catalysts, Appl. Catal. A Gen. 161 (1997) 59–78.

[233] E. Rytter, N.E. Tsakoumis, A. Holmen, On the selectivity to higher hydrocarbons in Co-based Fischer-Tropsch synthesis, Catal. Today. 261 (2016) 3–16.

[234] S.C. LeViness, S.R. Deshmukh, L.A. Richard, H.J. Robota, Velocys Fischer-Tropsch Synthesis Technology - New Advances on State-of-the-Art, Top. Catal. 57 (2014) 518–525.

[235] A.Y. Khodakov, R. Bechara, A. Griboval-Constant, Fischer–Tropsch synthesis over silica supported cobalt catalysts: mesoporous structure versus cobalt surface density, Appl. Catal. A Gen. 254 (2003) 273–288.

[236] N. Tsubaki, S. Sun, K. Fujimoto, Different Functions of the Noble Metals Added to Cobalt Catalysts for Fischer-Tropsch Synthesis, J. Catal. 199 (2001) 236–246.

[237] C. Liu, J. Li, Y. Zhang, S. Chen, J. Zhu, K. Liew, Fischer-Tropsch synthesis over cobalt catalysts supported on nanostructured alumina with various morphologies, J. Mol. Catal. A Chem. 363–364 (2012) 335–342.

[238] S. All, B. Chen, J.G. Goodwin Jr., Zr Promotion of Co/SiO2 for Fischer-Tropsch Synthesis, J. Catal. 157 (1995) 35–41.

[239] F. Rohr, O.A. Lindvåg, A. Holmen, E.A. Blekkan, Fischer-Tropsch Synthesis over Cobalt Catalysts Supported on Zirconia-Modified Alumina, Catal. Today. 58 (2000) 247–254. https://abingdonsharedfiles.box.com/s/ra45il116u85ym5rwmtymwowpqb9blkb.

[240] P. Osorio-Vargas, N.A. Flores-González, R.M. Navarro, J.L.G. Fierro, C.H. Campos, P. Reyes, Improved stability of Ni/Al2O3 catalysts by effect of promoters (La2O3, CeO2) for ethanol steam-reforming reaction, Catal. Today. 259 (2016) 27–38.

[241] S. Vada, B. Chen, J.G. Goodwin, Isotopic Transient Study of La Promotion of Co/Al2O3 or CO Hydrogenation, J. Catal. 153 (1995) 224–231.

[242] B. Ernst, L. Hilaire, A. Kiennemann, Effects of highly dispersed ceria addition on reducibility,

activity and hydrocarbon chain growth of a Co/SiO2 Fischer–Tropsch catalyst, Catal. Today. 50 (1999) 413–427.

[243] G.J. Haddad, B. Chen, J.G. Goodwin, Jr., Effect of La3+ Promotion of Co/SiO2 on CO Hydrogenation, J. Catal. 161 (1996) 274–281.

[244] T. Mochizuki, D. Hongo, T. Satoh, N. Koizumi, M. Yamada, Improvement of the Fischer-Tropsch synthesis activity of Co/SiO2 catalyst by the stepwise impregnation method with chelating agents, Catal. Letters. 121 (2008) 52–57.

[245] A.J. Van Dillen, R.J.A.M. Terörde, D.J. Lensveld, J.W. Geus, K.P. De Jong, Synthesis of supported catalysts by impregnation and drying using aqueous chelated metal complexes, in: J. Catal., 2003: pp. 257–264.

[246] L. He, B. Teng, Y. Zhang, M. Fan, Development of composited rare-earth promoted cobalt-based Fischer-Tropsch synthesis catalysts with high activity and selectivity, Appl. Catal. A Gen. 505 (2015) 276–283.

[247] G.J. Haddad, B. Chen, J.G. Goodwin, Jr., Characterization of La3+-Promoted Co/SiO2 Catalysts, J. Catal. 160 (1996) 43–51.

[248] N. Koizumi, T. Mochizuki, M. Yamada, Preparation of highly active catalysts for ultra-clean fuels, Catal. Today. 141 (2009) 34–42.

[249] A.S. Bambal, E.L. Kugler, T.H. Gardner, D.B. Dadyburjor, Effect of Surface Modification by Chelating Agents on Fischer–Tropsch Performance of Co/SiO2 Catalysts, Ind. Eng. Chem. Res. 52 (2013) 16675–16688.

[250] A. Jean-Marie, A. Griboval-Constant, A.Y. Khodakov, F. Diehl, Influence of sub-stoichiometric sorbitol addition modes on the structure and catalytic performance of alumina-supported cobalt Fischer-Tropsch catalysts, Catal. Today. 171 (2011) 180–185.

[251] S. Zeng, Y. Du, H. Su, Y. Zhang, Promotion effect of single or mixed rare earths on cobalt-based catalysts for Fischer-Tropsch synthesis, Catal. Commun. 13 (2011) 6–9.

[252] G.R. Johnson, A.T. Bell, Effects of Lewis acidity of metal oxide promoters on the activity and selectivity of Co-based Fischer-Tropsch synthesis catalysts, J. Catal. 338 (2016) 250–264.

[253] T. Mochizuki, T. Hara, N. Koizumi, M. Yamada, Novel preparation method of highly active Co/SiO2 catalyst for Fischer-Tropsch synthesis with chelating agents, Catal. Letters. 113 (2007) 165–169.

[254] R.M. Smith, A.E. Martell, Critical stability constants, enthalpies and entropies for the formation of metal complexes of aminopolycarboxylic acids and carboxylic acids, Sci. Total Environ. 64 (1987) 125–147.

[255] B.H. Davis, Fischer-Tropsch synthesis: Comparison of performances of iron and cobalt catalysts, in: Ind. Eng. Chem. Res., 2007: pp. 8938–8945.

[256] E.F. Sousa-Aguiar, F.B. Noronha, J.A. Faro, The main catalytic challenges in GTL (gas-to-liquids) processes, Catal. Sci. Technol. 1 (2011) 698–713.

[257] J. Hong, P.A. Chernavskii, A.Y. Khodakov, W. Chu, Effect of promotion with ruthenium on the structure and catalytic performance of mesoporous silica (smaller and larger pore) supported cobalt Fischer-Tropsch catalysts, Catal. Today. 140 (2009) 135–141.

[258] T.O. Eschemann, J. Oenema, K.P. De Jong, Effects of noble metal promotion for Co/TiO2 Fischer-Tropsch catalysts, Catal. Today. 261 (2016) 60–66.

[259] G. Jacobs, T.K. Das, Y. Zhang, J. Li, G. Racoillet, B.H. Davis, Fischer-Tropsch synthesis: Support, loading, and promoter effects on the reducibility of cobalt catalysts, Appl. Catal. A Gen. 233 (2002) 263–281.

[260] K.M. Cook, H.D. Perez, C.H. Bartholomew, W.C. Hecker, Effect of promoter deposition order on platinum-, ruthenium-, or rhenium-promoted cobalt Fischer-Tropsch catalysts, Appl. Catal. A Gen. 482 (2014) 275–286.

[261] G. Słowik, A. Gawryszuk-Rżysko, M. Greluk, A. Machocki, Estimation of Average Crystallites Size of Active Phase in Ceria-Supported Cobalt-Based Catalysts by Hydrogen Chemisorption vs TEM and XRD Methods, Catal. Letters. 146 (2016) 2173–2184.

[262] T.E.W. Jr., Metal Particle Size Determination of Supported Metal Catalysts, Catal. Rev. 8 (1974) 117–134.

[263] F. Pinna, Supported metal catalysts preparation, Catal. Today. 41 (1998) 129–137.

[264] M.D. Shannon, C.M. Lok, J.L. Casci, Imaging promoter atoms in Fischer-Tropsch cobalt catalysts by aberration-corrected scanning transmission electron microscopy, J. Catal. 249 (2007) 41–51.

[265] A.M. Saib, A. Borgna, J. van de Loosdrecht, P.J. van Berge, J.W. Geus, J.W. Niemantsverdriet, Preparation and characterisation of spherical Co/SiO2 model catalysts with well-defined nano-sized cobalt crystallites and a comparison of their stability against oxidation with water, J. Catal. 239 (2006) 326–339.

[266] T.K. Das, G. Jacobs, P.M. Patterson, W.A. Conner, J. Li, B.H. Davis, Fischer-Tropsch synthesis: Characterization and catalytic properties of rhenium promoted cobalt alumina catalysts, Fuel. 82 (2003) 805–815.

[267] V. V Rozanov, O. V Krylov, Hydrogen spillover in heterogeneous catalysis, Russ. Chem. Rev. 66 (2007) 107–119.

[268] E. Iglesia, S.L. Soled, R.A. Fiato, G.H. Via, Bimetallic Synergy in Cobalt Ruthenium Fischer-Tropsch Synthesis Catalysts, J. Catal. 143 (1993) 345–368. doi:10.1006/jcat.1993.1281.

[269] B. Hammer, J.K. Norskov, Theoretical Surface Science and Catalysis — Calculations and Concepts, Adv. Catal. 45 (2000) 71–129.

[270] J.K. Nørskov, F. Abild-Pedersen, F. Studt, T. Bligaard, Density functional theory in surface chemistry and catalysis., Proc. Natl. Acad. Sci. U. S. A. 108 (2011) 937–43.

[271] F.H. Ribeiro, A.E.S. Von Wittenau, C.H. Bartholomew, G. Somorjai, A, Reproducibility of Turnover Rates in Heterogeneous Metal Catalysis: Compilation of Data and Guidelines for Data Analysis, Catal. Rev. 39 (1997) 49–76.

[272] G. Jacobs, W. Ma, P. Gao, B. Todic, T. Bhatelia, D.B. Bukur, B.H. Davis, The application of synchrotron methods in characterizing iron and cobalt Fischer-Tropsch synthesis catalysts, Catal. Today. 214 (2013) 100–139.

[273] G.R. Johnson, S. Werner, A.T. Bell, An Investigation into the Effects of Mn Promotion on the Activity and Selectivity of Co/SiO2 for Fischer-Tropsch Synthesis: Evidence for Enhanced CO

Adsorption and Dissociation, ACS Catal. 5 (2015) 5888–5903.

APPENDIX A: CNT ACID TREATMENT SETUP

Figure A.1 Acid treatment (functionalization) set-up for CNTs

APPENDIX B: FTS SETUP

Figure B.1 Fixed-bed reactor for Fischer-Tropsch experimental set-up in the lab

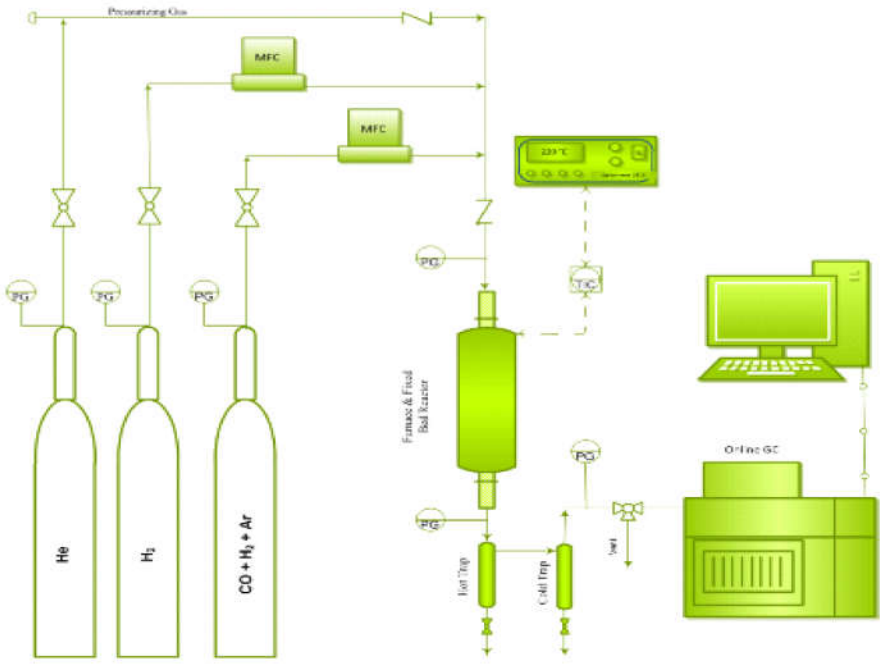

Figure B.2 Schematic for Fischer-Tropsch reaction set-up

APPENDIX C: CALIBRATION CURVES USED FOR FIXED-BED FT REACTOR

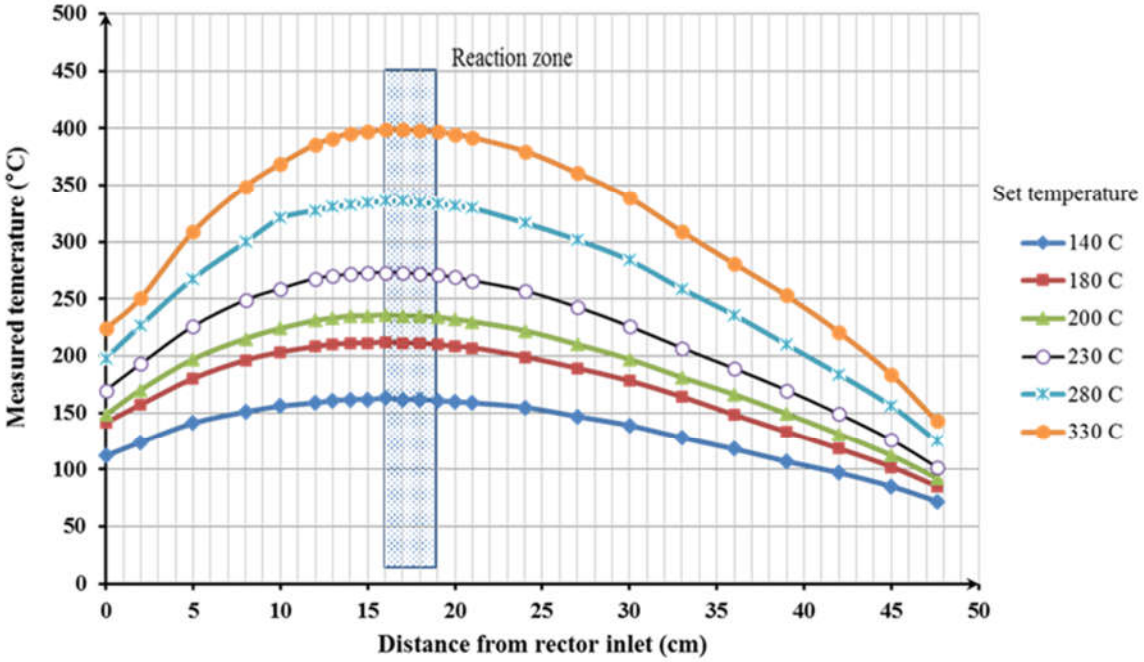

Figure C.1 Temperature profile along the fixed-bed FT reactor

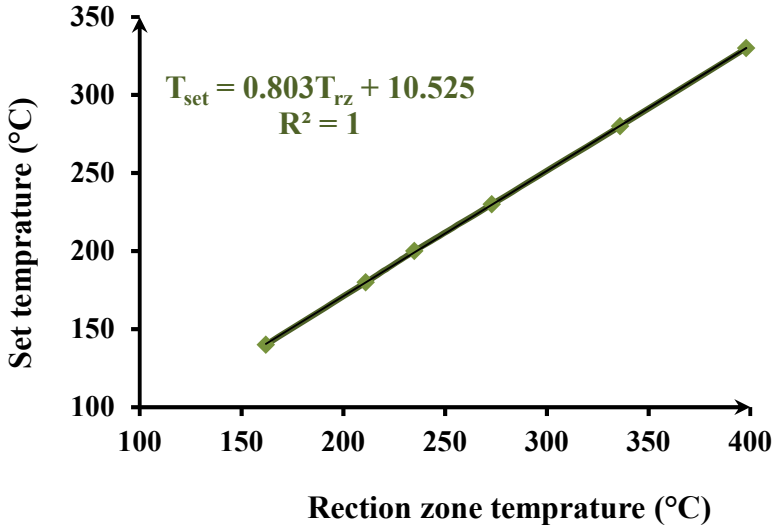

Figure C.2 Temperature calibration curve for reaction zone in FTS reactor

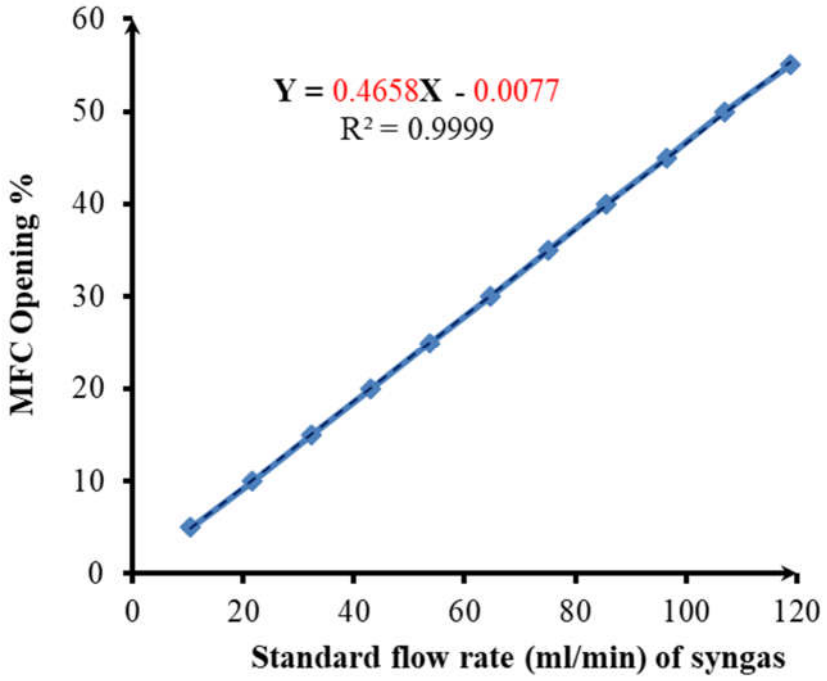

Figure C.3 Mass flow controller (MFC) calibration for syngas flow into FT reactor

APPENDIX D: SUPPORTING INFORMATION FOR CHAPTER 4

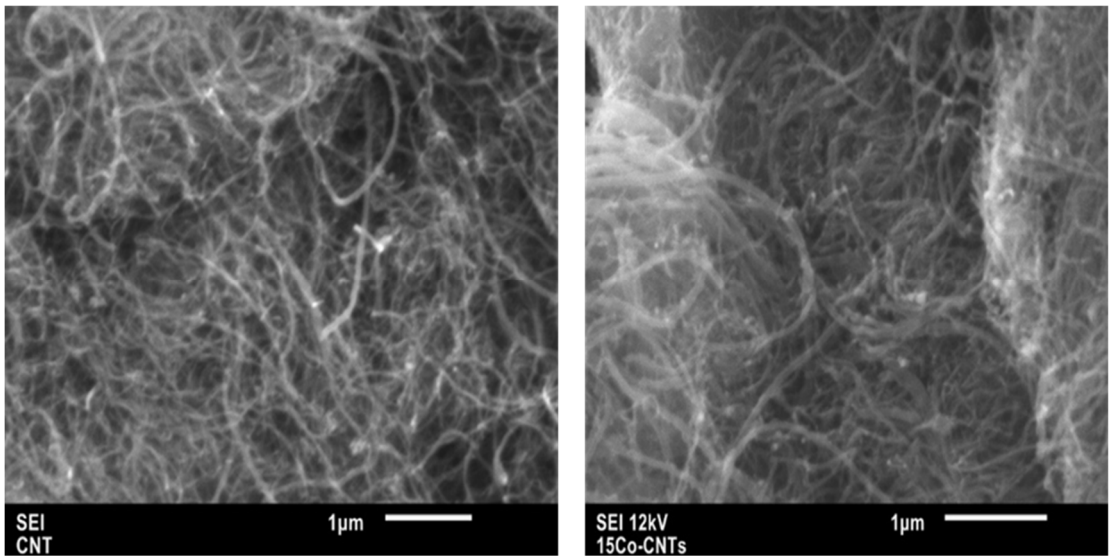

Figure D.1 SEM micrographs of CNTs (left) and 15Co/CNT35 catalyst (right) with 25 K magnification.

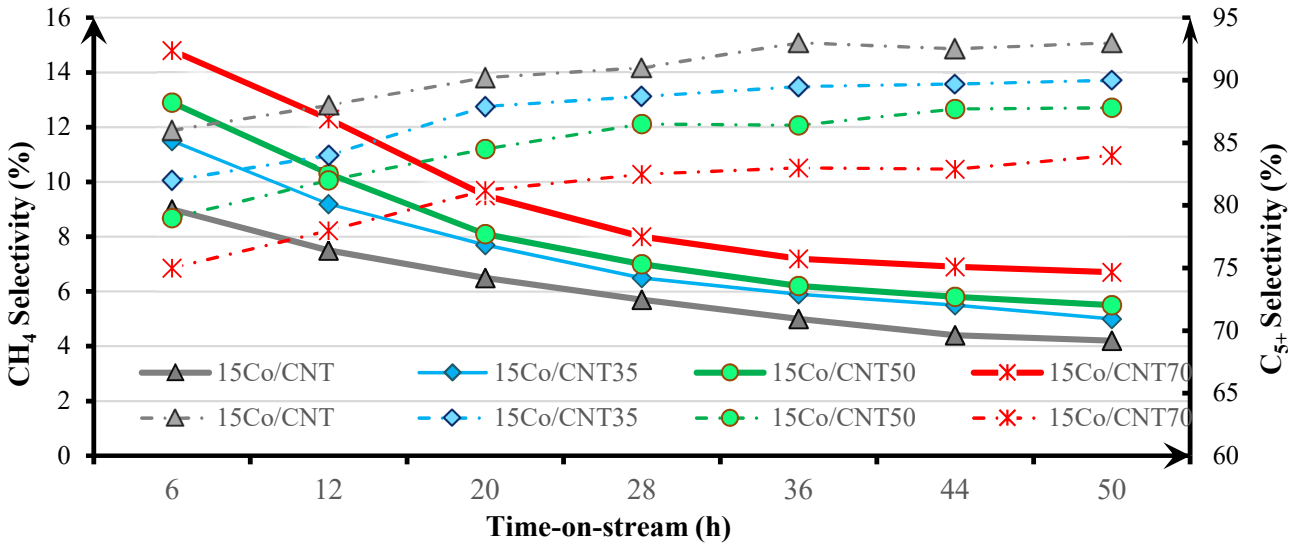

Figure D.2 CH_4 (solid lines) and C_{5+} selectivities (dashed lines) for 15Co/CNT and 15Co/CNTX catalysts.

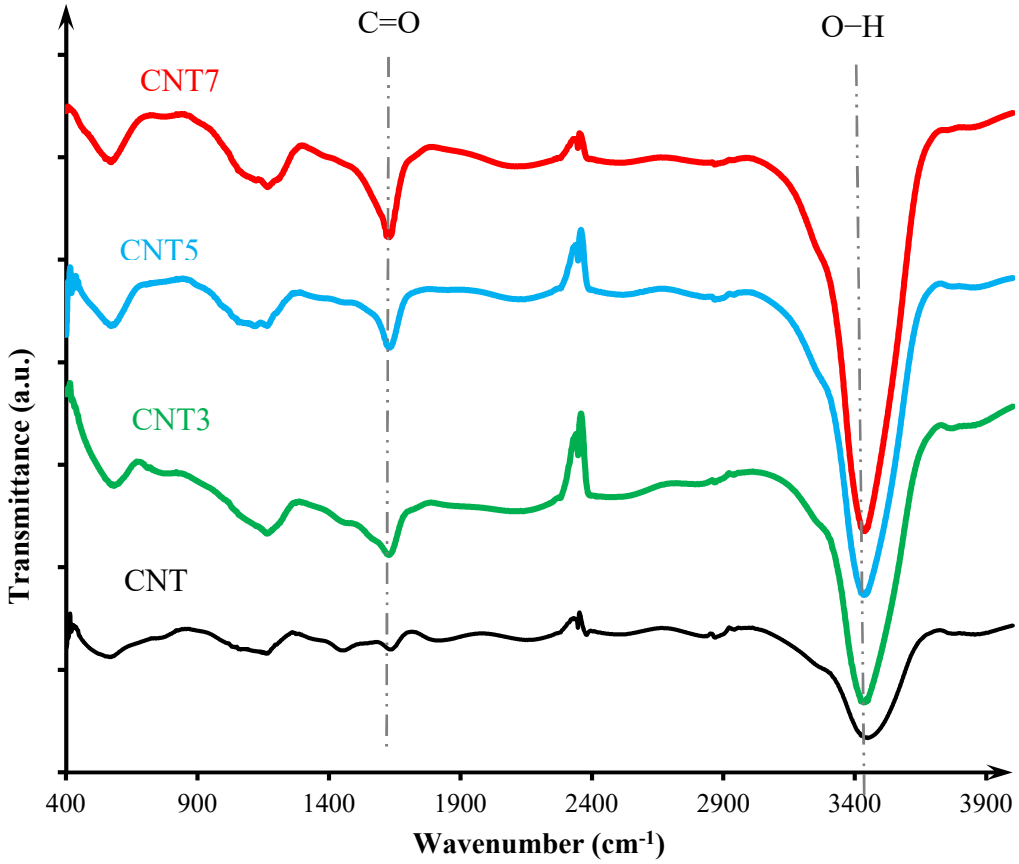

Figure D.3 FTIR spectra of pristine CNT and CNTX (treated with different concentrations of nitric acid).

APPENDIX E: SUPPORTING INFORMATION FOR CHAPTER 6

Table E.1 Some literature date on methane and CO_2 selectivity for cobalt catalyst in FTS

Catalyst	T (°C)	P (MPa)	Syngas Flow	S_{CO_2}(%)	S_{C_4}(%)	Reference
15Co(E)/m-Al_2O_3	230	2.76	900 h^{-1}	2.5	15.1	Present work
15Co(E)/m-Al_2O_3	220	1.38	600 h^{-1}	2.0	7.8	Present work
Co/SiO_2	230	2.41	~ 12000 h^{-1}	-[a]	16.6	[234]
10Co/SBA-15	210	0.1	-	-[a]	15.2	[235]
10Co-0.2Pt/SiO_2	240	1.03	-	9.5	13.8	[236]
10Co/CNTs	240	1.03	10 $g.h.mol^{-1}$	1.6	17.5	[72]
15Co/Al_2O_3	210	1.03	4 $SL.g^{-1}.h^{-1}$	-[a]	14.23	[237]

[a] The CO_2 selectivity has not been reported.

Table E.2 Experimental design, CO conversion and C_{5+} selectivity for 15Co(A)/m-Al_2O_3 catalyst

Temperature (˚C)	Pressure (MPa)	GHSV (h^{-1})	CO Conversion (%)	C_{5+}Selectivity (%)
220	1.38	600	44	84.3
220	2.07	900	41	83.9
220	2.76	1200	34	83.2
230	1.38	900	55	81.4
230	2.07	1200	50	81
230	2.76	600	62	82.4
240	1.38	1200	65	78.7
240	2.07	600	74	79.7
240	2.76	900	70	79.4

Table E.3 ANOVA data on CO conversion for 15Co(A)/m-Al_2O_3 catalyst

Source	DF	Adj. SS	Adj. MS	F-Value	P-Value
Temperature	2	1352	676	289.71	0.003
Pressure	2	0.67	0.333	0.14	0.875
GHSV	2	160.67	80.333	34.43	0.028
Residual	2	4.67	2.333		
Total	8	1518			

Table E.4 ANOVA data on C_{5+} selectivity for 15Co(A)/m-Al_2O_3 catalyst

Source	DF	Adj. SS	Adj. MS	F-Value	P-Value
Temperature	2	30.8356	15.4178	375.03	0.003
Pressure	2	0.0622	0.0311	0.76	0.569
GHSV	2	2.0422	1.0211	24.84	0.039
Residual	2	0.0822	0.0411		
Total	8	33.0222			

Table E.5 Experimental design, CO conversion and C_{5+} selectivity for 15Co(W)/m-Al_2O_3 catalyst

Temperature (˚C)	Pressure (MPa)	GHSV (h^{-1})	CO Conversion (%)	C_{5+}Selectivity (%)
220	1.38	600	30	87.3
220	2.07	900	27	87
220	2.76	1200	22	86.5
230	1.38	900	39	84.5
230	2.07	1200	33	84.1
230	2.76	600	46	85.3
240	1.38	1200	47	81.5
240	2.07	600	57	82.6
240	2.76	900	51	82.2

Table E.6 ANOVA data on CO conversion for 15Co(W)/m-Al_2O_3 catalyst

Source	DF	Adj. SS	Adj. MS	F-Value	P-Value
Temperature	2	962.89	481.444	154.75	0.006
Pressure	2	1.56	0.778	0.25	0.8
GHSV	2	160.22	80.111	25.75	0.037
Residual	2	6.22	3.111		
Total	8	1130.89			

Table E.7 ANOVA data on C_{5+} selectivity for 15Co(W)/m-Al_2O_3 catalyst

Source	DF	Adj. SS	Adj. MS	F-Value	P-Value
Temperature	2	35.0689	17.5344	3945.25	0
Pressure	2	0.0822	0.0411	9.25	0.098
GHSV	2	1.6022	0.8011	180.25	0.006
Residual	2	0.0089	0.0044		
Total	8	36.7622			

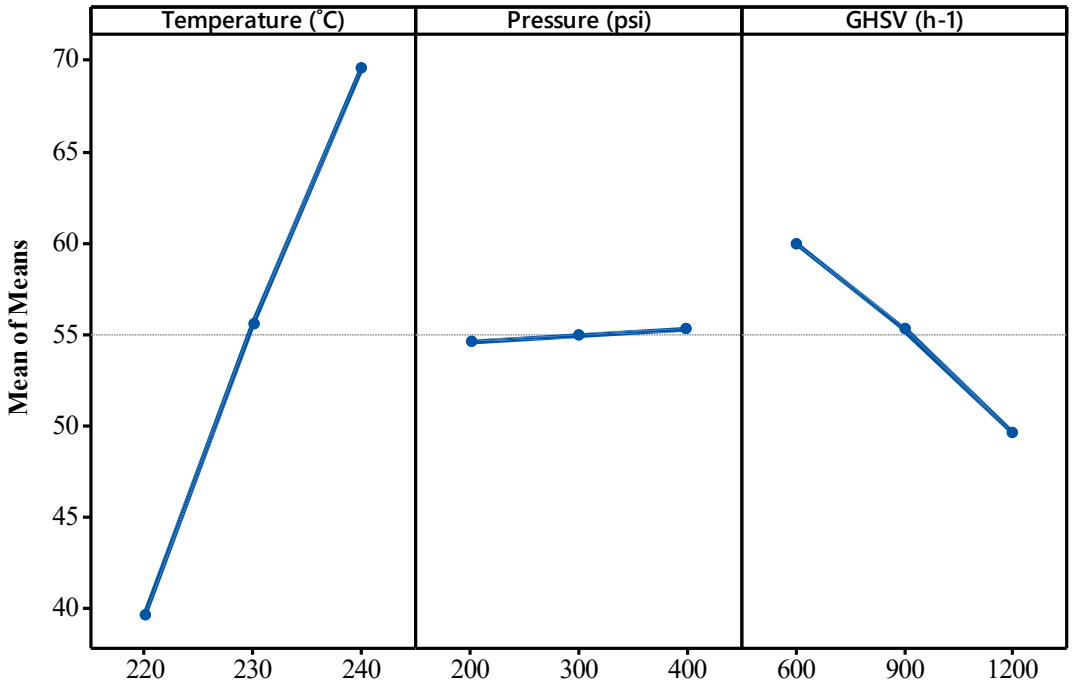

Figure E.1 Main effect plot means of CO conversion (%) for 15Co(A)/m-Al_2O_3 catalyst

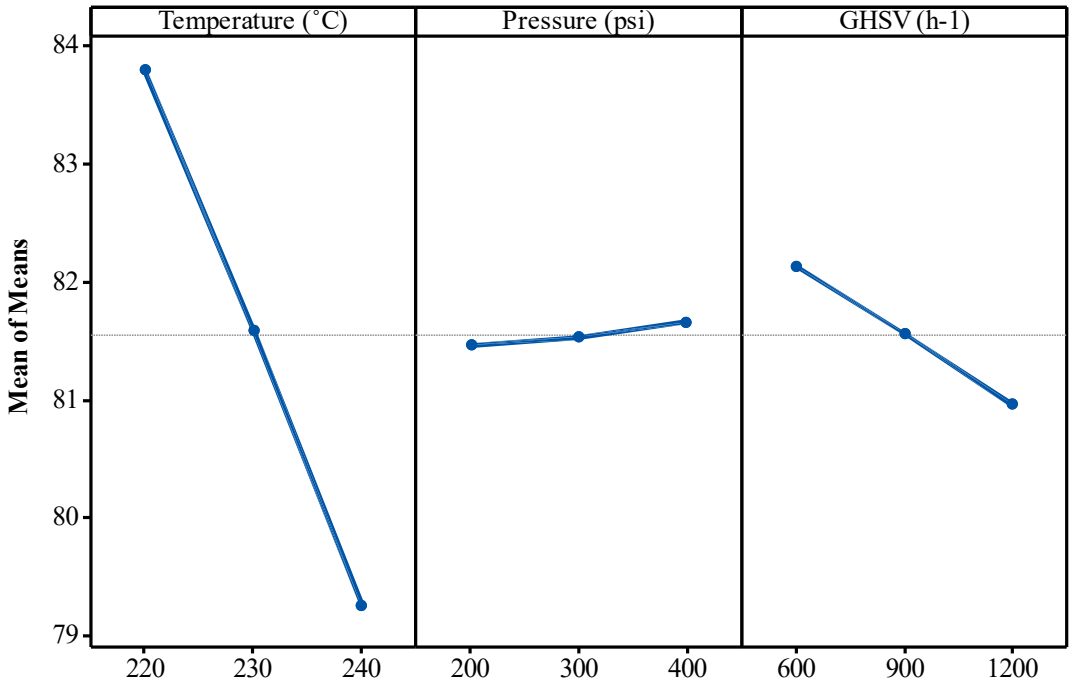

Figure E.2 Main effect plot means of C_{5+} selectivity (%) for 15Co(A)/m-Al_2O_3 catalyst

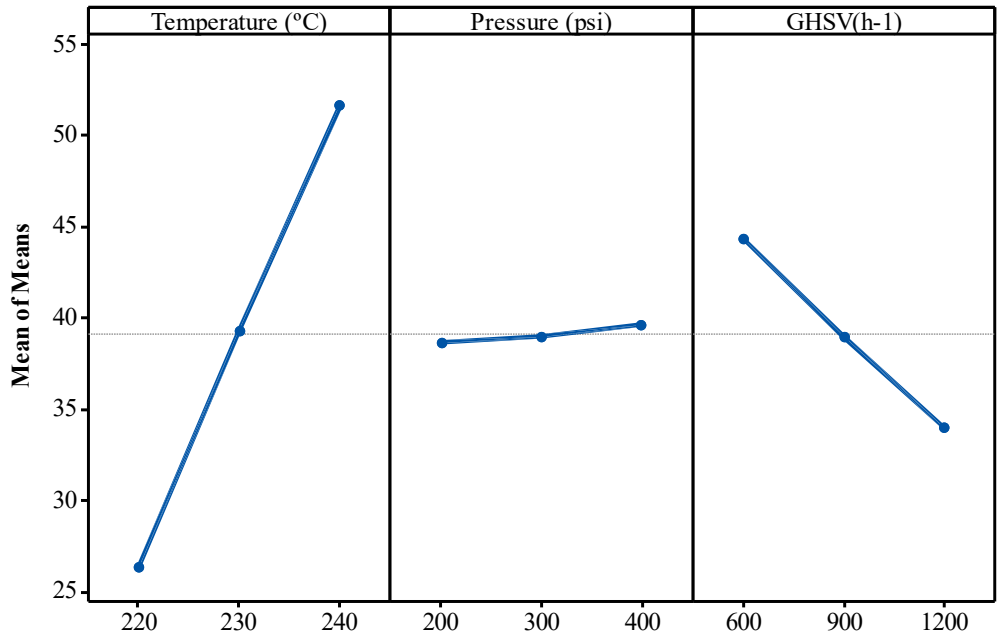

Figure E.3 Main effect plot means of CO conversion (%) for 15Co(W)/m-Al_2O_3 catalyst

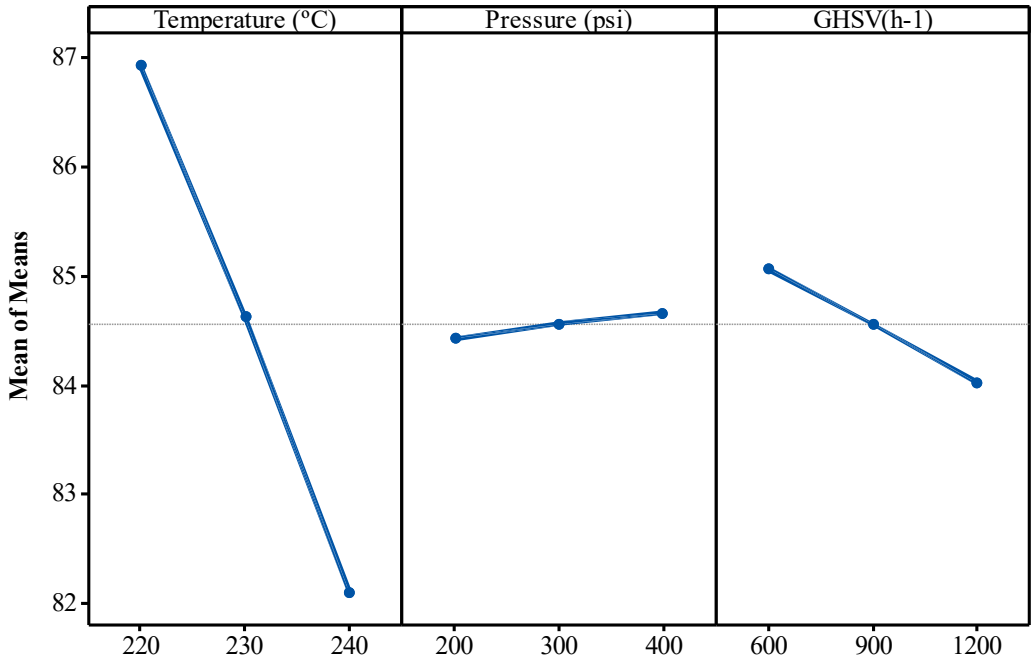

Figure E.4 Main effect plot means of C_{5+} selectivity (%) for 15Co(W)/m-Al_2O_3 catalyst

APPENDIX F: SUPPORTING INFORMATION FOR CHPATER 8

Table F.1 The fitting data for the XANES spectra of the oxidized catalysts using Athena software

Catalyst	included data points	R-factor	Chi-square	Reduced Chi-squar	CoO weight[1]	Co_3O_4 weight
Co/mAl_2O_3	112	0.01345	0.27404	0.00247	0.000	1.000
$CoRu/mAl_2O_3$	113	0.01212	0.25313	0.00228	0.000	1.000
$CoRe/mAl_2O_3$	112	0.01467	0.29587	0.00269	0.004	0.996
$CoPt/mAl_2O_3$	112	0.01569	0.32746	0.00295	0.000	1.000
$CoIr/mAl_2O_3$	113	0.01380	0.29063	0.00262	0.004	0.996
$CoMn/mAl_2O_3$	113	0.00695	0.13683	0.00123	0.001	0.999
CoY/mAl_2O_3	112	0.01663	0.34099	0.00310	0.000	1.000

1. Weights forced between 0 and 1.

Table F.2 Time-on-stream data for activity and selectivity of the promoted catalysts

$CoRu/mAl_2O_3$				$CoRe/mAl_2O_3$				$CoPt/mAl_2O_3$			
TOS	CO Conv. (%)	CH_4 Selec. (%)	C_{5+} Selec. (%)	TOS	CO Conv. (%)	CH_4 Selec. (%)	C_{5+} Selec. (%)	TOS	CO Conv. (%)	CH_4 Selec. (%)	C_{5+} Selec. (%)
10	79.0	3.9	96.0	13	86.7	11.8	86.7	13	91.6	13.4	86.0
15	86.2	6.3	93.5	20.5	96.7	15.6	82.0	20.5	98.8	14.2	84.4
21	91.2	9.3	90.3	35	96.4	22.2	74.5	35	97.3	16.9	81.3
31	94.7	14.1	84.6	44.5	93.0	22.2	74.6	44	93.1	18.7	79.2
47	92.3	16.2	82.0	59	90.3	21.0	75.9	58	90.2	19.9	77.0
65	90.2	16.1	81.4	68	88.3	20.3	77.4	68.5	88.6	19.1	77.6
80	87.9	15.9	81.7	81	86.2	18.4	78.0	81.5	87.1	18.2	78.1
92	86.9	15.7	81.6	92.5	85.7	17.8	79.3	92.5	85.0	18.0	78.5
115	86.3	15.4	82.3	107	84.8	17.0	80.1	104.5	83.1	17.5	79.1
				125	84.1	16.5	80.7	125.0	81.6	17.1	79.6
$CoIr/mAl_2O_3$				$CoMn/mAl_2O_3$				CoY/mAl_2O_3			
TOS	CO Conv. (%)	CH_4 Selec. (%)	C_{5+} Selec. (%)	TOS	CO Conv. (%)	CH_4 Selec. (%)	C_{5+} Selec. (%)	TOS	CO Conv. (%)	CH_4 Selec. (%)	C_{5+} Selec. (%)
12	89.3	10.2	89.1	10	66.3	4.8	94.9	10	60.4	8.2	91.3
19.5	98.6	12.3	86.0	21	70.3	9.3	89.6	26	**71.4**	10.4	86.3
32.5	98.1	18.0	79.7	38	68.7	13.0	84.3	37	68.5	14.6	82.1
43	93.3	20.6	76.7	45.5	66.9	14.6	82.1	50	65.4	19.4	76.1
57.5	88.2	21.1	75.7	58.5	65.5	16.0	82.0	61	63.8	19.3	76.6
67.5	85.9	21.6	74.8	70	63.9	14.9	80.2	72	62.6	18.9	76.8
79.5	84.0	21.4	74.9	84	63.3	14.6	81.2	84.5	61.9	18.3	77.5
92	82.5	21.0	75.3	98	63.0	15.0	81.8	97	61.3	17.8	78.6
104.5	81.8	19.6	76.0	115	62.8	14.5	82.2	118	61.1	18.3	79.4
120	80.2	19.1	76.8								

Table F.3 Surface area of the deconvoluted TPR profiles

Catalyst	1st main peak surface area (cm^3 STP/g)	2nd main peak surface area (cm^3 STP/g)
Co/mAl_2O_3	15.5	35.6
$CoRu/mAl_2O_3$	21.2	50.8
$CoRe/mAl_2O_3$	19.1	49.1
$CoPt/mAl_2O_3$	22.4	47.8
$CoIr/mAl_2O_3$	22.1	49.8
$CoMn/mAl_2O_3$	20.3	38.5
CoY/mAl_2O_3	18.1	44.3

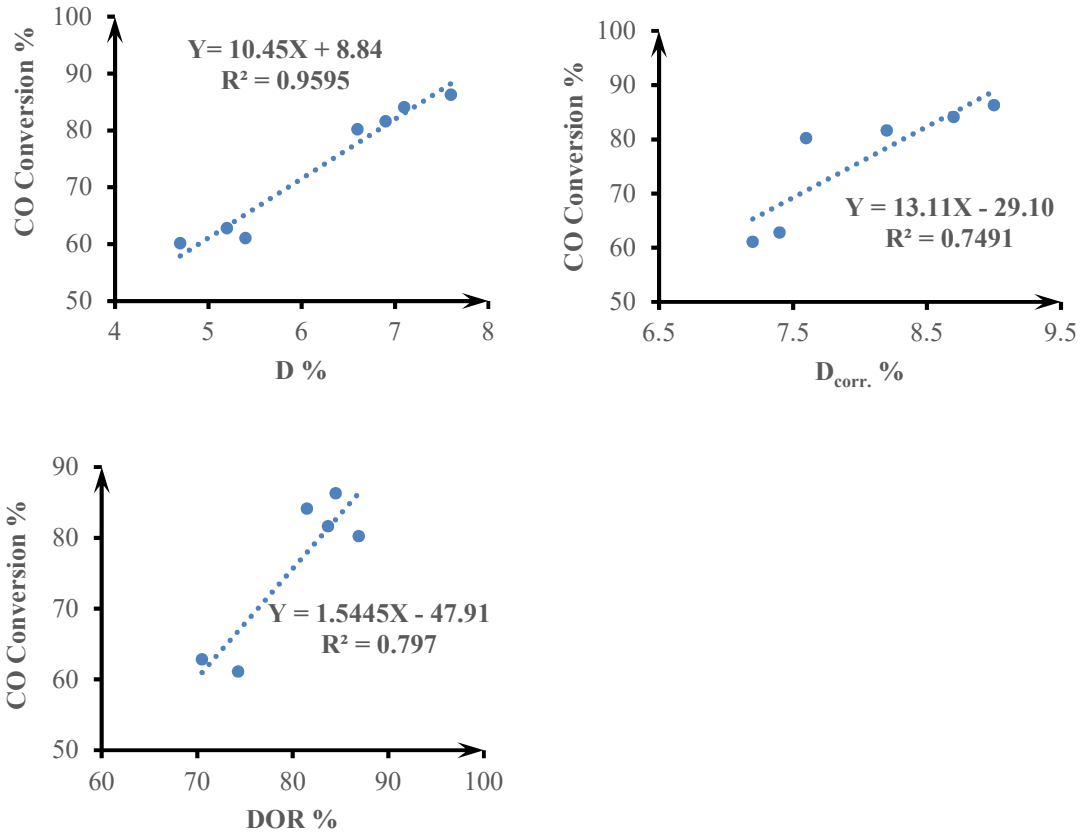

Figure F.1 Correlation between CO conversion and apparent dispersion, corrected dispersion and degree of reduction

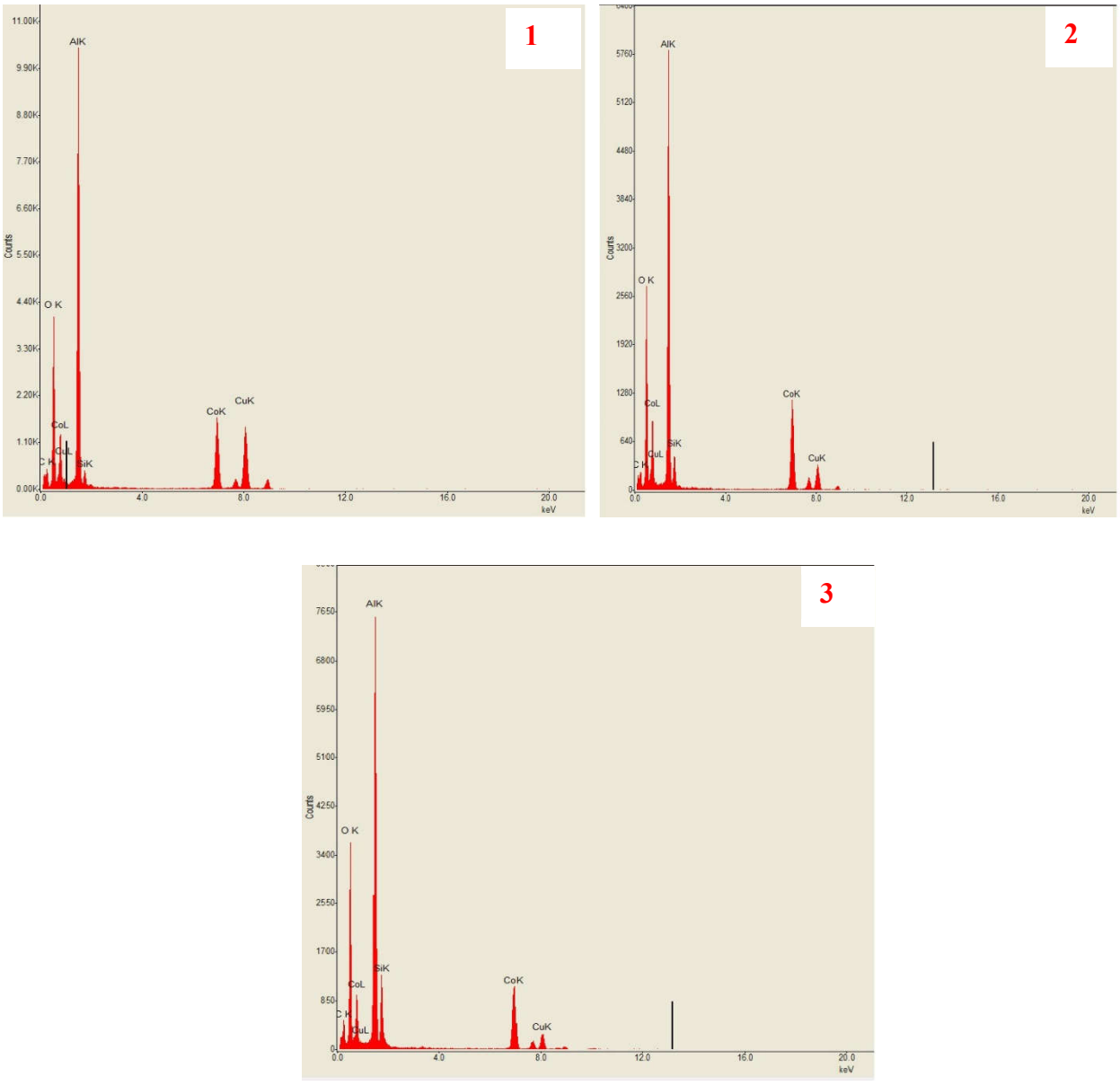

Figure F.2 EDAX mapping of (1) Co/mAl_2O_3, (2) CoRu/mAl_2O_3, (3) CoMn/mAl_2O_3.

APPENDIX G: PERMISSION TO REUSE THE PUBLISHED PAPERS, TABLES, PICTURES

Copyright Clearance Center RightsLink®

Home | Account Info | Help

ELSEVIER

Chapter: 7.20 Fischer–Tropsch Synthesis: Catalysts and Chemistry
Book: Comprehensive Inorganic Chemistry IIFrom Elements to Applications, Volume 4
Author: J. van de Loosdrecht,F.G. Botes,I.M. Ciobica,A. Ferreira,P. Gibson,D.J. Moodley,A.M. Saib,J.L. Visagie,C.J. Weststrate,J.W. Niemantsverdriet
Publisher: Elsevier
Date: Jan 1, 2013
Copyright © 2013, Elsevier

Logged in as:
Vahid Vosoughi
University of Saskatchewan
Account #:
3001213041
LOGOUT

Order Completed

Thank you for your order.

This Agreement between University of Saskatchewan -- Vahid Vosoughi ("You") and Elsevier ("Elsevier") consists of your license details and the terms and conditions provided by Elsevier and Copyright Clearance Center.

Your confirmation email will contain your order number for future reference.

printable details

License Number	4232951080218
License date	Nov 20, 2017
Licensed Content Publisher	Elsevier
Licensed Content Publication	Elsevier Books
Licensed Content Title	Comprehensive Inorganic Chemistry IIFrom Elements to Applications, Volume 4
Licensed Content Author	J. van de Loosdrecht,F.G. Botes,I.M. Ciobica,A. Ferreira,P. Gibson,D.J. Moodley,A.M. Saib,J.L. Visagie,C.J. Weststrate,J.W. Niemantsverdriet
Licensed Content Date	Jan 1, 2013
Licensed Content Pages	33
Type of Use	reuse in a thesis/dissertation
Portion	figures/tables/illustrations
Number of figures/tables/illustrations	2
Format	both print and electronic
Are you the author of this Elsevier chapter?	No
Will you be translating?	No
Original figure numbers	Table 1. Fischer–Tropsch synthesis, current commercial plants and plants under construction and Table 7. Fischer–Tropsch Reaction Mechanisms
Title of your thesis/dissertation	DEVELOPMENT OF SUPPORTED COBALT CATALYST FOR FISCHER-TROPSCH SYNTHESIS
Expected completion date	Jan 2018
Estimated size (number of pages)	190
Requestor Location	University of Saskatchewan 57 Campus Dr. Saskatoon, SK S7N 5A9 Canada Attn: University of Saskatchewan
Total	0.00 CAD

Figure G.1 Permission to use Table 2.1 and Table 2.2

Permission Request Form: Vahid Vosoughi

CONTRACTS-COPYRIGHT (shared) <Contracts-Copyright@rsc.org>
Fri 11/10/2017 7:42 AM

Dear Vahid

The Royal Society of Chemistry hereby grants permission for the use of the material specified below in the work described and in all subsequent editions of the work for distribution throughout the world, in all media including electronic and microfilm. You may use the material in conjunction with computer-based electronic and information retrieval systems, grant permissions for photocopying, reproductions and reprints, translate the material and to publish the translation, and authorize document delivery and abstracting and indexing services. The Royal Society of Chemistry is a signatory to the STM Guidelines on Permissions (available on request).

Please note that if the material specified below or any part of it appears with credit or acknowledgement to a third party then you must also secure permission from that third party before reproducing that material.

Please ensure that the published article carries a credit to The Royal Society of Chemistry in the following format:

[Original citation] – Reproduced by permission of The Royal Society of Chemistry

and that any electronic version of the work includes a hyperlink to the article on the Royal Society of Chemistry website.

Regards

Gill Cockhead
Publishing Contracts & Copyright Executive

Gill Cockhead
Publishing Contracts & Copyright Executive
Royal Society of Chemistry,
Thomas Graham House,
Science Park, Milton Road,
Cambridge, CB4 0WF, UK
Tel +44 (0) 1223 432134

Winner of The Queen's Award for Enterprise, International Trade 2013

noreply@rsc.org
Thu 11/2/2017 3:32 AM

To: contracts-copyright@rsc.org <Contracts-Copyright@rsc.org>;
Cc: Vosoughi, Vahid;

Name : Vahid Vosoughi
Address :

57 Campus Dr.,
University of Saskatchewan,
Saskatoon,
Saskatchewan, S7N 5A9,
Canada

Tel :
Fax :
Email : v.vosoughi@usask.ca

I am preparing the following work for publication:

Article/Chapter Title : THESIS: DEVELOPMENT OF SUPPORTED COBALT CATALYST FOR FISCHER-TROPSCH SYNTHESIS
Journal/Book Title :
Editor/Author(s) : Vahid Vosoughi
Publisher : University of Sasktchewan

I would very much appreciate your permission to use the following material:

Journal/Book Title : Catalysis in the Refining of Fischer-Tropsch Syncrude,, 2010
Editor/Author(s) : Arno de Klerk, E. Furimsky
Volume Number : 978-1-84973-080-8
Year of Publication : 2010
Description of Material : Figure 3.1 Industrially applied Fischer–Tropsch reactor technologies.
Page(s) : 14

Any Additional Comments :

Permission to use one picture mentioned above

Figure G.2 Permission to use Figure 2.1

Copyright Clearance Center RightsLink®

Home | Account Info | Help

Title: Fischer–Tropsch synthesis in a microstructured reactor

Author: Rune Myrstad,Sigrid Eri,Peter Pfeifer,Erling Rytter,Anders Holmen

Publication: Catalysis Today

Publisher: Elsevier

Date: September 2009

Logged in as:
Vahid Vosoughi
University of Saskatchewan

LOGOUT

Order Completed

Thank you for your order.

This Agreement between University of Saskatchewan -- Vahid Vosoughi ("You") and Elsevier ("Elsevier") consists of your license details and the terms and conditions provided by Elsevier and Copyright Clearance Center.

Your confirmation email will contain your order number for future reference.

printable details

License Number	4220680889294
License date	Nov 02, 2017
Licensed Content Publisher	Elsevier
Licensed Content Publication	Catalysis Today
Licensed Content Title	Fischer–Tropsch synthesis in a microstructured reactor
Licensed Content Author	Rune Myrstad,Sigrid Eri,Peter Pfeifer,Erling Rytter,Anders Holmen
Licensed Content Date	Sep 1, 2009
Licensed Content Volume	147
Licensed Content Issue	n/a
Licensed Content Pages	4
Type of Use	reuse in a thesis/dissertation
Portion	figures/tables/illustrations
Number of figures/tables/illustrations	1
Format	both print and electronic
Are you the author of this Elsevier article?	No
Will you be translating?	No
Original figure numbers	Fig. 2. SEM image of a catalyst foil and picture of the microstructured reactor.
Title of your thesis/dissertation	DEVELOPMENT OF SUPPORTED COBALT CATALYST FOR FISCHER-TROPSCH SYNTHESIS
Expected completion date	Jan 2018
Estimated size (number of pages)	190
Requestor Location	University of Saskatchewan 57 Campus Dr. Saskatoon, SK S7N 5A9 Canada Attn: University of Saskatchewan
Total	0.00 CAD

Figure G.3 Permission to use Figure 2.2

Figure G.4 Permission to use the paper: “Comparison of nitrogen adsorption and transmission electron microscopy analyses for structural characterization of carbon nanotubes”

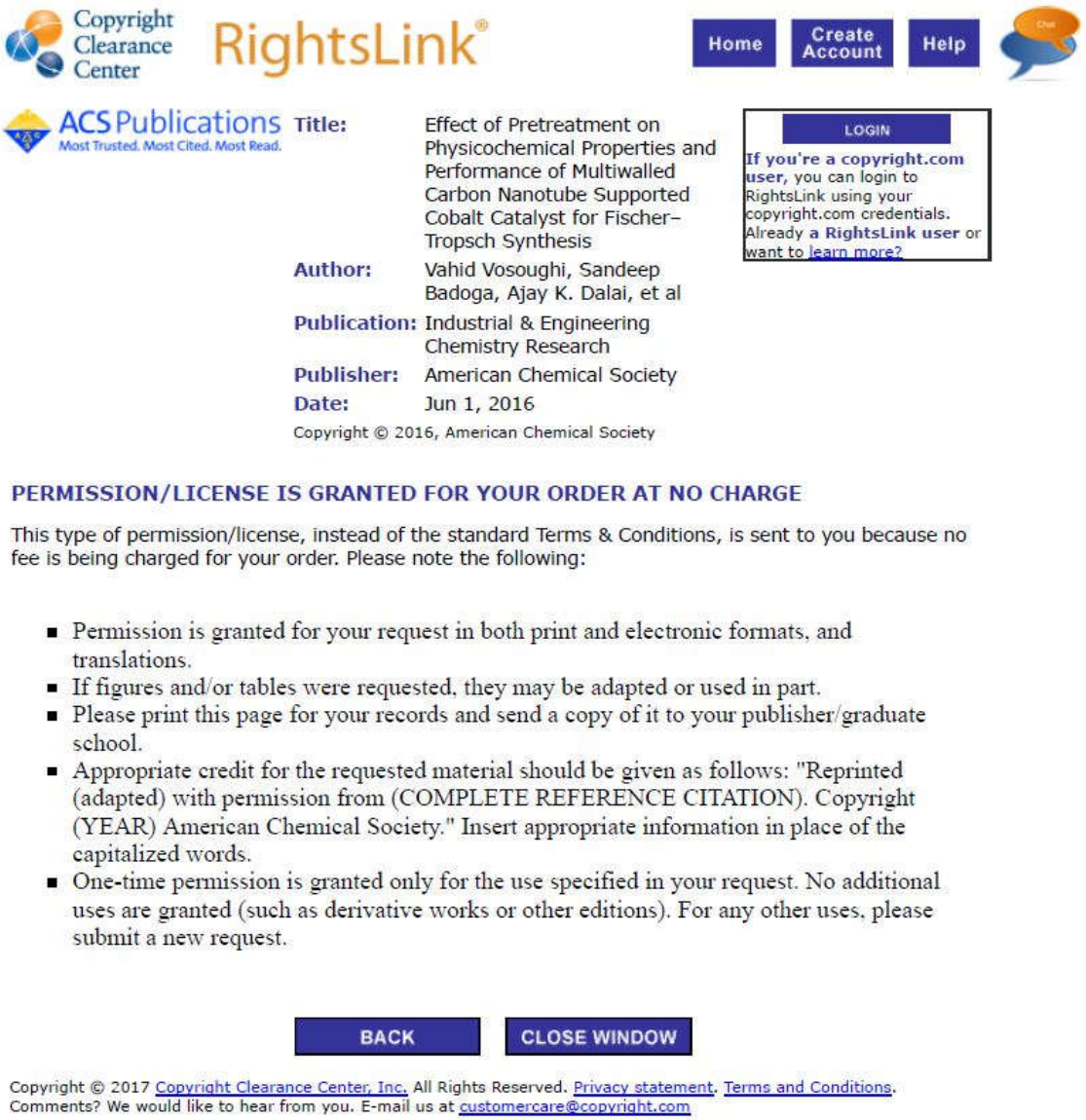

Figure G.5 Permission to use the paper: “Effect of Pretreatment on Physicochemical Properties and Performance of Multiwalled Carbon Nanotube Supported Cobalt Catalyst for Fischer−Tropsch Synthesis”

Figure G.6 Permission to use the paper: “Performance of promoted Iron/CNT catalyst for Fischer−Tropsch Synthesis: Influence of pellet shapes and binder loading”

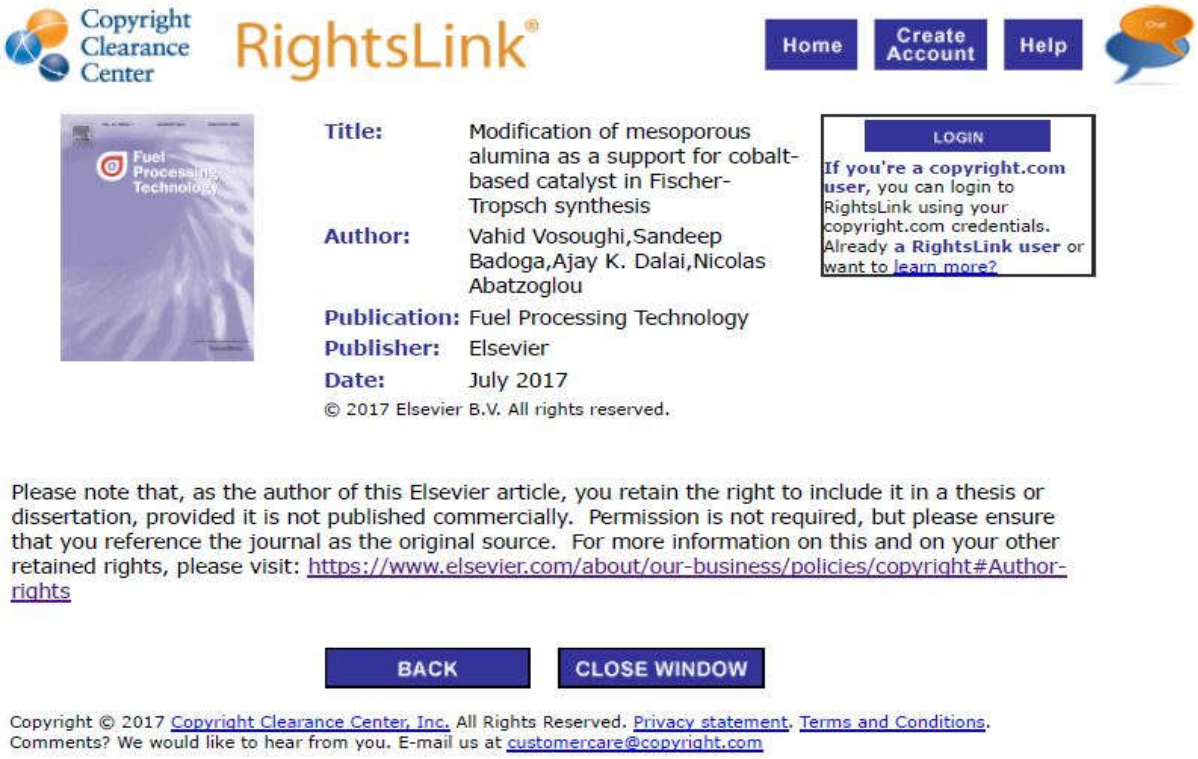

Figure G.7 Permission to use the paper: “Modification of mesoporous alumina as a support for Co-based catalyst in Fischer–Tropsch Synthesis”

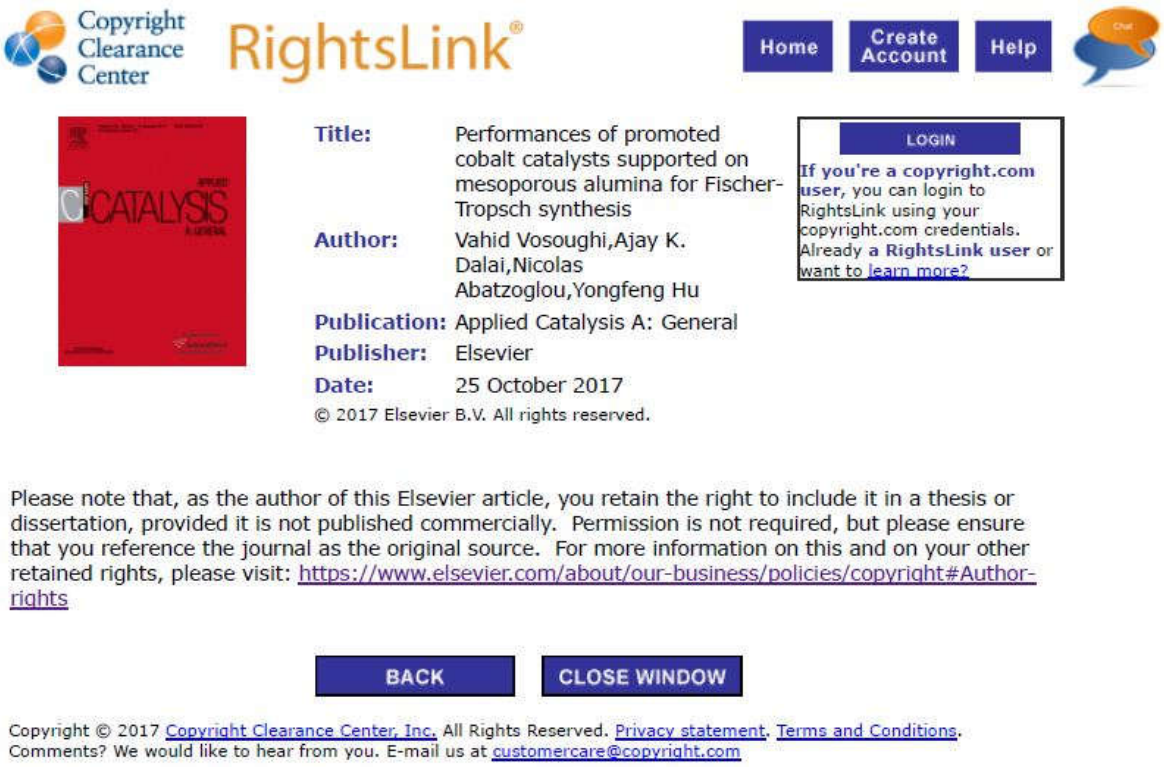

Figure G.8 Permission to use the paper: “Performances of promoted cobalt catalysts supported on mesoporous alumina for Fischer−Tropsch synthesis”